6th International Online Conference on Electronics, Materials Engineering & Nano-Technology

# IEMENTech 2022

organized by

Dept. of Electronics & Comm. Engg.
Institute of Engineering & Management

2nd to 4th December 2022

# 2022 6th International Conference on Electronics, Materials Engineering & Nano-Technology (IEMENTech)

Organized By
Dept. of
Electronics & Communication Engineering

Edited By
Dr. G. S. Taki, Dr. Ratna Chakrabarty, Prof. Mili Sarkar,
Prof. Soumik Kumar Kundu, Prof. Samit Karmakar

December 2-4, 2022
**Virtual Conference**

# Contents
## Contributory Papers

| | | |
|---|---|---|
| *1570871195* | *Codebook Optimization Using Jaya Algorithm for Image Compression* | Suvojit Acharjee |
| *1570866146* | *Haze Wireless Sensor System Development and Measurement* | Kama Azura Othman |
| *1570871199* | *Effect Of Modulation Index On Total Harmonic Distortion And Individual Harmonics In A Single-Phase Five Level SPWM Based CHML Inverter-A* | Gautam Ghosh |
| *1570871212* | *Null Placement in Uniform Linear Array by Phase Control of Edge Elements* | Sandipan Mitra |
| *1570871279* | *Comparative Study of GaN HEMT on Recent Trends and Future Scope Along with It's Applications* | Avishek Saha |
| *1570871228* | *Optical Property Study of Electro-Deposited Tin Oxide Thin Film* | Uddipan Agasti |
| *1570865994* | *To Produce High Resolution Deep Space Images Using Real-Enhanced Super Resolution General Adversarial Networks* | Varad Abhijit Joshi |
| *1570866584* | *Optimizing Deep Learning Neural Networks: Brain to Computer Interface EEG-Based Imagined Word Prediction for Speech Disability* | Babu Chinta |
| *1570870334* | *9's Complement Encoder Using QCA Schematics* | Ratna Chakrabarty |
| *1570871277* | *Development & Property Study of Partially Depleted Silicon-On-Insulator MOSFET* | Bidyendu Ghoshal |

# Using an RFID card with a password to open a door

OUESSE Mohamed E. A., Baboucar DIATTA, Mohamed SALL and Adrien BASSE
*Dept. of Information and Communication Technologies*
*Alioune Diop University of Bambey*
Bambey, Senegal
omea82@yahoo.fr, baboucar.diatta@uadb.edu.sn,
mohamed.sall@uadb.edu.sn and adrien.basse@uadb.edu.sn

Ridha BOUALLEGUE
*Innov'Com Lab, Sup'Com*
*Université de Carthage, Tunisie*
Tunis, Tunisie
ridha.bouallegue@gmail.com

***Abstract*—Security is of paramount importance in homes, schools, offices and industries. Traditional mechanisms such as locks and keys, door chains etc. have all shown their limitations. These limitations include: the key can break in the lock; the lock can be defective; the key can be stolen or fraudulently duplicated resulting in unauthorized access to a building. This article describes the development of a system to secure access to a building.**
**In this system, users who are authorized to access the building are identified by their radio frequency identification (RFID) card and authenticated by a password. This system provides an effective means of controlling the entry and exit of authorized persons, as well as preventing the entry of unauthorized users and reporting intrusion attempts.**
**To set up this project, we need to acquire a radio frequency identification (RFID) reader, an RFID module, an LCD screen, an ESP8266 MCU node, a database manager and a website.**

***Keywords*—RFID, Password, Security, ESP8266**

## I. Introduction

Home automation brings together technologies from electronics, automation, computing and telecommunications in order to provide technical solutions to meet the needs of user comfort, security and communication that the can be found in public or private living and working places such as homes, hotels, businesses, shops and among others. Home automation not only opens up new possibilities in the field of home automation, but also provides a means for individuals to control and manage their environment. Thanks to this new technology, the occupant will be better able to manage his work and living environment in terms of safety, comfort, communications and household applications.

Currently, the most common way to open or close a door is the physical use of a metal key. But this mechanical system poses many problems because the keys can be lost, misplaced or broken and/or stuck in the lock.

With the digital revolution, more and more devices and objects of our daily life are becoming more intelligent, connectable to networks and controllable with a smartphone or thanks to sensors. Indeed, the evolution of technology now makes it possible to design work and housing spaces that are better suited both in construction and in revolution. These advances are made possible thanks to electronics and the new design of communication networks both inside and outside homes.

One solution to solve said problems is the creation of an access system with an RFID card. This method will allow people with an access badge to open a door. Badges are interesting alternatives. However, another problem arises in that badges can be stolen; the purpose of this paper is to secure said RFID card.

## II. State of the art

The smart home is one of several topics that have attracted significant research attention in recent years. Home automation allows the monitoring and automatic control of homes without human intervention [3], [4] and [5]. Indeed, home automation makes the house smart by allowing it to perform many functions, having a very important impact on the daily life, like the comfort, the energy efficiency, the safety and the environment. Domestic security being an important and fundamental aspect of comfort and fulfillment in the living environment, a lot of efforts have been made in research to propose solutions in the face of the increasing criminality and robbery rate. It is in this sense that many research works have proposed systems that allow identification by radio frequency (RFID) to secure and make the living environment more pleasant.

This is the case in [6] where a brief review of RFID systems was carried out. This review takes into account all the solutions both with chips and without chips. The authors of this work have presented a classification of the main types of sensors in the form of a diagram, and for each type of sensor, the principle of operation is presented and discussed. The paper also presents the main uses of radio frequency identification (RFID) sensors in case of Internet of Things (IoT). In [7], a system for identification and automatic authentication is proposed for deployment at the doors of every home, office, campus, and building to authenticate authorized persons. In the system, a gate lock can be managed by an RFID card. Radio Frequency Identification (RFID) represents a wireless solution for managing the access control system. This strategy not only lowers the cost but also improves the reliability and ease of use and maintenance of the authentication system. In [8], the authors propose a solution that improves the management of

home control and supervises all the house access points that are commonly susceptible to trespassers and burglars.

The suggested solution relies on person identification with the help of detection method and radio frequency identification (RFID) as a technique to improve the efficiency of house security systems. A remote server in the cloud is used to analyze and identify the person who wishes to have the authorization to get into the home. The proposed system records any unlawful intrusive activities at the house's door or windows. In [9], the authors combined RFID systems and wireless sensors to leverage their benefits and overcome limitations to enable new applications in the scope of Internet of Things.

## III. Presentation the ESP8266 NodeMCU

### A. Definition

The NodeMCU ESP8266 which is an Open Source programmable microcontroller with Arduino IDE and having an integrated Wifi module ideal for Connected Objects is an IoT platform, hardware and software, based on an ESP8266 WIFI SoC manufactured by Expressif System.Male and female side connectors allow modules to be inserted on the breadboard. The Wi-Fi wireless interface that allows the creation of wireless access point and the hosting of a server manages the sending and receiving of data on the Internet.

Thanks to this, it is possible to create a server which hosts a Web page making it possible to control the microcontroller remotely.

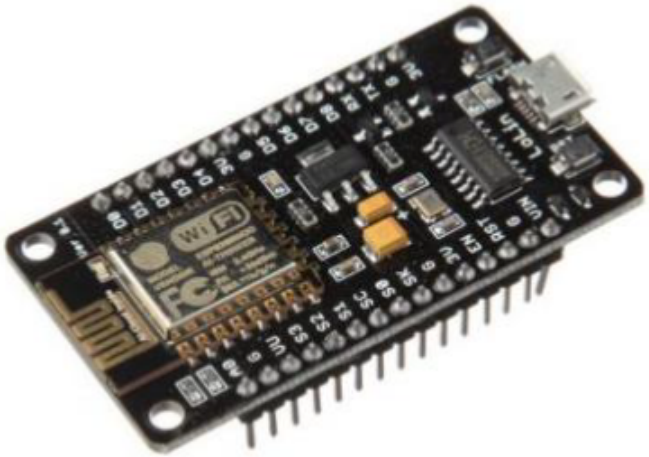

Fig. 1. NodeMCU

### B. Principle of operation

The ESP8266 Node MCU contains an ESP-12 module containing a 32-bit microprocessor. It incorporates a Wi-Fi transceiver that allows it to connect to existing networks or to set up its own network.
The nodeMCU ESP8266 which is the solution of an autonomous Wifi network provides a gateway to manage the communication between the microcontroller and the Wifi module. It is also capable of relaunching stand-alone applications. This module is designed with an integrated USB port and a rich assortment of pins. To connect the nodeMCU to the computer and flash it seamlessly, we have need a micro USB cable.

### C. The different pins

The microcontroller has 16 GPIOs (11 Digital I/O) available on the development board pins. On the 25 pins, we have:

- 4 PWM outputs
- Some pins are reserved for serial communication protocols (SPI, I2C, Serial).

Note also the presence of two push buttons:

- Rst allows you to reset the card (reset)
- Flash allows you to launch a memory flashing sequence, without having to play with the PINs. Useless when using the Arduino IDE.

It also has an analog input called ADC. The conversion is done on 10 bits, so a value from 0 to 1023 and the maximum value corresponds to an input of 1 Volt.

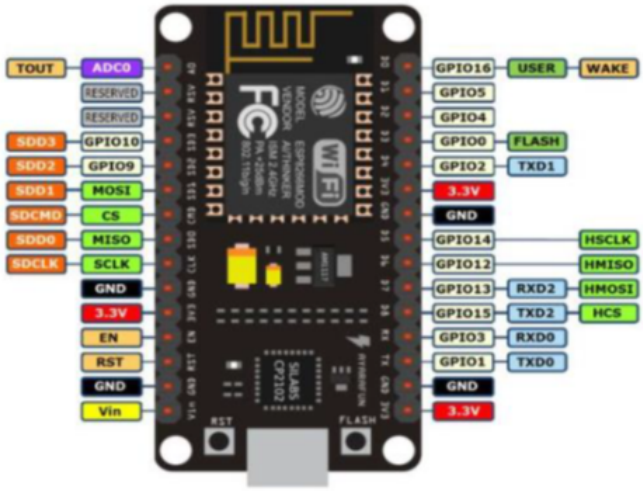


Fig. 2. NodeMCU Pins

TABLE I
NodeMCU Pins

| IO index | ESP8266 pin | IO index | ESP8266 pin |
|---|---|---|---|
| D0 [*] | GPIO16 | D7 | GPIO13 |
| D1 | GPIO5 | D8 | GPIO15 |
| D2 | GPIO4 | D9 | GPIO3 |
| D3 | GPIO0 | D10 | GPIO1 |
| D4 | GPIO0 | D11 | GPIO9 |
| D5 | GPIO14 | D12 | GPIO10 |
| D6 | GPIO12 | | |

### D. Supply Mode

The NodeMCU can be powered in several ways:

- Via the USB port: this voltage is also exposed via the VU pin.

- Via the various 3 v pins: in this case, the ESP is supplied directly, there is no longer any regulation, which therefore offers minimum consumption.
- By the Vin pin, which supports up to 20 volts and goes directly to the regulator.

## IV. The RFID module

### A. Presentation of the RFID module

RFID or Radio Frequency Identification is a radio frequency card that records and retrieves data remotely [1].

Without physical or visual contact, this technology uniquely identifies the object or person wearing the tag . Invisible frequencies, magnetic fields or radio waves are used.

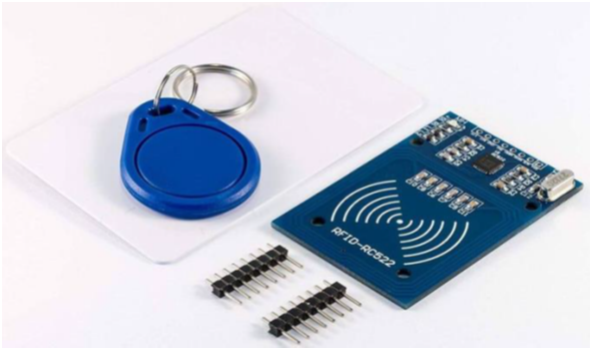

Fig. 3. RFID module

### B. The functioning of RFID chips and tags

RFID retrieves data through radio waves [2]. A secure form of data transfer, it also enables P2P communication with NFC-enabled devices. The RFID system consists of an RFID tag (called a tag), an RFID reader and an antenna. During a transfer, the RFID tag is interrogated by the reader, which transmits a signal to the tag through the antenna. The label returns requested information.

### C. Types of labels (tags)

There are three:

- Passive tags such as access badges only respond to questions and requests from a reader. Passive RFID works in read-only since the chip does not have a battery and must be moved towards the reader to be read. A powerful electromagnetic signal is then sent to it, which activates the RFID chip and reads the information it contains.
- Active tags: they have an energy source integrated into the chip, they are autonomous and do not need the reader's energy to transmit their data.
- BAP (battery assisted passive) tags: record information using sensors.

### D. Types of media for RFID chips and NFC chips

- RFID cards and RFID badges: personal identification, contactless payment, company access control, loyalty card transport
- RFID contactless PVC label: identification and traceability, efficient and affordable RFID technology.
- Labels and vignettes: identification of goods, keeping stock and making inventories, fight against counterfeiting, transparency for the use of products, promotion at events.
- Bracelets: identification of people, remote payment, promotion taking into account certain events.
- Key fobs and badges: facilitating entry and exit for residents, premises and car parks and the use of the RFID badge for access to businesses.
- Microchips under the skin: identification of animals.

### E. Reader frequencies and distances

The frequency is the characteristic that establishes communication between the chip and the antenna. All chips on the market have differences in their functionality. Chips have a variation in operating frequencies and also a variation in read distance. The higher the frequency, the greater the read distance. Compared to these parameters, we notice that the chip will be more or less powerful and more expensive depending on its criteria.RFID chips are divided into three types of usage frequencies:

- Low frequency (125Khz): reader distance 0.5m, transfer rate 1kb/s.
- High frequency (13.56 Mhz): reader distance 1m, transfer rate 25kb/s.
- Very high frequency (UHF): reader distance 3 to 6m, transfer rate 28kb/s.

## V. Language and development tools

### A. The PHP language

PHP: Hypertext Preprocessor which is known by its acronym PHP (self-referential acronym) is a free licensed programming language used mainly for the design of dynamic websites via an http server. PHP, which can be used by any interpretation language locally and for free, is object-oriented.

PHP which facilitated the creation of many websites such as Facebook and Wikipedia is one of the bases for the creation of some dynamic sites and web applications. The PHP language is often associated with the MySQL database server and the Apache server so that it can integrate into HTTP servers such as nginx or IIS. It generates HTML, CSS or XHTML code, data or PDF files. For Linux and Windows operating systems, LAMP and Wamp server are used respectively.

This language, which is free, free, simple to use and easy to install, requires a good understanding of the usual functions and also an acute knowledge of the security problems linked to said language [10].

### B. HTML and CSS languages

1- HTML:

HTML (HyperText Markup Language) is a markup language derived from the Standard Generalized Markup Language

(SGML, a more general purpose markup language. It allows to create and structure Web pages. Web pages use HTML format. These HTML pages are generated in whole or in part automatically. Otherwise, they are written with a text editor.

If the HTML language makes it possible to display pages of a wide variety of content, formatting, animations and others. It also has the quality of being able to be written with a simple text editor, which avoids the use of a specific application. However, the markup syntax must be respected, even if certain deviations are tolerated. You can write HTML yourself in the case of a static page, or let a script produce HTML on the fly. Simply create a file with the suffix .html and open it in a web browser, giving the file path prefixed with the protocol file:// or double-click or right-click and select open with your web browser.

2- CSS:
The term CSS is the English acronym for Cascading Style Sheets which can be translated as ”cascading style sheets”. CSS is a computer language used on the Internet to format HTML or XML files. But also style sheets are called CSS files that include code. The latter allows you to manage the design of a page in HTML. HTML can be formatted using tags provided for this purpose.

These days it’s more preferable to use CSS and only use XHTML for content. The advantage of using a CSS file for formatting a site lies in the possibility of modifying all the titles of the site at once by modifying a single part of the CSS file. Without this CSS file, it would be necessary to modify each title of each page of the site. Other strengths are noticeable. It is possible to create a specific style sheet for printing documents. This makes it possible to remove all style effects and all unnecessary parts during printing. Thus, a style sheet can be used for mobile phone users, which makes it easier to manage formatting for the small screens of these devices.

This book takes up the W3C specifications of which CSS is a part, but by making them intelligible to the uninitiated and by adding advice, examples, tips... It requires knowledge of the basics of the HTML language as a prerequisite. , possibly XHTML for which CSS may become absolutely necessary [12].

### C. WampServer

WampServer est un environnement de dveloppement local ou en ligne pour les applications Web dynamiques. WampServer travaille dans l’environnement Windows en proposant Apache HTTP Server, PHP pour l’interprtation du langage de script, MySQL et aussi phpMyAdmin pour l’administration Web des SGBD MySQL. Il comprend tous les logiciels ncessaires pour excuter des applications Web PHP sur une machine locale. Il dispose d’une interface d’administration permettant de grer et d’administrer ses serveurs au travers d’un tray icon. WampServer permet aux dveloppeurs de tester leur code et d’apporter des modifications sans avoir le tlcharger sur un serveur en direct [13].

### D. Sublime Text

Sublime Text is a text editor coded in Python and C++ which presents an original interface as well as numerous functionalities. Among these, you will have syntax highlighting, autocompletion and several search tools. A sidebar, also called a minimap, offers the ability to quickly navigate and preview your source code.

In addition, you will have the means to use macros to automate your tasks and simplify your work. In the same line, the software integrates the automatic backup of your projects. Sublime Text also stands out thanks to the many programming languages compatible with JavaScript, C, C++ , C# , LaTeX, Perl, PHP, Ruby, CSS, SQL, XML and even XLS standards. This text editor displays a sleek and neat interface that is simple and pleasant to use. Finally, note that this software is offered here in a free trial version [14].

## VI. System design and result

### A. General Architecture

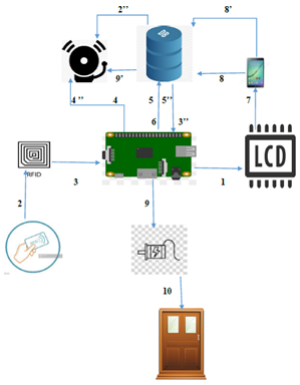


Fig. 4. General Architecture

Legend :
1: the LCD screen displays Welcome then Scan your badge 23. 2: the person presents the RFID card. 3: the RFID module scans the card. 4: verification of the existence of the UID of the scanned card in the database. 5: If the map is saved in the database. 6: The LCD screen displays ”Enter your password”. 7: The person types the IP address of the MCU (192.168.43.109) on the URL. He accesses the web page which allows him to enter his password. 8: The system checks whether the password entered matches the one stored in the database. 9: If the password is correct the servo motor starts moving and pulls the door hook. 10: The door opens. 8’: The password does not match the one in the database. 9’: The buzzer triggers an alarm. 2”: the map does not exist at the database level. 3: The LCD screen displays Bad badge. 4”: The alarm sounds.

### B. Detailed explanation

We create a database called arduino containing the following four tables:
- Card; - Passenger; - Door; - Passage.
The following class diagram presents the configuration.

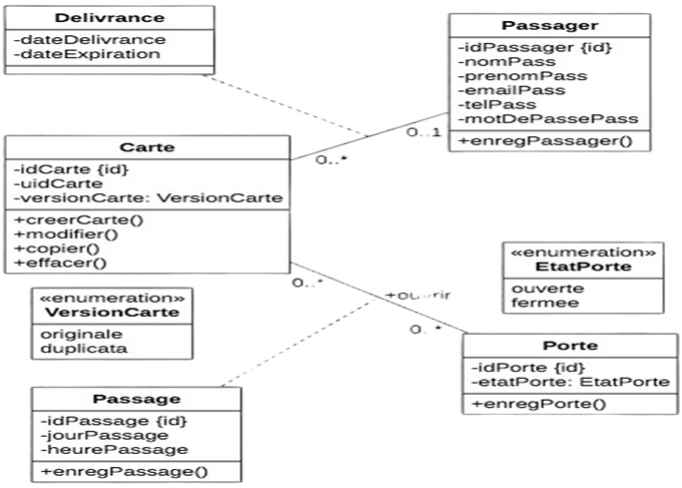


Fig. 5. System class diagram table

On the other hand, in the log table are stored the personal information of all the people who tried to open the door as well as the exact date and time of the attempt as well as the state of the door.

The system works as follows:

- The LCD screen displays a welcome message and asks the person to scan their badge;
- The person presents the card in front of the RFID module;
- The system retrieves the UID of the card then checks its existence in the database;
- If the UID exists in the database, the screen asks the person to enter their password.
- The person connects to the same network as the MCU in order to access the web page to enter their password.
- The system checks if the password entered is the same as that of the card presented.
- If the password is correct, the motor runs and the door opens.
- And the card owner information is directly recorded in the log table as well as the exact time, date and status of the door opening (Door status: open).
- Otherwise the LCD screen displays an error message and the buzzer sounds.
- And card owner information is recorded directly in the log table along with the exact time, date and status of the door opening (Door Status: Closed).
- However if the UID of the card does not exist the LCD screen displays an error message and the buzzer sounds.
- The UID of the card is recorded directly in the log table as well as the time, the date and the exact state of the opening of the door (State of the door: Closed).

### C. Presentation of the webpage


Fig. 6. Home page

*1) Presentation of the home page:*

*2) Opening page presentation:* This page allows the user to enter their password.


Fig. 7. Opening page

*3) Modify page presentation:* It allows a user to modify his password saved at the database level by typing the UID of his card.


Fig. 8. Edit page

### D. Connecting the various Arduino components with the ESP8266

## VII. Conclusion

At the end of our work, we were able to intelligently manage a living or working space through connected objects, including the automatic opening of a door via an RFID card with a password.
First of all, the user presents the badge or the RFID card which is scanned by the RFID module and the system checks the existence of the card at the database level. Then, if the card is well registered then it connects to the network in order to access the web page to enter its password. Otherwise the

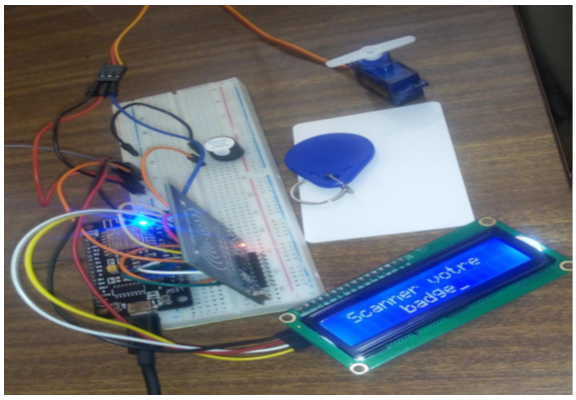


Fig. 9. Connecting the set

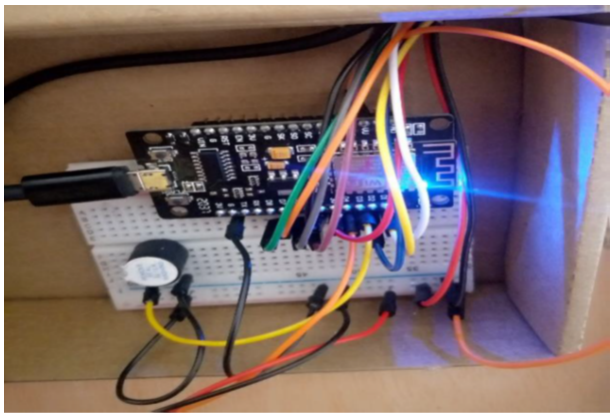

Fig. 10. front of the door

system gives an alert and stops. And finally the door opens if the password is correct. Otherwise an alarm will be triggered. We hope that this project will be the basis for further studies.

## REFERENCES

[1] R. Colella and L. Catarinucci, "Electromagnetic Design of UHF RFID Tags Enabling a Novel Method to Retrieve Sensor Data," in IEEE Journal of Radio Frequency Identification, vol. 2, no. 1, pp. 23-30, March 2018.

[2] M. Zgaren, S. Mohamad, A. Amira and M. Sawan, "EPC Gen-2 UHF RFID tags with low-power CMOS temperature sensor suitable for gas applications," 2016 14th IEEE International New Circuits and Systems Conference (NEWCAS), Vancouver, BC, 2016, pp. 1-4.

[3] S. Kaur, R. Singh, N. Khairwal and P. Jain, "Home Automation and Security System", Adv. Comput. Intell. An Int. J., vol. 3, no. 3, pp. 17-23, 2016.

[4] M. Mrinal, L. Priyanka, M. Saniya, K. Poonam and A. B. Gavali, "Smart home - Automation and security system based on sensing mechanism", Proc. 2017 2nd IEEE Int. Conf. Electr. Comput. Commun. Technol. ICECCT 2017, pp. 1-3, 2017.

[5] P. Shelke, S. Kulkarni, S. Yelpale, O. Pawar, R. Singh and K. Deshpande, "A NodeMCU Based Home Automation System", Int. Res. J. Eng. Technol., vol. 9001, pp. 127-129, 2008, [online] Available: www.irjet.net.

[6] Martin, F., Velez, P., Munoz-Enano, J., & Su, L. (2023). RFID Sensors for IoT Applications.

[7] Myint, H., & Tun, M. Z. (2020). Secure Door Control System using RFID Card. International Journal of Advances in Scientific Research and Engineering, 6(04), 69-73.

[8] Hamzah, A. S., & Abdul-Rahaim, L. A. (2022, May). Smart Homes Automation System Using Cloud Computing Based Enhancement Security. In 2022 5th International Conference on Engineering Technology and its Applications (IICETA) (pp. 164-169). IEEE.

[9] Landaluce, H., Arjona, L., Perallos, A., Falcone, F., Angulo, I., & Muralter, F. (2020). A review of IoT sensing applications and challenges using RFID and wireless sensor networks. Sensors, 20(9), 2495.

[10] https://fr.wikipedia.org/wiki/PHP

[11] https://fr.wikipedia.org/wiki/Hypertext_Markup_Language

[12] https://fr.wikibooks.org/wiki/Le_langage_CSS

[13] https://www.01net.com/telecharger/windows/Internet/editeur_de_site/fiches/28739.html

[14] https://www.clubic.com/telecharger-fiche430809-sublime-text.html

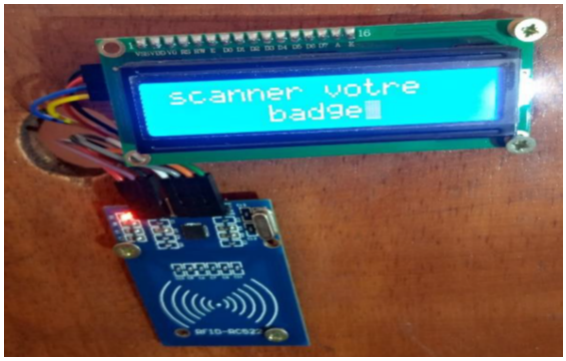


Fig. 11. Behind the door

# Feedback Linearization for Nonlinear Control of a Magnetic Levitation System

**Raghuwansh Singh, Prashant Kumar, Suman Halder**

Department of Electrical Engineering, National Institute of Technology, Durgapur, 713209, India
rs.22ee1105@phd.nitdgp.ac.in

## Abstract.

In this research, a Feedback Linearization approach is devised for use in a Magnetic Levitation System (MLS). In order to levitate a ferromagnetic ball, a Non-Linear Control (NLC) with input and output feedback linearization algorithms of differential geometry was created. This method was used in conjunction with a controller for linear state feedback in the outer loop. During the process of putting together MLS, the real-time experimental data for the electromagnetic force were noticed. The amount of force exerted is directly related to the amount of current that is flowing as well as the location of the ferromagnetic ball that is going to be levitated by the electromagnetic force that is being applied. Unlike a standard PID controller, the output results highlight the usefulness of the newly built NLC.

***Keywords.*** Electromagnetic, NLC, PID, Feedback Linearization

## 1. INTRODUCTION

This Magnetic levitation system (MLS) is an experimental setup that uses the principle of electromagnetism for levitates ferromagnetic ball. MLS concept minimizes friction by eliminating mechanical touch between moving parts and stationary parts [1]. MLS's many benefits can be attributed to the friction it eliminates minimum noise, the ability to work in a high-vacuum setting, and maximum accurate positioning system. MLS has three types of forces: the force that propulsion, the force that lifts, and the force that guides [2]. The propulsion force is responsible for moving portion ahead, the levitation force hang the moving part, and the guidance force keeps tracking it from derailing. If the nature of attractive force is present, then magnetic suspension works while the nature of force is repulsive then the principle of magnetic levitation occurs. MLS offers a wide range of uses, including the capacity to perform tasks in a very low-pressure setting [2]. Due to continuous need of levitation of ball the parameters also change with respect to time and mathematical modelling will consist of nonlinear in nature. Several attempts have been made to simulate and control the MLS [1-3]. Several initiatives to simulate and maintain control of the MLS have been made. [1-3]. The bulk of design techniques are linear in nature, magnetic levitation is a process that exhibits nonlinear behaviour which is characterised by a nonlinear differential equation [4-6]. Tracking performance in a linear model, on the other hand,

degrades rapidly as the deviation from the nominal operating point grows. Nonlinear modelling, rather than linear modelling, is required to assure an extremely extended range of travel for a ferromagnetic ball while keeping effective tracking. As a result, for system modelling, Parameters are estimated in real time using experimental data.

The MLS is modelled in this paper using the electromagnetic concepts. combining input-output feedback control with nonlinearity as steady state. Fig. 1 Shows of the MLS law is devised based on this developed model. Additionally, real-time data is used to estimate the electromagnetic force, which depends on the input magnetising current and the location of the ferromagnetic ball that the input force would lift. The proposed controller's superiority over a typical PID controller is established at the conclusion.

## 2. MAGNETIC LEVITATION SYSTEM DYNAMIC MODELLING

The MLS under mathematical modelling is a magnetic field that can be adjusted by voltage, a ferromagnetic ball can be lifted. The actuator is a ferromagnetic core coil with the sensor detecting ball condition relative to the centre coil. The ferromagnetic ball, which only possesses one degree of freedom. Fig. 1 depict a schematic diagram of the system MLS parts as an electromagnet sensor, ferromagnetic ball and sensors along with a PC Connected interfacing card a signal conditioner and its accompanying cable. Total of two inputs are received by the system. Variations in power supply, coil temperature, and ball forces cause disturbances. To simulate the dynamic behaviour of a magnetic levitation system the electromagnet & mechanical subsystem can be studied. [3].

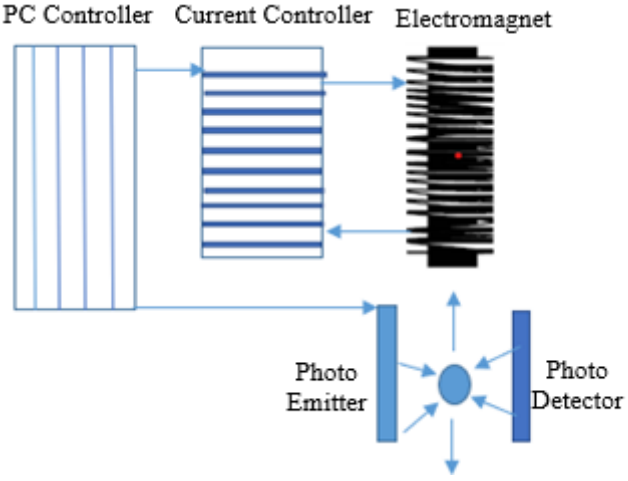


Fig. 1 Diagrammatic representation of the MLS

In magnetic levitation, the magnetic force is generated by the current running through the coil, this magnetic force is calculated by Kirchhoff's voltage law, and the magnetic field is computed by the principle of Biot-Savart law. The magnetic and gravitational fields are applied on the ferromagnetic ball. The free body model shown in Fig. 2 can be used to write the force equation using Newton's Laws of Motion.

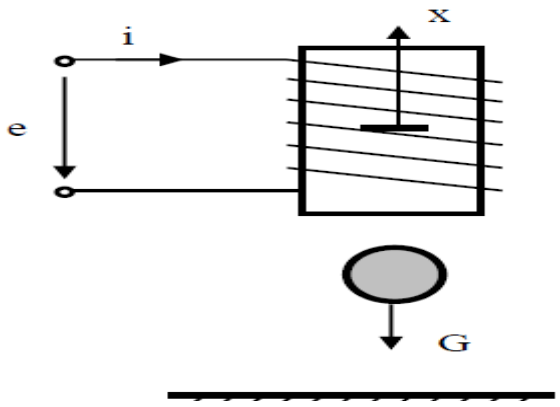


Fig. 2 MLS Free body diagram

In this system, there are three inputs. They are as follows:

1. Adjust the ball's vertical position using the set point.

2. Signal of reference input

3. Disturbances, such as fluctuation to the power supply, change in the coil's temperature, and external pressures applied on the ball A magnetic levitation system's dynamic behavior can be modelled by the study of electromagnetic and mechanical subsystems.

A ferromagnetic ball experiences both magnetic and gravity forces. The magnitude of an electromagnetic force is proportional to the amount of the current flowing through it and its distance of ball $F(x,i)$

$$F(x,i) - mg = ma \tag{1}$$

$$F(x,i) - mg = m\frac{d^2x}{dt^2} \tag{2}$$

$$m\frac{d^2x}{dt^2} = F(x,i) - mg \tag{3}$$

$$m\ddot{x} = F(x,i) - mg \tag{4}$$

$$\ddot{x} = \frac{F(x,i)}{m} - g \tag{5}$$

Now we must compute F(x, i) for the ball distance with respect to the Actuator. Given is the magnetic field produced by a brief section of wire dl carrying a current of I is given as

$$dB = \frac{\mu_o}{4\prod}\frac{idl \times r}{r^3} \tag{6}$$

Using current I and radius a to create a circular path then magnetic field is calculated as

$$B = \frac{\mu_o i}{2} \frac{a^2}{(a^2+d^2)^{3/2}} \tag{7}$$

$$r = \sqrt{a^2 + d^2} \tag{8}$$

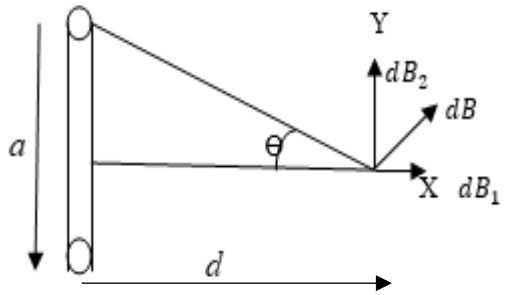


Fig. 3 shows the magnetic field of a circular contour

Because of field symmetry, the magnetic field in the y direction is 0, hence the magnetic field exists only in the x direction. N is the total number of turns, while n is the number of turns per unit length. The magnetic field of an electromagnet causes the ball to develop a magnetic dipole and get magnetized as a result. Thus, the magnetic force acting on the induced dipole and gravity are the two forces acting on the ball.

$$\sin\theta_1 = \frac{r}{\sqrt{(l+x)^2 + r^2}} \tag{9}$$

$$\sin\theta_2 = \frac{r}{\sqrt{r^2 + x^2}} \tag{10}$$

The magnetic field of an electromagnet induces Ball contains a magnetic dipole that magnetizes. The acceleration caused by gravity is responsible for the downward force that is operating on the ball. Additionally, the magnetic force that is acting on the induced dipole in the upward direction also contributes to this force. A solenoid (or an electromagnet) with N turns is denoted by ADEF having radius of r and a length of l. Total axial field generated by all turns We can deduce that

$$B = \int dB \tag{11}$$

$$B = \frac{\mu_o}{2} nI \frac{r^2}{(r^2 + l^2)^{3/2}} dx \tag{12}$$

$$B = \frac{\mu_O}{2} nI \left[ \frac{X + l}{\sqrt{r^2 + (X + l)^2}} - \frac{X}{\sqrt{r^2 + X^2}} \right] \tag{13}$$

Because of the multiple turn's layers of the electromagnet coil, the inner radius $r_1$ and outer radius are $r_2$. The magnetic field is

$$dB = \frac{\mu_O}{2} nI \left[ \frac{X+l}{\sqrt{r^2+(X+l)^2}} - \frac{X}{\sqrt{r^2+X^2}} \right] ndr \tag{14}$$

$$dB = \frac{\mu_O}{2} n^2 I \left[ \begin{array}{l} \dfrac{X+l}{\sqrt{r^2+(X+l)^2}} - \\ \dfrac{X}{\sqrt{r^2+X^2}} \end{array} \right] dr \tag{15}$$

We get by integrating eq. (12) $r_1$ from to $r_2$

$$B = \frac{\mu_O}{2} n^2 I \int_{r_1}^{r_2} \left( \frac{X+l}{\sqrt{r^2+(X+l)^2}} - \frac{X}{\sqrt{r^2+X^2}} \right) dr \tag{16}$$

$$B = \frac{\mu_O}{2} n^2 I \left[ \begin{array}{l} (X+l) \displaystyle\int_{r_1}^{r_2} \frac{1}{\sqrt{r^2+(X+l)^2}} dr \\ -X \displaystyle\int_{r_1}^{r_2} \frac{1}{\sqrt{r^2+X^2}} dr \end{array} \right] \tag{17}$$

$$B = C_1 I G(X) \tag{18}$$

Where $C = \dfrac{\mu_o n^4}{8} s$

The Magnetic force on the ball is experienced as

$$f = \frac{B^2}{2\mu_o} s \tag{19}$$

S denotes the surface of the substance that is traversed by the magnetic flux.

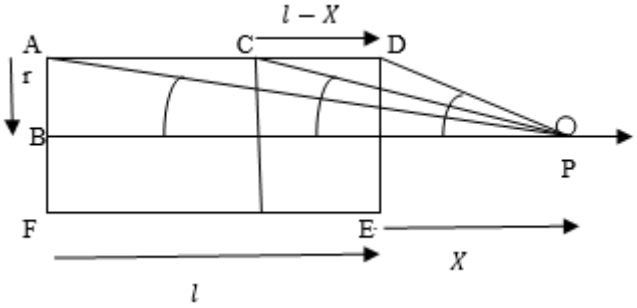


Fig. 4 Ball and coil combination demonstrating magnetic force

## 3. DESIGN OF NON-LINEAR CONTROLLER

### 3.1. Feedback Linearization

One of the most prevalent approaches in practical nonlinear control design is to turn nonlinear models into linear ones. The feedback linearization approach is divided into two parts: state and feedback. The first is input transformation, while the second is output transformation [5]. Using this strategy, we can algebraically turn a nonlinear MLS into a linear one without ignoring the nonlinear element. Feedback Linearization is not the same as Jacobian Linearization. Concept of Lie derivative use in Feedback Linearization technique, by the use of two vector fields f and g, where f (x) and g(x) are the system matrix and input matrix respectively.

$$\dot{X} = f(X) + g(X)u \tag{20}$$

$$y = h(X) \tag{21}$$

$$\text{Where } X = \begin{bmatrix} x_1 \\ x_2 \end{bmatrix} = \begin{bmatrix} x \\ i \end{bmatrix}$$

Because the nonlinear dynamics equation is

$$i = k_1.u \tag{22}$$

$$\begin{aligned} m\ddot{x} &= mg - k.\frac{i^2}{x^2} \\ \ddot{x} &= g - \frac{k}{m}.\frac{i^2}{x^2} \end{aligned} \tag{23}$$

$$\begin{aligned} x &= x_1 \\ \dot{x}_1 &= x_2 \\ \dot{x}_2 &= g - \frac{k}{m}.\left(\frac{i^2}{x^2}\right) \end{aligned} \tag{24}$$

$$\dot{x}_2 = g - \beta\left(\frac{u^2}{x_1^{\,2}}\right) \text{ where } \; i = k_1 u \tag{25}$$

$$f(X) = \begin{bmatrix} x_2 \\ g \end{bmatrix} \;,\; g(X) = \begin{bmatrix} 0 \\ \dfrac{-\beta}{x_1^{\,2}} \end{bmatrix} \tag{26}$$

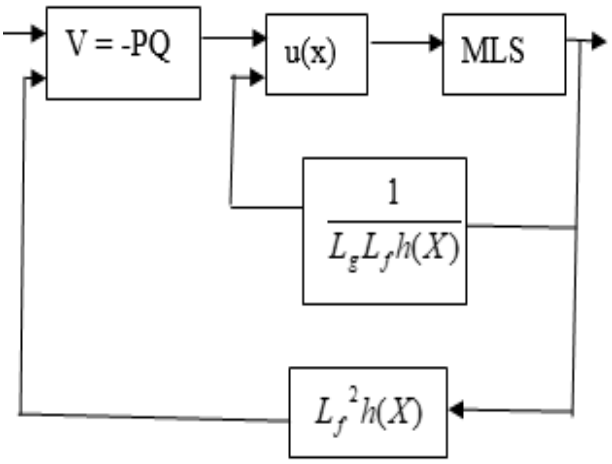


Fig. 5 Controller Design Block Diagram

The MLS nonlinear system can be linearized by in a region if two conditions are met by two vectors $f(x)$ and $g(x)$ and it would be linearizable in a region $\delta$ if two condition will be satisfied [6].$[g, ad_f g, .....ad_f^{\,n-1} g]$should be controllable and other one $[g, ad_f g, .....ad_f^{\,n-2} g]$ satisfied for linear system. State vector for MLS is $x_3 =$ Speed $x_2 =$ Position & $x_1 =$ Current.

$$(x_1, x_2, x_3)^T = (I, y, \frac{dy}{dt}) \tag{27}$$

$$X = \begin{bmatrix} x_1 \\ x_2 \\ x_3 \end{bmatrix} = \begin{bmatrix} I \\ y \\ \dfrac{dy}{dt} \end{bmatrix} \tag{28}$$

Lie derivative nonlinear dynamics equation [3]

$$h(x) = x_2$$
$$L_f h(x) = \frac{\partial h}{\partial x} f(x) = x_3 \tag{29}$$
$$L_f{}^2 h(x) = \frac{\partial h}{\partial x}\frac{\partial f}{\partial x} f(x)$$

$$L^2{}_f h(x) = g - \frac{1}{m}\left(\frac{x^2{}_1}{-1.07 + 14.58x_2 - 64.81x_2{}^2 + 119.10x_2{}^3}\right) \tag{30}$$

Space transformation $Q = \psi(x)$

$$Q = \begin{pmatrix} \psi_1(x) \\ \psi_2(x) \\ \psi_3(x) \end{pmatrix} \tag{31}$$

$$\psi_1(x) = h(x), \psi_2(x) = L_f h(x), \psi_3(x) = L_f{}^2 h(x) \tag{32}$$

$$Q = \begin{pmatrix} \\ x_2 \\ x_3 \\ g - \frac{1}{m}\left(\frac{x_1{}^2}{-1.07 + 14.58x_2 - 64.81x_2{}^2 + 119.10x_2{}^3}\right) \end{pmatrix} \tag{33}$$

For new states $Q_i = \psi_i(x)$

$$L^2{}_f h(x) = \left\{ g - \frac{1}{m}\left(\frac{x_1{}^2}{-1.07 + 14.58x_2 - 64.81x_2{}^2 + 119.10x_2{}^3}\right)\right\} \tag{34}$$

$$\dot{Q} = \begin{pmatrix} Q_2 \\ Q_3 \\ d(Q) + c(Q) \end{pmatrix} \tag{35}$$

$$\dot{Q} = CQ + DV_K \tag{36}$$

When differentiation output occurs up until we receive input u, a synthetic input v for nonlinear feedback u is being received [5].

$$\begin{aligned} y^r &= L_f{}^r h + L_g(L_f{}^{r-1} h)U \\ V &= L_f{}^r h + L_g(L_f{}^{r-1} h)U \end{aligned} \tag{37}$$

Where r is the relative degree, the control variable for MLS (r=3) should be

$$u(X) = \frac{-L_f{}^3 h(X)}{L_g L_f{}^2 h(X)} + \frac{1}{L_g L_f{}^2 h(X)} v \tag{38}$$

The system is now linear and controllable, and it can be stabilised using the state feedback law. $v = -PQ$ , Where $P(P_1, P_2, P_3)$ is pole placement technique.

## 4. RESULT AND DISCUSSION

### 4.1. Identification

If the electromagnetic force $F(x,i)\ \alpha \frac{i^2}{x^2}$ and the ball location from the coil act in polynomial form, then we can write

$$F = \frac{I^2}{b_0 + b_1 x + b_2 x^2 + b_3 x^3} \tag{39}$$

Here $b_0, b_1, b_2, and\, b_3$ is the polynomial coefficient, we experimented the data from the MLS Experimental setup.
Data are collected in such a way that the least value of the present particular levitation position is obtained. Using least square fitted data, the polynomial's parameter is obtained.

$$\begin{aligned} b_0 &= -1.07 \\ b_1 &= 14.58 \\ b_2 &= -64.81 \\ b_3 &= 119.10 \end{aligned} \tag{40}$$

Proportional Integral Derivative (PID) Controller is used to perform analysis on MLS. The most common type of PID Controller is

$$G_c(s) = K_p(1 + \frac{1}{\tau_i s})(1 + \tau_d s) \tag{41}$$

While the MLS linearized model is

$$G_p(s) = \frac{-0.0025}{S^2 + 0.0075} \tag{42}$$

From $G_p(s)$ Due to its inherently unstable character, the MLS mathematical model is linearized around the nominal operating point of $y = 5mm$.

### 4.2. Simulation

The proposed STC was numerically simulated in the MATLAB of SIMULINK® is used. The MLS in the Control and System Lab in BIT, Mesra, Ranchi, was subjected to the proposed STC. It was decided to use the goal trajectory as a step signal to validate the STC's trajectory tracking performance. Fig. 6 shows that MLS Identification technique for the applied force. Fig. 7 show the findings for both the desired & actual ball position. The ball position tracking

error curves with a sinusoidal input were detected. calculates that PID has a tracking error of 0.66 mm, while NLC has a tracking error of 0.25 mm. The control input voltage with respect to desired PID and NLC are shown in Fig. 10.

TABLE 1: MLS PHYSICAL PARAMETERS

| S.No | Physical Representation | Physical Parameter | Dimension |
|---|---|---|---|
| 1 | I | Input Current | (0 -3) Amp |
| 2 | V | Input Voltage | (0 -5) Volt |
| 3 | M | Ball Mass | 0.021 Kg |
| 4 | X | Ball Start | 5 mm |
| 5 | X | Ball's Destination | (5-25) mm |
| 6 | C | Magnetic Constant | 0.0000824 Kg |
| 7 | g | Gravity Constant | 9.8 m/Sec.Sec |

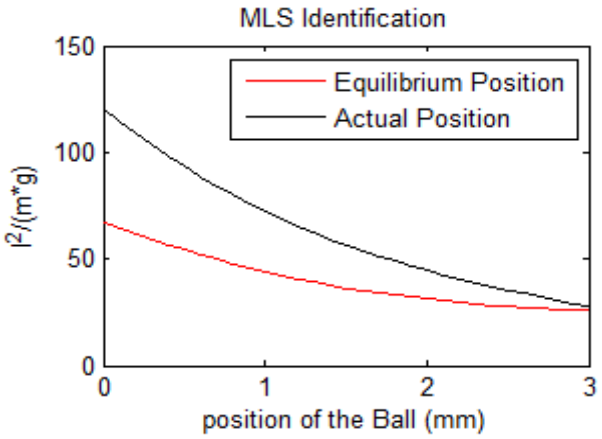


Fig. 6 Ball Position for Controller Design

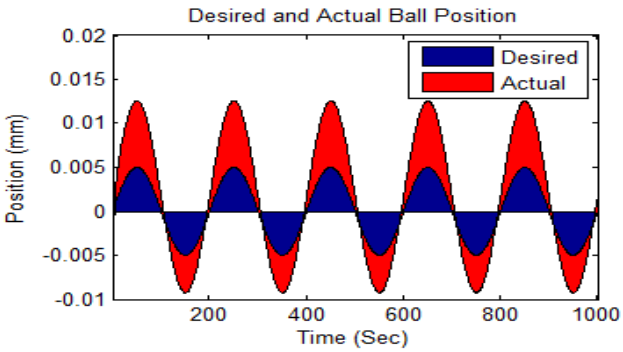


Fig. 7 Ball Position for Controller Design

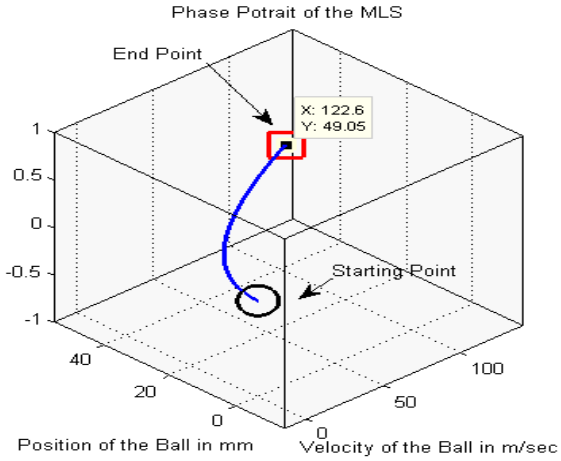


Fig. 8 Phase Potrait of MLS system without Controller

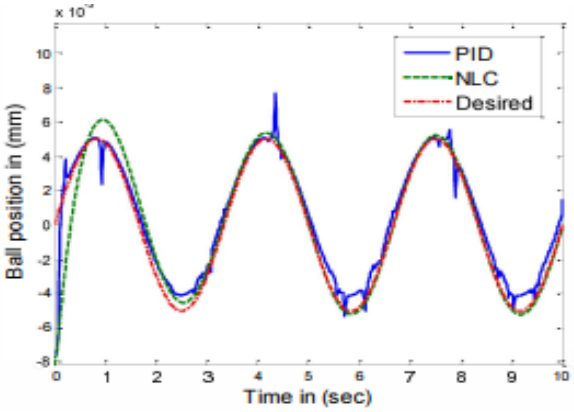


Fig. 9 Ball position due to intended sinusoidal input

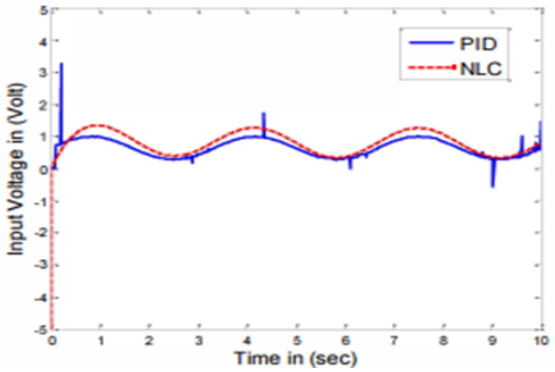


Fig. 10 Control input due to intended sinusoidal

Both the position and velocity of the ball are shown on the graph of the MLS state with respect to time that can be found in Fig. 6. The nature of both of these variables is nonlinear. The

MLS identification for the actual position and equilibrium position can be seen in Fig. 7. The actual position of the ball, as well as the position that should be, is shown in Fig. 8. The Phase Portrait of the MLS system is shown in Fig. 9, which does not include a Controller. As in Fig. 10, the result shows that there is minimum variation appears in between PID and NLC. The findings of the simulation demonstrate that the suggested NLC is capable of producing an adequate amount of adaptive torque despite the existence of sensor noise and nonlinearity in the system.

## 5. CONCLUSION

The concept developed for a Single input and single output MLS system & designed controller feedback linearization for lie derivatives to control the MLS in presence of nonlinearities. The developed NLC was applied to an MLS and produced the required outcome. The simulation findings show that the applied MLS provides adequate resilient compared to a fixed gain, torque under system nonlinearity and sensor noises traditional PID controller under comparable conditions. The work that came before could be improved in the future to construct reliable controllers that are nonlinear and are based on a nonlinear model of the MLS's dynamics.

## 6. REFERENCES

[1] M. J. Khan, M. Junaid, S. Bilal, S. J. Siddiqi and H. A. Khan, "Modelling, Simulation & Control of Non-Linear Magnetic Levitation System," IEEE Conference on Multi-Topic Conference, pp. 1-5, 2018. doi: 10.1109/INMIC.2018.8595598.

[2] Y. Gao, R. Wei, J. Wang, Q. Ge and Y. Zheng, "Study on Electromagnetic Force Characteristics of Asymmetric 8-Figure Coils in EDS System," IEEE International Electrical and Energy Conference, pp. 671-677, 2022. doi: 10.1109/CIEEC54735.2022.9845889.

[3] A. Abbas et al., "Design and Control of Magnetic Levitation System," 2019 International Conference on Electrical, Communication, and Computer Engineering, pp. 1-5, 2019. doi: 10.1109/ICECCE47252.2019.8940711.

[4] M. Sherif, D. Victor and A. El-Badawy, "Real-Time Control of a Magnetic Levitation System," International Conference on Microelectronics, pp. 280-283, 2019. doi: 10.1109/ICM48031.2019.9021705.

[5] M. Hypiusová, D. Rosinová and A. Kozáková, "Comparison of State Feedback Controllers for the Magnetic Levitation System," Cybernetics & Informatics, 2020, pp. 1-6, 2020. doi: 10.1109/KI48306.2020.9039889.

[6] K. R. S and S. K. V., "Gradient based Optimal State Feedback Control design for Feedback Linearizable Nonlinear Nonaffine system," International Conference on Energy, Power and Environment: Towards Clean Energy Technologies, pp. 1-6, 2021. doi: 10.1109/ICEPE50861.2021.9404412.

[7] R. V. Gandhi and D. M. Adhyaru, "Feedback linearization based optimal controller design for electromagnetic levitation system," International Conference on Control, Instrumentation, Communication and Computational Technologies, pp. 36-41, 2016. doi: 10.1109/ICCICCT.2016.7987916.

[8] Magnetic Levitation Control Experiments 33-942S, Feedback Instruments Ltd.,East Sussex ,UK

[9] JJ Siotine, Applied Nonlinear ControL Englewood Cliffs, NJ: PrenticeHall, l991.

## Biographies

**Raghuwansh Singh** received the bachelor's degree in Electronics & Instrumentation engineering from Dr. M.G.R University in 2009, the master's degree in Control System from BIT Mesra in 2014, and currently pursuing Doctor of Philosophy degree in Electrical Engineering from NIT Durgapur.

**Prashant Kumar** completed his BTech (Electrical Engineering, 2013) and ME (Electrical, 2016) from Maulana Abul Kalam Azad University of Technology, West Bengal and National Institute of Technical Teachers Training and Research, Chandigarh, respectively. He is currently pursuing his PhD under the supervision of Dr. Suman Halder at Electrical Engineering Department, National Institute of Technology Durgapur, India.

**Suman Halder** completed his BE (Electrical, 2001), ME (Electrical, 2004) and PhD (Engineering, 2009) from Jadavpur University, respectively. He is associated with NIT Durgapur, India from 2014 and currently working on biomedical instrumentation and signal analysis.

# Modelling of Deposition of Small Particles from the Vapour State on a Thin Film

**Rahul Basu**

*Emeritus Professor, JNTU*

*Hyderabad, Telengana, raulbasu@gmail.com*

## Abstract.

The Technology of film deposition onto a substrate has found use in many areas, including coatings for stealth applications, diamond film coatings, and tool coatings for hardness. A model is developed for the direct transformation from the vapour state to solid state, and related to the boundary conditions and other material parameters. Spherical particle Morphology is used for the modeling. Apart from a theoretical formulation and solution, a numerical approach with a graphical solution using computational tools is attempted. The effect of various boundary conditions and material parameters is found by numerical simulation. The results can be used in effective film deposition by tuning of parameters.

**Keywords**. ***–Sublimation, eigenvalues, diffusion, moving boundary problem, thin film***

## 1. INTRODUCTION

Very few substances are known to sublimate directly to vapur without passing through the liquid phase. Among these are Iodine, carbon, naphthalene, dry ice and a few others. The reverse process known as deposition occurs in, for example, water vapour to ice in the form of frost. In the following it is attempted to illustrate the deposition of diamond from vapour for varying imposed conditions.

The production of diamond films and crystals from vapour by various reduction reactions has recently been applied to industrial application. Diamond film has interesting physical and chemical properties. The properties relating to sublimation were catalogued Hoch etal [1], by pressure measurement methods. Production of artificial diamonds was perhaps the earliest motive for technology development, yet the costs were prohibitive. More recently, diamond coatings and films were developed and have industrial use [2,3 ]. Some of the methods include CVD and plasma assisted CVD, [4]. A 2D model for the CVD of SiN was proposed by Evans [5]

## 2. MATHEMATICAL MODEL

The diffusion equations for thermal and mass transport in spherical coordinates can be transformed by a simple change of variable to one dimension. By U=rT

Where $K \nabla^2 T = \rho c_p \, dT/dt$ (1)

$K( 1/r^2 \, d/dr(r \, dT/dr)) = \rho c_p \, dT/dt$ (2)

$K/r^2[d/dr(r^2 \, dT/dr)] = K/r \, d^2U/dr^2 = \rho c_p \, d(U/r)/dt$

$= \rho c_p / r \, (dU/dt)$ (3)

So $K \, d^2U/dr^2 = \rho c_p \, (dU/dt)$, whence using similarity variable $\eta = r/(\alpha t)^{1/2}$ (4)

$U'' + \eta/2 \, U' = 0$ (5)

similarly for mass transfer.

Applying the transformation $U' = p$

$p' = -\eta/2 \, p$, which is easily solved. (6)

One solution is $( \ln p) = - \eta^2/4 + A$ (7)

$P = U' = A \exp(-\eta^2/4) d\eta + B$, whence (8)

$U = A \, erf ( \eta/2) + B\eta$, $T = U/r$

Applying the energy balance across the phase interface,

$K \, d\Theta/d\eta = L\rho \, ds/dt$ (9)

Since $\eta = r/(at)$ ½

Using the chain rule, the result becomes

$K \, d(U/r)/d\eta = L\rho \, ds/dt$, after simplifications

$K \, d(U/r)/d\eta = L\rho \, \alpha \, \Lambda^2/2$ (10)

Further substitution and simplification gives the balance

$KA[\Lambda \exp(-\Lambda^2/4) - erf(\Lambda/2)] = \rho L \Lambda^3 \alpha/2$ (11)

where A is a constant depending on the B.C.

## 3.RESULTS

The properties for water ice as given in Paterson[5]

Water : $k_2 = 0{\cdot}00144$ Cal/cm. sec.° K. $K_2 = 0{\cdot}00144$ cm.²/sec.
Ice : $k_1 = 0{\cdot}0053$ Cal/cm. sec.° K. $K_1 = 0{\cdot}0155$ cm.²/sec.
and $L\rho$ (ice) $= 73{\cdot}6$ Cal/cm.³

For ice –vapour the value for $L\rho = 618$ Cal/cm$^3$

For the spherical geometry, well known solutions have been given for conduction by Carslaw Jaeger [6 ], and for phase melting by Paterson [7 ].

Using the solution from [7] for simplicity,

$$\frac{q}{4\pi} e^{-\alpha^2/4K_2} - \frac{k_1 \alpha \Theta}{1 - \frac{\alpha}{2}\sqrt{\frac{\pi}{K_1}}\, e^{\alpha^2/4K_1}\, \operatorname{erfc}\left(\frac{\alpha}{2\sqrt{K_1}}\right)} = \frac{L\rho\alpha^3}{2} \qquad (12)$$

q is a point source strength and $\Theta$ the initial temperature. Putting Q=0, and varying the initial temperature from -5 to 5, solutions for $\alpha$ are obtained as shown in Fig 1.

plot $\quad -0.0053 \times \dfrac{T}{1 - \frac{x}{2}\sqrt{\frac{\pi}{0.0155}}\, \exp\left(\frac{x^2}{4 \times 0.0155}\right) \operatorname{erfc}\left(0.5 \times \frac{x}{\sqrt{0.0155}}\right)} = 613.6 \times 0.5\, x^2 \quad T = -5 \text{ to } 5$

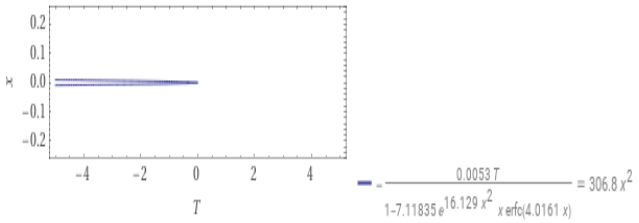


Fig. 1 Solutions for water vapour-ice From values in[7]

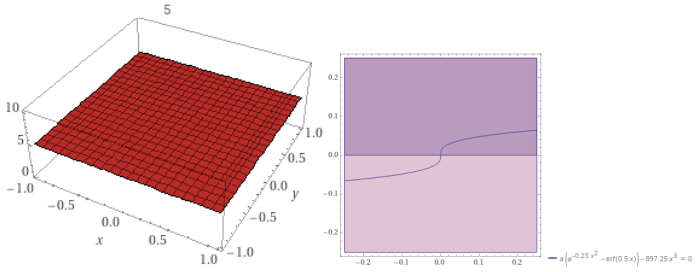

Fig 2. Implicit plot for ice

Using the solution obtained for U, for Diamond , if A=1

$$e^{-x^2/4}\,x - \operatorname{erf}\left(\frac{x}{2}\right) = 122\,485.\,x^3 \qquad (13)$$

Applying Wolfram similar graphs are obtained, eigenvalues as

A=1 Solution x ≈ -0.00188628634813420...

A=5 x ≈ -0.00421785051971876...

It can be seen that the rate changes with A, depending on the B.C. By WOLFRAM using plot function on the expression

| A (exp(-0.25 x x) - erf(0.5 x)) + x^3×(-122.485)

the form of solution varying with A is shown below:

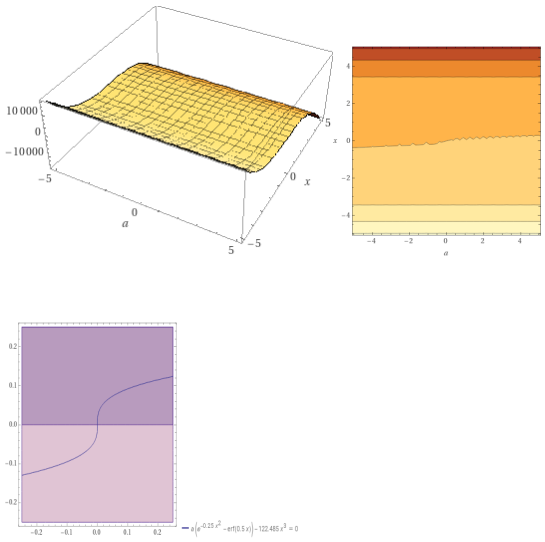

Fig.3. Contour and implicit plots of diamond for x vs A

Thus variations can be obtained by either adjusting the heat transfer rate or the initial temperatures. Using the formula in Paterson (5) with initial temperature as the variable, varing from -5 to 5, the results obtained are as:

manipulate

plot $\dfrac{(6\,a)}{\left(1-0.333772\,e^{0.035461\,x^2}\,x\right)\operatorname{erfc}(0.188311\,x)} = 104242\,x^2$ $x = a - 5$ to $5$

varying $a$ (14)

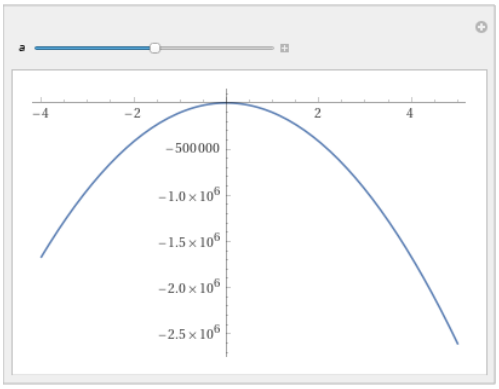


Fig 4. Solution of (14)

TABLE 1

Sublimation rate of Carbon vs initial temperature

| Initial temperature | Sublimation value |
|---|---|
| 5 | -.0495 |
| 4 | -.0441 |
| 3 | -.0382 |
| 2 | -.0311 |
| 1 | -.022 |

As a benchmark value, take the eigenvalue as .01, then the radius over time given by $r= \Lambda(\alpha t)^{1/2} = .026t^{1/2}$

Using the formula based on heat transfer rate (13), the thickness over time is $.001t^{1/2}$

4. **Discussion and Conclusion**

By using the substitution developed for the spherical deposition in (11), it appears that the variation depends on the cubic power of the eigenvalue Λ. However the deposition rate for diamond is far less than that of ice. Similar results are obtained if the formula developed in [7] for initial temperature as the condition is used. The temperature of transformation at equilibrium is conventionally taken at the triple state, Chaoping [9 ]

The physical model for deposition of crystals like diamond can be presumed to start with spherical nuclei in the nano regions. Since facets of crystal grow with equal probability in all preferred directions, the spherical model is a reasonable mathematical assumption. Most commonly, the amorphous version of the deposit occurs. Since graphite is more stable than diamond, it is difficult to obtain the crystalline form of the element, .

The phase diagram below shows the various regions where diamond formation is possible, using pressure. It can be seen that the production of diamond requires pressure of 40 to 50 GPa and temperatures of 2000K to 3000K.

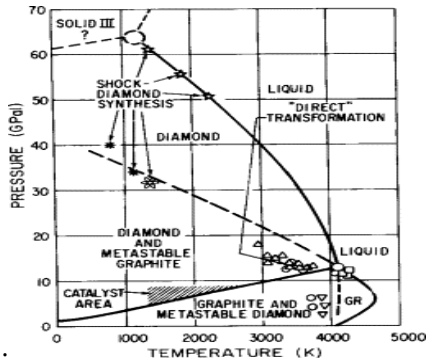


Fig.5 Pressure Temperature diagram for diamond

( from Wenthorf and devries [ 8 ])

Sublimation kinetics have also been evaluated for graphite and graphene by Long [10], where variation in surface properties of nano particles is stated to affect ensemble averaged estimates.

Due to the slow rates in direct deposition, other methods using reduction of carbon compound vapours and gases have been applied commercially. Apart from the initial attempts at high pressure and temperature, the expense involved for industrial production has made successful efforts a closely guarded area.

**5.REFERENCES**

[1] Hoch M, BPE, Dingledy DP etal, "The Heat of Sublimation of Carbon, *J Phys Chem*, 59, 2, 1955

[2] Ladwig A, Koch R, Wensky E, "Atmospheric Plasma Deposition of DLC coatings", *Diamond Related Materials, 18, 1129-1133, 2009*

[3] Roy, M. "Protective Hard Coatings for Tribological Applications. Materials Under Extreme Conditions"*, 259–292.* doi:10.1016/b978-0-12-801300-7.000,2017

[4] Ohring, M. "Chemical Vapor Deposition. Materials Science of Thin Films"*, 277–355.* doi:10.1016/b978-012524975-1/50009-4,2002

[5] Evans G, Greif R, "A two-dimensional model of the chemical vapour deposition of silicon nitride in a low-pressure hot-wall reactor including multi-component diffusion", *Int. J. Heat Mass Transfer*. Vol. 37. No. 10. pp. 1535-1543, 1994

[6] Carslaw HS Jaeger JC, *Conduction of Heat in Solids*, OUP, 1986

[7] Paterson S, "Propagation of a Boundary of Fusion*",GlasgowMathJnl*,1952,DOI:10.1017/S2040618500032937

[8] Wentorf, R. H., & DeVries, R. C. High-Pressure Synthesis (Chemistry). *Encyclopedia of Physical Science and Technology, 365–379.* doi:10.1016/b0-12-227410-5/00968-6 ,2003

[9] Chaoping M, Guangdon Z,Zhiwei Z, "A Modified S-L-G Phase equation of states", *ACS Omega* , 7, 9322-9332,2022

[10] Long B, Lau C, Rodriguez D etal, "Sublimation Kinetics for Individual Graphite and Graphene Nanoparticles (NPs): NP-to-NP Variations and Evolving Structure-Kinetics and Structure-Emissivity Relationships", *J. Am. Chem. Soc.*, 142, 33, 14090–14101, 2020

## Biographies

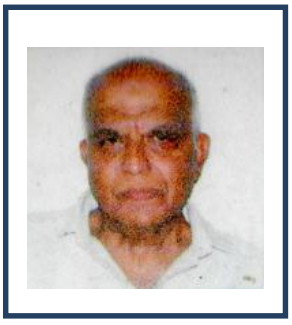

Rahul Basu received the bachelor's degree in Mechanical engineering from the California Institute of Technology in 1970, the master's degree in Materials Science and engineering from the University of California, LA in 1973, and the doctorate degree in from Eurotechnical University in 1991, respectively. After working at the Indian Institute of Science, and DRDO on forming of super alloys and rotor dynamics, receiving three Indian Patents, he is currently an Emeritus Professor, UGC with JNTU and VTU Bangalore. His research areas include amorphous alloys, Nano composites and Renewable Energy. He has been serving as a reviewer for many highly-respected journals.

# Effect of Mixed Modifiers on Electrical Mechanism of Zinc-Phosphate Amorphous Semiconducting Glass

**[1, 2]Arpan Mandal, [3, *] Dipankar Biswas, [4]Rittwick Mondal, [5]Bidyut Kumar Ghosh, [2]Nipu Modak**

[1] *Mechanical Engineering Department, Regent Education and Research Foundation, Kolkata 700121, India*

[2] *Mechanical Engineering Department, Jadavpur University. Kolkata-700032, India*

[3, *] *Electronics & Communication Engineering Department, Regent Education and Research Foundation, Kolkata 700121, India*

[4]*Chowhatta High School, Birbhum, West Bengal 731201, India*

[5]*Electrical Engineering Department, Regent Education and Research Foundation, Kolkata 700121, India*

*Email: dipankar_aec@rediffmail.com*

## Abstract.

The impact of $MoO_3$ and $TeO_2$ inclusion on electrical and dielectric mechanisms of the zinc-phosphate host glass matrix has been reported in this communication. The well-known melt quenching route has been employed to produce glass nanocomposite systems. The formation of superimposed nanocrystallites of $ZnMoO_4$, $Mo_5TeO_{16}$ and $TeO_3$ within the amorphous glass matrix is established by XRD spectra. The well-known Debye-Scherrer approach has been used to estimate the typical nanocrystallite size ($d_C$). The semiconducting nature of glasses has been demonstrated from their DC conductivity. The small polaron hopping process causes nonlinearity in DC conductivity, which is different from AC conductivity. The modified correlated barrier-hopping (CBH) model explains the mechanism of AC conduction. The DC and AC activation energies are found to decrease with the accumulation of $TeO_2$ in glass matrices.

**Keywords**. Glass nanocomposite; Almond-West formalism; Small polaron hopping; AC and DC Conductivity; Modified CBH model

## 1. INTRODUCTION

Recent years have seen a rise in interest in zinc-phosphate glasses due to its low UV cut-off wavelength, exceptional chemical strength, thermal constancy, and outstanding electrical conduction [1, 2]. Because of their high thermal expansion coefficient, lower melting temperature, and excellent UV transmission, phosphate glasses are of tremendous technological and scientific attention for both practical and theoretical applications [3]. When compared to Pb-based glasses, their weak chemical stability frequently limits their ability for real-world sealing applications. To improve the poor chemical stability of phosphate glasses, the controlled accumulation of oxides such as CuO, $MoO_3$, SnO, $Sb_2O_3$, and $V_2O_5$ [3] has already been found to be effective.

Due to the remarkable modifications in the physical and structure properties seen in $ZnO$-$P_2O_5$ system, the presence of ZnO into phosphate glasses is quite fascinating [4]. Better chemical stability is achieved by using ZnO such as a network modifier or former, which also results in a wider glass-forming region and lower glass transition temperatures [5]. The glass doped with $TeO_2$ is challenging to make at large concentrations because of the potential for quick amorphization and phase separation during cooling. As a result, different kinds of defects may occur in $TeO_2$-doped glass during the melt quenching procedure. To improve the tellurite glassy network's ability to create glass, metaphosphate can be added [6, 7]. As a result, after being doped with $P_2O_5$ as a glass making agent, $MoO_3$ as a network modifier, and ZnO as network stabilizer, $TeO_2$-doped glass can be made utilizing the quench of melt method. Electro-optical applications are made possible by the electrochromism properties and improved ionic conductivity of phosphate glass systems doped with $MoO_3$. Mo ions can be found inside glass network as octahedral and tetrahedral structural units because they can exist in two unique valence states, $Mo^{6+}$ and $Mo^{5+}$ [8, 9]. Due to the development of $TeO_4$ trigonal bipyramids, doping $ZnO$-$P_2O_5$ glasses with $TeO_2$ results in changing structural. To determine the most suitable glassy system for more effective applications, we have investigated the results of including both $MoO_3$ and $TeO_2$ as mixed modifiers in $ZnO$-$P_2O_5$ glasses in the present work. The purpose of this research is to use the melt quenching method to synthesise three quaternary glassy systems that have the chemical formula $0.60ZnO\text{-}0.10P_2O_5\text{-}0.30[((1\text{-}x)\ MoO_3\text{-}xTeO_2]$. One of the main objectives of this communication is to examine the X-ray diffraction (XRD) patterns to investigate the microstructure. In order to evaluate each sample's semiconducting nature and DC conductivity, the small polaron hopping hypothesis is applied. Almond-West formalism and the well-known Jonscher's Universal Law have both been used to analyze the conductivity of the present glassy systems.

## 2. EXPERIMENTAL PROCEDURE

The unique chemical composition $0.60ZnO\text{-}0.10P_2O_5\text{-}0.30[((1\text{-}x)MoO_3\text{-}xTeO_2]$ has been used to synthesize three quaternary glassy nanocomposite systems. ZnO, $MoO_3$, $P_2O_5$, and $TeO_2$ in the proper amount in powder form, all with 99% purity, have been methodically assorted in an alumina crucible according to the stoichiometry of each composition. Initial temperature of the high-temperature electrical furnace is then set to 150°C, and then, it rises at a rate of 10°C/min while the alumina crucible is placed inside the furnace. We cautiously notice the form of the assortment in the furnace every five minutes and record the temperature at which the composite melts. At temperatures between 770°C and 890°C, three samples of quaternary glass (x = 0.1, 0.2, and 0.3) are melted. The entire melt of each composition has been immediately cooled at 25°C among two superbly polished metal plates in order to form semi-transparent glassy samples with thicknesses of 1-2 mm. To perform the structural measurement, the as-quenched solid glasses are converted into adequate powder form by grinding appropriately. Density (ρ) of the as-prepared glasses has been perceived using the Archimedes principle and acetone is used as the immersion liquid. The quaternary glass samples have been tested for density and molecular weight, which are then applied to calculate the molar volumes. An X-ray diffractometer has been used to examine the X-ray diffraction patterns using CuKα radiation. By using the two-probe method and LCR meter, electrical measurements have been conducted. To operate as an electrode, a highly conductive silver paste has been coated on both surfaces of the glass sample. At a range of temperatures, electrical conductivity of glasses has been evaluated in a wide frequency range.

## 3. RESULTS AND DISCUSSIONS

### *3.1. Investigation of Physical Parameters*

To determine the nature of structural reforms in amorphous glassy or polycrystalline materials, ρ is a fundamental characteristic or physical feature. Molecular weight, constituent element fraction, and glass structure type all have a significant impact on oxide glass density. The average values of ρ of all glasses have been determined using the well-known Archimedes principle (Eq. 1) using the following expression [11].

$$\rho = \left( \frac{W_{air}}{W_{air} - W_{acetone}} \right) \times \rho_{acetone} \qquad (1)$$

By applying the derived values of ρ, the following equation can be employed to determine the molar volume [11].

$$V_M = \sum \frac{x_i \times M_i}{\rho} \qquad (2)$$

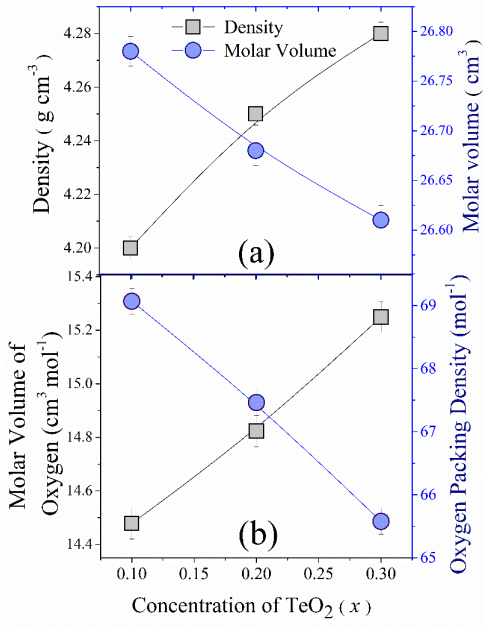


**Figs. 1(a)** Estimated values of ρ and $V_M$, and **(b)** composition dependence of $V_O$ and OPD.

As the amount of $TeO_2$ ($x$) rises, the association between $V_M$ and ρ of all examined samples is revealed in Fig. 1(a). $TeO_2$ and $MoO_3$ have molecular weights of 159.6 and 143.94 g/mol, respectively. When $TeO_2$ is added to the glass matrix, the values of ρ increase as the amount of $MoO_3$ decreases. The compactness of the glass network increases as the value of ρ

rises, which causes the bond length to decrease as the concentration of $TeO_2$ rises ($x$) [12]. As the amount of $TeO_2$ rises, $V_M$ values decrease, which is also seen in Fig. 1. (a). With the addition of $TeO_2$, the decremental bond length and higher stretching force constant produce compact glass structures, which leads to the declining nature of $V_M$ value [12].

Molar volume of oxygen ($V_O$) and oxygen packing density (OPD) have been assessed in order to better realize the glass structure using associations based on the corresponding values of ρ and $V_M$ [13].

$$V_O = \frac{V_M}{\sum_i x_i n_i} \tag{3}$$

and

$$OPD = 1000C\left(\frac{\rho}{M}\right) \tag{4}$$

In the above equations, $n_i$ is the quantity of oxygen atoms found inside each oxide, C is the amount of oxygen atoms available within every unit of the formula, and M is the molecular weight.

For all glass nanocomposites, the computed $V_O$ and OPD values are shown in Fig. 1(b). $TeO_2$ is added to the MoO3-ZnO-$P_2O_5$ glass structure, which results in a reduction in NBO bonds as $V_O$ rises and OPD falls. This study shows that fewer NBO bonds improve the compactness of glass structure and improve the density of as-prepared glasses [13].

**Table 1:** Several computing parameters from XRD spectra

| x (mol%) | 2θ (Degree) (±0.10) | FWHM | Identified Phase | h | k | l | $d_c$ (±0.06) | Crystalinity (%) (±0.05) |
|---|---|---|---|---|---|---|---|---|
| 0.15 | 36.12 | 0.1903 | $ZnMoO_4$ | 0 | 2 | 1 | 31.67 | 2.21 |
| 0.25 | 31.75 | 0.1995 | $Mo_5TeO_{16}$ | -3 | 2 | 1 | 41.42 | 3.34 |
| | 34.27 | 0.2123 | $TeO_3$ | 1 | 1 | 0 | | |
| | 36.12 | 0.2003 | $ZnMoO_4$ | 0 | 2 | 1 | | |
| 0.35 | 31.75 | 0.1874 | $Mo_5TeO_{16}$ | -3 | 2 | 1 | 49.65 | 4.56 |
| | 34.27 | 0.1612 | $TeO_3$ | 1 | 1 | 0 | | |
| | 35.45 | 0.1623 | $Mo_5TeO_{16}$ | -3 | 2 | 1 | | |
| | 36.12 | 0.1887 | $ZnMoO_4$ | 0 | 2 | 1 | | |

### *3.2. Analysis of XRD Spectra*

Glassy systems with $TeO_2$ doping are shown with their spectra in Fig. 2. Crystallinity can be seen inside the amorphous glassy matrix as evidenced by the distinct peaks and defined widths in the XRD patterns. This leads to the claim that a small number of nanocrystallites are formed within the glassy, amorphous network. The subsequent relation determines the degree of crystallinity for every glassy system and the projected values are presented in Table 1.

$$\%\ Crystallinity = 100 \times \frac{Area\ of\ crystalline\ peak}{Total\ area\ under\ the\ patterns} \tag{5}$$

For the effect of the mixed modifier, it has been perceived that the percentage crystallinity values rise as more nanocrystallite phases emerge in zinc phosphate glass matrices. The available literature data has been used to identify and index the nanophases of specific diffraction peaks.

Table 1 demonstrates that the identified nanocrystallites of $ZnMoO_4$ [14], $Mo_5TeO_{16}$ [15] and $TeO_3$ [16] are developed within the glassy matrix.

Using the Debye-Scherrer equation, the values of $d_c$ have been estimated [17].

$$d_c = \frac{0.89\lambda}{\beta\cos\theta} \tag{6}$$

The assessed values of $d_c$ for all three quaternary glasses are tabulated in Table 1.

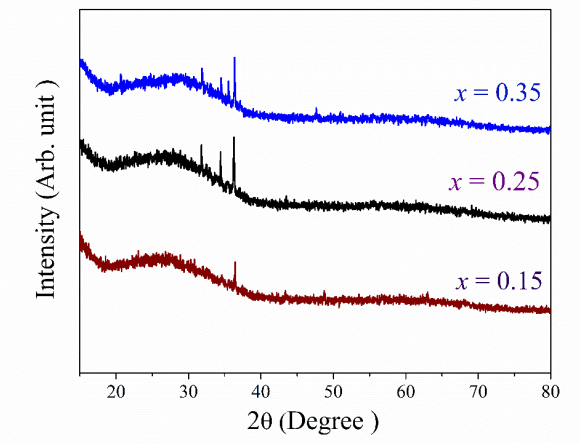


**Fig. 2.** Recorded XRD spectra of all glasses

### *3.3. Electrical Conduction Mechanism*

This section provides an in-depth assessment of mechanism of electrical conductivity of $TeO_2$ and $MoO_3$ doped zinc phosphate glass systems at a wide range of temperatures.

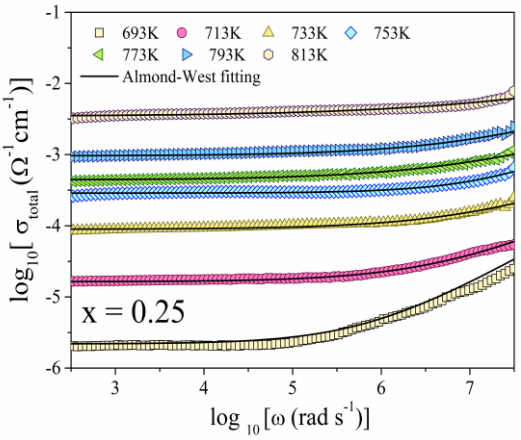


**Fig. 3.** $\sigma_{total}$ spectra of $x$ = 0.25 glassy system

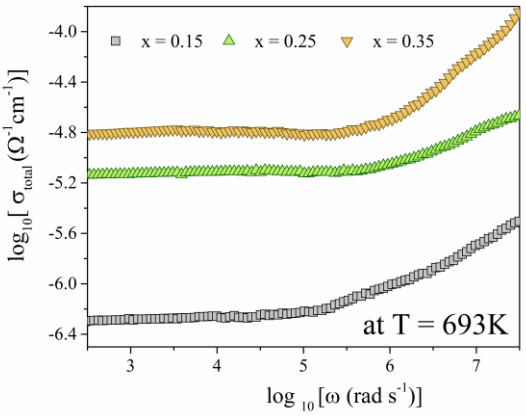


**Fig. 4.** $\sigma_{total}$ spectra off three quaternary glass systems at T = 693K.

$\sigma_{total}$ spectra of glass with $x$ = 0.25 and three glasses at a fixed temperature T = 693K are revealed in Figs. 3 and 4, respectively.

As seen in Figs. 3 and 4, the values of $\sigma_{total}$ rise as the temperature rises, indicating non-linear properties and the semiconducting characteristics of glasses under investigation. The lower frequency portion has a nearly frequency-independent $\sigma_{total}$ spectrum (plateau or flat area), which is a property of DC conductivity ($\sigma_{dc}$). The conductivity spectrum displays an almost linear characteristic at higher frequencies.

It is perceived from Fig. 4 that the glass system of $x$ = 0.35 (higher $TeO_2$ content) reveals higher conductivity.

The Almond-West formalism, which is represented by the succeeding equation, has been used to explore the electrical conduction mechanism of $MoO_3$ and $TeO_2$ doped zinc phosphate glass systems [4, 17].

$$\sigma_{total} = \sigma_{dc}\left[1 + \left(\frac{\omega}{\omega_H}\right)\right]^p \qquad (7)$$

Here, the parameter p stands for the frequency exponent, and $\omega_H$ for the crossover frequency. As shown in Fig. 3, curve fitting of entire conductivity data is utilized to assessment of these parameters.

The resultant values of $\omega_H$ of three quaternary glasses are plotted with inverse of applied temperatures, as shown in Fig. 5(a). The behaviour of temperature dependence is verified in Fig. 5(a), which also demonstrates that the value of $\omega_H$ rises with temperature. The nature of $\omega_H$ in a glass according to Arrhenius is explained by the following equation [18].

$$\omega_H = \omega_e \, exp\left(-\frac{E_H}{K_B T}\right) \quad (8)$$

The operative attempt frequency is denoted by $\omega_e$ in the equation above, while the Boltzmann constant is signified by $K_B$.

The polaron migration activation energy ($E_H$) for disordered materials is defined as the minimum quantity of energy necessary for small polarons to hop between localized sites that are parted from one another by a potential barrier [18]. In Fig. 5(b), it can be realized that the values of $\omega_H$ rise as $TeO_2$ is added, while $E_H$ exhibits an inverse relationship with $\omega_H$.

The Almond-West formalism yields the values for $\sigma_{dc}$ that are totally temperature-dependent, and the non-linear behavior of $\sigma_{dc}$ is caused by the influence of several conduction mechanisms. The subsequent equation can be used to represent the temperature-dependent $\sigma_{dc}$.

$$\sigma_{dc} = \sigma_{High} \exp\left(-\frac{E_{High}}{K_B T}\right) + \sigma_{Low} \exp\left(-\frac{E_{Low}}{K_B T}\right) \quad (9)$$

From the equation above, two dissimilar sorts of DC conductivity mechanisms may be inferred: $\sigma_{dc}$ at high temperatures ($\sigma_{high}$) and $\sigma_{dc}$ at low temperatures ($\sigma_{low}$). The DC conduction ($\sigma_{High}$) mechanism, which operates at higher temperatures, depends solely on the amount of formed defects states inside the mobility gap, which is determined by the amount of amorphousness in the glassy systems [18].

As opposed to this, the DC conduction ($\sigma_{low}$) mechanism at low temperatures relies on polarons hopping among a variety of produced defects or localized states and relies on the tunnelling mechanism among the nearby potential barriers [19].

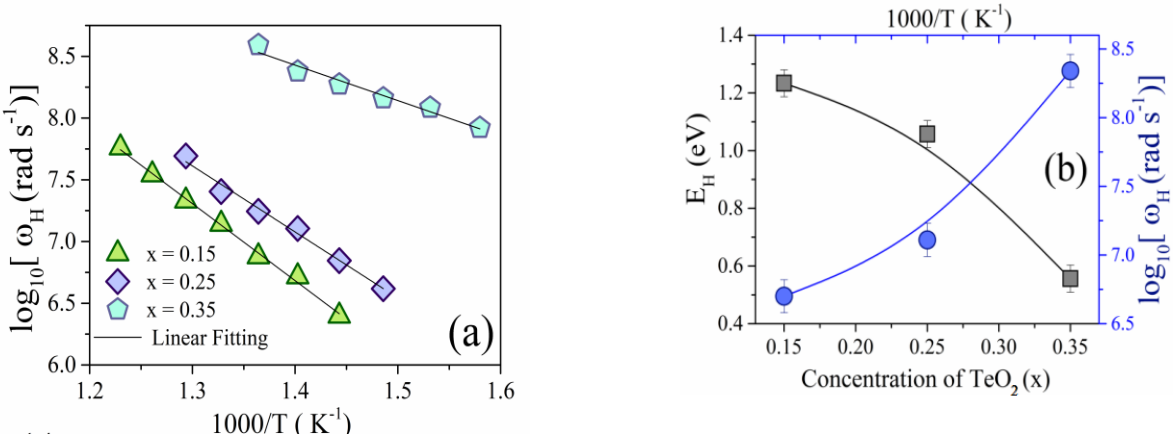


**Fig. 5 (a)** Temperature dependency of $\omega_H$ and **(b)** composition dependency of $E_H$ and $\omega_H$

**Table 2:** Different types of estimated activation energies.

| Composition (x, mol%) | Activation energy (DC) $E_{high}$ (eV) | $E_{low}$ (eV) | Activation energy (AC) $E_{ac}$ (eV) |
|---|---|---|---|
| 0.15 | 2.22 | 1.31 | 1.02 |
| 0.25 | 1.87 | 1.12 | 0.93 |
| 0.35 | 1.64 | 0.73 | 0.74 |

Fitting with linear equation of the acquired $\sigma_{dc}$ spectra, as shown in Fig. 6(a), predicts two different types of DC activation energies, $E_{Low}$ and $E_{High}$, for the lower and higher frequency zones, respectively. The values of $E_{Low}$ and $E_{High}$ gradually decrease under the impact of $TeO_2$ in the $ZnO\text{-}P_2O_5$ glassy network, which is supported by the tabulated values of $E_{Low}$ and $E_{High}$ in Table 2. As a result, the amount of $TeO_2$ increases with the conductivity of the glasses.

The mechanism of AC conductivity of polycrystalline and amorphous glasses is described by the Jonscher universal power-law, which is frequency- and temperature-dependent. [20]

$$\sigma(\omega) = A\omega^S \quad (10)$$

The power-law exponent (s) and constant parameter A are used to calculate the glass system's polarizability strength. The difference between the $\sigma_{total}$ and the estimated $\sigma_{dc}$ is subtracted to acquire the AC conductivity ($\sigma_{ac}$) of glasses. Fig. 6(b) establishes the quaternary glass sample's dependence on temperature and frequency. The chance of charge carriers escaping to the conduction state is increased with the rise in temperature due to an increase in lattice vibration. Conduction thus improves, leading to a decrease in activation energy.

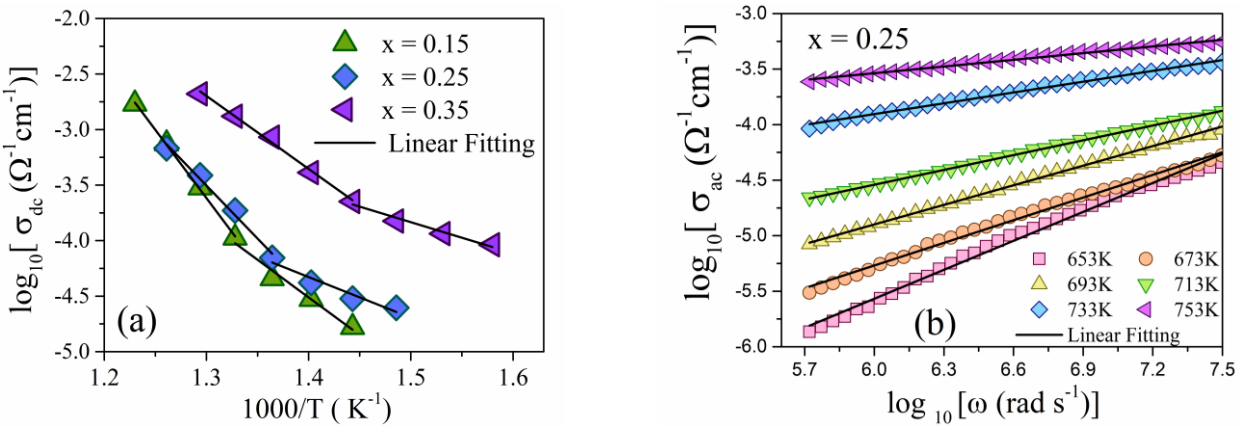


**Fig. 6 (a)** Temperature-dependent $\sigma_{dc}$ of glasses and **(b)** Frequency-dependent $\sigma_{ac}$ of glass sample x = 0.25.

Table 2 provides the activation energies ($E_{ac}$) related to each glass sample's AC conduction mechanism as determined by the fitting with linear equation of the $\sigma_{ac}$ data. For the glass with $x$ = 0.25, the alterations in AC with frequency are displayed in Fig. 6(b). $E_{ac}$ is the necessary energy required for disordered or semiconducting glass to overcome the barrier potential and start the AC conduction process. As $TeO_2$ replaces the transition metal oxide $MoO_3$, it has been noticed that the values of $E_{ac}$ are falling. $TeO_2$ content thus improves the AC conduction of the glass system.

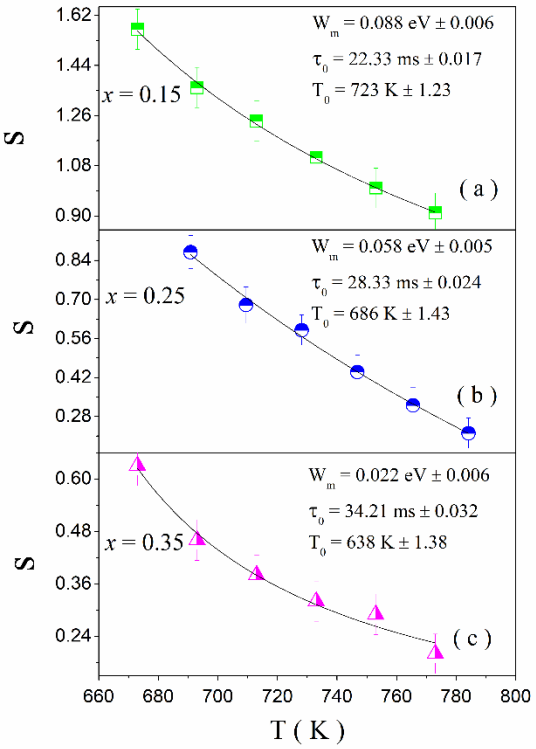


**Fig. 7(a-c)** S versus T plots and modified CBH model fittings of all glass samples.

As seen in Fig. 7(a), the temperature dependence of $\sigma_{ac}$ is projected to occur at higher frequency ranges. The fluctuation of "s" with temperature aids in the adaption of the optimal AC conduction mechanism. According to Fig. 7(a-c), the expected values of "s" for respective glass drop as temperature rises. When "s" declines as temperature rises in disordered or amorphous glassy materials, Pike and Elliott's CBH model offers a precise description of the mechanism of $\sigma_{ac}$ [17]. As stated in CBH model, conduction occurs as a result of charge carriers (electron or microscopic polarons) hopping over the potential barrier; the amount of energy required to do so is determined by the Coulombic interaction separating the two sites. Jumps between two localized sites are thought to have symmetric jumping possibilities per unit of time, which means they can happen both forward and backward. Little polarons or charge carriers hop when the barrier separating two suitably defined sites is thermally activated.

For glassy systems with greater values of s, the conventional CBH model is inappropriate. It is important to alter the typical CBH model in the manner described below in order to acquire the correct values for all fitting parameters. [18]

$$s = 1 - \frac{6K_B(T - T_0)}{w_m + K_B(T - T_0) * \ln(\omega\tau_o)} \quad (11)$$

As presented in Fig. 7 (a-c), values of fitting parameters hopping barrier potential ($W_m$), Debye relaxation time ($\tau_0$), and ideal thermodynamic temperature of glass transition ($T_0$) are estimated from fitting with modified CBH model (Eq. 11). It has been noted that the $\sigma_{ac}$ of the glassy system reduces as $TeO_2$ content is added to glassy matrices, which causes the values of $W_m$ to decrease.

## 4. SUMMARY AND CONCLUSIONS

It is established that the volumetric mass density of all semiconductor glasses having the common formula 0.60ZnO-0.10$P_2O_5$-0.30[((1-x)$MoO_3$-x$TeO_2$] prepared by the quenching of melt process increases steadily with increasing of $TeO_2$ (x) content, while the $V_M$ decreases since the greater compaction structure of glasses. With the addition of $TeO_2$, the glassy system becomes more compact because the values of $V_O$ and OPD are continuously increasing and decreasing. The presence of $ZnMoO_4$, $Mo_5TeO_{16}$, and $TeO_3$ nanocrystallites on amorphous glass matrices is established by XRD patterns. Values of $d_c$ and the crystallinity (%) both rise with $TeO_2$ content. Total conductivity spectra analysis revealed frequency-independent ($\sigma_{dc}$) and frequency-dependent ($\sigma_{ac}$) regions. In both cases, conductivity increased with an increase in temperature due to changes in the bond structures of the glassy systems and the emergence of the defect or localized states, exhibiting semiconductor behavior. The values obtained of the minimum acceptable energy for small polaron migration ($E_H$) and $E_{ac}$ drop as $\sigma_{ac}$ rises. The fact that the power-law exponents (s) decrease as temperature rises suggests that the AC conductivity mechanism is a perfect match for the modified CBH model. As the AC conductivity rises, the value of the CBH model parameter Wm drops. According to the findings of the current study, structural changes and conduction processes are significantly influenced by the presence of $TeO_2$ and $MoO_3$ as mixed modifiers in the glassy matrix of ZnO-$P_2O_5$.

## 5. REFERENCES


[1] J. Tang, Y. Huang, M. Sun, J. Gou, Y. Zhang, G. li, Y. Kang, J. Yang, Z. Xiao, J. Lumin., "Spectroscopic characterization and temperature-dependent upconversion behavior of $Er^{3+}$ and $Yb^{3+}$ co-doped zinc phosphate glass", Journal of Luminescence, vol. 197 pp. 153–158, 2018

[2] N. Radouane, A. Maaroufi, B. Ouaki, C. Poupin, R. Cousin, B. Duponchel, D.P. Singh, A.H. Sahraoui, M. Depriester, "Thermal, electrical and structural characterization of zinc phosphate glass matrix loaded with different volume fractions of the graphite particles", J. Non-Cryst. Solids, vol. 536, pp. 119989, 2020.

[3] Y.B. Singh, D. Biswas, S.K. Shah, S. Shaw, R. Mondal, A.S. Das, S. Kabi, L.S. Singh, "Investigation of optical properties and electrical conductivity mechanism of $Fe_2O_3$–$Sm_2O_3$–ZnO–$P_2O_5$ quaternary glass nanocomposite systems", Materialia, vol. 15, pp. 100963, 2021.

[4] D. Biswas, A.S. Das, R. Mondal, A. Banerjee, D. Deb, A. Dutta, S. Bhattachacharya, S. Kabi, L.S. Singh, "Study of microstructure and electrical conduction mechanisms of quaternary semiconducting glassy systems: Effect of mixed modifiers", J. Non-Cryst. Solids, vol. 542, pp. 120104, 2020.

[5] D. Jain, V. Sudarsan, R.K. Vatsa, C.G.S. Pillai, "Luminescence studies on ZnO–P2O5 glasses doped with $Gd_2O_3$:Eu nanoparticles and $Eu_2O_3$", J. Lumin. Vol. 129 (5), pp. 439-443, 2009.

[6] V.A.G. Rivera, D. Manzani, Technological Advances in Tellurite Glasses, Elsevier, vol. 2, pp. 1–100, 2017.

[7] R.K. Brow, "Review: the structure of simple phosphate glasses", J. Non-Cryst. Solids, vol. 263–26, pp. 1–28, 2000.

[8] P.S. Rao, P.M.V. Teja, A.R. Babu, C. Rajyasree, D.K. Rao, "Influence of molybdenum ions on spectroscopic and dielectric properties of $ZnF_2$-$Bi_2O_3$-$P_2O_5$ glass ceramics", J. Non-Cryst. Solids, vol. 358, pp. 3372–3381, 2012.

[9] M.A. Ghauri, S.A. Siddiqi, W.A. Shah, M.G.B. Ashiq, M. Iqbal, "Optical properties of zinc molybdenum phosphate glasses", J. Non-Cryst. Solids, vol. 355, pp. 2466–2471, 2009.

[10] K. Vosejpkova, L. Koudelka, Z. Cernosek, P. Mosner, L. Montagne, B. Revel," Structural studies of boron and tellurium coordination in zinc borophosphate glasses by $^{11}B$ MAS NMR and Raman spectroscopy", J. Phys. Chem. Solid, vol. 73, pp. 324–329, 2012.

[11] S. Hassanien, I. Sharma, A.A. Akl, "Physical and optical properties of a-Ge-Sb-Se-Te bulk and film samples: Refractive index and its association with electronic polarizability of thermally evaporated a-$Ge_{15-x}Sb_xSe_{50}Te_{35}$ thin-films", J. Non-Cryst. Solids, vol. 531, pp. 119853, 2020.

[12] R.K.N. Ningthemcha, D. Biswas, R. Mondal, A.S. Das, S. Kabi, D. Ghosh, L.S. Singh, B. Deb, "Study of mixed modifier effect on dielectric and optical properties of zinc-phosphate based ternary and quaternary nanocomposite systems", Journal of Non-Crystalline Solids, vol. 591, pp. 121701, 2022.

[13] D.P. Singh, G.P. Singh," Conversion of covalent to ionic behavior of $Fe_2O_3$–$CeO_2$–PbO–$B_2O_3$ glasses for ionic and photonic application", Journal of Alloys and Compound. Vol. 546, pp. 224–228, 2013.

[14] J. Meullemeestre, E. Penigault, Bull. Soc. Chim. Fr., vol. 10 pp. 3669–3674, 1972.

[15] Y. Arnaud Y, J. Guidot, C. R. Seances Acad. Sci., Ser. C, vol. 282, pp. 631–634, 1976.
[16] M. Dusek, J. Loub, "X-ray Powder Diffraction Data and Structure Refinement of $TeO_3$", Powder Diffraction, vol. 3, pp. 175–176, 1988.
[17] R.K.N. Ningthemcha, D. Biswas, Y.B. Singh, D. Sarkar, R. Mondal, D. Mandal, L.S. Singh, "Temperature and frequency dependent electrical conductivity and dielectric relaxation of mixed transition metal doped bismuth-phosphate semiconducting glassy systems", Materials Chemistry and Physics, vol. 249, pp. 123207, 2020.
[18] D, Biswas, R.K.N. Ningthemcha, A.S. Das, L.S. Singh, "Structural characterization and electrical conductivity analysis of $MoO_3$–$SeO_2$–ZnO semiconducting glass nanocomposites", J. Non-Cryst. Solids, vol. 515, pp. 21–33, 2019.
[19] A. Ihyadn, A. Lahmar, D. Mezzane, L. Bih, A. Alimoussa, M. Amjoud, M. El. Marssi, I.A. Luk'yanchuk, "Structural, elelectrical and energy storage properties of BaO–Na2O–Nb2O5–WO3–P2O5 glass–ceramics system", Mater. Res. Express, vol. 6, pp. 115203, 2019.
[20] D. Biswas, A. S. Das, R. Mondal, A. Banerjee, A. Dutta, S. Kabi, L. S. Singh, "Structural properties and electrical conductivity mechanisms of semiconducting quaternary nanocomposites: Effect of two transition metal oxides", J. Phys. Chem. Solids, vol. 144, pp. 109505, 2020.
[21] A.K. Jonscher, "Dielectric Relaxation in Solids", London: Chelsea Di Electrics, pp. 10–152, 1983.

## Biographies

**Arpan Mandal** received the bachelor's degree in Mechanical Engineering from WBUT (MAKAUT) University in 2012, the master's degree in Production Engineering from Jadavpur University in 2017, and the pursuing philosophy of doctorate degree in Mechanical Engineering from Jadavpur University, respectively. He is currently working as a Faculty in the Department of Mechanical Engineering, Regent Education and Research Foundation. His research areas include glass composites.

**Bidyut Kumar Ghosh** received the bachelor's degree in Electrical Engineering from WBUT (MAKAUT) University in 2009, the master's degree in Electrical Devices and Power Systems from WBUT (MAKAUT) University in 2013. He is currently working as a Faculty in the Department of Electrical Engineering, Regent Education and Research Foundation. His research areas are Structural properties of Ionic System, Electrical Conduction and Dielectric relaxation of Ionic system etc.

**Nipu Modak** received the bachelor's degree in Mechanical Engineering from North Bengal University in 2002, the master's degree in Mechanical Engineering Machine Design Specialization from BESU Shibpur in 2004, and the philosophy of doctorate degree in Engineering from Jadavpur University in 2011, respectively. He is currently working as Professor at the Department of Mechanical Engineering, Faculty of Engineering, Jadavpur University. His research areas include Microfluidic transport and separation in MEMS scale application and characteristic analysis of composite, ceramic and nano structured material. He has been serving as a reviewer for many respected journals and conferences.

**Rittwick Mondal** is a post graduate in Physics from Madurai K. University, has a distinguished career of 13 years of teaching Physics in secondary schools, under west Bengal Govt. He has published sixteen research papers in the International SCI journals of repute. His research area includes glass and glassy nanocomposites, Magnetic perovskites, optical properties of mixed former glassy nano composite systems, Green synthesis of Nano particles, and topological analysis of chalcogenide glassy systems. He has been serving as a reviewer for many reputed journals.

**Dr. Dipankar Biswas** is currently working as an Associate Professor in Department of Electronics & Communication Engineering, Regent Education and Research Foundation Barrackpore, West Bengal, India. Having completed his B.E. Degree from University of Burdwan, he started his journey of teaching and research since. Afterwards he completed his M.Tech. from WBUT. And while continuing his teaching and research obsession, he persuaded and got his PhD degree from National Institute of Technology Manipur**.** Now has more than 16 years of experience teaching in various engineering colleges. Alongside teaching, he has also been indulged in many high-quality researches producing more than 35 high original research articles in various international journals of high repute. His research areas include composite materials, chalcogenide glass, glass ceramic, glucose sensor etc. He has been serving as a reviewer for many reputed journals.

# Effect of Transition Metal Oxides on Optical and DC Conduction Mechanism of Zinc-Phosphate Amorphous Semiconducting Glass

**[1,3]Souvik Brahma Hota , [2]Ashes Rakshit , [3]Debasish Roy,**
**[2]Debtanu Patra , [4,*] Dipankar Biswas**

*[1]Department of Mechanical Engineering, Techno India University, Bidhannagar, Salt Lake, Kolkata 700091, West Bengal, India.*
*[2]Department of Mechanical Engineering, Regent Education and Research Foundation, Barrackpore, Kolkata 700121, India*
*[3]Department of Mechanical Engineering, Jadavpur University. Kolkata-700032, India,*
*[4, *]Department of Electronics & Communication Engineering, Regent Education and Research Foundation, Barrackpore, Kolkata 700121, India,*
*Mail id: dipankar_aec@rediffmail.com*

## Abstract.

It has been investigated how the incorporation of transition metal oxides impacts on physical, electrical and optical characteristics of zinc phosphate glasses developed by the standard melt quenching method. Some nanophases $ZnP_4O_{11}$, $Zn_{2.5}MoVO_8$, $Zn[MoO_4]$ and $MoV_2O_8$ have been found to superimpose on amorphous glassy matrices. The acquired X-ray diffraction data have been used to determine the polycrystalline structure, crystallinity levels, and formed nanocrystallites's average size. UV-visible spectra of glass systems have been examined, which shows that the electronic transition is indirect. On the basis of their ultraviolet edges, the Optical Band Gap Energy and Urbach Energy have been estimated. The current glassy systems exhibit semiconducting characteristics, as evidenced by the non linear nature of DC conductivity and various activation energies at high and low temperatures. In addition, tiny polarons that hop via defect or localized sites are accountable for the DC conduction mechanism. Using Mott and Greaves variable range hopping models, DC conductivity has been explained.

**Keywords**. Glass nanocomposite; Optical Band gap; DC Conductivity; Mott's and Greaves model.

## 1. INTRODUCTION

In countless technological fields, including electronics, sensors, reflecting windows, optical filters, optical switches, and electro-optic devices, glass nanocomposites are being used extensively [1,2]. Addition of transition metal ions (TMI) leads to the structural and characteristics changes of glass nano-composites have recently been identified as promising research areas in non-linear optics. Due to their potential to yield several valence states, TMI incorporation in glass networks has been one of the methods used to create incredibly cheap luminous devices [3]. Due to their inherent ability in adopting many structural forms, such as octahedral, bipyramidal and polyhedral coordination environments in different oxidation states, vanadates have drawn a significant amount of attention. They have remarkable optical and electrical properties as a result of the compositions' formation of a $V_2O_5$ layered structure [4]. The $V^{5+}$ ion is bonded in a $VO_4^{3-}$ group with the number of four $O^{2-}$ ions in tetrahedral symmetry, as seen by the structural behaviour of $V_2O_5$. The vanadate glass system's structure is composed of a layered chain of $VO_4$ polyhedron units [4]. Transition metal oxide (TMO) such as molybdenum trioxide modifies the structure of the glass instead of acting normally as a glass-forming oxide by merging octahedral $MoO_6$ or tetrahedral $MoO_4$ structural parts along with some other glass-forming oxides, as for example phosphorus pentoxide ($P_2O_5$), vanadium pentoxide ($V_2O_5$)etc. As Mo ions have existence in both the stable $Mo^{6+}$ (accepter level) and $Mo^{5+}$ (donor level) valence states and form $MoO_4$ tetrahedral units, the addition of $MoO_3$ can result in more packed glassy systems [5]. $MoO_3$-doped glasses made of phosphate have electro-optical characteristics that are advantageous for a number of technological applications [6].

On the other hand, zinc oxide (ZnO) modifies the sensitive features of the glass while also influencing its structure and stabilizing the glass network. In view of the fact that zinc cations in glassy materials can adopt both four and

six-fold coordination with oxygen ions, this is conceivable [7]. It is noteworthy that nanocomposites of ZnO-doped glass have excellent economical possibilities because they have wide application in many technological fields, including dielectric layers, varistors, and barrier ribs of plasma displays [7]. The process of hopping from the lower to the higher valence states can be initiated by portable charge carriers or tiny polarons, that can improve electrical transport characteristics of phosphate glasses doped with TMI. Doped glasses with two TMIs can achieve a super-exchange of electrons between redox ion pairs to a significant extent, or "hopping" which results in the non-linear features of activation energy [8]. Because of the combined transition metal-ion effect, this nonlinearity arises [9]. The electrical conduction process is influenced by the spreading of hopping distances of charge carrier or the electron's energy variances located at distinct potential wells as charged impurity atoms are present [10]. Additionally, variances in oxygen coordination or thermally induced structural vibrations cause variations in electrical conduction mechanism as well as the required activation energy for the conductivity procedure [10].

The initial goal of this study is the melt quench synthesis of three quaternary glassy systems with the formula $0.15P_2O_5$–$0.35ZnO$-$0.50(1-x)\ MoO_{3-x}V_2O_5$) Due to the existence of two TMOs, $V_2O_5$ and $MoO_3$, we are able to analyze the mechanism of DC conduction for quaternary glass systems with the nature of mixed transition ion effect. The exploration of the structural and optical absorption characteristics of glass systems using XRD(X-ray diffraction)and Ultraviolet-visible absorption methods are another significant focus of this work.

## 2. EXPERIMENTAL PROCEDURE

The unique chemical composition $0.15P_2O_5$–$0.35ZnO$-$0.50(1-x)MoO_3$-$xV_2O_5$) has been used to synthesize three quaternary glassy nanocomposite systems ($x$ = 0.1, 0.2, and 0.3) with combined modifier oxides ($MoO_3$ and $V_2O_5$). ZnO, $MoO_3$, $P_2O_5$, and $TeO_2$ in the proper amount in powder form, all with 99% purity, have been methodically assorted in an alumina crucible according to the stoichiometry of each composition. The temperature of the high-temperature electrical furnace is then set to 150°C, and then, it rises at 10°C/min heating rate while the alumina crucible is placed inside the furnace. We cautiously notice the form of the assortment in the furnace every five minutes and record the temperature at which the composite melts. At temperatures between 770°C and 890°C, three samples of quaternary glass ($x$ = 0.1, 0.2, and 0.3) are melted. The entire melt of each composition has been immediately cooled at a temperature of 25°C among two metal plates (superbly polished) in order to form translucent glassy specimens of 0.3-0.5 mm of thickness. To perform the structural measurement, the as-quenched solid glasses are converted into fine powdery form by grinding appropriately. The famous principle of Archimedes is used to find out the density of the as-prepared glass samples and acetone is used as the immersion liquid. The quaternary glass samples have been tested for density and molecular weight, which are then applied to calculate the molar volumes. An X-ray diffractometer has been used to examine the X-ray diffraction patterns using CuKα radiation with 1.541 Å of wavelength and a range of 10° - 80°, operating at 4° /min scanning rate with 0.02° step size. Glassy samples that have already been prepared are coated with high conductive silver paste on both sides in order to work as electrodes for electrical studies. With a high-precision LCR metre, the resistance of the silver-coated glass samples has been measured using the two-probe process at a range of temperatures between 60 and 550 °C.

## 3. RESULTS AND DISCUSSIONS

### *3.1. Investigation of Physical parameters*

To determine the structural reforms nature in amorphous glassy or polycrystalline samples, density (ρ) is a fundamental feature or physical characteristic. Molecular weight, constituent element fraction, and glass structure type all have a significant impact on oxide glass density. The mean values of ρ of all glass specimens have been determined by well-known principle Archimedes (Eq. 1) by utilizing the following expression.

$$\rho = \left(\frac{W_{air}}{W_{air-W_{acetone}}}\right) \times \rho_{acetone} \quad (1)$$

$\rho_{acetone}$ refers to the density of the acetone (immersion liquid). While $W_{acetone}$ stands for the sample's weight when soaked in acetone and $W_{air}$ refers to the glass sample's weight when suspended in air [11].

By applying the derived values of ρ, the following equation can be employed to determine the molar volume of individual sample [11].

$$V_M = \Sigma \frac{x_i M_i}{\rho} \quad (2)$$

In Eq. (2), $x_i$ and $M_i$ denotes the molar ratio and molecular weight of the $i^{th}$ oxide, correspondingly.

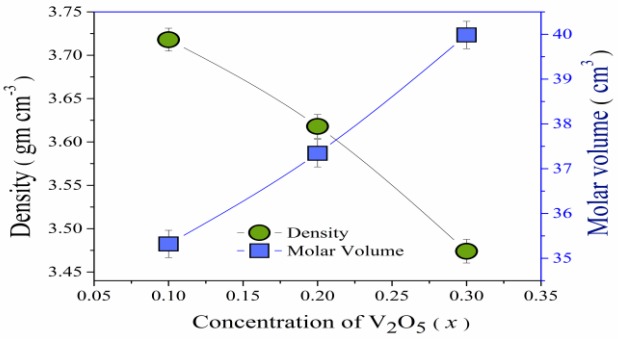


**Fig. 1.** Evaluated values of ρ and $V_M$

The alterations in ρ(density) and $V_M$ (molar volume) values with deviations in concentration (x) of $V_2O_5$ are shown in Fig. 1, along with the typical inverse relationship between $V_M$ (molar volume) and ρ(density). Because $V_2O_5$ has a greater molecular weight (181.88 g mol-1) than $MoO_3$ (143.94 g $mol^{-1}$) does, the composition formulation predicts that the molecular weight of all specimens increase as the $V_2O_5$ (x) concentration rises. Incorporating $V_2O_5$ into the glass-matrix thus works as a glass modifier, increasing the amount of non bridging oxygen (NBO) ions that in turn accelerates the dissociation of covalent bonds inside the network [12].

On the other hand, $V_M$ (molar volume) has a strong correlation to the material's internal spatial organization. The variation in estimated $V_M$ (molar volume) values as a function of the molar ratio of $V_2O_5$ is shown in Fig. 1. Less glass structure compaction results from the rising nature of $V_M$ (molar volume), which also helps to increase bond length. By calculating the average values of V-V separation ($d_{V-V}$), it is possible to confirm that the reduced compaction of quaternary glass structures is caused by $V_2O_5$ inclusion.

The value of $d_{V-V}$ has been assessed from the volume of 1-mol of V ($V_M^V$) and Avogadro's number ($N_A$) by the subsequent relationships.

$$d_{v-v} = \left(\frac{V_M^V}{N_A}\right)^{1/3} \quad (3)$$

Where,

$$V_M^V = \frac{V_M}{2(1-x_{V-ion})} \quad (4)$$

The $<d_{V-V}>$ value increases from 3.32 Å to 3.45 Å gradually with an increament in $V_2O_5$ concentration ($x$).Consequently, the decrement in density and the rising nature of Molar Volume for as-quenched nano-composites are actively supported by the effect of the presence of $V_2O_5$ considerably expanding the quaternary glass network.

### *3.2. Analysis of* X-ray diffraction *Spectra*

The XRD patterns of $V_2O_5$ doped glass systems are exhibits in Fig. 2. The XRD patterns display sharp peaks with definite widths, which specify the crystallinity is there inside the amorphous translucent glass matrix. On the basis of this, it can be claimed that nanocrystallites(in a small number ) are coinciding on the amorphous translucent glass matrix.

The subsequent relation determines the degree of crystallinity for every glassy system and the evaluated values are tabularized in Table 1.

$$\%\, Crystallinity = 100 \times \frac{Area\ of\ crystalline\ peak}{Total\ area\ under\ the\ patterns} \quad (5)$$

For the effect of the mixed modifier, it has been perceived that the percentage crystallinity values rise as more nanocrystallite phases emerge in zinc phosphate glass matrices. The available literature data has been used to identify and index the nanophases of specific diffraction peaks.

Table 1 demonstrates that the identified nanocrystallites of $ZnP_4O_{11}$ [13], Zn [$MoO_4$] [14], $Zn_{2.5}MoVO_8$ (ICDD-50-1894) and $MoV_2O_8$ [15] are developed within the glassy matrix.

Using the Debye-Scherrer equation, the sizes of detected nanocrystallite ($d_c$) have been evaluated [16].

$$d_C = \frac{0.89\lambda}{\beta \cos\theta} \quad (6)$$

In Eq. (6), β symbolizes the full width at half maximum (FWHM), θ denotes the angle of Bragg diffraction, and λ refers to the wavelength (1.54 Å) of the Cu-Kα X-ray radiation employed. The evaluated $d_c$ values for all three quaternary glasses are listed and tabulated in Table 1.

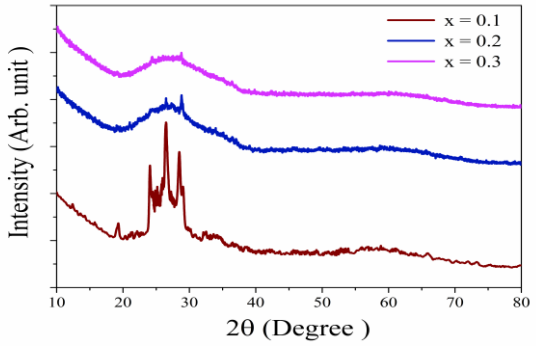


**Fig. 2**. XRD Spectra of all glasses

**Table 1:** Several estimated parameters from XRD spectra

| Composition (x, mol%) | 2θ (Degree) (±0.10) | FWHM | Nanocrystallite Phase | h | k | l | $d_c$ (Average) (±0.06) | Crystalinity (%) (±0.05) |
|---|---|---|---|---|---|---|---|---|
| 0.1 | 19.67 | 0.3234 | $ZnP_4O_{11}$ | 1 | 2 | -1 | 37.45 | 11.04 |
| | 24.11 | 0.1654 | Zn [$MoO_4$] | 0 | 1 | 2 | | |
| | 26.54 | 0.1673 | $Zn_{2.5}MoVO_8$ | 1 | 2 | 2 | | |
| | 28.36 | 0.2621 | $MoV_2O_8$ | 4 | 0 | 1 | | |
| 0.2 | 26.54 | 0.1874 | $Zn_{2.5}MoVO_8$ | 1 | 2 | 2 | 21.08 | 4.54 |
| | 28.36 | 0.2112 | $MoV_2O_8$ | 4 | 0 | 1 | | |
| 0.3 | 28.36 | 0.2321 | $MoV_2O_8$ | 4 | 0 | 1 | 16.76 | 2.43 |

### *3.3. Analysis of UV-Visible Absorption Spectra*

When analyzing structural alterations for optically influenced transitions and figuring out the optical direct or indirect bandgap energy of glassy amorphous systems, the spectra of optical absorption are essential [16]. The indirect transitions that emerge close to the band gap of the glassy structure have been observed and studied in order to accurately estimate the optical bandgap energy ($E_{opt}$) from the plotting of the photon energy (hv) and absorption coefficient (α) [16]. The following equation determines the value of $E_{opt}$ from the UV-Vis electromagnetic waves absorption coefficient [16].

$$\alpha h\vartheta = \left[A\left(h\vartheta - E_{Opt}\right)\right]^m \quad (7)$$

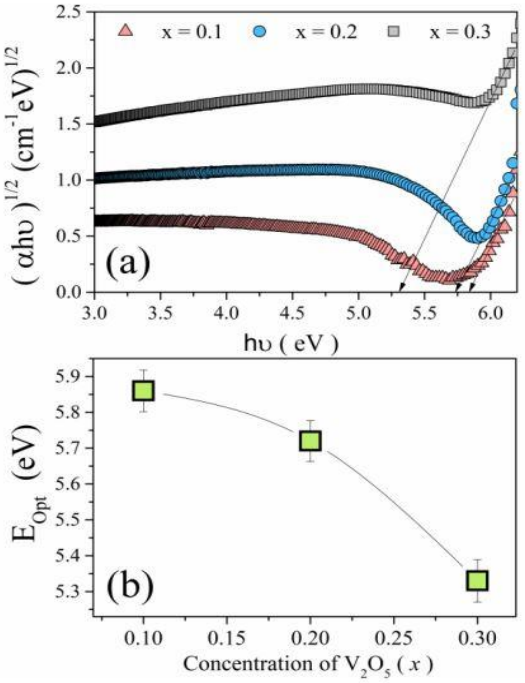


**Fig. 3(a)** Tauc's plot and **(b)** composition-dependent $E_{Opt}$

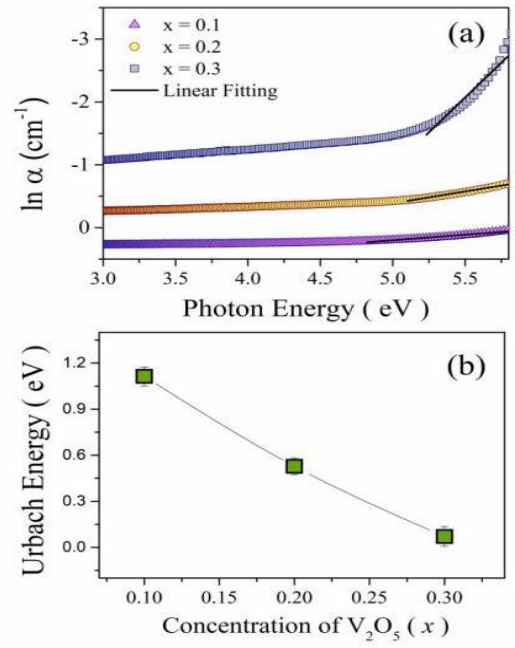


**Fig. 4(a)** ln α versus hυ and **(b)** composition-dependent $E_U$

Here, A stands in for the band tailing parameter's constant value. Depending on how the inter-band electronic movement behaves, the exponent (m) value is selected. Fig. 3(a) displays Tauc's plots of all the systems under study with the selective value of m is equal to 2 (for an indirectly permitted movement).

The values of $E_{opt}$ of all glass nano-composite are revealed in Fig. 3(b). $E_{opt}$ values of the quaternary systems drops with rising $V_2O_5$ content. All glass nanocomposite systems exhibit the same trend in the variation of $E_{opt}$ and average size of nanocrystallite ($d_C$) (Table 2), i.e., the $E_{opt}$ value is directly correlated with the $d_C$ value.

The degree and nature of disorganization inside the glass-matrix are often correlated with Urbach Energy ($E_U$). The term "Urbach energy" ($E_U$) or "band tail energy" refers to the exponentially tailing portion of the non linear curve corresponding to absorption coefficient (ln α) vs hν that is situated near the optical bandgap. The values of the $E_U$ are calculated by subtracting the slope's inverse from the linear fitting technique of the linear component in the lower photon energy section, as shown in Fig. 4 (a). The values of the $E_U$ for each system of amorphous glass are calculated using the succeeding relation of Urbach's empirical rule.

$$\alpha = \alpha_0 \exp\left(\frac{h\upsilon}{E_U}\right) \quad (8)$$

Here, $\alpha_0$ is used to symbolize the constant band tailing parameter. In Fig. 4(b), estimated values of composition-dependent Urbach energy ($E_U$) vs molar percentage of $V_2O_5$ ($x$) are revealed (b). With more $V_2O_5$ ($x$) presence, there are fewer defects, which resulted in narrower localised states, which in turn resulted in a reduced optical band gap. This decrease in Urbach energy indicates that defects are decreasing gradually.

### *3.4. Analysis of DC-Conductivity*

Fig. 5 displays the temperature-dependent DC-conductivity of glass specimens. Fig. 5 shows the nonlinear nature of the $\sigma_{dc}$ and how it increases with $V_2O_5$ content. Because the $\sigma_{dc}$ is nonlinear, it is feasible that polarons or carriers with numerous equivalent activation energies are involved in the conduction mechanism [4]. The electron in the small polaron hopping process moves from one localized place to another [4].

The nonlinear curve can be separated into two discrete linear areas. With the assistance of the least square linear fit data, we estimated the activation energies of DC conductivity at low as well as high temperature areas, and Table 2 contains the results. The activation energy ($E_{dc}$) values for low and high-temperature DC conductivity are

found to decline as DC conductivity increases, which is strongly in accordance with the tiny polaron hopping theory [17].

The conduction's activation energy, and subsequently the DC conductivity, are influenced by the mean separation ($R_V$) between $V^{4+}$ and $V^{5+}$ ions during the hopping process. The conduction's activation energy, and the mean spacing ($R_V$) are highly correlated. The mean separation between $V^{4+}$ and $V^{5+}$ ions ($R_V$) can be determined from the association using $N_{V\text{-ions}}$ (V-ion concentration) from Eq. (9).

$$N_{V-ions} = \frac{mol\,\%\,of\,oxide \times N_A \times \rho}{Molecular\,weight\,of\,Composition\,(M)} \quad (9)$$

and,

$$R_V = \left(\frac{1}{N_{v-ion}}\right)^{\frac{1}{3}} \quad (10)$$

From Table 2, it can be shown that as $N_{V\text{-ions}}$ rise, $R_V$ falls. As a result, more NBOs develop in the matrix of amorphous glassy system, $\sigma_{dc}$ increases.The polaron radius ($R_P$), which has been determined using the $R_V$ values, has been calculated using the relation shown below and is shown in Table 2.

$$R_P = \left(\frac{\pi}{6}\right)^{1/3}\left(\frac{R_V}{2}\right) \quad (11)$$

Table 2 shows that the radii of polarons decrease with increasing DC conductivity.

**Table 2:** Several estimated parameters associated with DC conduction mechanism

| x (%) | $E_{Low}$ (eV) | $E_{High}$ (eV) | $R_P$ (Å) | $N(E_{FM})$ x $10^{27}$ ($eV^{-1}/cm^3$) | $N(E_{FG})$ x $10^{26}$ ($eV^{-1}/cm^3$) |
|---|---|---|---|---|---|
| 0.1 | 1.01 | 2.06 | 7.2 | 1.96 | 2.23 |
| 0.2 | 1.32 | 2.63 | 6.1 | 9.75 | 5.59 |
| 0.3 | 1.56 | 3.18 | 5.5 | 14.4 | 7.89 |

In the lower-temperature zone, a tiny polaron or charge carrier may hop from one localized site and another within the optical bandgap or mobility gap, in accordance with Mott's Variable Range Hopping (VRH) hypothesis. When the localized sites are accessible at the Fermi energy level and the density of states (DOS) is finite, Mott VRH takes place. The following equation represents the VRH conductivity mathematical formula [17].

$$\sigma_{dc} = A\,exp\left[-\left(\frac{T_0}{T}\right)^{0.25}\right] \quad (12)$$

The value of constant parameter $T_0$ is determined by the subsequent equation [17]

$$T_0 = \frac{16\alpha^3}{K_B N(E_{FM})} \quad (13)$$

Here, the DOS which is at the Fermi energy level inferred from Mott's VRH model is symbolized by $N(E_{FM})$, the localization distance of wave function of polaron is symbolized by $\alpha^{-1}$ and $T_0$ stands for the typical temperature. In Fig. 6 (a), DC-conductivity is displayed in proportion to $T^{-0.25}$ after the research outcomes are put into Eq. (12). The $N(E_{FM})$ values have been determined using Eq. (12) and the evaluated values are shown in Table 2 under the assumption that $\alpha^{-1}$ = 10 Å for localized sites and utilizing the slope of linear fit spectra (Fig. 6(a) solid red lines) have been taken into consideration. Table 2 demonstrates that $N(E_{FM})$ rises with composition. These findings demonstrate that the most important part of the conduction process is the rising concentration of $V_2O_5$ (x).

At temperatures above half the Debye temperature ($\theta_D/2$), the temperature dependency of the $\sigma_{dc}$ data can't be justified by Mott's model. However, Greaves developed a dominating VRH model for this region temperature above ($\theta_D/2$) that is temperature-dependent. For the DC conductivity, Greaves proposed the following expression [17]:

$$\sigma_{dc}T^{0\cdot5} = A'\,exp\left[-\left(\frac{T_0'}{T}\right)^{0.25}\right] \quad (14)$$

The value of constant parameter $T_0'$ is determined by the subsequent equation [17]

$$T_0' = \frac{19.4\alpha^3}{K_B N(E_{FG})} \quad (15)$$

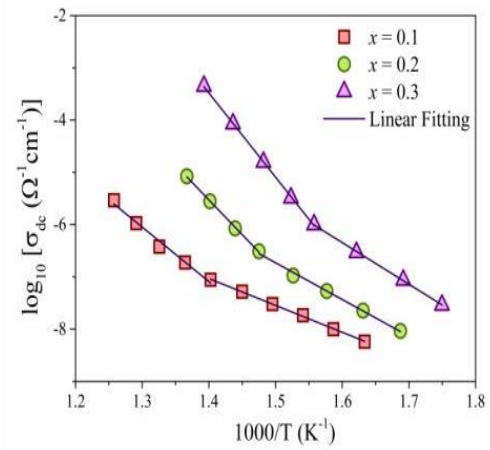


Fig. 5. DC conductivity with reciprocal temperature

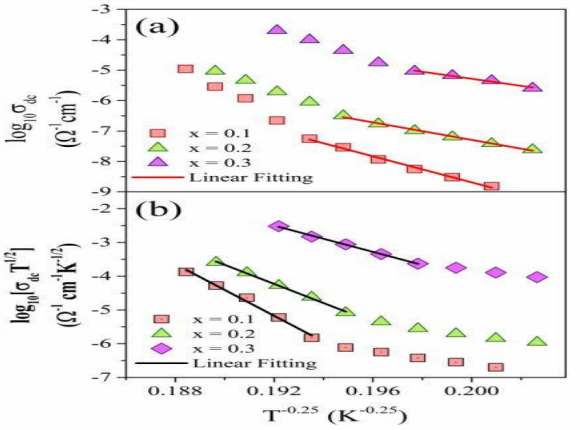


**Fig. 6(a)** Mott's VRH and **(b)** Greaves VRH model representation.

where $N(E_{FG})$ is the DOS at the Fermi level according to VRH model of Greaves. Fig. 6(b) shows a plot of log $(\sigma T^{1/2})$ against $T^{-0.25}$. Greaves' model is sufficient enough for meeting to the experimental results, as seen in Fig. 6(b). The values of $N(E_{FG})$ have been determined for the higher temperature zone using $\alpha^{-1} = 10$ Å for localized sites, the slopes of the linear best fit data in Fig. 6(b), and Eq. (14), and they are shown in Table 2. Additionally, $N(E_{FG})$ rises with composition ($x$), which is accordant with $\sigma_{dc}$ once more.

## 4. SUMMARY AND CONCLUSIONS

Utilizing the melt of quenching process, three quaternary samples of glass nanocomposite with the chemical formulation $0.15P_2O_5$-0.35ZnO-0.50(1-x) $MoO_3$-x$V_2O_5$ with x values as 0.1, 0.2, and 0.3 have been developed. The formation of different-sized nanocrystallites that are superposed upon an amorphous glassy matrix is confirmed by XRD patterns. Due to structural changes, the assessed value of $E_{opt}$ and $E_U$ both decrease with increasing $V_2O_5$ content. The Urbach energy is declining, which means that more defect or localized sites have evolved inside the gap of mobility to support the mechanism of tiny polaron hopping. $\sigma_{dc}$ shows non-linearity in its nature, that indicates semiconductor properties for all samples of glass nanocomposites. Additionally, the accumulation of $V_2O_5$ into the glass network alters the bond formation of the glass structure by enhancing the density of defect or localized sites. With more $V_2O_5$ present, the DOS at the Fermi level rises, improving conductivity, according to the investigation of $\sigma_{dc}$ with Mott's and Greaves' model.

## 5. REFERENCES

[1] A. Bajaj, A. Khanna, B. Chen, J.G. Longstaffe, U.W. Zwanziger, J.W. Zwanziger, Y. Gómez, F. González, 'Structural investigation of bismuth borate glasses and crystalline phases', J. Non-Cryst. Solids, vol. 355, pp. 45–53, 2009.

[2] S. Bale, S. Rahman, 'Optical absorption and EPR studies on (70−x) $Bi_2O_3$–x$Li_2O$–30(ZnO–$B_2O_3$) (0 ⩽ x ⩽ 20) glasses', J. Non-Cryst. Solids, vol. 355, pp. 2127–2133, 2009.

[3] J. Meyer, S. Hamwi, M. Kröger, W. Kowalsky, T. Riedl, A. Kahn, 'Transition metal oxides for organic electronics: energetics, device physics and applications', Adv. Mater., vol. 24 (40), pp. 5408–5427, 2012.

[4] A.S. Das, D. Biswas, M. Roy, D. Roy, S. Bhattacharya, 'Effect of V2O5 concentration on the structural and optical properties and DC electrical conductivity of ternary semiconducting glassy nanocomposites', J. Phys. Chem. Solids, vol. 124, pp. 44–53, 2019.

[5] L. Bih, M. Elomari, J.M. Reau, M. Hadded, D. Boudlich, A.M. Yocaubi, A. Nadiri, 'Electronic and ionic conductivity of glasses inside the $Li_2O$–$MoO_3$–$P_2O_5$ system', Solid State Ion., vol. 132, pp. 71–85, 2000.

[6] G. Poirier, F.S. Ottoboni, F.C. Cassanjes, A. Remonte, Y. Messaddeq, S.J.L. Ribeiro, 'Redox behavior of molybdenum and tungsten in phosphate glasses', J. Phys. Chem. B, vol. 112, pp. 4481–4487, 2008.

[7] Allan B. Rosenthal, Stephen H. Garofalini, 'Structural role of zinc oxide in silica and soda-silica glasses', J. Am. Ceram. Soc., vol. 70 (11), pp. 821–826, 1987.

[8] S. Annamalai, R.P. Bhatta, I.L. Pegg, B. Dutta, 'Mixed transition-ion effect in the glass system: $Fe_2O_3$-MnO-$TeO_2$ ', J. Non-Cryst. Solids, vol. 358, pp. 1380–1386, 2012.

[9] I. Kashif, S.A. Rahman, A.A. Soliman, E.M. Ibrahim, E.K. Abdel-Khalek, A. G. Mostafa, A.M. Sanada, 'Effect of alkali content on AC conductivity of borate glasses containing two transition metals', Physica B, vol. 404, pp. 3842–3849, 2009.

[10] M.G. El-Shaarawy, 'Physical studies on ternary vanadium–phosphate glasses', J. Phys. Soc. Jpn., vol. 71 (4), pp. 1118–1125, 2002.

[11] A. S. Hassanien, I. Sharma, A.A. Akl, 'Physical and optical properties of a-Ge-Sb-Se-Te bulk and film samples: Refractive index and its association with electronic polarizability of thermally evaporated a-$Ge_{15-x}Sb_xSe_{50}Te_{35}$ thin-films", J. Non-Cryst. Solids, vol. 531, pp. 119853, 2020.

[12] I. Kashif, S.A. Rahman, A.A. Soliman, E.M. Ibrahim, E.K. Abdel-Khalek, A. G. Mostafa, A.M. Sanad, 'Effect of alkali content on AC conductivity of borate glasses containing two transition metals', Physica B, vol. 404, pp. 3842–3849, 2009.

[13] C.B. Doelle, D. Stachel, I. Svoboda, H. Fuess, 'Crystal structure of zinc ultra-phosphate, $ZnP_4O_{11}$ ', Z. Kristallogr. Vol. 203, pp. 282–283, 1993.

[14] J. Meullemeestre, E. Penigault, 'Les molybdates neutres de zinc', Bull. Soc. Chim. Fr., vol. 10, pp. 3669–3674, 1972.

[15] P. Pailleret, J. Borensztajn, W. Freundlich, A. Rimsky, Structure crystalline de la phase $MoV_2O_8$, C.R. Seances Acad. Sci. Ser. C., vol. 263, pp. 1131–1133, 1966.

[16] D. Biswas, A.S. Das, R. Mondal, A. Banerjee, D. Deb, A. Dutta, S Bhattacharya, S Kabi, L S Singh, "Study of microstructure and electrical conduction mechanisms of quaternary semiconducting glassy systems: Effect of mixed modifiers", J. Non-Cryst. Solids, vol. 542, pp. 120104, 2020.

[17] D. Biswas, R.K.N. Ningthemcha, A.S Das, L.S. Singh, 'Structural characterization and electrical conductivity analysis of $MoO_3$–$SeO_2$–ZnO semiconducting glass nanocomposites', J. Non-Cryst. Solids, vol. 515, pp. 21–33, 2019.

## Biographies

| | |
|---|---|
|  | **Souvik Brahma Hota** received the bachelor's degree in Aeronautical Engineering from Anna University in 2016, the master's degree in Mechanical Engineering from Techno India University in 2018, and the perusing philosophy of doctorate degree in Mechanical Engineering from Jadavpur University, respectively. He is currently working as a Faculty in the Department of Mechanical Engineering, Techno India University, West Bengal, India. His research areas include glass ceramics composites, electroless coating, surface technology, nano coating, micro alloying, material characterizations etc. |
|  | **Ashes Rakshit** passed his B tech from Swami Vivekananda Institute Of Science and Technology. He passed his M.tech from Kalyani Government Engineering College. Currently he is working as an Assistant Professor in Department of Mechanical Engineering Regent Education and Research Foundation, Barrakpore, West Bengal, India. His research interest is composite materials. |
|  | **Dr. Debasish Roy** received the bachelor's degree in Mechanical Engineering from University of North Bengal in 1986, the master's degree in Mechanical Engineering from Jadavpur University in 1989, and he persued philosophy of doctorate degree in Mechanical Engineering from Jadavpur University in 2004, respectively. He is currently working as a Professor in the Department of Mechanical Engineering, Jadavpur University, West Bengal, India. His research areas include fluid mechanics, hydro power, composite materials, glass ceramics etc. |
|  | **Debtanu Patra** passed his B tech from Haldia Institute of Technology. He passed his M.tech from NITTTR , Kolkata. Currently he is working as an Assistant Professor in Department of Mechanical Engineering Regent Education and Research Foundation, Barrakpore, West Bengal, India. His research interests are Friction Stir Welding, composite materials etc. |
|  | **Dr. Dipankar Biswas** is currently working as an Associate Professor in Department of Electronics & Communication Engineering, Regent Education and Research Foundation Barrackpore, West Bengal, India. Having completed his B.E. Degree from University of Burdwan, he started his journey of teaching and research since. Afterwards he completed his M.Tech. from WBUT. And while continuing his teaching and research obsession, he persuaded and got his PhD degree from National Institute of Technology Manipur**.** Now has more than 16 years of experience teaching in various engineering colleges. Alongside teaching, he has also been indulged in many high-quality researches producing more than 30 high original research articles in various international journals of high repute. His research areas include composite materials, chalcogenide glass, glass ceramics, glucose sensor etc. |

# Alteration of Parameters Influencing Charge Infusion of Organic Device with Multi Walled Carbon Nanotubes (MWCNTs)

Sudipta Sen*, N. B. Manik
*Department of Physics Jadavpur University, Kolkata-700032, India*
*Corresponding Author Email: sagnike000@gmail.com

**Keywords:** Interfacial Barrier, MWCNT, Turn - on Voltage, Trap Concentration

## ABSTRACT

In this work, we will analyze one of MWCNTs' most important applications in the area of organic electronics. When an organic dye is sandwiched between two metallic electrodes, one of the main challenges for organic dye-based devices is the inadequate flow of active charge carriers at the metal-organic junction. High trap energy and high interfacial barrier are responsible for poor movement of active charge carriers. Improvement of charge carrier flow will increase conductivity, lower the turn-on voltage, and enable the devices to be used in various industrial uses if the traps and barrier at the metal-organic junction can be reduced. In this case, we have added MWCNTs to this organic dye-based device and investigated how they affect the interfacial characteristics. Present work will be revealing for further research into the impact of carbon nanotubes on charge infusion in organic devices.

## 1. INTRODUCTION

Due to their high aspect ratios, exceptional thermal and electrical properties, and large exterior area, carbon-based nanomaterials (CBNs) like single-walled carbon nanotubes (SWCNTs), multi-walled carbon nanotubes (MWCNTs), fullerenes, graphenes, and carbon-based quantum dots (CQDs) find substantial applications in numerous research fields [1-2]. Out of the varieties of CBNs, we have selected MWCNT for this study. Numerous SWCNTs are embedded inside to create MWCNTs, a unique type of carbon nanotube. MWCNTs have great electrochemical properties as well as outstanding thermal conductivity [3]. Current work studies an application of MWCNT in organic dye-based devices. Organic dye-based devices have many appealing characteristics including versatility, affordability, light weight, and large area fabrication [4]. But these important features of these devices become predominated by some insuperable hindrances at metal – organic junction when dyes are intercalated between two metallic electrodes. Device performance is greatly impacted by the metal-organic junction's poor flow of active charge carriers. Organic devices are highly susceptible to traps because of their amorphous structure [5]. As these two factors are analytically proportional to one another, higher trap concentration also results in higher junction barrier [6]. Both of these parameters can be decreased to enhance active carrier flow at the metal-organic interface, which will increase conductivity and result in a lower turn-on voltage. This is why we have included MWCNT in the organic device to investigate its impact on trap concentration and the interface barrier. Regarding formation of organic device, our organic substance of choice is the Phenosafranin (PSF) dye, which is intercalated in between Indium Tin Oxide (ITO) coated glass slide and aluminum. High trap concentration and interfacial barrier at ITO/PSF dye interface have been taken into account only. In both lack and presence of MWCNT, the prepared organic device containing PSF dye has its current-voltage (I-V) characteristics examined. The device's current flow has been examined using the Richardson-Schottky (R-S) thermionic emission method [7]. Additionally, the Norde technique has been used to verify the consistency of interfacial barrier value derived from the prepared device's I-V characteristics.

## 2. MATERIALS AND SAMPLE PREPARATION

Fig. 1(a) depicts PSF dye's structural composition. This colour is a cationic phenazinium group dye that can act as an energy sensitizer and is utilized in numerous biological photochemical processes [8]. PSF pigment has the empirical formula $C_{18}H_{15}ClN_4$. PSF dye and MWCNT were purchased from Sigma Aldrich in St. Louis, Missouri, and Sisco Research Laboratories in India, respectively. Fig. 1(b) depicts MWCNT's structure.

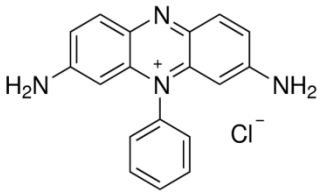


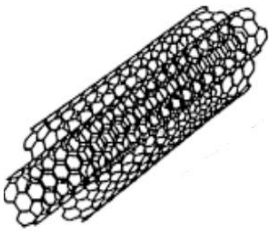

**(a)** **(b)**

**Fig. 1** Structure of **(a)** PSF dye and **(b)** MWCNT

Poly Methyl Methacrylate (PMMA) has been used as an inert binder in this study. The method for creating PMMA solution has already been described in one of our previous works [9]. The PMMA solution contains 2 mg PSF dye and is stirred for an additional 30 minutes. The next step involves splitting the solution equally into two test containers that have already been cleaned. PSF solution without MWCNT is present in one test container. To make the PSF with MWCNT solution, MWCNT is added individually to the other test tube. On an ITO-coated glass that has already been cleansed, the created PSF dye solution is spin-coated and then dried. Similar solution is also spin-coated on Al electrode. PSF dye-based device without MWCNT is formed by intercalating ITO and Al electrodes. A similar procedure is used to make the MWCNT-based PSF dye-based device. After that, these devices are dried for 24 hours in vacuum desiccators before being characterized. Fig. 2 displays a schematic of the constructed device.

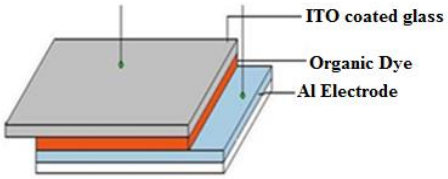


**Fig. 2** Schematic of the Organic Device

## 3. MEASUREMENTS

Keithley's 2400 source measure unit is used to determine I-V relationship. Same methodology is used as described in an earlier published work of us [10]. Operating voltage is from 0 V to 5 V with 1000 ms delay and with increments of 0.25 V. The experimental area is maintained at $27^0$C.

## 4. RESULTS AND DISCUSSIONS

The R-S model has been used to estimate the current flow, as mentioned in equation (1)

$$I = AA^*T^2 \exp\left(-\frac{q\phi_b}{kT}\right)\left(\exp\left(\frac{qV}{nkT}\right)\left[1 - \exp\left(\frac{-qV}{kT}\right)\right]\right) \quad (1)$$

$$I_0 = AA^*T^2 \exp\left(-\frac{q\phi_b}{kT}\right) \quad (2)$$

Equation (3) can be used to calculate the junction barrier.

$$\phi_b = \frac{kT}{q}\ln\left(\frac{AA^*T^2}{I_0}\right) \quad (3)$$

All of the symbols have their standard meanings in this context [11–12]. Fig. 3 displays the I-V properties of the device with and without MWCNT. Fig. 3 shows that presence of MWCNT causing the current flow to almost triple.

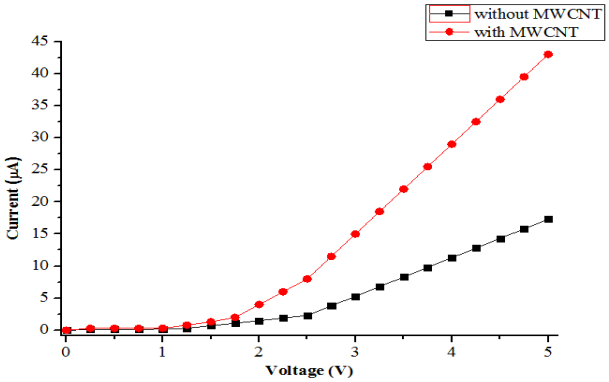


**Fig. 3** I-V plot of PSF dye without and with MWCNT

Semi-logarithmic I-V features have now been plotted in Fig. 4 with and without MWCNT to determine the interfacial barrier at contact.

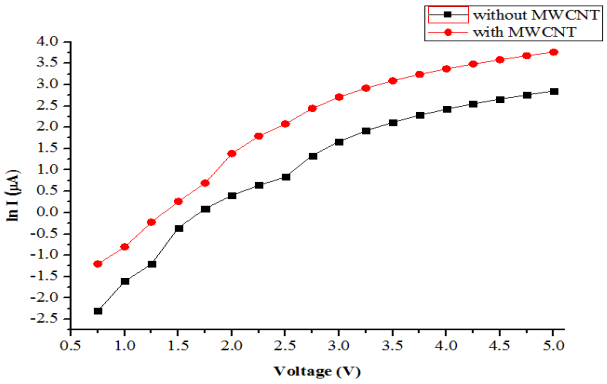


**Fig. 4** ln I-V plot of PSF dye without and with MWCNT

Equation (4) can be used to describe trap energy ($E_t$).

$$E_t = mkT \tag{4}$$

Where, all of the symbols have their standard meanings in this context [13] and m is derived from ln I – ln V plot of the device with and without MWCNT, which is depicted in Fig. 5.

By comparing equations (3) and (4), it can be concluded that, when other factors are taken into account, $\phi_b \propto E_t$ when $E_t$ remains unchanged. Therefore, barrier at metal-organic contact also diminishes as the charge trapping effect does. Analytically saying, both factors are proportional to one another and are thus correlative.

The Norde formula which has been expressed in equation (5) has been used to estimate the barrier [14-15].

$$\phi_b = F(V_{min}) + \frac{V_0}{\gamma} - \frac{1}{\beta} \tag{5}$$

Where, the notations have their standard meaning.

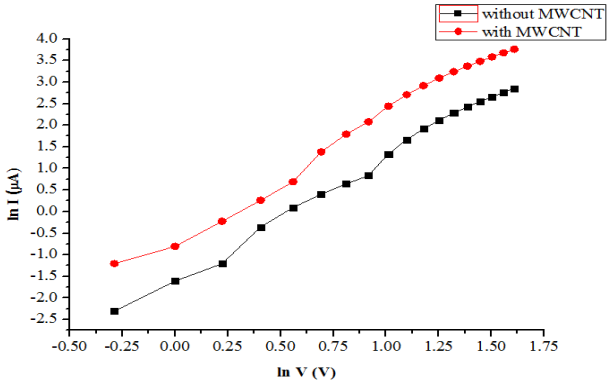


**Fig. 5** ln I- ln V plot of PSF dye without and with MWCNT

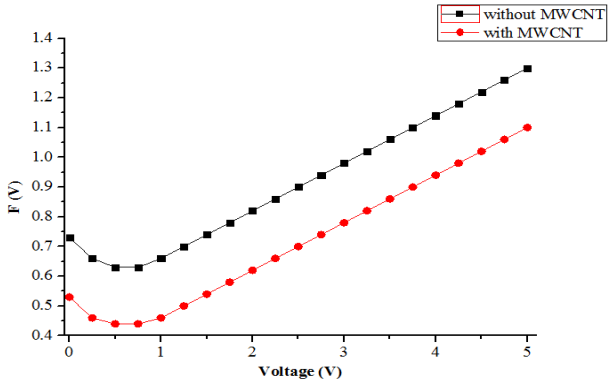


**Fig. 6** Norde function plot of PSF dye without and with MWCNT

Table 1 displays the turn-on voltage, trap energy, and interface barrier values in absence and in presence of MWCNT. According to Table 1, the trap energy and interfacial barrier that influence charge infusion at the junction have been substantially reduced by MWCNT. This has improved charge infusion at the contact and improved the device's conductivity. When MWCNT is used in an organic device, the aspect ratio greatly changes the electrical properties. The improved flow of charge carriers is made possible by MWCNT's higher aspect ratio, which also lowers the percolation threshold of electrical conductivity.

**Table 1: Estimation of Turn - on voltage, Trap energy, Interfacial barrier of organic devices without and with MWCNT**

| PSF Dye Based Device | Turn - on Voltage (V) | Value of "m" | Trap Energy (eV) | Interfacial Barrier (eV) using I-V characteristics | Interfacial Barrier (eV) Using Norde Function |
|---|---|---|---|---|---|
| without MWCNT | 2.50 | 2.05 | 0.053 | 0.81 | 0.76 |
| with MWCNT | 1.50 | 1.85 | 0.048 | 0.75 | 0.69 |

## 5. CONCLUSIONS

According to the current research, certain MWCNT characteristics enable the reduction of traps and interfacial barriers that influence the current circulation at the junction area. By filling in traps, MWCNT essentially increases the number of conductive paths in the organic device. The higher aspect ratio of MWCNT plays a critical part in lowering traps and contact barriers, resulting in better conductivity, as the percolation threshold of electrical conductivity decreases with higher aspect ratio. As the turn-on voltage decreases with MWCNT, the device will turn on at lower voltages; this is also due to the organic device's increased flux of mobile charge carriers. Both the I-V and Norde methods have been used to measure the contact barrier with and without

MWCNT. Both approaches remain congruous with one another, showing a significant lowering of the contact barrier in the presence of MWCNT. This study will be helpful because it demonstrates one of the device physics applications of MWCNT in organic electronics.

## REFERENCES


1. K. D. Patel, R. K. Singh and H.W. Kim, "Carbon based-nanomaterials as an emerging platform for theranostics", Materials Horizons, 2019, **6**, 434-469

2. C. Cha, S. R. Shin, N. Annabi, M. R. Dokmeci and A. Khademhosseini, "Carbon-based nanomaterials: multifunctional materials for biomedical engineering", ACS Nano, 2013, **7**, 2891–2897

3. D. K. Patel, H. B. Kim, S. D. Dutta, K. Ganguly and K.T. Lim, "Carbon Nanotubes-Based Nanomaterials and Their Agricultural and Biotechnological Applications", Materials, 2020, **13**, 1-28

4. Q. Zhang, W. Hu, H. Sirringhaus and K. Müllen, "Recent Progress in Emerging Organic Semiconductors", Advanced Materials, 2022, **34**, 1-4

5. H. F. Haneef, A. M. Zeidell and O. D. Jurchescu, "Charge carrier traps in organic semiconductors: a review on the underlying physics and impact on electronic devices", Journal of Materials Chemistry C, 2020, **8**, 759-787

6. S. Sen and N. B. Manik, "Correlation between barrier potential and charge trapping under the influence of Titanium Di oxide nanomaterials in organic devices", Results in Materials, 2020, **8**, 1-6

7. A. Kumatani, Y. Li, P. Darmawan, T. Minari and K. Tsukagoshi, "On Practical Charge Injection at the Metal/Organic Semiconductor Interface", Scientific Reports, 2013, **3**, 1-6

8. S. Sen and N. B. Manik, "Effect of Zinc Oxide (ZnO) Nanoparticles on Interfacial Barrier Height and Band Bending of Phenosafranin (PSF) Dye-Based Organic Device", Journal of Electronic Materials, 2020, **49**, 4647-4652

9. S. Sen and N. B. Manik, "Study on the Effect of 8 nm Size Multi Walled Carbon Nanotubes (MWCNT) on the Barrier Height of Malachite Green (MG) Dye Based Organic Device", International Journal of Advanced Science and Engineering, 2020, **6**, 23-27

10. S. Sen and N. B. Manik, "Effect of back electrode on trap energy and interfacial barrier height of crystal violet dye-based organic device", Bulletin of Materials Science, 2020, **43**, 1-4

11. H. M. J. Al-Ta'ii, Y. M. Amin and V. Periasamy, Calculation of the Electronic Parameters of an Al/DNA/p-Si Schottky Barrier Diode Influenced by Alpha Radiation", Sensors, 2015, **15**, 4810-4822

12. Z. Harrabi, S. Jomni, L. Beji and A. Bouazizi, "Distribution of barrier heights in Au/porous GaAs Schottky diodes from current–voltage–temperature measurements", Physica B, 2010, **405**, 3745-3750

13. S. Chakraborty and N. B. Manik, "Improvement of electrical and photovoltaic properties of methyl red dye based photoelectrochemical cells in presence of single walled carbon nanotubes", Frontiers of Optoelectronics, 2015, **8**, 289-297

14. H. Norde, "A modified forward I-V plot for Schottky diodes with high series resistance", Journal of Applied Physics, 1979, **50**, 5052-5053.

15. A. Kocyigit, M. Yılmaz, Ş. Aydogan and Ü. Incekara, "The effect of measurements and layer coating homogeneity of AB on the Al/AB/p-Si devices", Journal of Alloys and Compounds, 2019, **790**, 388-396

**Biographies**

**Sudipta Sen** is a UGC Senior Research Fellow (UGC-SRF) and currently pursuing Ph.D in the Department of Physics, Jadavpur University, Kolkata, India. He completed his M. Tech in Optics and Optoelectronics from University of Calcutta, in 2016 and he had secured First class first position in the M. Tech examination. He completed his B. Tech in Electronics and Communication from Calcutta Institute of Engineering and Management, Kolkata, West Bengal in 2013. He has qualified Graduate Aptitude Test in Engineering (GATE) in Electronics and Communication Engineering (EC) and in Physics (PH) and he has also qualified UGC –NET (JRF and LS) in Electronic Science. His research areas include the electrical characterization of different organic electronic devices, materials science, nanotechnology, optoelectronic devices, organic solar cells etc. He has published several research articles in numerous reputed International journals such as Springer – Nature, Elsevier, AIP publishing house etc. He has also attended several National and International conferences, seminars, workshops.

**Nabin Baran Manik** is a professor in Department of Physics, Jadavpur University, Kolkata, India. He received his Ph.D. degree from Jadavpur University, Kolkata, India, in 1998 and right after that he joined as lecturer in Physics Department of the same university. In 2004, he was awarded Better Opportunities for Young Scientists in Chosen Areas of Science and Technology (BOYSCAST) Fellowship of Department of Science and Technology (DST), Govt. of India and did his Post Doctoral work at Leibniz-Institut für Festkörper- und Werkstoffforschung (IFW), Dresden, Germany. He is working in the area of development of photovoltaic devices using semiconducting conjugated polymers and organic dyes, low temperature instrumentation, characterization of optoelectronics devices at low temperature. Several students have completed their Ph.D. under his supervision. Different research projects from different funding agencies were undertaken by him. He had also delivered invited talk in different national and international conferences. He has different publications both at national and international journals.

# Stabilization and Control of Quadcoptor

**Kalyani Mamidi*, Jayati Dey****

*Master of Technology (M.Tech.) Student, **Faculty, Senior Member IEEE
National Institute of Technology Durgapur, Department of Electrical Engineering, Durgapur 713209
Contact Email: **jayati.dey@ee.nitdgp.ac.in

## Abstract.

The present work considers a sliding mode (SM) control strategy for control of quad-coptor and stabilization. First, a proportional derivative (PD) sliding surface is considered in order to achieve control of aircrafts. Variation in reference angles are allowed, and external disturbances are applied as well. The sliding mode control (SMC) with PD sliding surface achieves the reference tracking instantaneously. However, this control scheme cannot achieve tracking in presence of disturbances. Furthermore, an integral sliding surface is augmented with the proportional derivative one for disturbance rejection. Integral sliding surface is designed and implemented in simulation for quadrotor. The results are showcased which demonstrates that the PID SMC is successfully performing tracking even in presence of disturbances.

**Key words:** PID sliding surface, PD sliding surface, Sliding Mode control, Disturbance rejection, Quadcopter.

## 1. INTRODUCTION

In recent era, vehicle modernization is rapidly receiving interest of the researchers. Both unmanned ground and aerial vehicles are of great concern to scientists and engineers because of their field of application specifically in military surveillances, risk and rescue operations [1]-[6]. Unmanned aerial vehicles reach the places whwre UGV fails such hill top, flood affected areas, dense forest etc. Nowadays Quadcoptors are also replacing manned and fixed wing UAVs. Therefore stabilization and control of such systems plays a major role for fruitful operation of quadcoptor in specific object oriented applications. Literature review reveals that many works have already been reported in this domain. Proportional (P), Integral (I), Derivative (D) controllers, LQR control, Fuzzy based control, Sliding Mode (SMC) control are few approaches those have been applied for quadcoptors [7-11]. Out of these, SMC demonstrates a promising robust control approach which can achieve control even in presence of uncertainties. Keeping this in view, the objective of this work is set as development of a proportional derivative (PD) sliding surface for control and stabilization of UAVs. Variation in reference attitude angles are allowed, and some disturbances are applied as well. The SMC with PD sliding surface achieves satisfactorily the reference tracking. However, this control scheme fails to achieve disturbance rejection Hence, an integral sliding surface is introduced for disturbance rejection.

Arrangement of the present work is given next. Section II is on the presentation of the mathematical modeling of the quadrotor. Section III describes concepts of SMC with PD and PID sliding surfaces. Section IV showcases the simulation results. Section V includes Conclusions.

## 2. MATHEMATICAL MODEL OF QUADCOPTER

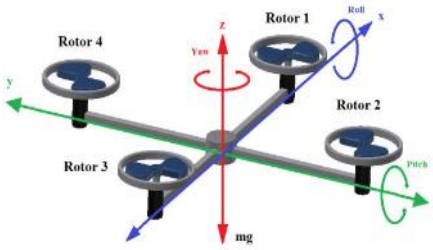


Fig. 1. Configuration of A Quadcoptor

The linear and angular positions and velocities are considered as the states of a quadrotor which altogether twelve in number where, $x, y$ and $z$ denote the linear positions along the $x, y$, and $z$ directions. $\dot{x}$,$\dot{y}$ and $\dot{z}$ denote linear velocities in the x, y, and z directions. $\phi$, $\theta$, and $\psi$ denote, respectively, the roll, pitch and yaw angles, and $\dot{\phi}, \dot{\theta}$ and $\dot{\psi}$denote the corresponding velocities. The configuration of the quadcopter under consideration is depicted in Fig. 1.

Dynamics characteristics of the quad-coptor is modeled by eqns. (1)-(6). $d_h(t), d_\phi(t), d_\theta(t), d_\psi(t)$ are the disturbances acting on quadrotor.

$$\ddot{x} = \frac{(\sin\psi \sin\phi + \cos\psi \sin\theta \cos\phi)U1 - A_x\dot{x}}{m} \quad (1)$$

$$\ddot{y} = \frac{(\sin\psi \sin\phi - \cos\psi \sin\theta \cos\phi)U1 - A_y\dot{y}}{m} \quad (2)$$

$$\ddot{z} = \frac{-mg + (\cos\phi \cos\theta)U1 - A_z\dot{z}}{m} + d_h(t) \quad (3)$$

$$\ddot{\phi} = \frac{\dot{\theta}\dot{\psi}(I_{yy} - I_{zz}) - J_r\dot{\theta}\Omega_r + l(U2)}{I_{xx}} + d_\phi(t) \quad (4)$$

$$\ddot{\theta} = \frac{\dot{\phi}\dot{\psi}(I_{zz} - I_{xx}) + J_r\dot{\phi}\Omega_r + l(U3)}{I_{yy}} + d_\theta(t) \quad (5)$$

$$\ddot{\psi} = \frac{\dot{\theta}\dot{\phi}(I_{xx} - I_{yy}) + (U4)}{I_{zz}} + d_\psi(t) \quad (6)$$

**Table 1.Quadcopter dynamic system parameters**

| System parameters | Description |
|---|---|
| $I_{xx}, I_{yy}, I_{zz}(kgm^2)$ | Moments of inertia |
| m (kg) | Mass of the vehicle |
| l (m) | Arm length of Quad-copter frame |
| b ($Ns^2$) | Coefficient of Thrust |
| $J_r(kgm^2)$ | Moment of inertia of the rotor |

Where$U_i$ , i = 1, 2, 3, 4 are the control forces for the quad-copter, which are as:

$$U_1 = b\left(\Omega_1{}^2 + \Omega_2{}^2 + \Omega_3{}^2 + \Omega_4{}^2\right) \quad (7)$$

$$U_2 = bl\left(-\Omega_2{}^2 + \Omega_4{}^2\right) \quad (8)$$

$$U_3 = bl\left(-\Omega_1{}^2 + \Omega_3{}^2\right) \quad (9)$$

$$U_4 = d\left(-{\Omega_1}^2 + {\Omega_2}^2 - {\Omega_3}^2 + {\Omega_4}^2\right) \quad (10)$$

$$\Omega_r = (-\Omega_1 + \Omega_2 - \Omega_3 + \Omega_4) \quad (11)$$

$\Omega_r$denotes the resultant angular speed of the motors and gravitational acceleration $g = 9.81m/s^2$.

## 3. SLIDING MODE CONTROL

Sliding Mode Control [3] involves sliding surface and equivalent control which is designed to enforce the error vector toward the sliding surface [6]. Based on the governing equations (1)-(6), there are four control equations described by (15)-(18) which are designed so as to maintain the reference set point even in presence of external disturbances. The signal $U_1$ is developed and designed for guaranteed reference tracking of altitude and the others control inputs $U_2$, $U_3$ and $U_4$ are designed for controlling the attitude angles.

**A) PD SMC:**

First, the sliding surface is taken as as follows:

$$s = \dot{e} + \lambda e \quad (12)$$

Where $e = z_d - z$ is the error between the reference and actual for the altitude. $\lambda > 0$ is a design parameter. The control force U(t), involves an equivalent part, $u_{eq}(t)$, which is continuous and a discontinuous part $u_D(t)$. That is:

$$U(t) = u_{eq}(t) + u_D(t) \quad (13)$$

Nonlinear $u_D(t)$ behaves as a switching component. Gain $k_D$ is a design parameter which helps to reach the phase. The well-known problem of Chattering can be significantly attenuated for the control law which is represented as:

$$u_D(t) = k_D \frac{s(t)}{|s(t)|+\delta} \quad (14)$$

The parameter $\delta$ is to be tuned so as to achieve chattering reduction. The complete controller equations are [15] as follows.

$$U_1 = \left(g + \lambda(\dot{z}_d - \dot{z}) + \ddot{z}_d + \frac{k_D s}{|s|+\delta}\right)\frac{m}{\cos\theta\cos\phi} \quad (15)$$

$$U_2 = \left[\lambda\left(\dot{\phi}_d - \dot{\phi}\right) + \ddot{\phi}_d - \dot{\theta}\dot{\psi}\left(\frac{I_y - I_z}{I_x}\right) + \frac{J_r\dot{\theta}\Omega_r}{I_x} + \frac{K_D s}{|s|+\delta}\right]\frac{I_x}{l} \quad (16)$$

$$U_3 = \left[\lambda\left(\dot{\theta}_d - \dot{\theta}\right) + \ddot{\theta}_d - \dot{\phi}\dot{\psi}\left(\frac{I_z - I_x}{I_y}\right) - \frac{J_r\dot{\phi}\Omega_r}{I_y} + \frac{K_D s}{|s|+\delta}\right]\frac{I_x}{l} \quad (17)$$

$$U_4 = \left[\lambda\left(\dot{\psi}_d - \dot{\psi}\right) + \ddot{\psi}_d - \dot{\phi}\dot{\theta}\left(\frac{I_x - I_y}{I_z}\right) + \frac{K_D s}{|s|+\delta}\right]I_z \quad (18)$$

**B) PID Sliding Mode Control:**

Now the sliding surface is given as:

$$s = \dot{e} + \lambda_1 e + \lambda_2 \int e\,dt \quad (19)$$

Where $\lambda_1, \lambda_2 (> 0)$ are tuning parameters. Applying the sliding condition, $\dot{s} = 0$, one can find out:

$$u_{eq} = (g + \lambda_1(\dot{z}_d - \dot{z}) + \lambda_2(z_d - z) + \ddot{z}_d)\frac{m}{\cos\phi\cos\theta} \quad (20)$$

Hence, one finally obtains

$$U_1 = (g + \lambda_1(\dot{z}_d - \dot{z}) + \lambda_2(z_d - z) + \ddot{z}_d + k_D\frac{s(t)}{|s(t)|+\delta})\frac{m}{\cos\phi\cos\theta} \quad (21)$$

Assuming reference as step signal $\dot{z}_d = 0$, $\ddot{z}_d = 0$. $\ddot{z}$ is obtained as:

$$\ddot{z} + \lambda_1 \dot{z} + \lambda_2 z = \lambda_2 z_d + k_D \frac{s}{|s|+\delta} + d \quad (22a)$$

Which is for PD only is given by

$$\ddot{z} + \lambda \dot{z} = k_D \frac{s}{|s|+\delta} + d \quad (22b)$$

$\lambda_1 \; and \; \lambda_2$ are responsible for the stability of response. A Lyapunov function is defined as $\boldsymbol{V = \frac{1}{2} s^2 > 0}$ . $\dot{V}$ must be negative-definite which necessitates $k_D > 0$ . It follows from the dynamic of the quadrotor as described by (22a) and (22b) for PD and PID SMC, respectively, that a disturbance pulse gets attenuated exponentially with PID-SMC which remains present with constant amplitude for PD-SMC.

## 4. RESULTS

This portion demonstrates the performance of the PD SMC showcasing the response of the quadcoptor system under consideration corresponding to different reference points for altitude, attitude angles. Further, the response of the whole closed loop system is investigated in presence of disturbances. First, the PD SM controller is applied for the altitude and attitude control. The reference values are set as $z_d$ = 1m, $\phi_d$=5°, $\theta_d$=5°, $\psi_d$=5°.

**Table 2.Tuning parameters**

| Parameter | Altitude and Attitude Angles | | | |
|---|---|---|---|---|
| | **z** | $\boldsymbol{\phi}$ | $\boldsymbol{\theta}$ | $\boldsymbol{\psi}$ |
| $\boldsymbol{\lambda}$ | 68 | 5 | 5 | 5 |
| $\boldsymbol{K_D}$ | 100 | 100 | 100 | 100 |
| $\boldsymbol{\delta}$ | 0.3 | 0.3 | 0.3 | 0.3 |

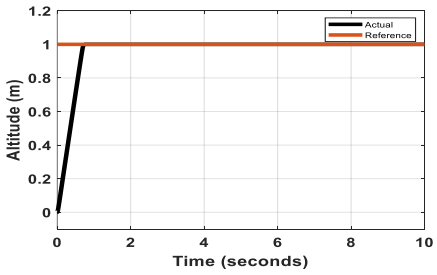


Fig.1 Altitude Response with PD SMC

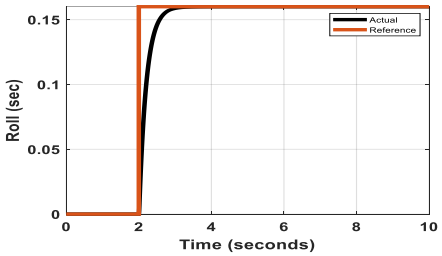


Fig.2 Roll response with PD SMC

A disturbance pulse train is applied at altitude of amplitude 30N and period 100 sec and pulse width 50%. Another disturbance pulse train is applied at roll of amplitude 2.5N and period 100 sec and pulse width 50%. So, PD sliding surface is responding to the disturbance but it is not rejecting the disturbance as shown in Figure 5 and 6 for altitude and roll, respectively. These figures show that the disturbance is present in the responses with constant magnitude. The performance may be improved by adding an integral part to the PD sliding Surface. The PID SMC is then implemented for the altitude and attitude angles. A disturbance is applied at 100s. The integral action rejects the disturbance and the responses are maintained at their reference values which are not possible with PD only. It is observed that the disturbance is attenuated in notable amount in case of PID SMC.

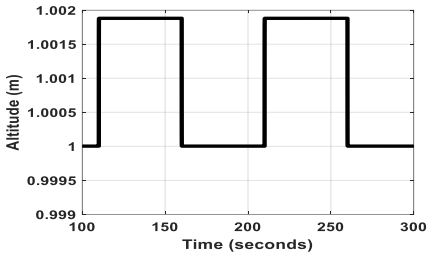


Fig. 6. Altitude Response with PD SMC in presence of disturbances

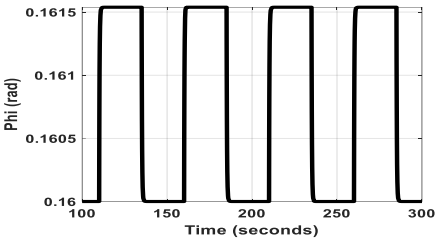


Fig. 7. Roll Response with PD SMC in presence of disturbances

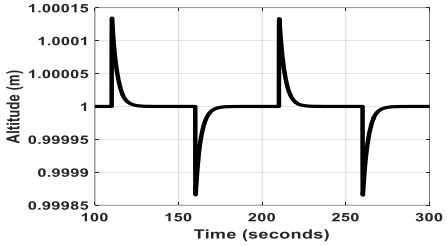


Fig. 8. Altitude Response with PID SMC in presence of disturbance

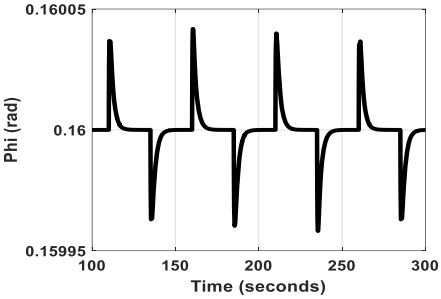


Fig. 9. Roll Response with PID SMC in presence of disturbance

## 5. CONCLUSION

The presented work develops a SMC based on PD sliding surface for full control of a quadrotor. The PD-SMC is tested analytically and through simulations. The simulation results show a successful tracking performance. However, this control scheme fails to achieve tracking when disturbances are applied. An integral sliding surface is augmented with the PD SMC to enable tracking of altitude and attitude commands even in presence of disturbances. The simulations verify the theoretical claim made towards disturbance rejection capability of PID-SMC.

## 6. REFERENCES

[1] B. Kamel, M. C. S. Santana, and T. C. De Almeida, ‘‘Position estimation of autonomous aerial navigation based on Hough transform and Harris corners detection,’’ in Proc. 9th WSEAS Int. Conf. Circuits, Syst., Electron., Control Signal Process., 2010, pp. 148–153.

[2] F. Fraundorfer et al., ‘‘Vision-based autonomous mapping and exploration using a quadrotor MAV,’’ in Proc. IEEE/RSJ Int. Conf. Intell. Robots Syst., Vilamoura, Portugal, Oct. 2012, pp. 4557–4564.

[3] D. Erdos, A. Erdos, and S. E. Watkins, ‘‘An experimental UAV system for search and rescue challenge,’’ IEEE Aerosp. Electron. Syst. Mag., vol. 28, no. 5, pp. 32–37, May 2013.

[4] Y. Naidoo, R. Stopforth, and G. Bright, ‘‘Development of an UAV for search & rescue applications,’’ in Proc. IEEE Africon, Livingstone, Zambia, Sep. 2011, pp. 1–6.

[5] J. A. Benito, G. Glez-de-Rivera, J. Garrido, and R. Ponticelli, ‘‘Design considerations of a small UAV platform carrying medium payloads,’’ in Proc. IEEE Conf. Design Circuits Integr. Syst., Madrid, Spain, Nov. 2014, pp. 1–6.
[6] B. Y. Suprapto, M. A. Heryanto, H. Suprijono, J. Muliadi, and B. Kusumoputro, ‘‘Design and development of heavy-lift hexacopter for heavy payload,’’ in Proc. IEEE Int. Seminar Appl. Technol. Inf. Commun., Semarang, Indonesia, Oct. 2017, pp. 242–247.
[7] Samir Bouabdallah. "Design and control of quad rotors with application to autonomous flying". Ph.D. Thesis. École Polytechnique Federale de Lausanne. 2007.
[8] C Balas. Modelling and Linear Control of a Quadrotor. MSc Thesis. Cranfield University.School Of Engineering.Academic year 2006-2007.
[9] G. Szafranski, R. Czyba .”Different Approaches of PID Control UAV Type Quadrotor.” Proceedings of the International Micro Air Vehicles conference 2011 summer edition
[10] Utkin, V. I., (1977), “Variable Structure Systems With Sliding Modes”, Transactions of IEEE on Automatic Control, AC – 22, pp. 212 – 222.
[11] Marco Herrera et. al. , “Sliding Mode Control: An approach to Control a Quadrotor”, 2015 Asia-Pacific Conference on Computer Aided System Engineering, OCT 2015,DOI 10.1109/APCASE.2015.62
[12] H. L. N. N. Thanh, S. K. Hong: “Quadcopter Robust Adaptive Second-Order Sliding Mode Control” IEEE ACCESS, vol 6, pp. 66850-66860, 2018

## Biographies

**Kalyani Mamidi** received the Bachelor degree in Electrical and Electronics Engineering from Andhra University, Visakhapatnam in the year 2018,and the degree of Master of Technology in Electrical Engineering, with specialization Power Electronics and Machine Drives, from National Institute of Technology, Durgapur, in 2022 . She is currently working in Smart SoC Solutions and Pvt. Ltd. as Physical Design Engineer in VLSI domain in Hyderabad.

**Jayati Dey** received the degree of Bachelor of Electrical Engineering in 2000 from Jadavpur University, Kolkata, Master of Engineering in 2003 from Bengal Engineering College, Shibpur, and Doctor of Philosophy degree in 2007 from IIT Kharagpur, India. She is currently serving as an Associate Professor in the Department of Electrical Engineering, National Institute of Technology Durgapur, India. Her research interests are periodic compensation, robotics and mechatronics, Unmanned Vehicles.. She has authored about 75 research papers in International Journals and Conference.

# FPGA Based Smart Home Automation Device Controller

Hiranmayi Mannem[1], Y. Chalapathi Rao[2], K. Swetha Reddy[3]

[1]M. Tech Scholar, VNR VJIET, Hyderabad-500090, India, hiranmaimannem@gmail.com
[2]Associate Professor in ECE, VNR VJIET, Hyderabad-500090, India, chalu.8421@gmail.com
[3]Assistant Professor in ECE, VNR VJIET, Hyderabad-500090, India, swethareddy_k@vnrvjiet.in

## Abstract

Due to technology advancements, everything is becoming smarter today. Home automation is one of these most intelligent things. Network-enabled digital technology has been rapidly incorporated into home automation in recent years. With the use of these technologies, it is now possible to automate the home by increasing the connectivity to many appliances. Wise control of electrical and electronic gear in a house or business is known as home automation. The primary concerns of home automation are safety, security, and comfort. This paper proposes a smart home automation controller that interfaces gadgets and sensors to a field programmable gate array (FPGA) to control security and comfort. Home automation controller design carry out tasks including water level indication, door lock security, light on or off depending on door open/close, alerting of windows, and managing of electronic appliances. Xilinx ISE and Verilog HDL were used to implement the suggested design on the FPGA.

**Keywords**—Alarms, FPGA controller, Sensors, Smart Home, Verilog HDL.

## 1. INTRODUCTION

Security is a significant part of any business, it is exceptionally useful for humankind to foster a framework that will forestall any break-ins to the home. There are numerous things in an individual's home that are valuable and important, and home automation systems can help secure them. With just one click, you can control the doors, windows, fire alarm, and temperature, ensuring that they are all secure. To control these devices from one place without having to get to the specific location for each action, whether the occupants are home, out, or just sitting in one place[1]. In a certain order, the controller checks each of the devices periodically . A controller or any gadget associated with all other gadgets that should be secured and control the framework. All devices communicate through sensors attached to them. A home automation system can fulfil such needs by providing a secure and comfortable living environment.

This undertaking is to plan a regulator, which gives a robotized home security framework at a reasonable cost [2]. The boundary sensors associated with the regulator will give the expected signs that will actuate regulator to process and make the predetermined move. A framework is intended to control well-being, solace and savvy water tank sign, alarm, charging caution water alert charging alert, windows caution and solace applications are likewise evolved in this undertaking. This undertaking can be stretched out later to control more gadgets or cycles and besides can be web empowered.

## 2. LITERATURE SURVEY

Ravi Payal, et al [3] security framework recognizes the fire and gate crashers through the entryway, window and carport. Advanced frameworks configuration is the underpinning of savvy home task. Solace and reliability of a house are directed by using this undertaking. Shrewd home robotization is carried out with a savvy Verilog code in this paper. Security, safety and solace are constrained by interacting gadgets and sensors to handle programmable entryway exhibit contracted as FPGA. The code has been incorporated on Xilinx tool. FSM ideas are utilized. Re-enacted waveforms a reacquired and confirmed

Carl J. Debono et al [4] "Implementation of a Home Automation System through a Central FPGA Controller" Innovation headway's have made conceivable the execution of inserted frameworks inside home machines. This has included new capacities and components, in any case, as a general rule, the implementations are elite, and frameworks organization is ludicrous constantly. Notwithstanding, there is a rising interest for splendid homes, where machines answer subsequently to varying regular terms and can be conveniently supervised with one ordinary contraption. This paper presents a likely game plan by which the client controls contraptions by using a central FPGA controller to which the devices and sensors are communicated. Command is passed to the FPGA from a mobile by interfacing it with Bluetooth. The results are basic, practical and it is a versatile system, turning it into a decent possibility for future keen home arrangements

Prasanna S. Bhoite, et al [5],"Wireless Signal Transmission utilizing an Android Portable and FPGA", Today's organizing innovation utilizes remote frameworks generally for the Web of Things (IOT). Trade of control orders and information between gadgets should be possible utilizing remote innovation in spite of the fact that they were at first intended for voice correspondence frameworks. The equipment utilized for the venture incorporate a Bluetooth module communicated with FPGA board, an Android portable with blue term application introduced on it and a Drove light associated with the FPGA board to show the effective transmission. The remote innovation is the most encouraging and famous innovation to control gadgets remotely subsequently the work in this paper, with some change and improvement, can be utilized to fabricate the proficient remote-controlled applications.

IOT utilizes Wi-Fi to trade information remote for huge distances utilizing Web. IOT module (ESP8266) is utilized to control the home modern machines in far off regions anyplace on the planet. Sequential Correspondence trades the information among FPGA and IOT module.

## 3. HOME AUTOMATION

The great target of this proposed framework is to give the framework for minimal price and simple to use alongside that has high reliability and well-being. This framework is utilized to beat the downsides. The idea of this framework is to supervise the gadgets inside the house. The home automation block diagram is shown in fig.1.

As Home Computerization is an association of hardware, correspondence, and electronic marks of connection that work to organize customary contraptions with one another through the Web. Every contraption has sensors and is related through Wi-Fi, so we can manage them from PDA or tablet whether we are at home, or a long ways off[6]. This enables us to switch on the lights, cease the front doorway, or even switch 0ff the power..

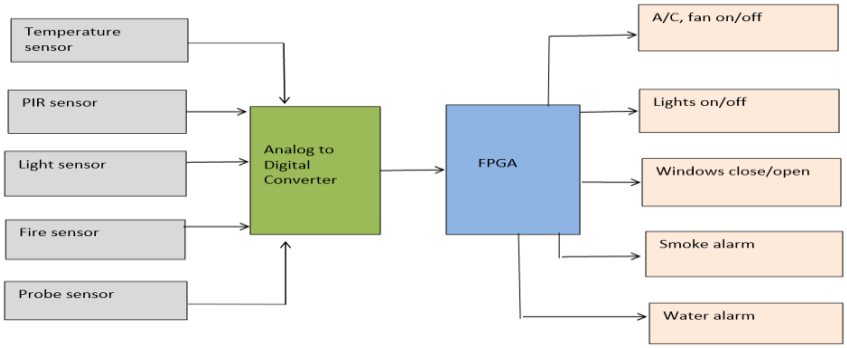


Fig 1: Home Automation Block Diagram

There are three principal components of a home Automation framework:

**Sensors** can screen changes in sunlight, temperature, or movement identification. Home Automation frameworks can then change those settings (and that's just the beginning) to the inclinations.

**Regulators** allude to the gadgets like PCs, tablets or cell phones used to send and get messages about the situation with robotized highlights in home.

**Actuators** might be light switches, engines, or mechanized valves that control the genuine instrument, or capability, of a home mechanization framework. They are customized to be initiated by a remote order from a regulator.

### *3.1 Sensor Module*

*1) Temperature Sensor:*

Here we are involving LM35 as temperature sensor. For this situation we will get the result which is relative to the temperature, the worth will be in degree Celsius. LM35 is more precise than ordinary thermistor. There won't be event of oxidation due to the use of fixing over the hardware. On contrasting and thermocouple LM35 produces higher result voltages. Since it is delivering higher result voltage, there is no need of independent intensification. Through involving this addition as well as decrement in the temperature can comprehend. It is having most extreme stockpile voltage of 35v and greatest result voltage of 6v.[7]

*2) PIR Sensor:*

A PIR motion sensor recognizes the movement of things.This sensor is widely utilized with an ultimate objective of wellbeing alerts. It recognizes the movement of any article in its surroundings. This sensor includes pyroelectric sensor, which can recognize the infrared radiation at various stages. It doesn't emanate the genuine energy anyway gets the energy inertly. It perceives the radiation from the surroundings. With temperature the presence of human or an article can be recognized. The PIR sensor doesn't discharge and convey the energy. The

Pyro sensor sees the advancement of an article variations in temperature. The perceived radiation changes over into electrical sign. Then, this sign boats off the outcome that is the caution. Alert indicates that a person has gone inside.

*3) Light Sensor:*

Here, the radiance sensor is using LDR. This LDR involves photoresistor which is includes silicon material. This sensor responds as soon as it recognizes the light. When the light beams fall on it, then, at that point, quickly the resistor likewise changes. At the point when the light level expands the opposition esteem additionally increments. At the point when the light level declines the opposition esteem likewise diminishes. The LDR will perceive the light through that resistor it responds to it and it will ship off framework according to it. With the goal that consequently the capabilities will work. The resistor diminishes in the brilliant and expansion in dim. In this lengthy frequency resistors are utilized. The light sensors is available in various models, sizes and shapes.

*4) Fire/Smoke Sensor:*

The smoke sensor senses the fire/smoke in our surroundings. Smoke sensor is a functioning assurance to individuals which cautions individuals with the alert. Whenever there is an existence of fire/smoke these sensors will turn on. The smoke sensor sees the infrared fire streak technique which permits recognizing the fire and intensity. It will answers effectively at specific reach .When the sensor distinguishes the smoke, it will convey a message to the caution framework to actuate , then the caution gives alert with the sound. Utilizing this sensor, the harm of the frameworks is limited.

*5) Probe/Water Level Sensor:*

To measure the water quantity and for recording data this sensor will be useful . At a point when the water quantity is peak or less this sensor conveys a message to the board to set off the alert. To deal with the water quantity the test sensor assists with controlling it. On the off chance that the water is unfilled in tank, the test sensor will identify the conductivity of opposition in it then it sends the data through a signal. By utilizing the caution the client receives the data regarding the measure of the tank.

### *3.2 Security Module*

Security module includes door lock and windows alerting.

*1. Door Lock:*

When an individual at the door step enters the secret key accurately it initiates to the high and unlocks the entryway consequently if not the caution will ring.If the client fails to remember the secret key or mistypes the secret key abruptly, they can attempt the secret key again by tolerating the message which they will get to their account.The initial step is to introduce the counter to nothing.Once the counter is set, four-digit secret phrase is placed. Assuming that the got secret phrase is right, entryway is opened else count is augmented by one. In the event that the count isn't equivalent to three, secret phrase can be returned again else assuming count is equivalent to three, the entryway is locked.[8]

*2. Windows Alerting:*

The sensor detects the climate, assuming that it is downpour/wind/thunder the windows will close any other way windows will open. Flow chart for door lock is shown in fig.2.

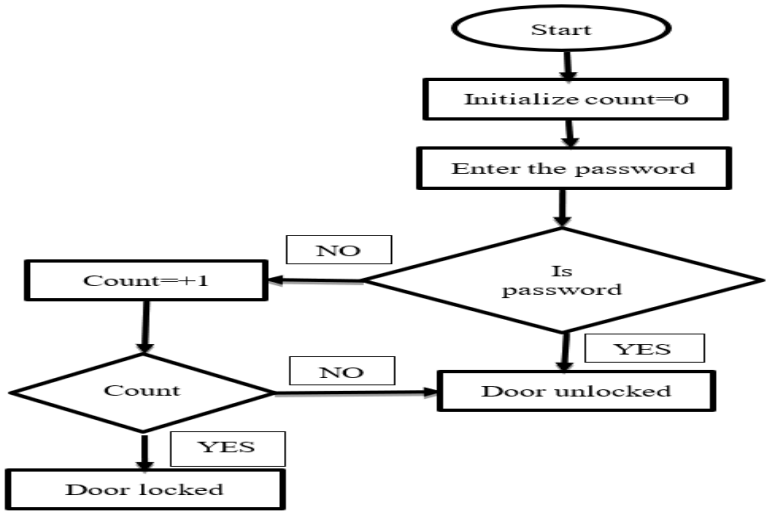


Fig 2: Flow chart for door lock

### *3.3 Comfort Module*

Comfort module includes Lights ON/OFF based on door open/close and water level indicator**.**

*A. Water Level Indicator**:***

The tank is full or not is demonstrated using a water level pointer with the assistance of a signal.

*B. Automatic Lights On/Off Based on Door Open/Close:*

After unlocking the door, the PIR sensor senses the event of entering the house. The stream graph for programmed lights on/off in view of entryway open/close is displayed in fig.3. The initial step is to introduce the sensor, here we are utilizing the PIR sensor to detects the article development. Assuming the sensor detects the item development (i.e., entryway open) the lights will be ON any other way lights will OFF.

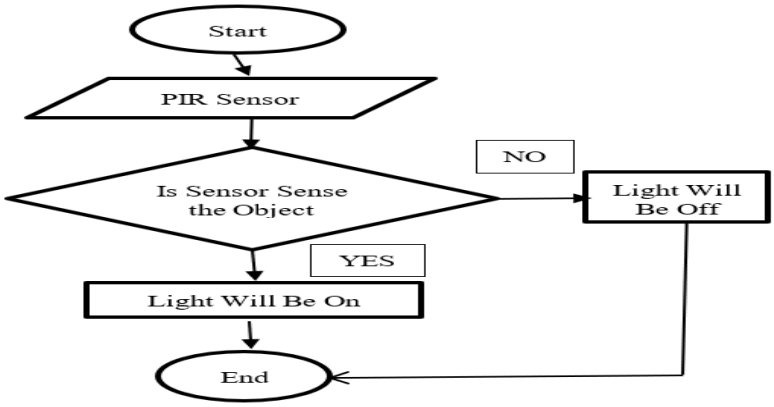


Fig.3: Flow chart for automatic light on/off

### *3.4 Safety Module*

*A. Water Alarm**:***

So these are initially in starting stage, these are position to zero phase just so next activity we resemble assuming condition resembles we on the engine the water level beginnings increment we are given 4 cycle input that mean most elevated esteem is 15 right so level comes till 14 addition is finished yet it not over stream then the condition is in else on the off chance that not increase then, at that point, remain in same condition or, more than likely caution rings .

*B. Fire Alarm*

When fire level beginnings increment, we are given 4-digit input that mean most elevated esteem is 15 right so level comes till 14 augmentation is finished yet it not over stream then the condition is in else on the off chance that does not increase then stay in same condition or, more than likely alert rings.[9]

*C. Current Alarm*

So current is fundamentally in starting stage these are position to zero phase just so next activity we resemble assuming condition resembles we on the meter it ought to have greatest number of readings just so the perusing level beginnings increment we are given 8 bit input that mean most elevated esteem is 256 watts right so level comes till 250watts augmentation is finished yet it not get more number then the condition is in else on the off chance that not increase then, at that point, remain in same condition or, in all likelihood caution rings.

*D. Charging Alarm*

Charging are fundamentally in beginning stage these are position of zero phase just so next activity we resemble assuming that condition resembles we on the switch the battery level beginnings increment we are given 4 bit input that mean most elevated esteem is 15 right so level comes till 14 addition is finished however it not over charged then the condition is in else in the event that not increase then, at that point, remain in same condition or probably caution rings.

*E. Motor Alarm ON/OFF:*

- Water level sensor senses the level of the water in the tank, note down the recordings.
- If the water level is less than the value 3 then alarm is ON and then have to ON the motor, water is pumping
- If the water level reaches to the value 10 or greater than 10 then alarm goes to OFF and then have to OFF the motor.

### *3.5 Verilog HDL*

In the VLSI industry, Verilog is a gear entrancing language utilized to show electronic systems. Verilog HDL is one of the most customarily elaborate language in the arrangement, check, execution of mechanized reasoning chips at the RTL of consultation. This is like manner used in the check of straightforward and going against message circuit. The design in Verilog holds pecking order of elements that are subsequently attached and functions as total framework.[10].

## 4. RESULTS

### *A. RTL Schematic*

The RTL schematic is truncated as the register transfer level it signifies the blueprint of the architecture and is utilized to check the planned design to the ideal design that we are needing improvement. Fig.4, fig.5 and fig.6 are showing the RTL Schematics of different modules.


Fig.4: RTL Schematic of smart home safety

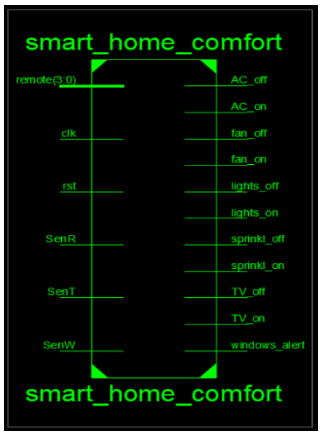


Fig.5: RTL Schematic of smart home comforts

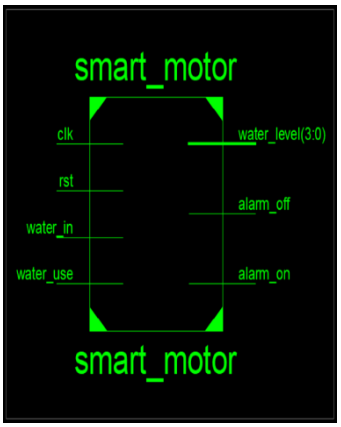


Fig.6: RTL Schematic of smart motor

### *B. Technology Schematic*

The innovation schematic makes the portrayal of the architecture in the LUT design ,where the LUT is consider as the boundary of region that is utilized in VLSI to appraise the engineering plan .the LUT is consider as a square unit the memory distribution of the code is addressed in there LUTs in FPGA. The technology schematics and simulation results of smart home modules are shown in fig.7 to fig.12.

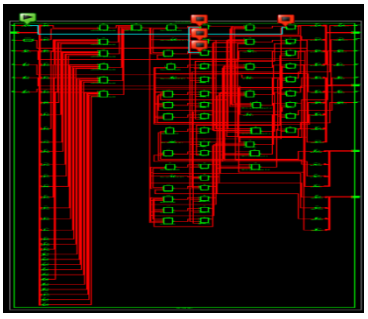

Fig.7: Technology Schematic of smart home safety

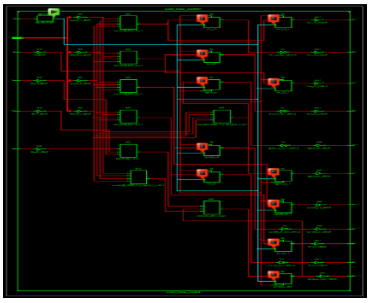

Fig.8: Technology Schematic of smart home comforts

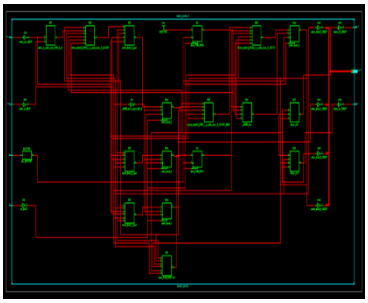

Fig.9: Technology Schematic of smart motor

### *C. Simulation Waveforms*

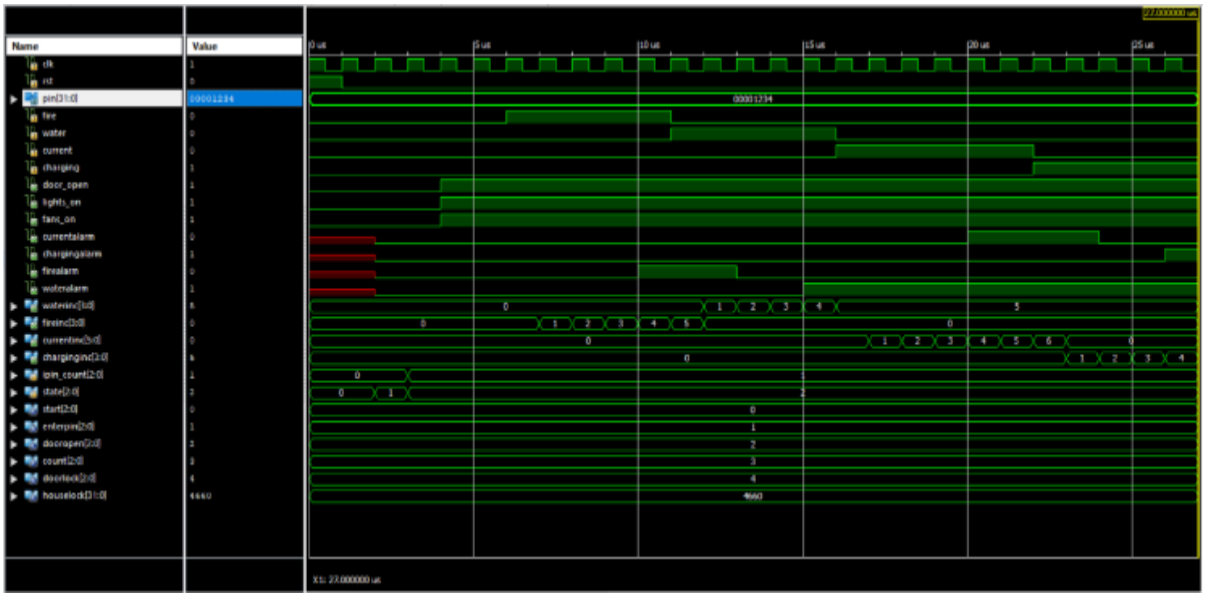

Fig.10: Simulated Waveforms of smart home safety

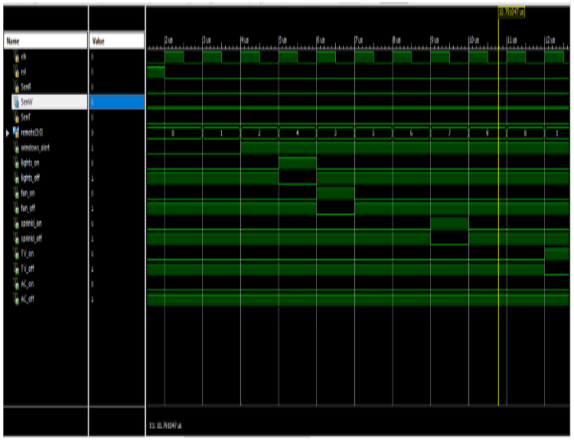

Fig.11: Simulated Waveforms of smart home comforts

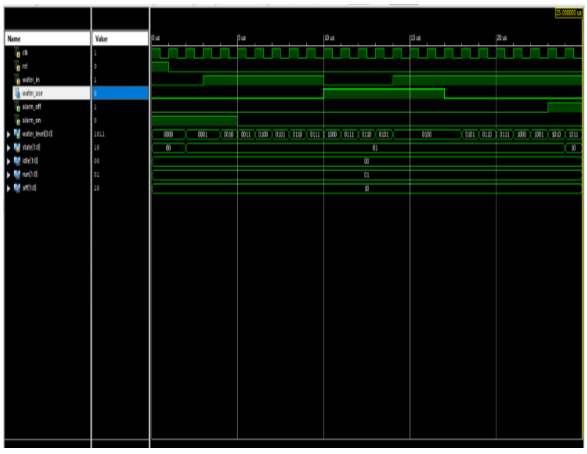

Fig.12: Simulated Waveforms of smart home motor

## 5. CONCLUSIONS AND FUTURE SCOPES

The goal of this paper is to plan a regulator at a reasonable cost which contains a robotized In-house security framework. This kind of controller is minimal expense and it very well may be upgraded to cutting edge regulator by rolling out couple of improvements. It is extremely simple to utilize and we can coordinate with some other device. The Savvy home works on the way of life of the control of the home gadgets. The essential boundaries are security and solace of a home. Home Computerization includes shrewd monitor and control of gadgets in home. In this undertaking, Savvy home mechanization regulator was proposed in which Security and solace is constrained by connecting gadgets and sensors. Home Computerization regulator configuration performs tasks, for example, water level pointer, entryway lock security, light on or off in view of entryway open/close, windows cautioning, controlling of electronic machines are planned . This proposed plan executed and integrated on Xilinx ISE vertex low power utilizing Verilog HDL.

For future advancements, there are couple of suggestions for making this framework an attractive item. Execute the equipment part by utilizing the sensors and gadgets. Simply fabricating it on a chip makes it a gadget that can be installed to a computer and so on. Improve it as web empowered to remotely control the framework. The proposed plan was entirely adaptable so we can expand similar plan with additional security and solace applications in future.

The dream is a future where data is bestowed among devices and human without relying upon manual commitment of individual bytes. There are a few new advancements which can turn into a piece of home soon:

- Increased efficiency, control, and customization
- Integration of Smart home devices
- Child Monitoring
- Smart spaces outside homes
- Development of smart appliances

## REFERENCES


[1] N.Chintaiah, K. Rajasekhar, V. Dhanraj, "Automated Advanced Industrial and Home Security using GSM and FPGA", International Journal of Computer Science and Information Technologies, vol. 2(4), 2011.

[2] Dr. Sanjeev Sharma, "FPGA Based Cost Effective Smart Home Systems", International Conference on Advances in Communication and Computing Technology, Ahmednagar, India. February, 2018.

[3] Ravi Payal, Akanksha Saxena, Beena Chanda, "Implementation of Smart Home through FPGA using Verilog Hardware Descriptive Language", IEEE International Conference on Advent Trends in Multidisciplinary Research and Innovation (ICATMRI),Buldhana, India, December 2020, 10.1109/ICATMRI51801.2020. 9398499.

[4] Carl J. Debono; Kurt Abela, "Implementation of a home automation system through a central FPGA controller",16th IEEE Mediterranean Electrotechnical Conference, Yasmine Hammamet, Tunisia,March 2012, DOI:10.1109/MELCON.2012.6196513.

[5] Prasanna S. Bhoite , Madan B. Mali, "Wireless Signal Transmission using an Android Mobile and FPGA", International Journal of Advanced Research in Computer and Communication Engineering, E&TC, Vol. 5, Issue 5, May 2016

[6] P.A Bawiskar and Prof R . K. Agrawal, "FPGA Based Home Security System", International Journal of Innovative Research in science Engineering and Technology, Vol. 4, Issue 12,December 2015, DOI:10.15680/IJIRSET.2015.0412139.

[7] Nikhat Parvin, Pramod Kumar Jain, Devendra Singh Ajnar, "Automated and Secured Smart Home through FPGA Controller", International Journal of Innovative Technology and Exploring Engineering, Volume-8 Issue-11, September, 2019.

[8] Greeshma Arya, "Smart Home Implementation using Verilog Hardware Descriptive Language", International Journal of Engineering Research & Technology (IJERT),Vol. 11 Issue 02, February, 2022.

[9] Kandepi Madhuri B Likhith Sai Bysani Sai Sirisha, "A Home Automation System Design Using Hardware Descriptive Tools", International Journal of Engineering Research & Technology, Vol. 2 Issue 7, July, 2013.

[10] Komol Arafat Gani, Farzana. Yasmin, A B M Najmul. Karim Iqbalur. Rahman, "Home Automation System Design Using Verilog Hardware Descriptive Language", International Conference on Recent Trends in Computer and Information Engineering, December, 2013.

# Review of DC arc fault detection


| | |
|---|---|
| **Krunal Shivkumar Panpaliya,**[1]<br>*Dept. of Electrical Engineering,*<br>*Prof Ram Meghe College of*<br>*Engineering and Management,*<br>*Badnera* Amravati, Maharashtra<br>krunalpanpaliya@gmail.com | **Dr. M. S. Ali**[2]<br>*Dept. of Electrical Engineering,*<br>*Prof Ram Meghe College of*<br>*Engineering and Management,*<br>*Badnera* Amravati, Maharashtra<br>softalis@gmail.com |



## Abstract.

DC electric system related to power is used in many system across the globe. The development related to technology of renewable energy apart from the application in the field of power electronics it was observed that the DC network for the distribution of the power used so that there shall be proper integration of renewable resources. There are different advantages of this system but the disadvantage includes DC arc faults. DC arc faults occurred when high voltage DC buses are used in the electrical components. There are different accidents occurred because of the DC arc faults introduction in the different situations. The present work consists of the review on the different methods to be used for the detection of the DC arc faults and devices can be used for the detecting the location of it. Several authors used methods related to AI, experimental test-bed was prepared, analytical and simulations of the models are also carried out.



**Keywords:** DC, arc, fault and voltage


## 1. INTRODUCTION

When the arc which was not intended considered to be the fault in arc and it is generally created when current flow through some path which was not planned and this lead to a condition of fire. The diagnosis of the fault is to be carried out and the purpose behind this is to isolate faults especially for the system which are defective. But this task is considered to be of extraordinary skill. Therefore the system of automation in the diagnosis is very important [1]. The MATLAB power system Blockset was used along with Arc Model Blockset, this is one of the library useful to make the models related to arc.

The validation is also carried out is the study while the program is made to study arc and its interaction with circuit [2]. The detection of the fault was proposed and this techniques is used when there is processing in terms of the fundamental voltage which are synchronized. Here the utilization of the current phasors for the case of arcing apart from the faults which are permanent. [3]. The methodology was adopted for the detection of faults which are single phase, in particular when the resistance in the fault is varied up to 15 kΩ, distribution system adopted was radial. This method is obtained through program of ATP where the realization of arc model is considered the representation of arc which was universal [5].

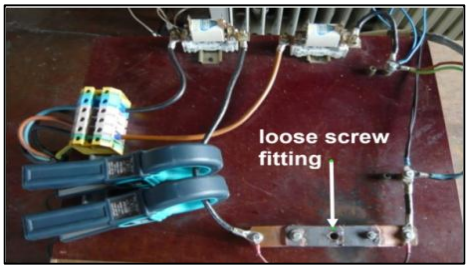


Fig.1.1. Measurement set-up arranged for series arc fault

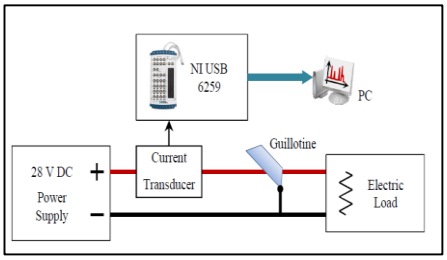


Fig. 2.1. Experimental set-up used in the fault detection [10]

## 2. TWO ARC FAULTS (SERIES AND PARALLEL)

It was observed that generally two type of the faults in arc generated, especially in case of switchgear having low voltage. Parallel and series arc faults are two types of arc which is responsible for the damages to system of switchgear [6]. The performance of the device was studied in the experiments [7] for the test. The investigation of PV system and behaviour of it was carried out for the both type of faults in the arc. [8].

TABLE I. SUMMARY FOR DIFFERENT METHODS USED FOR DETECTION OF AN ARC FAULTS

| Reference | Year | Type of Analysis | Findings |
|---|---|---|---|
| [5] | 2007 | Discrete Wavelet Transform | Enhancement in Arc reignitions |
| [6] | 2010 | Fourier analysis | Detection of fault in arc when the load current is measured in switchgear. |
| [11] | 2013 | Analytical | Analytical expressions depending upon different parameters are obtained |
| [12] | 2014 | Fast Fourier Transform and Wavelet decomposition | Wavelet transformation method has more rapid detection system |
| [13] | 2017 | Wavelet transform and Convolutional Neural Network | The method was useful under different conditions of the fault and factors of interference |
| [14] | 2019 | Random forest method, wavelet packet transform | Random forest method gave higher performance for the detection of arc fault |
| [15] | 2021 | Frequency spectral analysis | Considered indicators useful to detect presence of an arc, integration of algorithm to be used for detecting arc fault |
| [16] | 2021 | Artificial neural network, fuzzy system | Average performance for the detection of arc faults found to be same in both analysis methods. |

To differentiate the parallel arc fault and series arc faults the alternative method was studied. The suppression of arc faults was also studied, there was possibility of de energization in case of series arc faults and parallel arc faults through some methods [9]. The identification of arc is carried out through innovative approach when the two different parameters are evaluated. Parameters included current spikes with concurrency rate apart from specific energy [10].

## 3. SERIES ARC FAULT DETECTION

To detect the arc series fault the PV system was studied where the use of circuit interrupters used as the protection purposes. The DC switching with fast acting was used in the system of protection. The current solution having discrete frame differentiation had been used in the

detection system [17- 19]. The heuristic model was used since it was easy for the simulation of arc for the kind of voltage level as well as different level of the current. The noise intensity of the arc for the frequency band of below 50 kHz increases considerably for the case of faulting of the arc [20]. The nonlinear loads and complex loads in terms of the load of power electronics considered and analysis was carried out. For the case of detecting arc faults different parameters of the current including average, median, variance, and distance between minimum and maximum values analysed [21]. The electric arc was studied for the calculation of transient resistance especially for the case of short circuits, the mathematical expressions are derived. The simulation in the MATLAB was also carried out,[22]. The reduction of the effect having hot spot and the detection of DC arc fault was studied through various research papers [23]. The review was carried out on the location detection and detection of an arc fault for the case of DC photovoltaic grid. The simulation models had been studied for the results in terms of the different analysis like Fourier Transform on the arc faults [24]. The review was carried out on the detection of the faults using AI methods; the diagnosis was also carried out in the PV system. The AI considered being useful tool for the different application including solar [25]. The different algorithms were studied and then classified in to groups i.e. heuristic and classic methods. Different algorithms related to these methods were studied in detail[26]-[27].

## 4. EXPERIMENTAL DATA

The loop current was captured with the help of current transformer having frequency of 600 Hz, this was helpful for filtering disturbances having low frequency especially for the case of dust and changes in the weather. The input was given in terms of the current signal with 20 kHz rate of sampling. Photovoltaic emulator was connected in the series with arc generator apart from single 1.5 kW phase inverter-Sunny Boy [28]. An inverter generally have the switching device with higher frequency i.e. in the range of 10-20 kHz. The analysis of the arc fault detection system considered when the current signal having 48.33-93.99 kHz frequency modules had been extracted [29]. The AC arc fault experimental system consisted AC supply of power, load box, resistance, contactor, sensor and generator of arc with the standard UL1699. These different components played a vital role for the system [30]. The experimental set-up consisted power supply with 10 kW keysight, opal 4510, generator of an arc, power electronic circuit. Opal 4510 used for the controlling buck converters and resitors, the constant power loads connected in parallel with 14A- input current, 200V-output voltage [31].

## 5. SIMULATION

For the purpose of simulation there are different models which can be used. The empirical models includes Nottingham arc model, Hall arc model, Myer arc model, Viicheck model, stokes model, Oppenlander arc model, Paukert arc model and modified Paukert arc model [32]. The simulation of the electric arc can be carried out in software tools and these are available in the software. For the case of the black box models the simulation was carried out in the MATLAB Simulink. When this tools used then the analysis carried out for system of power in the time domain, differential equations were solved which helped for the understanding of component behaviour [33]. The Simulink used for the arc model consists of the block named ‘Hit crossing’, this used for detection for the case of current as

input cross the value of 0. The adjustment of the stepsize carried out so that the simulation get the cross value. 'Step' block in terms of the Simulink used for controlling separation of contact in case of breaker of circuit [2]. The simulation of the arc models is carried out in the MATLAB software for the arc current with different units i.e. 12.5 kA to 40 kA, in this tool model of Hochrainer and Cassie was used. The results obtained in the Simulink had been compared with the experimental tests carried out on the short circuit with same arc current [34]. For studying variation of arc faults in the PV components, arc current with changes in the long-time are collected through the experimental set-up. Habedank arc model was considered for the case of simulation of U-I characteristics related to model of arc. The interaction was studied for the series arc model and the algorithm related to Maximum Power Point tracking [35].

## 6. ALGORITHM

Support vector machine is considered to be best algorithm for the supervised learning purposes. The important thing behind the support vector machine part is the creation of hyperplane having the highest margin that is available in between two classes adjacent to each other. This is helpful for bounding the error which is generalized for the case of model [36]. Heuristic search method used for investigating approximate value. Due to this the arc modelling was carried out in precise way [37]. The discrete wavelet transform was used apart from the deep neural network so that the detection of arc faults can be improved with accuracy. While calculating the wavelet transform, Mallat algorithm theory was used. When the approximation considered then sequence for the closed loop subspace used. The wavelet function i.e. Sym8 was used for performing different five levels of the decomposition of wavelet for the case of sampling signals of current [38]. The neural network was dependent on the gradient evidence which was related to the error function. It was observed that the BP neural network is not useful in the case of initial value was not considered appropriately [39]. Deep convolutional neural network is considered to be unusual kind of the neural network. This considered having very good performance in the field of vision for computer and processing of image [40] .AFD algorithm was used and it was found that to get accurate AFD in the Intel Arc considered to be have impact for the interpreting correctly LL outputs. When the fault detection needed to be carried which dependent on MLT where the learning algorithm have been used and trained. This consisted experimental data for learning different relation for the parameters of input and output. Training was given to the data obtained from the model having predicted PV [41].

## 7. CONCLUSIONS

There is tremendous growth in the economic level and this leads to the increase in the electrification for commercial and residential use. This also leads to the increase in the electricity loads and ultimately this becomes the reason for the potential hazards. The use of DC in electrical components considered to be the development in the field of power electronics as well as the renewable resources. When the DC network is to be used then the protection should be the key part of the network. From the various research papers it was observed that the DC arc faults are increased because of higher DC voltage, difficult to

detect arc faults. The possibility in the tripping when the noises are created in the power electronic devices.

## 8. REFERENCES


[1] W. G. Fenton, T. M. McGinnity and L. P. Maguire, "Fault diagnosis of electronic systems using intelligent techniques: A review," IEEE Transactions on Systems, Man, and Cybernetics, Part C (Applications and Reviews), vol. 31, p. 269–281, 2001.

[2] P. H. Schavemaker and L. Van Der Sluis, "The arc model blockset," in Second IASTED International Conference POWER AND ENERGY SYSTEMS, Crete, 2002.

[3] Y.-H. Lin, C.-W. Liu and C.-S. Chen, "A new PMU-based fault detection/location technique for transmission lines with consideration of arcing fault discrimination-part I: theory and algorithms," IEEE Transactions on power delivery, vol. 19, p. 1587–1593, 2004.

[4] I. Zamora, A. J. Mazon, K. J. Sagastabeitia and J. J. Zamora, "New method for detecting low current faults in electrical distribution systems," IEEE Transactions on Power Delivery, vol. 22, p., 2007.

[5] N. I. Elkalashy, M. Lehtonen, H. A. Darwish, M. A. Izzularab and I. T. Abdel-maksoud, "Modeling and experimental verification of high impedance arcing fault in medium voltage networks," IEEE Transactions on Dielectrics and Electrical Insulation, vol. 14, p. 375– 383, 2007.

[6] P. Müller, S. Tenbohlen, R. Maier and M. Anheuser, "Characteristics of series and parallel low current arc faults in the time and frequency domain," in 2010 Proceedings of the 56th IEEE Holm Conference on Electrical Contacts, 2010.

[7] J. Andrea, P. Schweitzer, E. Tisserand, P. Roth and S. Weber, "Calibrated ac and dc arcing fault generator," in 2010 Proceedings of the 56th IEEE Holm Conference on Electrical Contacts, 2010.

[8] J. Flicker and J. Johnson, "Electrical simulations of series and parallel PV arc-faults," in 2013 IEEE 39th Photovoltaic Specialists Conference (PVSC), 2013.

[9] J. Johnson, M. Montoya, S. McCalmont, G. Katzir, F. Fuks, J. Earle, A. Fresquez, S. Gonzalez and J. Granata, "Differentiating series and parallel photovoltaic arc-faults," in 2012 38th IEEE P Conference

[10] R. Grassetti, R. Ottoboni and M. Rossi, "A novel algorithm for the parallel arc fault identification in DC aircraft power plants," in 2012 IEEE International Instrumentation and Measurement Technology Conference Proceedings, 2012.

[11] N. Marković, S. Bjelić, J. Živanić and U. Jakšić, "Numerical simulation and analytical model of electrical arc impedance in the transient processes," Elektronika, Energetika, Elektrotechnika, Przegląd Elektrotechniczny, p. 113–117, 2013.

[12] Z. Wang, S. McConnell, R. S. Balog and J. Johnson, "Arc fault signal detection-Fourier transformation vs. wavelet decomposition techniques using synthesized data," in 2014 IEEE 40th (PVSC), 2014.

[13] M.-F. Guo, X.-D. Zeng, D.-Y. Chen and N.-C. Yang, "Deep-learningbased earth fault detection using continuous wavelet transform and convolutional neural network in resonant grounding distribution systems," IEEE Sensors Journal, vol. 18, p. 1291–1300, 2017.

[14] Z. Yin, L. Wang, Y. Zhang and Y. Gao, "A novel arc fault detection method integrated random forest, improved multi-scale permutation entropy and wavelet packet transform," Electronics, vol. 8, p. 2019

[15] G. Artale, G. Caravello, A. Cataliotti, and G. Tine, "Characterization of DC series arc faults in PV systems based on current low frequency spectral analysis," Measurement, vol. 182, p. 109770, 2021.

[16] R. Janarthanan, R. U. Maheshwari, P. K. Shukla, and P. K. Shukla, , "Intelligent detection of the PV faults based on artificial neural network and type 2 fuzzy systems," Energies, vol. 14, p. 6584, 2021.

[17] M. Rabla, E. Tisserand, P. Schweitzer and J. Lezama, "Arc fault analysis and localisation by cross-correlation in 270 V DC," in 2013 IEEE 59th Holm Conference on Electrical Contacts (Holm 2013),

[18] N. L. Georgijevic, M. V. Jankovic, S. Srdic and Z. Radakovic, "The detection of series arc fault in photovoltaic systems based on the arc current entropy," IEEE Transactions on Power Electronics, vol. 31, p. 5917–5930, 2015.

[19] S. Dhar and P. K. Dash, "Fault detection and location of photovoltaic based DC microgrid using differential protection strategy," IEEE Transactions on Smart Grid, vol. 9, p. 4303–4312, 2017.

[20] S. Lu, B. T. Phung and D. Zhang, "Study on DC series arc fault in photovoltaic systems for condition monitoring purpose," in Australasian Universities Power Engineering Conference (AUPEC), 2017.

[21] H.-L. Dang, J. Kim, S. Kwak and S. Choi, "Series DC arc fault detection using machine learning algorithms," IEEE Access, vol. 9, p. 133346–133364, 2021.

[22] X. Yao, "Dc arc fault detection and protection in dc based electrical power systems," 2015.

[23] Z. Wu, Y. Hu, J. X. Wen, F. Zhou and X. Ye, "A review for solar panel fire accident prevention in large-scale PV applications," IEEE Access, vol. 8, p. 132466–132480, 2020.

[24] K. R. Fulzele, P. P. Gajbhiye and V. M. Jape, "Different techniques for ARC flash and fault analysis and classification," 2020.

[25] A. Abubakar, C. F. M. Almeida and M. Gemignani, “Review of Artificial Intelligence-Based Failure Detection and Diagnosis Methods for Solar Photovoltaic Systems,” Machines, vol. 9, p. 328, 2021.
[26] M. Sedighizadeh, A. Rezazadeh, N. I. Elkalashy and others, “Approaches in high impedance fault detection a chronological review,” Advances in Electrical and Computer Engineering, 2019
[27] P. C. Hatton, M. Bathaniah, Z. Wang and R. S. Balog, “Arc generator for photovoltaic arc fault detector testing,” in 2016 IEEE 43rd Photovoltaic Specialists Conference (PVSC), 2016.
[28] S. Lu, T. Sirojan, and E. Ambikairajah, “DADCGAN: An effective methodology for DC series arc fault diagnosis in photovoltaic systems,” IEEE Access, vol. 7, p. 45831–45840, 2019.
[29] J.-C. Gu, D.-S. Lai, J.-M, and M.-T. Yang, “Design of a DC series arc fault detector for photovoltaic system protection,” IEEE Transactions on Industry Applications, vol. 55, p. 2464–2471, 2019.
[30] Y. Gao, L. Wang, Y. Zhang and Z. Yin, “Research on AC arc fault characteristics based on the difference between adjacent current cycle,” in PHM-Qingdao, 2019.
[31] V. Le and X. Yao, “Ensemble machine learning based adaptive arc fault detection for dc distribution systems,” in 2019 IEEE (APEC), 2019.
[32] V. Le, X. Yao, C. Miller and T.-B. Hung, “Series Arc Fault Detection and Localization in DC Distribution Based on Master Controller,” in 2020 IEEE (ECCE), 2020.
[33] S. Lu, B. T. Phung and D. Zhang, “A comprehensive review on DC arc faults and their diagnosis methods in photovoltaic systems,” Renewable and Sustainable Energy Reviews, vol. 89, 2018.
[34] N. S. Mahajan, K. R. Patil and S. M. Shembekar, “Electric Arc model for High Voltage Circuit Breakers Based on MATLAB/SIMULINK,” Interantional Journal of Science, Spritualtiy, Business and Technology (IJSSBT), vol. 1, 2013.
[35] P. Katare, R. Chennu, S. S. Reddy, A. Awasthi and B. Ramachandra,“Evaluation of arc conductance for high current fault arcs,” in 2017 7th International Conference on Power Systems (ICPS), 2017.
[36] X. Li, C. Pan, D. Luo and Y. Sun, “Series DC arc simulation of photovoltaic system based on Habedank model,” Energies, vol. 13, p. 1416, 2020.
[37] N. Ghaffarzadeh and A. Azadian, “A comprehensive review and performance evaluation in solar (PV) systems fault classification and fault detection techniques,” 2018.
[38] Z. Wang and R. S. Balog, “Arc fault and flash detection in photovoltaic systems using wavelet transform and support vector machines,” in 2016 IEEE 43rd (PVSC), 2016.
[39] K.-H. Park, H.-Y. Lee, M. Asif and B.-W. Lee, “Parameter identification of dc black-box arc model using non-linear least squares,” The Journal of Engineering, vol. 2019, p. 2202–2206, 2019.
[40] Q. Yu, Y. Hu and Y. Yang, “Identification Method for Series Arc Faults Based on Wavelet Transform and Deep Neural Network,” Energies, vol. 13, p. 142, 2019.
[41] X. Han, D. Li, L. Huang, H. Huang, J. Yang, Y. Zhang, X. Wu and Q Lu, “Series arc fault detection method based on category recognition and artificial neural network,” Electronics, vol. 9, p. 1367, 2020.

## Biographies

**Krunal S Panpaliya** received the bachelor's degree in Electrical engineering from Pune University in 2011, the master's degree in Electrical & Electronics engineering from Sant Gadge baba Amravati University in 2015, and He is currently pursuing philosophy of doctorate degree in Electrical Engineering from Sant Gadge baba Amravati University in 2019. He is currently working as an Assistant Professor at the Department of Electrical Engineering, Faculty of Engineering, Sant Gadge baba Amravati University. His research areas include FACTS, protection system, deep learning, power system & Artificial intelligent. He has been serving as a reviewer for many highly-respected journals.

# PREDICTION OF FOREST FIRES USING MACHINE LEARNING

**Indranil Basu*, Sayantan Sarkar, Suswan Biswas**
*Dept. of Electronics and Communication Engineering*
*Institute of Engineering and Management, Kolkata, India*

*Corresponding Author: indranil.basu@iemcal.com

## Abstract.

Forest fires are one of the most threatening consequences of climate change. Not only do forest fires cause serious harm to the ecological balance, but they also threaten human lives and property. Predictive tools are essential for early detection and control of such an emergency. Machine Learning tools harness powerful algorithms to analyse and predict the patterns observable in natural calamities like forest fires. This project would implement Regression and Artificial Neural Networks for the prediction of forest fires. Individual machine learning models would be analysed and compared to determine the most accurate model. Since, determination of forest fire susceptibility in specific areas involves factors that have non-linear relationships, regression, and deep learning techniques would be used for prediction purposes. Every instance in our dataset would be mapped a corresponding susceptibility value based on forest fire risk factors by the ML models. Predictions obtained from such algorithms would be compared using ROC-AUC, Mean Absolute Error (MAE), and Root Mean Squared-Error (RMSE) evaluation metrics. The results highlighted would help in efficient control and disaster management by not only pinpointing specific high-risk areas but also allow timely intervention to prevent further spread.

**Keywords**. Regression, Artificial Neural Network, susceptibility value, ROC-AUC, Mean Absolute Error (MAE), Root Mean Squared-Error (RMSE)

## 1. INTRODUCTION

Forest fires are one of the most threatening consequences of climate change. Not only do forest fires cause serious harm to the ecological balance, but they also threaten human lives and property. Forest fires are capable of driving species of organisms to extinction if not controlled.

Besides, forest fires are also one of the significant contributors to atmospheric pollution and global warming as a result of different emissions that release harmful gasses into the atmosphere including CO2 and SO2.

We all know about the Amazon Rainforest wildfire back in 2019, and we are all aware of how devastating the fire was, with over 906 thousand hectares of forest within the Amazon biome having been lost to fires in 2019. Similar devastating forest wildfires have occurred across California, USA; British Columbia, Canada; Turkey and many other forests across the globe. The frequency and occurrence of forest-fires have seen a boom over the last decade. Predictive tools based on Machine Learning algorithms are essential for early detection and control of such an emergency. If forest fires can be predicted, then we can take preventive measures to save the environment from a lot of damage by controlling environmental pollution.

## 2. OBJECTIVE

Machine Learning tools harness powerful algorithms to analyse and predict the patterns observable in natural calamities like forest fires. This model implements logistic regression techniques and other machine learning classification tools as well as artificial neural networks for the prediction of forest fires. Individual machine learning tools would be analysed and compared to determine the most accurate model.

Determination of forest fire susceptibility in specific areas involves factors that have non-linear relationships such as humidity, temperature variance over a period, wind patterns, and so on. Therefore, nonlinear logistic regression, and deep learning techniques would be used for prediction purposes. Every instance in our dataset would be mapped a corresponding susceptibility value based on forest fire risk factors by the ML models.

Predictions obtained from such algorithms would be compared using ROC-AUC, Mean Absolute Error (MAE), and Root Mean Squared-Error (RMSE) evaluation metrics. The results highlighted would help in efficient control and disaster management. It would not only pinpoint specific high-risk areas but also allow timely intervention to prevent further spread.

## 3. METHODOLOGY

We will use the images captured by the thermal cameras of the satellites for the dataset, which will be fed into the ML models for analysis. By using computer vision libraries like TensorFlow and OpenCV, we will analyse the extent of the red color of a particular portion of the image and then map

that to a corresponding susceptibility value using regression techniques. After the analysis, the model will give us a probability value of the susceptibility of wildfire for a specific latitude and longitude, using which we can predict regions where there are high chances of forest fires. Besides, we will be adding a statistical based approach to our current image-based approach that will include different non-linear factors like wind direction, wind speed, temperature variance and so on.

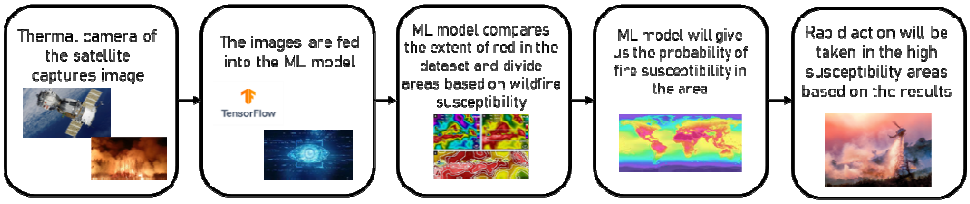


Fig 1. BLOCK DIAGRAM

Our system will operate in five layers, which are shown alongside.

- The 1st level will be the thermal image, which will be captured by the satellites.
- The 2nd level will be the different image datasets that will be formed after accumulating all the pictures from the sources.
- The 3rd level will be the different ML models where the image datasets will be fed into. We will initially train these models with the help of some datasets that we have acquired.
- The 4th level will be the Analysis Level, where using computer vision, the images will be analysed. The different models will be using different ML algorithms, so we will compare them to get the best possible result.
- In the 5th and final levels, the probability values of the susceptibility of wildfires for a particular region will be fed back to the server.

## 4. RESULTS AND ANALYSIS

For the time being, we have developed a python program that can detect the temperature of each region of a given input image after analysing the extent of redness using different computer vision libraries like OpenCV.

If the following thermal image is given as input to the program, then after analysing, it will give us the temperature of the required regions of the image.


Fig 2. Input image


Fig 3. Output image

The temperature values are shown in degrees Fahrenheit. Each temperature value is mapped to a corresponding susceptibility value using different regression techniques that can be used for the prediction of forest fires. Besides, we will be adding a statistical-based approach to our current image-based approach that will include different non-linear factors like wind direction, wind speed, temperature variance, and so on. Since the factors are non-linear, we'll be using neural networks. By combining both these approaches, the results obtained would be more accurate.

## 5. CONCLUSION

In this model we have not used a single algorithm but have applied multiple machine learning models using different algorithms to fetch the most accurate and reliable result. The results obtained are more accurate than the models currently in use. A detailed analysis report on the likelihood of wildfires in various forests around the world would be generated. The results highlighted would help in efficient control of environmental pollution and disaster management.

## 6. REFERENCES


[1] Sriram Ganapathi Subramanian, Mark Crowley, “Using Spatial Reinforcement Learning to Build Forest Wildfire Dynamics Models from Satellite Images”, Front. ICT, 19 April 2018Sec. Environmental Informatics and Remote Sensing

[2] Ahmed M. Elshewey, Amira. A. Elsonbaty, ‘Forest Fires Detection Using Machine Learning Techniques’, Journal of Xi'an University of Architecture & Technology

[3] Suwei Yang, Massimo Lupascu, Kuldeep S. Meel, "Predicting Forest Fire Using Remote Sensing Data And Machine Learning", https://doi.org/10.48550/arXiv.2101.01975, Thirty-Fifth AAAI Conference on Artificial Intelligence (AAAI-21)

[4] Aditi Kansal, Yashwant Singh, Nagesh Kumar, Vandana Mohindru, “Detection of forest fires using machine learning technique: a perspective”, Published 1 December 2015, 2015 Third International Conference on Image Processing (ICIIP)

[5] Tejas Sathyamurthi, “Comparison of Machine Learning Algorithms to Predict the Occurrence of Forest Fires”, Poster originally presented at RISE:2020, hosted by the Center for Research Innovation.

[6] David A.Wood, “Prediction and data mining of burned areas of forestfires:Optimized data matching and mining algorithm providesvaluable insight”,Artificial Intelligence in Agriculture, Volume 5,2021, Pages 24-42; https://doi.org/10.1016/j.aiia.2021.01.004

[7] S. Natekar, S. Patil, A. Nair and S. Roychowdhury, "Forest Fire Predictionusing LSTM" 2021 2nd International Conference forEmerging Technology (INCET), 2021, pp.1-5,doi: 10.1109/INCET51464.2021.9456113.

## Biographies

**Indranil Basu** is a faculty member in the Dept. Of Electronics and Communication Engineering, at Institute of Engineering and Management, Kolkata. His research interests are in Pattern Recognition, Machine Learning and Deep Learning, for applications to various domains like Econometrics, and ML-based Control Systems, and their algorithms.

**Sayantan Sarkar** is currently pursuing his bachelor's degree in electronics and communication engineering from Institute of Engineering and Management, Kolkata. His research areas include machine learning, deep learning, and VLSI systems.

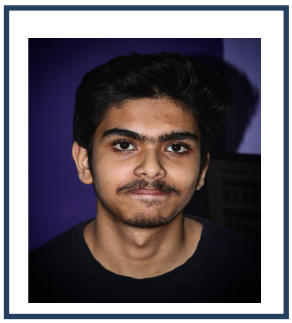

**Suswan Biswas** is currently pursuing his bachelor's degree in electronics and communication engineering from Institute of Engineering and Management, Kolkata. His research areas include mobile security and development, android manifest, mobile application development.

# *Studies on Programmable Metasurfaces Using Deep Learning Techniques*

***Trina Dwibedi[1], Sagnik Dutta[2], Debjit Paul[3], Raja Kumar[4], Gobinda Sen[5]***

[1-5] Department of Electronics and Communication Engineering, Institute of Engineering and Management, Kolkata, West Bengal, India

**Abstract**.

This study focuses on programmable metasurfaces that have shown great potential in shaping optical wavefronts in comparison to bulky geometric optics devices. These metasurfaces rely on meta-atoms, which are their fundamental building blocks and work by reflecting and scattering from their surfaces to achieve desired electromagnetic responses. The characterization of meta-atom structures with various physical and geometric parameters is a laborious process that demands a substantial amount of computational resources. This review investigates the use of a deep learning-based approach for meta-atom modeling, which can considerably reduce the time required for characterization while preserving accuracy. The suggested approach is founded on a convolutional neural network (CNN) architecture that can model meta-atoms with almost unrestricted 2D patterns, distinct lattice sizes, varying material refractive indices, and thicknesses. Furthermore, this method enables the prediction of a comprehensive spectrum response of a meta-atom within milliseconds, making it ideal for applications that necessitate rapid on-demand design and optimization of a meta-atom or metasurface.

**Keywords:** Programmable metasurface, meta-atom, deep learning, convolutional neural network, optimization.

## 1. INTRODUCTION

Metasurfaces are two-dimensional structures composed of subwavelength structures arranged in various shapes and distribution functions, which have been used in various applications such as spectrum filtering, holographic imaging, and polarization conversion [1], [2]–[4]. The subwavelength structures, known as meta-atoms, act like atoms or molecules of natural

materials and cause phase mutations when hit by electromagnetic waves. This allows metasurfaces to control the phase, amplitude, and polarization of reflected or transmitted waves in space. By changing the geometry of individual meta-atoms, desired responses can be achieved for complete control of light propagation. However, designing optimal meta-atom structures is a critical challenge due to the non-intuitive design process. Current design approaches include trial-and-error methods and optimization algorithms or deep neural networks (DNNs) based on inverse design methods.

Programmable metasurfaces, also called coding meta-surfaces, are a recent development that has the ability to manipulate electromagnetic waves in real-time [2], [5]-[7]. This is achieved by integrating active components, such as PIN diodes and varactors, into the metasurface elements. By changing the state of these components, the reflected wave's phase can be adjusted for each element, leading to complex spatial waveforms and more control over wave propagation. The quantization of element reflection phase into binary codes is another benefit of coding metasurfaces. For instance, the 1-bit code "0/1" indicates an element with two different reflection coefficients, while the 2-bit code "00/01/10/11" represents four additional states for the element reflection coefficients. Digital anisotropic coding metamaterials have been recently introduced as a means of controlling polarization with flexible and independent anisotropic coding sequences, enabling multiple functionalities with different polarizations. While most coding metasurfaces employ metallic subwavelength resonators at radio frequencies, there have been recent proposals for using high-permittivity dielectric materials that leverage Mie resonances, allowing for the possibility of all-dielectric coding metasurfaces for controlling electromagnetic waves. Compared to their metallic counterparts, dielectric resonator-based metasurfaces exhibit high efficiencies as they avoid the intrinsic non-radiative losses associated with metals.

This study utilizes deep learning methods to program a metasurface, which involves mastering internal rules from a vast amount of data. To achieve this, deep convolutional neural network is used to understand the coding techniques from conventional methods, such as the back-projection and nonlinear optimization approaches. By designing and training the neural network, we can create a data-driven routine for programming the metasurface.

## 2. METHODOLOGIES

**A. Back-Projection Method:** The back-projection (BP) method is a critical process for calculating the scattering pattern of a programmable metasurface comprise of M × N unit cells, based on the array-theory method. The back-projection method is capable of precisely forecasting the element phase when presented with a solitary beam direction. Nevertheless, its precision tends to diminish when confronted with intricate radiation pattern demands, like dual-beam directions with restrictions on the side-lobe levels. Calculating a coding matrix that satisfies all these limitations simultaneously can prove to be a difficult task, which is where optimization techniques come into play. By using optimization techniques, we can calculate the coding matrix, or discrete element phase, required in these situations [2].

**B. Nonlinear Optimization Approach:** In order to determine the coding matrix necessary for a particular scattering pattern of a metasurface, we must solve a non-linear and non-convex optimization problem. The primary goal of the optimization process is to minimize the discrepancy between the computed radiation pattern and the desired outcome, and this is typically accomplished through the use of stochastic nonlinear optimization algorithms such as genetic algorithm (GA) and particle swarm optimization (PSO). These algorithms repeatedly search for the optimal solution and are able to locate a global minimum that gives the metasurface optimal performance due to their randomness. This study employs GA to calculate the element codes required for programmable metasurfaces based on the desired scattering waveform. GA is a technique based on the principles of natural genetics [8] and has been extensively employed in electromagnetic and optical engineering to reduce the difference between the computed and desired beam pattern. Throughout the optimization process, the desired outcome can be transformed into the lower and upper pattern mask.

**C. Deep Learning Approach:** This study proposes the utilization of a fully convolutional neural network (ConvNet) based on deep learning to predict the coding matrix for the beam pattern requirement. The architecture of the proposed ConvNet is inspired by the VGG net [9] and comprises of eleven convolutional layers and five pooling layers.

The pooling layers introduce spatial pooling after the first, second, fourth, fifth, and sixth convolutional layers. The ConvNet architecture incorporates small-sized receptive fields that use 1×1, 3×3, 4×4, and 5×5 convolutional kernels. Using small convolutional kernels in layers 1 to 7 instead of relatively large kernels introduces more nonlinearity, making the ConvNet more discriminative. The ConvNet takes the required parameters of the scattering beam pattern as input and generates the coding matrix of the programmable metasurface that can produce scattering beam patterns that fulfill the input requirement as output. The generated scattering beam pattern should meet the requirement, and the ConvNet is trained to reduce the discrepancy between the computed and desired beam patterns.

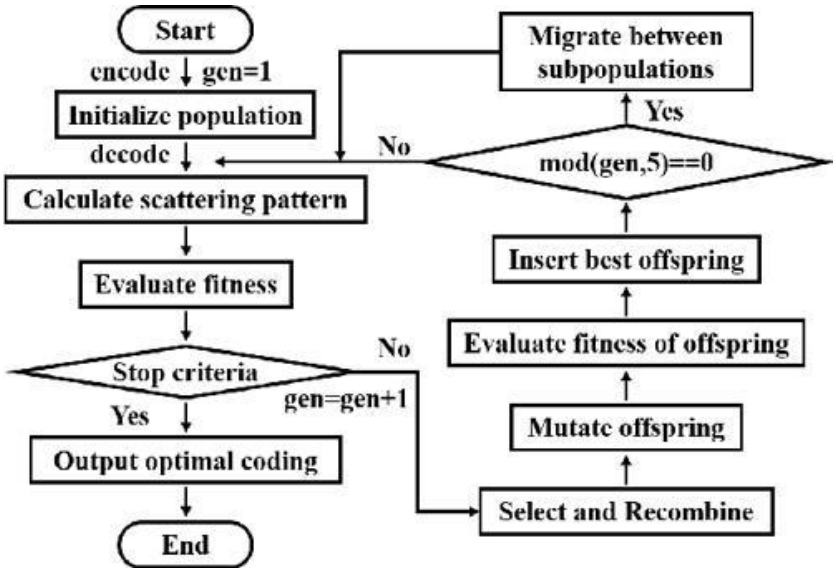


Fig.1 Multiple-population genetic algorithm flowchart.

## 3. CONCLUSION

This research investigates the potential of utilizing deep learning techniques to program metasurfaces for multi-beam steering. Employing a deep convolutional neural network, we can find the element codes to generate scattering patterns that meet given requirements. The findings indicate that this approach can compute coding matrices that produce beam patterns that are nearly identical, with computation taking only milliseconds. With precise control circuits, programmable metasurfaces can modulate EM waves in both the spatial and time domains, with applications in microwave, optical, and

acoustic engineering. Future studies aspire to expand this deep neural network to calculate more intricate wave scattering patterns. This research marks a preliminary foray into the application of deep learning techniques in electromagnetic engineering, which is usually dominated by the study and development of physical laws. With continued advancements in deep learning techniques, it is conceivable that machines will be able to "learn" from vast amounts of physical data and "comprehend" physical laws in specific boundary conditions. This literature review offers a persuasive illustration of how deep learning can be applied to calculate coding matrices for programmable metasurfaces in real-time. Furthermore, by augmenting the depth and scope of deep neural networks, we can substantially enhance their learning and generalization capabilities, which may further benefit their effectiveness in physical tasks such as this study.

## REFERENCES


1. N. I. Zheludev and Y. S. Kivshar, “From metamaterials to metadevices,” Nature Mater., vol. 11, no. 11, p. 917, 2012.
2. H. Yang et al., “A programmable metasurface with dynamic polarization, scattering and focusing control,” Sci. Rep., vol. 6, p. 35692, Oct. 2016.
3. C. L. Holloway, E. F. Kuester, J. A. Gordon, J. O’hara, J. Booth, and D. R. Smith, “An overview of the theory and applications of metasurfaces: The two-dimensional equivalents of metamaterials,” IEEE Antennas Propag. Mag., vol. 54, no. 2, pp. 10–35, Apr. 2012.
4. D. Lin, P. Fan, E. Hasman, and M. L. Brongersma, “Dielectric gradient metasurface optical elements,” Science, vol. 345, no. 6194, pp. 298–302, Jul. 2014.
5. T. J. Cui, M. Q. Qi, X. Wan, J. Zhao, and Q. Cheng, “Coding metamaterials, digital metamaterials, and programmable metamaterials,” Light Sci. Appl., vol. 3, no. 10, pp. e218 e218, Oct. 2014.
6. L. Li et al., “Electromagnetic reprogrammable coding-metasurface holograms,” Nature Commun., vol. 8, no. 1, p. 197, Aug. 2017.
7. B. Xie, K. Tang, H. Cheng, Z. Liu, S. Chen, and J. Tian, “Coding acoustic metasurfaces,” Adv. Mater., vol. 29, no. 6, Feb. 2017, Art. no. 1603507.
8. D. E. Golberg, Genetic Algorithms in Search, Optimization, and Machine Learning. Reading, MA, USA: Addison-Wesley, 1989.

9. K. Simonyan and A. Zisserman, “Very deep convolutional networks for large-scale image recognition,” 2014, arXiv:1409.1556. [Online]. Available: https://arxiv.org/abs/1409.1556

## Biographies:

**Trina Dwibedi**, currently pursuing the Bachelor's Degree in Electronics and Communication Engineering from Institute of Engineering and Management, Kolkata, 10th ICSE from Auxilium Convent School in 2017, and ISC (12th) from St. Francis Xavier School in 2019, respectively. Her research areas include deep learning, antennas, electromagnetic propagation and IoT design.

**Raja Kumar**, currently pursuing the Bachelor's Degree in Electronics and Communication Engineering from Institute of Engineering and Management, Kolkata, 10th CBSE from BDS Public School in 2017, and 12th RBSE from New public senior secondary school in 2019, respectively. His research areas include artificial intelligence, deep learning, machine learning, antennas and electromagnetic propagation.

**Debjit Paul**, currently pursuing the Bachelor's Degree in Electronics and Communication Engineering from Institute of Engineering and Management, Kolkata, 10th ICSE from Grace Ling Liang English School in 2017, and 12th ISC from Grace Ling Liang English School in 2019, respectively. His research areas include deep learning, machine learning, antennas, electromagnetic propagation, and data analytics.

Sagnik Dutta, currently pursuing the Bachelor's Degree in Electronics and Communication Engineering from Institute of Engineering and Management, Kolkata, 10th WBBSE from Narendrapur Ramkrishna Mission in 2017, and 12th CBSE from Bharatiya Vidya Bhavan in 2019, respectively. His research areas include artificial intelligence, deep learning, machine learning, antennas and electromagnetic propagation.

**Gobinda Sen** received his B.Tech degree in Electronics and communication engineering from the West Bengal University of Technology in 2010, and his M.Tech degree in Communication Engineering in 2013. He has obtained his Ph.D. (in Engineering) from the Electronics and Tele-Communication Engineering Department, Indian Institute of Engineering Science and Technology at Shibpur, Howrah, India in 2020. He is currently associated with the Electronics and Communication Engineering Department, Institute of Engineering and Management, Kolkata. His current research interests include metamaterial inspired structure for performance improvement of antenna, frequency selective surfaces, and microwave absorbers

# Instance Segmentation for Car Damage Detection with Mask-RCNN

**Rahul Rudra [1] , Praloy Sarker [2] , Farhan Hai Khan [3], Amartya Guha [4] and Romit Maity[5]**

*Institute of Engineering and Management[1-5], rahulrudra245@gmail.com, praloy40@gmail.com, njrfarhandasilva10@gmail.com, amartya.aa99@gmail.com, romitrmaity@gmail.com*

## Abstract

Detection of damage on cars is a task achievable by an image-based recognition method. This method of detection and calibration of exterior damage on a car would prove to be extremely useful for car insurers, car rentals, and car-repair services. Car damage reporting and penalty calculations have always been a challenging issue for licence companies and used car-selling companies. In this context, we put forward the application of deep learning and neural networks for building an architectural model of Mask R-CNN which can quantify the damaged surface area of the car. We use a deep feature prediction network for accurate instance segmentation of the damaged car parts. This study is an extension of business technologies to detect and quantify car scratches to address the problems faced by the used car industry and car rental companies. It will support businesses in eliminating middlemen and paving the way for a more objective system of pricing and insurance in the vehicle dealership market. For the proposed research a customised novel dataset was used consisting of images of damaged vehicles from multiple scenarios with precise labelling and annotation for image segmentation, and the Mask-RCNN model achieves a suitably high accuracy of over 93%.

**Keywords.** Mask-R CNN; Instance Segmentation; Image Recognition, Car Damage Detection, Deep Neural Networks, Object Detection, Machine Learning, Computer Vision, Deep Learning, Artificial Intelligence, Industry 5.0, Industrial Automation.

## 1. Introduction

For optimal damage detection for optimal damage detection and assessment, deep learning has been the state-of-the-art approach. For this study, the Mask-RCNN model detects the classified portion of the item and recognizes its location with severe damage. In the era of digitalization, machine vision has been introduced for a better solution by applying Automated Visual Inspection (AVI) [1] systems to have a quality output for eradication of defective products. we should follow machine-assembled auto inspection algorithms in industries to facilitate industrial automation.

For example, bright glass is one of them used on the outer sides and the threshold of the building in the wave of ultra-modern architecture [2]. The image-based surface scratches are created in the manufacturing process lines that lead to making weak materials. To have the uncorrupted products an engineer should be appointed for scratches and region-based Mask R-CNN ([1][2]) close to the surface of the bright glass items. Moreover, in the 21st-century of evolution, vehicular travel has increased exponentially, leading to hit-and-run cases and vehicle crashes. These haphazard road accidents can be detected for vital timed information to hospital authorities and can also be useful to insurance industries for vehicle rentals. They can further use the damage assessment to create reports for damage cost estimation with the vehicle model, base price, insurance premium values, and more to get a correct cost estimation approach. [4] Automated microscope camera scanning systems are needed to collect the image with scratches for building training and validation datasets for damage classification, this is essential for damage detection as manual humane approaches are often time taking and biased towards opinions and sometimes fueled by corrupted middlemen.

The prevailing market of the automobile industry directly leads to a substantial increase in the number of severe car accidents. With reference to the context, here we quantify deep-learning-based neural network architectural backbones with Mask-RCNN, viz., VGG-16 and VGG-19, for the inspection of car damage detection and its real-life assessment datasets [3]. With the increase of cars on the roads, the figures for car accidents have drastically increased. As a result, car damage is also increasing at an exponential rate [4]. So, it has become very important to identify car damages. We explore deep learning techniques for this purpose.

The proposed algorithm detects the damaged part of the car followed by its location and the intensity of the damage. An application of transfer learning for pre-trained VGG models over the Microsoft COCO (Common Objects in Context) [4] is being used to decrease the error rate of our proposed model. However, the characteristics classification of such phenomena is challenging due to scarcely visible damages and correlated inter-class mixing of damages with the vehicle body.

Many traditional computational-based machine-learning techniques were used to find out an automatic way out of the vehicle damage problem. Vehicle scratch detection is obtained by rendering the 3D CAD model of vehicles over the

damaged dataset. Several attempts were made to come up with a sustainable solution with the help of crown detection and satellite image processing. We used state-of-the-art object detection methods using CNN to train the damage detection model with our custom-labeled dataset [5]. Upon comparison with traditional target methods the target detection Mask-RCNN model architecture proves to be effective in case of small target detection [4], which is widely used in several domains - agriculture, construction, healthcare, and other fields.

The use of machine vision in case of identifying defects of the industrial finished goods is considered as surface defect inspection. These defects include but are not limited to scratches, pits, aberration, dust-sport, and stains. Manual inspection methods have been the traditional approaches and nowadays are not sufficient to achieve these purposes, on the other hand, the modern method of advanced computer vision is the only key method to identify the defects on the surface of the finished goods. Applying the automated visual inspection (AVI) [6] system we can easily recognize defective goods and remove them from the production scheme. Automated Visual Inspection (AVI) is itself the practised-hand inspector to solve all problems relating to surface defects inspection. The world's leading economic giants like the USA, India, Japan, Europe, and China have created a vast market all over the richest countries to perform their achievements using machine-based technology that was used for advanced deep learning [1, 20]. The system has also been upgraded such that it has a continued process for auto-detection and auto-removal as well. Instance segmentation is the science of image classification where each pixel of the image is assigned a class label. In other words, instance segmentation is the task of detecting and delineating each distinct object of interest appearing in an image. Mask R-CNN is the current state-of-the-art technology [8] for highly accurate mask detection for RoIs (Region of Interest). In this paper, we train the M-RCNN model to train and detect effective damage areas in an image/video [7]. This paper also presents a business extension of existing technologies to detect car scratches and quantify damages, in order to tackle the problems faced by the used car industry, traffic control system[17] and car rental companies for the automation of penalties that occurred due to these accidents.

Previous attempts at claims processing automation have been done using various approaches which have provided the bounding boxes for the scratches. But, due to the positional properties of vehicular damages, these detected bounding boxes do not cover the exact portions of the detected scratches and rather build up rectangles around them, which isn't feasible for calculating accurate damage costs. This research maps the damages to a multipoint feature polygon with various dynamic shapes rather than static ones.

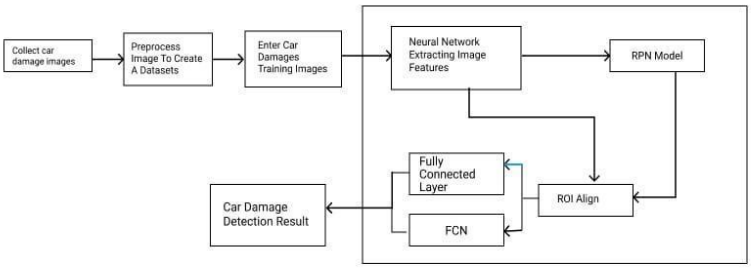


Fig.1: Car Damage Detection-Segmentation Framework

The image of the damaged part of the car is selected and collected according to the need and the data is marked with the VGG Image Annotator (VIA) tool from the Visual Geometry Group and converted into the widely used JavaScript Object Notation (JSON)[19] format which is further divided into a training set and test set with an 80%: 20% (762:191 images) split ratio with a total of 953 images obtained from the internet and labelled by the team. The algorithm here works in two ways. Firstly, the region proposal network scans and generates the Region of Interest (RoI). The second stage processes the proposal from the network and generates a bounding box and mask based on the class confidence. The car damage detection and segmentation system based upon this piece of research are presented in Fig.1.

### 1.1. Algorithmic Architectural Workflow:

(1) Pass an image for processing to a pre-trained ResNet50 + FPN (Feature Pyramid Network) network model to extract features and find compatible feature mappings.

(2) The feature map acquires a large number of candidate frames via RPN and uses a SoftMax separator to create dual front and rear editing, using these frames to determine a more accurate position of the candidate's frames. The information and filtering part of the ROI with non-high-pressure compression is performed next.

(3) Feature map and final ROI remaining in the RoIAlign layer, so that each ROI produces a feature map of a fixed size.

(4) Finally, flow flows through two branches, one branch entering a fully integrated layer of layout and deceleration and the other into a full network of pixel separation variables.

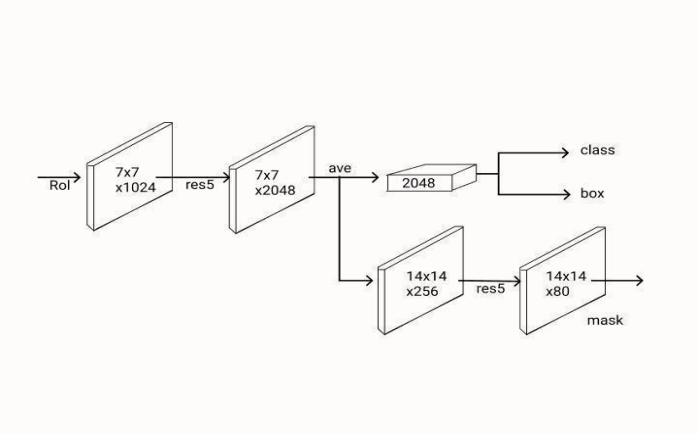


Fig 2: Mask Region-based CNN: M-RCNN Model built on the Faster-RCNN model architecture and used the Res-Net C4 map features

## 2. Machine Learning Pipeline

The ML Pipeline consists of four categories: Data Collection and Annotation, Network Training, Model Validation, and Model Deployment. Firstly, the data is collected for training the neural network, then we label the data using VGG Image Annotator (VIA) [14]) and the network is trained using TensorFlow and Keras Framework on Python with NVIDIA GPU Accelerations[18]. The source implementation is modified from Facebook AI and Research Team's Matterport Implementation . We then compute the model accuracy and finally, we deploy the model using Flask.

## 3. Detailed Methodology

### 3.1. Dataset Collection and Annotation Creation

As there is no publicly available data set for car damages by category, we have created our own novel dataset that includes images for different types of car damage. We consider seven types of damage often referred to as bump rot, door hammer, glass shatter, broken headlamp, broken tail lamp, scratch and crush in our image set for adding variance to the data. In addition, we also collected photos of the un-damaged cars for better training and to avoid false positives via overfitting. Also, two sets of classes were divided and labeled, which were the "background" and "scratch" to perform binary pixel-wise classification.

The proposed architecture constitutes deep learning with neural networks to mask and detect damages discovered on a vehicle's body. We use the state-of-the-art Mask-RCNN model to train our own custom model and get 93% accurate results to our predictions.

For this manuscript, we used the dataset from Kaggle [12, 21]. After performing some basic data cleaning, we annotated the image using the official VGG Image Annotator (VIA Tool) [14]. This annotator gives us our JSON (JavaScript Object Notation) file, which we use later for training and ground truth (GT) comparison.

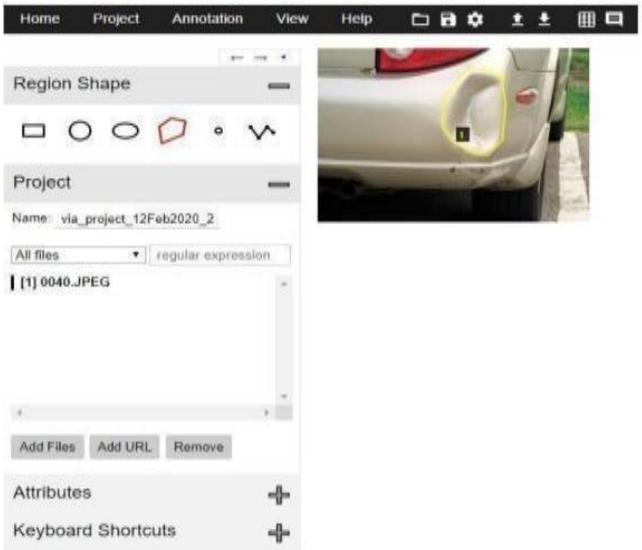

### 3.2. Data Annotation

After collecting the images, annotating them is the next step. The annotations will clearly demarcate the area of damage in each training image, which will help the model learn when training. The machine learning model requires the images in the training dataset to be annotated, which is to have the region of damage in an image identified and the boundary of the damaged area marked accurately. A sample example of an annotation from the used VGG Image Annotator (VIA), is shown in Fig.3. The annotations of the images are then stored in JSON format in the directory of the dataset and will be used while training.

### 3.3. Import dataset and Visualization

With the dataset and the annotations ready, the next step involves Data Wrangling and Data Visualization. Our version of Mask R-CNN is customised and built on top of the Matterport Mask RCNN GitHub repository from the Facebook AI and Research Team (FAIR). Images and annotations from the dataset will be loaded using a custom Data Loader class function with a configuration for training and inferences. Visualisation of Input (Images and Masks) can give us a view of how the mask would look when placed on the image and hence how the model would see it, also the variation in the data is important to prevent model overfitting.

In order to handle bounding boxes more consistently, it is better to compute the coordinates from the damage mask for the car images, instead of using these coordinates as a part of the input dataset.

### 3.4. Visualisation of Input (Images and Masks)

In Fig 4, we have taken five input images and have plotted the image along with their damage masks. Visualisations approve whether the annotation was done correctly or not.

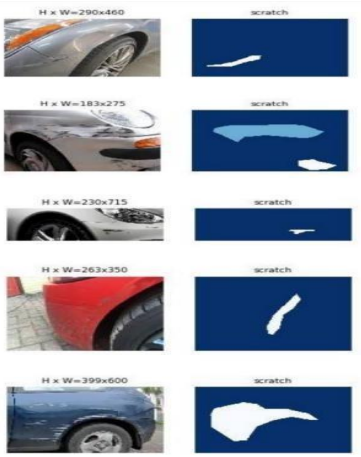


Fig.4 Plot of a subset from the full training dataset with their damage mask, image height included.

### 3.5. Bounding Box (BB) with annotated damage mask for typical car images

With the bounding box being computed from the damage mask and not passed as input, we can see that the coordinates of the bounding box give us a better estimation of the damaged area. This is shown in Fig 5, where it can be seen that the bounding box completely encloses the damage mask and hence gives us an idea that computing the coordinates by using this method will make our methodology robust and consistent over multiple images.

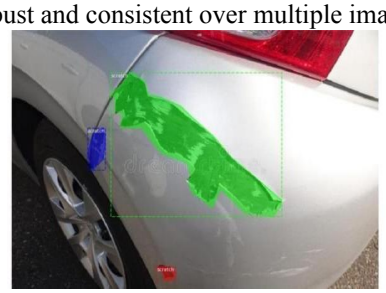

Fig.5 Damage mask on the car image with bounding boxes

### 3.6. Training model

Data was converted from VIA Image Annotator to valid COCO Annotation formats. Model heads were trained for 50 epochs and Fine Tuning of the model was performed for another 50 epochs. For training the model heads, the other weights are frozen and only the final layers are trained for the custom classes for faster convergence rates, whereas fine-tuning performs model optimization by modifying overall weights with slight adjustments. Both Dice Loss and RoI loss were chosen as the loss metrics for the image segmentation task. The model was trained with an initial learning rate of 0.01. The model was finally evaluated on the Intersection Over Union Score (IoU) for better accuracy and faster convergence,

pre-trained weights from the COCO dataset were used, instead of training the model from scratch using the Adam Optimizer, and ReduceLROnPlateau with patience of 15 epochs.

Data was split in an 80-20 ratio for training and testing. For instance, segmentation, the Mask-RCNN model was used. The losses used are explained below:

**Dice Loss:**

The Dice coefficient (DSC) is a measure of how closely two sets overlap. For instance, if two sets A and B perfectly overlap, DSC reaches its maximum value of 1. Otherwise, DSC begins to decline, eventually reaching 0 if the two sets do not overlap at all as referred in the next image [i].

$$D = \frac{2\sum_i^N p_i g_i}{\sum_i^N p_i^2 + \sum_i^N g_i^2}$$

**Intersection over Union:**

IoU is the area of overlap between the predicted segmentation and the ground truth divided by the area of union between the predicted segmentation and the ground truth, as shown on the image[ii] to the left.

### 3.7. Model Validation

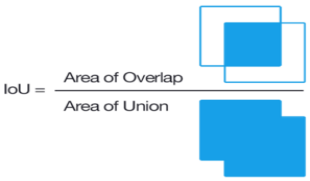


The model weights are inspected by plotting the variance in the weights. Link last training checkpoint for model for validation. This step performs a sanity check if your weights and biases are properly distributed. Perform a sanity check if weights and biases are properly distributed.

| Model | Precision | Recall | Accuracy without augmentation | Accuracy with augmentation |
|---|---|---|---|---|
| [22] VGG16 | 0.94 | 0.94 | 94.56 | 94.56 |
| [22] VGG19 | 0.91 | 0.91 | 94.57 | 95.22 |
| [23] Inception | 0.6175 | 0.5671 | 71.82 | 71.50 |
| [23] Alexnet | 0.6142 | 0.5809 | 70.85 | 73.91 |
| [23] Resnet | 0.8438 | 0.8110 | 88.24 | 87.92 |
| [24] VGG19 | 0.9220 | 0.9080 | 93.20 | 94.90 |
| [24] Resnet50 | 0.928 | 0.922 | 89.58 | 90.26 |

**Table 1**

The following Table 1 we can understand how precise a model is out of those predicted positives, and how many of them are actual positives. Precision is a good measure to determine accuracy only when the cost of negative is high. Recall actually measures how many of the actual positives a model captures by labelling it as positive. Applying the same understanding, we know that recall will be the model metric that we use to select our best model when a high value is associated with a positive. The model accuracy depends on precision and recall value. Accuracy can tell immediately if a model is being trained properly and how it can work in general. All performance accuracy of VGG19 is better than VGG16 even if its values of matrices are not larger than VGG16. Inception deep convoluted architecture, also known as GoogleNet, was developed by Google. The model consists of a basic unit and 'inception cell' where the performance of a series of convolutions on different scales and subsequently combine the result. Alexnet is one of the deepest convents designed to deal with complex scenes and ImageNet data classification work. The network was very similar to LeNet, but deeper, large and characteristic convoluted layers piled on top of each other. Per the low overfitting, AlexNet uses another technique called dropout. Unlike traditional sequential network architectures such as AlexNet, Overfit, and VGG, a form instead of ResNet of ''foreign architecture'' which relies on micro-architecture modules.

### 3.8. Prediction

Inspect model by performing prediction on test and validation to test the accuracy. Prediction on test image.

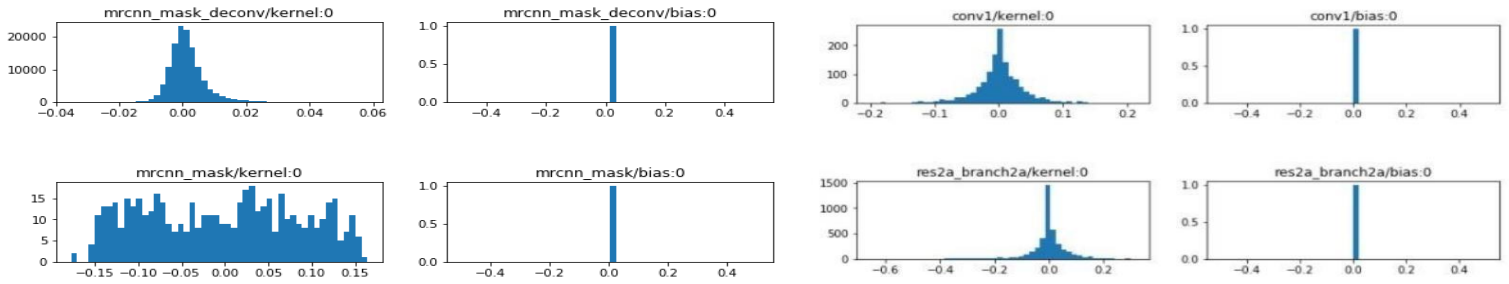

**Damage Localization**

With the same procedure, the authors have trained the dataset in such a way as to localize the damaged part. For each pixel in the test image,100 x 100 size is cropped all around then 224x224 predicts the background of the class. Damage is predicted by consideration of the fact if the particle exceeds a certain limit.

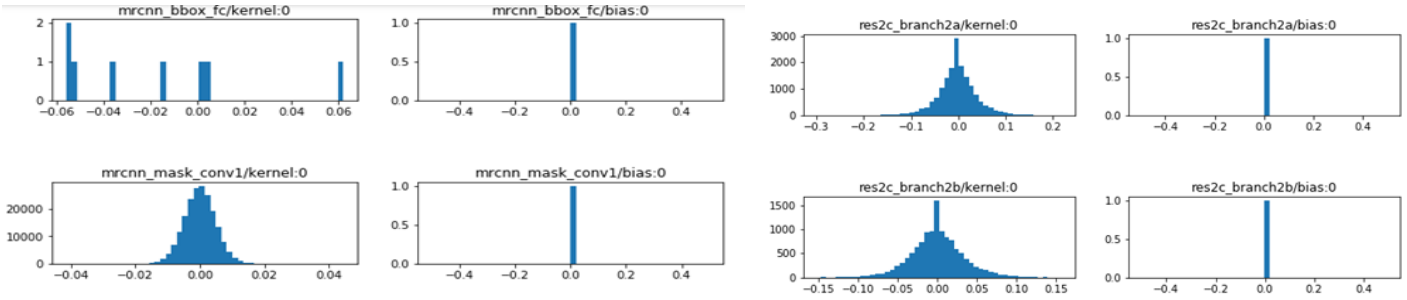


## 4. Business Implementation and Road Ahead

Car rental companies can install such proposed infrastructure architecture with the help of high-resolution cameras at different locations at particular angles for capturing standardized images of different body parts of the car, which can detect all possible exterior damages in the car. This software application can be advanced as a Mobile API which can further ease the verification process after detection and mask filter feature for the damaged car. This system of approach will be helpful for the rental evaluators, and resolution personnel in calibrating the relative damage area of the car. The best thing here is the users do not have to collect too many images or annotations as the architectural model training starts from trained weights('coco'), hence the time complexity is very less. This software technology can further be extended into detection systems of different types of visible car damages and its respective faults. The demand for improved customer service and improved experience is now so universal that customers are spoiled for choice. Therefore, it is not at all surprising. From booking a rental car to re-submitting a ticket, customers want a seamless experience at every stage. One can only make it faster and more responsive through automated technology.In case of damage here should be considered some points they are the location of damages, patterns of damages & types of damages to the car. The detection system of the damage must be developed for better information for the customers or users relating to rental cars. There is a higher need for automation to restore confidence in the car rental industry. Fortunately, the automation of car inspections and car damage assessments with AI makes fast, accurate, and data-driven deductions possible. Most importantly, these AI inspections are backed by documentary evidence, which improves reliability.

## 5. Conclusion Further Improvements

Our model performs quite well on random images from the Internet and generalises well for the scratches. This summarises that the model is trained well and has learned the scratch detection algorithm efficiently. Since our dataset (2400 images) is much smaller than the big AI datasets, viz., COCO (1,20,000 images), we do not expect to get better results from our model using the same approach. However, pre-segmentation of vehicles and then damage detection could be an improvement in the algorithm. The proposed algorithm relies on two steps: a pre-processing step, performed during the scanning process, and a post-processing step, where, using the information from the pre-processing step, defects can be detected with ease. And considering the analysis of the results, a claim can be made that the benefit from training on larger datasets will only magnify the performance of the model. Currently more and more research is being done towards creating deeper and different convolutional networks, which enables it to be used to address an increasing number of scenarios. As such, future work could focus on the application of similar models for the detection of imperfections on objects in other domains.

## 6. Acknowledgement

We'd like to thank Mr. Arjun Dutta, Product Architect at IQApex Labs for sponsoring us with the project and other necessary information regarding the design and development of the algorithm and conceptualizing the whole manuscript and our institution and professors for the opportunity and for guiding the way.

## 7. References

[1] Recent advances in surface defect inspection of industrial products using deep learning techniques. The International Journal of Advanced Manufacturing Technology (2021) 113:35–58. https://doi.org/10.1007/s00170-021-06592-8

[2] Image-based surface scratch detection on architectural glass panels using a deep learning approach. https://doi.org/10.1016/j.conbuildmat.2021.122717

[3] Phyu Mar Kyu and Kuntpong Woraratpanya. S.: Car Damage Detection and Classification. In: Proceedings of International Conference on Advances in Information Technology (IAIT2020), July 1-3, 2020, Bangkok, Thailand. ACM, New York, NY, USA, 6 pages. https://doi.org/10.1145/3406601.3406651

[4] Ranjodh Singh; Meghna P. Ayyar; Tata Venkata Sri Pavan; Sandeep Gosain; Rajiv Ratn Shah. S .: Automating Car Insurance Claims Using Deep Learning Techniques. In: 2019 IEEE Fifth International Conference on Multimedia Big Data (BigMM). https://10.1109/BigMM.2019.00-25

[5] Hiroya Maeda, Yoshihide Sekimoto, Toshikazu Seto, Takehiro Kashiyama, Hir Omata. S.: Road Damage Detection and Classification Using Deep Neural Networks with Smartphone Images, First published: 30 June 2018 https://doi.org/10.1111/mice.12387

[6] A generalized model for scratch detection. IEEE Transactions on Image Processin (Volume: 13, Issue: 1, Jan. 2004). DOI: 10.1109/TIP.2003.817231

[7] Car Damage Detection and Analysis Using Deep Learning Algorithms for Automotive. International Journal of Scientific Research Engineering Trends Volume 5, Issue 6, Nov-Dec-2019, ISSN (Online): 2395-566X

[8] Assessing Car Damage with Convolutional Neural Networks. 2021 International Conference on Communication information and Computing Technology(ICCICT) | 978-1-6654-0430-3/21/31.002021*IEEE* | *DOI:*10.1109/*ICCICT*50803.2021.9510069

[9] 2017 16th IEEE International Conference on Machine Learning and Applications (ICMLA). DOI: 10.1109/ICMLA.2017.0-179

[10] Hermans, L; Van der Auweraer, H; Mevel, L. S.: Health monitoring and Detection of a fatigue problem of a sports car, In: IMAC - PROCEEDINGS OF THE 17TH INTER- NATIONAL MODAL ANALYSIS CONFERENCE, VOLS I AND II, 3727 Pages: 42 - 48, lirias.kuleuven.be/875533?limo=0

[11] Blogs - Towards Data Science (Medium) Analytics Vidhya, Sourish Dey,Priya Dwivedi, @AnalyticsVidhya , analyticsvidhya.com/blog/2018/07/building-mask r-cnn-model-detectingdamagecars-python/,@Medium, towardsdatascience.com/cnn-application-detecting-car-exterior damage-full implementable-code-1b205e3cb48c

[12] Car damage detection - Kaggle Dataset, Anuj Shah (@anujms), Dataset- Car damage detection, kaggle.com/anujms/car-damage-detection

[13] An Expert System to Detect Car Damage by using CART Method. Prof. Dr. IKetut Gede Darma Putra, S.Kom., M.T., I KETUT GEDE DARMA PUTRA and Ni Made Ika Marini Mandenni, ST.,M.Kom, NI MADE IKA MARINI MANDENNI (2014) An Expert System to Detect Car Damage by using CART Method. Journal of Theoretical and Applied Information Technology (JATIT), 66 (3). ISSN 1992-8645. https://erepo.unud.ac.id/id/eprint/9794

[14] Abhisek Dutta; Andrew Zisserman, S.: The VIA Annotation Software for Images, Audio and Video, In: MM '19: Proceedings of the 27th ACM International Conference on Multimedia, pp. 2276–2279. https://doi.org/10.1145/3343031.3350535

[15] Automatic Paint Defect Detection and Classification of Car Body. Parisa Ka-mani, Elaheh Noursadeghi, Ahmad Afshar, Farzad Towhidkhah. 2011 7th Iranian Conference on Machine Vision and Image Processing. DOI:10.1109/IranianMVIP.2011.6121575

[16] Scratch Detection in Cars Using a Convolutional Neural Network by Means of Transfer Learning. International Journal of Applied Engineering Research ISSN

0973-4562 Volume 13, Number 16 (2018) pp. 12976-12982 © Research India Publications. http://www.ripublication.com

[17] A. Dutta et al., "Intelligent Traffic Control System: Towards Smart City," 2019 IEEE 10th Annual Information Technology, Electronics and Mobile Communication Conference (IEMCON), 2019, pp. 1124-1129, doi:10.1109/IEMCON.2019.8936188.

[18] Mask R-CNN Keras Implementation (@matterport), Waleed Abdulla, Mask RCNN Implementation, github.com/matterport/Mask*R*CNN

[19] E. Rathje and M. Crawford, S.: Using high resolution satellite imagery to detect damage from the 2003 northern Algeria earthquake, In: 13th World Conference on Earthquake Engineering, August 2004, pp. 1–6.

[20] Ayantika Dey and Darothi Baidhya, *Development of Intelligent Car Parking System*, vol. 1, no. 4, 2020, ISSN 2689-484X.

[21] A.Dutta et al., Farhan Hai Khan,COVID-19: Detailed Analytics & Predictive Modelling using Deep Learning, DOI: 10.32628/IJSRST207517

## Biographies

**Rahul Rudra** is currently pursuing bachelor's degree in computer science and engineering from the Institute of Engineering and Management, Kolkata, under MAKAUT. His interests and research areas include cyber security and machine learning

**Romit Maity** obtained his higher secondary education from DAV Public School and is currently pursuing a bachelor's degree in computer science and engineering from the Institute of Engineering and Management. His interests and research areas include deep learning, artificial intelligence and bioengineering.

**Praloy Sarker** obtained his higher secondary education from Ispahani Public School and College, Cumilla, Bangladesh and is currently pursuing a bachelor's degree in Information Technology from the Institute of Engineering and Management. His interests and research areas include deep learning and artificial intelligence.

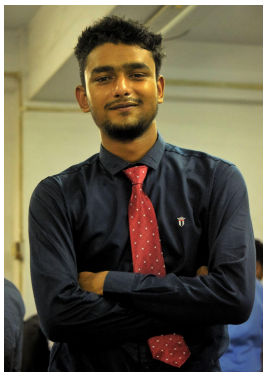

**Farhan Hai Khan** is a Software Engineer and an Independent Researcher with experience working wth competitive teams and emerging startups. His background in Artificial Intelligence, Machine Learning, Computer Vision & Deep Learning inform his technical and scientific approaches.He received the Director's Award for the Best Scientific Mind while pursueing Electrical Engineering from IEM Kolkata. He has also published research papers, journals & articles in reputed press such as IEEE, Springer, Taylor & Francis etc.

# Malignant Tumor Detection Performance Analysis using Convolutional Neural Networks and SVM Classifier Model

**Avik Pathak, Suswan Biswas, Koushani Bhattacharyya, Aparna Biswas,**

**Arindam Chakraborty , Soham Kanti Bishnu**

*Department of Electronics and Communication Engineering*

*Institute of Engineering and Management, Kolkata*

## Abstract.

An unusual mass of tissue in which some cells multiply and grow uncontrollably is called brain tumor. It starts growing inside the skull and interposes with the regular functioning of the brain. Brain tumors can be detected at an early stage using MRI or CT-scanned images when it is small. Early detection is very necessary as the tumor can possibly result in cancer. Tumor detection and removal is one medical issue that still remains challenging in the field of biomedicine as it is prone to human errors. We have tried to understand the effectivity in successfully detecting a malignant tumor through the implementation of Convolutional Neural Network using Binary Cross-Entropy and Categorical Cross-Entropy as loss functions along with SVM Classifiers and Logistic Regression. We do hope that our performance analysis helps other researchers and ML engineers to see the constraints and advantages of using these models for accurate prediction.

**Keywords**. Tumor detection, Convolutional Neural Network, Binary Cross-Entropy, Categorical Cross-Entropy, SVM Classifiers, Logistic Regression.

## 1. INTRODUCTION

There has been and will be extensive research on the Tumour Malignancy analysis from MRI reports and they strive to develop a model that most accurately predicts the malignancy and the tendency of a given tumor to be malignant in the future. The research developed by Boucif Beddad, Kaddour Hachemi, and Sundarapandian Vaidyanathan in the paper named 'Design and implementation of a new cooperative approach to brain tumor identification from MRI images'[10] have quite extensively treaded on this field and has given us some really helpful insights to develop the analysis and implement few newer techniques to get some unique insights into the project. Although the proposed segmentation algorithm was not directly used to train our datasets, the modeling techniques we used were analogous to the model we wanted to implement.

## 2. METHODOLOGY

### *2.1. Deriving Raw Data:*

The Datasets used in the analysis mainly consisted of MRI scan reports of 1000 images, both malignant and non-malignant.In SVC we reduced the pixels to 200 X 200 while in CNN , 64 X 64 image was used .

### *2.2. Data Preprocessing:*

The raw data that we have first needs to be converted to some numeric values such that we can perform certain operations on it. To do this the very fundamental step that needs to be performed is Importing the required libraries for the operations.

### *2.3. Dataset Operations :*

In machine learning, we have some raw data like images in this case which have a unique format of .jpg. We can't perform any operation on the data with this format as a machine understands only 1's and 0's, on a broader scale we may refer to them as elementary mathematical operations.

### *2.4. Splitting the Data:*

To analyze the performance of an algorithm, this is an extremely important technique that is used to check the model's accuracy over an unknown dataset that is extracted from the raw data. original dataset. A conventional flow chart of implementing train_test_split over a model would look like this:

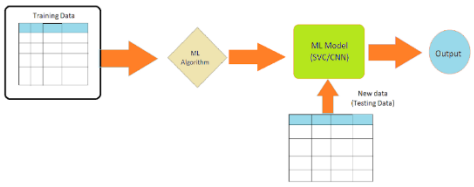


Generally, We refer to the raw training data as x_Train and The data label is stored in y_train. The testing data is referred to as x_test and the label of x_test is y_test.

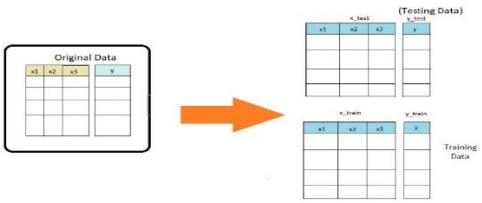


### *2.5. Feature Scaling of the Data:*

Feature Scaling is primarily used to remove the independent variables in the data and normalize the data such that we can apply mathematical methods to fit the data in an ML Algorithm.

## 3. OBSERVATIONS:

Coming to the most crucial part of our discussion, we have tried to observe how the Tumor detection model would perform as it is passed through SVC, simple Logistic Regression and finally, neural networks with a variation in loss and activation functions.

### *3.1. Logistic Regression Performance:*

**Evaluation**

```
In [18]: print("Training Score",lg.score(pca_train,ytrain))
         print("Testing Score", lg.score(pca_test,ytest))

         Training Score 1.0
         Testing Score 0.9591836734693877
```

As we can see, the logistic regression model shows a training score of 1 which means the data perfectly fit the curve. The testing score however is not good enough (as would be proved by the other models ).

### *3.2. Support Vector Machine(SVM) Performance Analysis:*

The model fits the data quite well and generates praiseworthy output, both in testing data and unknown data.

```
In [19]: print("Training Score",sv.score(pca_train,ytrain))
         print("Testing Score", sv.score(pca_test,ytest))

         Training Score 0.9938587512794268
         Testing Score 0.963265306122449
```

The training score, in this case, seems to be less than linear regression but the testing score improves from the previous model. Thus, when using known data, both models work perfectly.

For the known Set of “No Tumor” and “Malignant Tumour”

The result is:

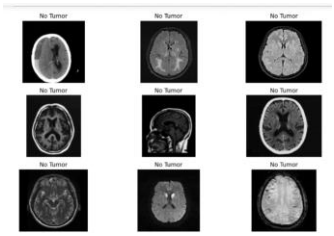

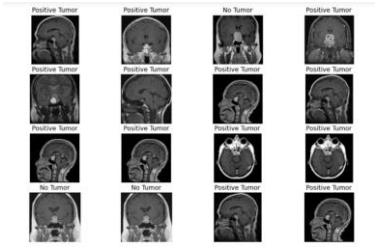

As we can see, in this model, if we take a probability of success observing this graph. It would roughly come around to 1316 which is quite good. Yet, can we do better is what all

ML engineers should be asking themselves. Here comes our last study, CNN (Convolutional Neural network).

### *3.3. Convolutional Neural Network:*

In CNN, accuracy score comes to be:

```
score, acc = model.evaluate(xtest, ytest,verbose=1, batch_size= 16)
print('test accuracy:', acc)

predict_x=model.predict(xtest)
classes_x=np.argmax(predict_x,axis=1)
print(classes_x)
```

```
16/16 [==============================] - 0s 16ms/step - loss: 0.0206 - accuracy: 0.9918
test accuracy: 0.9918367266654968
```

An extremely high-test score over the training data.The curves of accuracy vs epochs and loss vs epochs

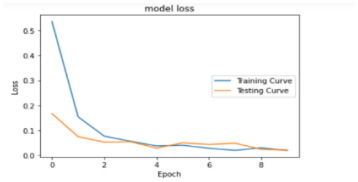


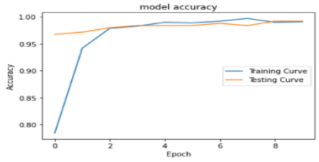


Let's now arrive at the observation of its performance with the unknown dataset.

With the 'No Tumor " dataset and "Malignant Tumor" dataset :

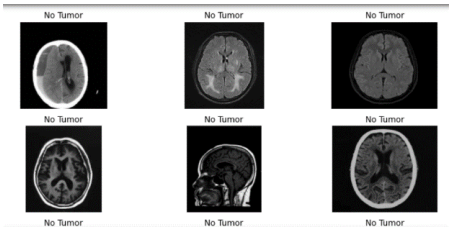


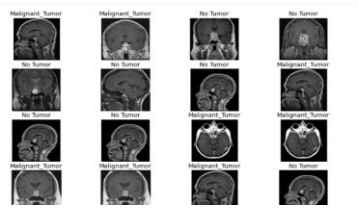

The data works fine.Quite interestingly, we find here that the probability of success over this data is just 816 which is just 0.5 which is really bad.Still, an interesting observation as it is. SVC remains to be leading in terms of success over unknown data, although it trails the neural network in terms of its accuracy score.

### *3.4. Categorical Cross Entropy:*

The Accuracy vs Epoch Curve and Loss vs Epoch Curve :

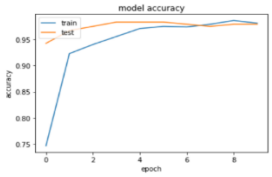


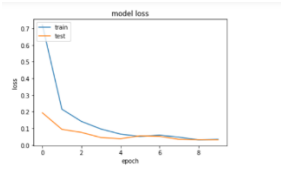


Accuracy with increasing epoch values is farely stable .Loss of the function is really less with increasing epochs.The probability of success comes out to be 816 again which is similar to the binary cross entropy result. It is pertinent to see that the accuracy score of the model over the training dataset was 0.979 which was less than that of binary cross-entropy.

## 4. FUTURE SCOPE

Improved models with higher accuracy may be developed using different machine-learning models.Our existing model does not take into account the age, gender, and prior medical history of a patient for detection. Developing a universal model to detect all kinds of tumors in its earliest stage will ensure the earliest detection of disorders which in turn will reduce the chances of spreading malignancy to other parts of the body.

## 5. CONCLUSION

In this paper we discussed the design of a model which shows if there are any traces of brain tumors using Magnetic Resonance Imaging (MRI) scans. The model performs segmentation of MRI scan images and pinpoints if there are any traces of tumor in the brain. From comparative analysis, it is clear that Deep Learning techniques and algorithms have great power and ability to handle large amounts of data.

## 6. REFERENCES

[1] Jahnavi Athalur., Application of Edge Detection for Brain Tumor Detection

[2] Dr. Navneet Singh Sikarwar., Image Processing Techniques for Brain Tumor Detection: A Review

[3] Hao Dong, Guang Yang, Fangde Liu, Yuanhan Mo & Yike Guo., Automatic Brain Tumor Detection and Segmentation Using U-Net Based Fully Convolutional Networks

[4] JavariaAmin, MuhammadSharif, MudassarRaza, TanzilaSaba, Muhammad AlmasAnjum ., Brain tumor detection using statistical and machine learning method

[5] Pankaj Sapra, Rupinderpal Singh, Shivani Khurana., Brain Tumor Detection Using Neural Network

[6] Agarap, Abien Fred. (2018). Deep Learning using Rectified Linear Units (ReLU)

[7] Huang, Shujun et al. “Applications of Support Vector Machine (SVM) Learning in Cancer Genomics.” Cancer genomics & proteomics vol. 15,1 (2018): 41-51. doi:10.21873/cgp.20063

[8] Sperandei, Sandro. “Understanding logistic regression analysis.” Biochemia medica vol. 24,1 12-8. 15 Feb. 2014, doi:10.11613/BM.2014.003

[9] Heny Pratiwi et al 2020 J. Phys.: Conf. Ser. 1471 012010

[10] “Design and implementation of a new cooperative approach to brain tumour identification from MRI images” Boucif Beddad, Kaddour Hachemi and Sundarapandian Vaidyanathan 10.1504/IJCAT.2019.097113 [doi]
[11] Maria Nazir, Sadia Shakil, Khurram Khurshid,
Role of deep learning in brain tumor detection and classification (2015 to 2020): A review, Computerized Medical Imaging and Graphics, Volume 91,2021,101940, ISSN 0895-6111
[12] Bhagya Patil, Vishwanath Barkpalli. A Perspective View of Cotton Leaf Image Classification Using Machine Learning Algorithms Using WEKA, 13 May 2021,
PREPRINT (Version 1) available at Research Square [https://doi.org/10.21203/rs.3.rs-502091/v1]
[13] KRajesh Babu et al 2021 J. Phys.: Conf. Ser. 1804 012174
[14] Computational Intelligence in Pattern Recognition,2020, Volume 1120,ISBN : 978-981-15-2448-6

## Biographies

**Avik Pathak** received the bachelor's degree in electronics and communication engineering from Institute of Engineering and Management in 2024 His research areas include deep learning, Optimizing Machine Learning/AI models ,

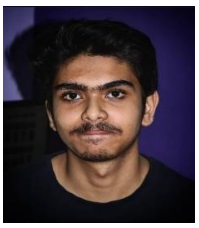

**Suswan Biswas** received the bachelor's degree in electronics and communication engineering from Institute of Engineering and Management in 2024 His research areas include mobile security and development, android manifest, mobile application development.

**Koushani Bhattacharya** received the bachelor's degree in electronics and communication engineering from Institute of Engineering and Management in 2024 Her research areas include blockchain and web3, web application development.

**Aparna Biswas** is presently a Scientific Officer in the faculty of Electronics and communication engineering at Institute of Engineering and Management(IEM) In Kolkata,India.

Mr. Arindam Chakraborty is currently an assistant professor at the Institute of Engineering and Management, Kolkata. He obtained his M. Tech. in Microelectronics and VLSI Design from the Jadavpur University – Kolkata, India. Mr. Chakraborty has published a number of papers in research Journals and chapters in books, and participated in different reputed conferences on solid state lighting, VLSI and IOT. His areas of interest include Solid State Lighting, Image Processing, Embedded System Design and IOT..

Soham Kanti Bishnu is presently is currently an Assistant Professor in the faculty of Electronics and communication engineering at Institute of Engineering & Management (IEM) in Kolkata, India. Prior to his recent appointment at IEM, he served as a researcher in CSIR-Central Glass and Ceramic Research Institute (CSIR-CGCRI).

# Predictive Analytics for Financial Forecasting – Past and Present

ParthaSarathi Paul
Department of Computer Science and Engineering
University of Engineering and Management, Kolkata
parthaspaul2014@gmail.com

Dr. Rajendrani Mukherjee
Department of Computer Science and Engineering
University of Engineering and Management, Kolkata
rajendrani.mukherjee@uem.edu.in

## Abstract.

Predicting prices of shares is an intractable problem and has drawn the attention of investors and computer scientists. This review paper explores machine learning techniques that have been used for the purpose of building effective share price prediction model, in the last decade or so. Various linear and non-linear machine learning algorithms, neural network structures, data sources and commonly used metrics for evaluation of results in the research papers have been categorized. The implementation methods and reproducibility have been studied. A summary of the technical papers is prepared as well as a brief description of each paper is included. The study has been carried out to investigate possibility of making profit through day trading on the stock market using relatively low computational power available to retail investors.

**Keywords**. Stock price prediction, LSTM, Neural Network

## 1. INTRODUCTION

The term stock market is used for exchanges where publicly held company shares are bought and sold. There are defined set of regulations which govern the operation of stock exchanges. The stock market allows buyers and sellers to meet, interact and transact. Stock market allows price discovery of shares and serve as a bell weather of overall economy. It ensures fair price, liquidity and transparency to participants' competing in open market. In olden days stocks were issued in physical form but nowadays the operations are done electronically with shares in dematerialized form.

Prediction of share prices lies in the interdisciplinary domains of finance and computer science. Although Efficient Market Hypothesis (EMH) states that price movement of share happens randomly and technical, fundamental or any other analysis will not yield consistent above average profit to investors. Any new information in the market is

immediately reflected in stock price and it is not possible to generate excess returns. However many researchers and investment houses disagree with the hypothesis and have beaten the market average consistently and made profit for their investors.

Satish et al. proposed a system for predicting intraday trading volume using VWAP (Volume Weighted Average Price) with expected alpha trajectories of stock prices at 5 to 30 minute intervals [2].In intraday trading an investor is allowed to transact in stocks during the day and square off his position at the end of the day. Vella and Ng used a hybrid method utilizing London Stock Exchange data at 1 min interval [3].Chang and Lee combined Genetic Algorithm (GA) and Markov Decision Process and proposed a new framework for stock price prediction and developed a decision support system for devising stock trading strategies to yield better results than benchmark[6]. Nelson et al. applied LSTM networks for analyzing and predicting stock market price movements using data from Brazilian Stock Exchange[7].

Intrinsic value of a company is evaluated in Fundamental analysis i.e. prospects, profits, long term plans and potential of the company, with a view to investing in the company in the long term. Technical analysis only evaluates charts and trends of current prices of the stock, with a view to short-term opportunity of making profit.

Today even a retail investor has access to a host of facilities available at affordable cost.The objective of retail investor is to invest in the stock market and get a return on his investment, which would be better than his chosen benchmark like return on bank fixed deposit rates. There are online brokers which allow an individual investor to trade in margin, allow usage of proprietary or bought-out software packages [25] for algorithmic trading enabling him/her to deal with large amount of data and learning relationships between input features and prediction target. They use models for prediction and algorithms for taking trading decision in the stock market. When a retail investor wants to invest in stock market, he has to interact with the stock exchange through a broker. The brokers have the approval of the stock exchange and the systems to allow online transactions directly with the exchange. There are brokers who allow investors to participate in multiple markets simultaneously, thereby spreading out risks and opportunities. Also market sentiment can be factored into decision making based on a collection of online news and twitter data.

Normally, a retail investor does stock trading manually by selecting and buying a particular stock and remains invested for a long period waiting for the value of the stock to appreciate and then sell it at a profit. Investment banks and portfolio management companies use algorithms to do stock trading. The potential of profit by stock trading through algorithms have attracted many asset management companies and investment banks. They are investing in artificial intelligenceresearch and deep learning models to make their trading decisions more profitable. However, despite the continuous new technical developments and participation of big players there is still a space more an ordinary retail investor to make enough profit to justify investing in stocks.
Although our focus is on trading application in stock exchanges, Machine Learning (ML) and Deep Learning techniques have been widely in many real life domains [21] [22]. The insights gained from this review will also apply for other time series prediction problems, for example, in Foreign Exchange, Cryptocurrency trading.

## 2. RELATED WORK

The price movements of stocks are dynamic, volatile and non-linear. Multiple factors e.g. global economic conditions, unexpected events, politics, affect local markets and a company's performance. This makes price prediction very challenging. A lot of data have to be analysed to find patterns in the data. Data Scientists, researchers, financial analysts continue to explore analytical techniques to detect trends in the stock market and / or individual stock. Algorithmic trading uses automated, pre-programmed trading strategies to execute orders.

Gandhmaland Kumarhave done a systematic review and study of techniques for price prediction in stock market. It is a review of 50 research papersand various research methods such asBayesian Model, Fuzzy Classifier, ANN, SVM classifier, NN, ML methods used for prediction of share prices [23].

Hu et al. conducted a survey of selected papers for prediction of Foreign Exchange prices and Stock prices using Deep Learning(DL) methods[24]. In this survey, papers are selected and classified according to different DL methods e.g. CNN, LSTM, DNN, RNN, RL and others. Results are presented through most used performance metrics e.g. Root Mean Square Error, Mean Absolute Percentage Error, Mean Average Error, Mean Square Error, Accuracy, Sharpe Ratio and Return Rate. Currency and Stocks exhibit similar behavior in many respects, both are affected by market sentiments and traders use technical indicators and charts to predict their behavior.

Sharma et al., conducted a survey of well-known efficient regression approaches such as Radial Basis Function (RBF) regression, Sigmoid Regression, Linear Regression for predicting the stock market prices which will increase their profits, while minimize their risks [27].

Kumar et al.surveyed various Core Computational Intelligence approaches (ANN, GA etc.) prediction of prices in major stock exchanges [26].

## 3. CHRONOLOGICAL ROADMAP OF CONDUCTED SURVEY

This survey has been done with 20 research papers during the year 2013 to 2021 from prominent databases like IEEE, Elsevier, Springer and others.
Based on the techniques used in the selected papers a chart has been prepared to get an idea of techniques used by researches, at a glance (Fig. 1).

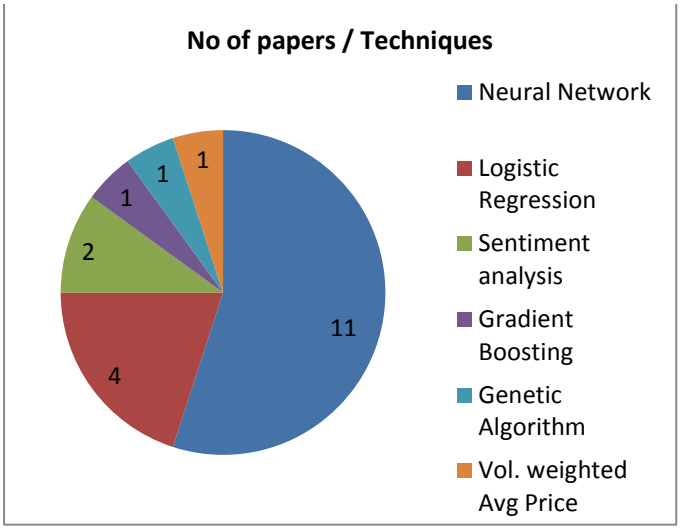


Fig 1: Methods/ techniques used vs.Number of research papers

The following chart shows the year-wise selection of papers, at a glance (Fig. 2).

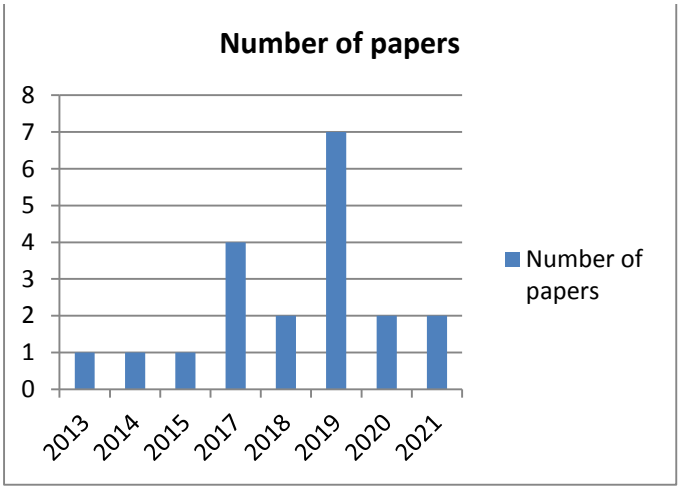


Fig 2 : Year-wise number of selected papers

Table 1 presented below, shows a chronologically arranged list of relevant technical papers that have been reviewed in the area of Predictive Analytics for financial forecasting with emphasis on stock price prediction.

Table 1: Summary of reviewed papers on financial forecasting

| Year | Author | Technique | Data Source |
|---|---|---|---|
| 2013 | Ticknor | Bayesian ANN | Microsoft & Goldman Sachs stock price [1] |
| 2014 | Satish et al. | Modified VWAP | DJIA and Russell 3000 stocks [2] |
| 2015 | Vella and Ng | Hybrid Fuzzy Logic with NN | London Stock Exchange [3] |
| 2017 | Ananthkumar et al. | Logistic Regression | BSE SENSEX data [4] |
| 2017 | Krauss et al. | Deep NN, GBT, RAF | S&P 500 data [5] |
| 2017 | Chang and Lee | MDP and GA | Taiwan Stock Exchange [6] |
| 2017 | Nelson et al | LSTM | Brazilian Stock Market [7] |
| 2018 | Selvin et al. | Deep Learning | NSE data [8] |
| 2018 | Hiranshahet al. | MLP, RNN, LSTM CNN | NSE data [9] |
| 2019 | Zhang et al. | Predictive Regression analysis, Recursive estimation window | Chinese Stock Exchange [10] |
| 2019 | Wei | LSTM with attention layer | Chinese Stock Market [11] |
| 2019 | Berradi and Lazaar | PCA and RNN | Casablanca Stock Exchange [12] |
| 2019 | Sun et al. | ARMA-GARCH-NN | US Stock Exchange [13] |
| 2019 | Karhunen | Algorithmic sign prediction using LR | Data from 11 stock markets [14] |
| 2019 | Long et al. | S&S kernel | Medical Industry data [15] |
| 2019 | Brzeszczyński and Ibrahim | modelled by stochastic parameter regressions | American, European and Australasian stock markets [16] |
| 2020 | Nevasalmi | Gradient Boosting | S&P 500 data used [17] |
| 2020 | Istiake et al. | Bidirectional LSTM | Google Stock Market data [18] |
| 2021 | Kumar | PSO-BPNN | Stock data from NSE [19] |
| 2021 | Kim and Suh | MOM and SWMOM | Stock data from US stocks [20] |

## 4. SURVEY DETAILING WITH INSIGHTS

In this section, we have detailed the findings of each research papers and found out the techniques, pros and cons faced by each researcher for their forecasting.

Various Neural Network based methodologies have been used for forecasting. Ticknor proposes Bayesian artificial neural network to forecast behavior of financial market [1]. Vella and Ng built a system adopting a hybrid method in conjunction with a popular neural network (NN) trend prediction model [3]. Krauss et al. analyzed Deep Neural Networks (DNN), Gradient-Boosted-Trees (GBT), Random Forests (RAF) and their effectiveness [5].

Nelson et al. studied the use of LSTM networks, on the problem of prediction of movements of share price, using data from Brazilian Stock Exchange[7]. Selvin et al. employed a sliding window for predicting future value of shares in the short term [8]. Hiranshah et al. used historical prices of stocks of a company and used various types of Deep Learning architectures for predicting stock price[9].Wei proposes a LSTM Neural Network with Attention layer, to overcome time-lag limitations of LSTM NN using three representative stocks of Chinese Stock Market[11]. Berradi and Lazaar integrated Principal Component Analysis (PCA) and Recurrent Neural Network (RNN) to predict stock price using data from Casablanca Stock Exchange [12].Sun et al. used a machine learning approach to capture intraday patterns for stock market shock forecasting using data from US stock market [13]. Istiake et al. suggested that Bi-directional LSTM performs better than LSTM when properly tuned model parameters are used[18]. The results obtained by the study of Kumar proved the PSO-BPNN (Particle Swarm Optimization-Back Propagation NN) showed highest prediction accuracy in intraday stock price [19]

Some researchers of the selected papers used Logistic Regression in their study. Ananthkumar et al. proposed Logistic Regression and certain macro financial variables to analyze which ratios are affecting stock prices [4]. Zhang et al. used Predictive Regression Analysis and Recursive estimation window[10]and Karhunen used logistic regressions, logistic regressions with regularization and classification for algorithmic sign prediction[14]. Brzeszczyński and Ibrahim investigated if magnitude and direction of returns can be modeled with stochastic parameter regressions to generate stock market trading signals[16].

Some researchers have used news contents and sentiments of the market in their strategies. Long et al.used a kernel of semantics and structures [15].Kim and Suh suggested sentiment-weighted trading for better performance in momentum and short term reversal situations[20].

Other strategies seen in the selected research papers are proposed by Satish et al. for predicting intraday trading volume using VWAP (Volume Weighted Average Price) with expected alpha trajectories of stock prices at 5 to 30 minute intervals[2].Chang and Lee combined Markov Decision Process (MDP) and Genetic Algorithms (GA) in a novel analytical framework to develop a decision support system stock trading strategies to yield better results than benchmark[6]. Nevasalmi proposed a new multinomial classification approach to forecast stock prices. He showed that in a real time trading simulation, machine

leaning method outperformed the benchmark buy and hold strategy. The gradient boosting algorithm performed best in both economic and statistical criteria used [17].

## 5. CONCLUSION

In some of the papers it can be seen that sophisticated AI/ML techniques have been used on historical data in order to predict future data. In intraday trading of stocks, it is important if the closing price of the day can be predicted one day in advance. In other words, from historical data up to the previous day, it is possible to predict the closing price of next day. Data of share prices is available from NSE which gives Opening price, Closing price, High, Low and Traded Volume. From this data various methods of predicting closing price of next day and accuracy thereof, have been studied.

For intraday trading, not only choosing the right stocks but also it is important to enter and exit at the correct time and the stakes can be high in margin trading. To achieve accuracy, technical analysis is the answer. A correct combination of technical indicators and Closing Price, predicted with AI methods, if used in a suitable trading algorithm to make BUY/SELL/HOLD decisions every 5 or 10 minutes, has the potential of beating a benchmark like Fixed Deposit interest or chosen Market Indices in the short to medium term.

## 6. REFERENCES


[1] J. L. Ticknor, "A Bayesian regularized artificial neural network for stock market forecasting," *Expert Systems with Applications*, vol. 40, no. 14, pp. 5501–5506, 2013, doi: 10.1016/j.eswa.2013.04.013.

[2] V. Satish, A. Saxena, and M. Palmer, "THE JOURNAL OF TRADING Predicting Intraday Trading Volume and Volume Percentages." [Online]. Available: www.iijournals.com

[3] V. Vella and W. L. Ng, "A Dynamic Fuzzy Money Management Approach for Controlling the Intraday Risk-Adjusted Performance of AI Trading Algorithms," *Intelligent Systems in Accounting, Finance and Management*, vol. 22, no. 2, pp. 153–178, Apr. 2015, doi: 10.1002/isaf.1359.

[4] IEEE Staff, *2017 IEEE 15th Intl Conf on Dependable, Autonomic and Secure Computing, 15th Intl Conf on Pervasive Intelligence and Computing, 3rd Intl Conf on Big Data Intelligence and Computing and Cyber Science and Technology Congress(DASC PicomDataComCyberSciTech)*. IEEE, 2017.

[5] C. Krauss, X. A. Do, and N. Huck, "Deep neural networks, gradient-boosted trees, random forests: Statistical arbitrage on the S&P 500," *European Journal of Operational Research*, vol. 259, no. 2, pp. 689–702, Jun. 2017, doi: 10.1016/J.EJOR.2016.10.031.

[6] Y. H. Chang and M. S. Lee, "Incorporating Markov decision process on genetic algorithms to formulate trading strategies for stock markets," *Applied Soft Computing*, vol. 52, pp. 1143–1153, Mar. 2017, doi: 10.1016/J.ASOC.2016.09.016.

[7] D. M. Q. Nelson, A. C. M. Pereira and R. A. de Oliveira, "Stock market's price movement prediction with LSTM neural networks," 2017 International Joint

Conference on Neural Networks (IJCNN), 2017, pp. 1419-1426, doi: 10.1109/IJCNN.2017.7966019.

[8] S. Selvin, R. Vinayakumar, E. A. Gopalakrishnan,

V.K. Menon and K. P. Soman, "Stock price prediction using LSTM, RNN and CNN-sliding window model," 2017 International Conference on Advances in Computing, Communications and Informatics (ICACCI), 2017, pp. 1643-1647, doi: 10.1109/ICACCI.2017.8126078.

[9] M. Hiransha, E. A. Gopalakrishnan, V. K. Menon, and K. P. Soman, "NSE Stock Market Prediction Using Deep-Learning Models," in *Procedia Computer Science*, 2018, vol. 132, pp. 1351–1362. doi: 10.1016/j.procs.2018.05.050.

[10] Y. Zhang, F. Ma, and B. Zhu, "Intraday momentum and stock return predictability: Evidence from China," *Economic Modelling*, vol. 76, pp. 319–329, Jan. 2019, doi: 10.1016/j.econmod.2018.08.009.

[11] D. Wei, "Prediction of Stock Price Based on LSTM Neural Network," in *Proceedings - 2019 International Conference on Artificial Intelligence and Advanced Manufacturing, AIAM 2019*, Oct. 2019, pp. 544–547. doi: 10.1109/AIAM48774.2019.00113.

[12] Z. Berradi and M. Lazaar, "Integration of Principal Component Analysis and Recurrent Neural Network to Forecast the Stock Price of Casablanca Stock Exchange," in *Procedia Computer Science*, 2019, vol. 148, pp. 55–61. doi: 10.1016/j.procs.2019.01.008.

[13] J. Sun, K. Xiao, C. Liu, W. Zhou, and H. Xiong, "Exploiting intra-day patterns for market shock prediction: A machine learning approach," *Expert Systems with Applications*, vol. 127, pp. 272–281, Aug. 2019, doi: 10.1016/J.ESWA.2019.03.006.

[14] M. Karhunen, "Algorithmic sign prediction and covariate selection across eleven international stock markets," *Expert Systems with Applications*, vol. 115, pp. 256–263, Jan. 2019, doi: 10.1016/J.ESWA.2018.07.061.

[15] W. Long, L. Song, and Y. Tian, "A new graphic kernel method of stock price trend prediction based on financial news semantic and structural similarity," *Expert Systems with Applications*, vol. 118, pp. 411–424, Mar. 2019, doi: 10.1016/J.ESWA.2018.10.008.

[16] J. Brzeszczyński and B. M. Ibrahim, "A stock market trading system based on foreign and domestic information," *Expert Systems with Applications*, vol. 118, pp. 381–399, Mar. 2019, doi: 10.1016/J.ESWA.2018.08.005.

[17] L. Nevasalmi, "Forecasting multinomial stock returns using machine learning methods," *The Journal of Finance and Data Science*, vol. 6, pp. 86–106, Nov. 2020, doi: 10.1016/J.JFDS.2020.09.001.

[18] M. A. Istiake Sunny, M. M. S. Maswood, and A. G. Alharbi, "Deep Learning-Based Stock Price Prediction Using LSTM and Bi-Directional LSTM Model," in *2nd Novel Intelligent and Leading Emerging Sciences Conference, NILES 2020*, Oct. 2020, pp. 87–92. doi: 10.1109/NILES50944.2020.9257950.

[19] K. C. S, "Hybrid models for intraday stock price forecasting based on artificial neural networks and metaheuristic algorithms," *Pattern Recognition Letters*, vol. 147, pp. 124–133, Jul. 2021, doi: 10.1016/j.patrec.2021.03.030.

[20] B. Kim and S. Suh, "Overnight stock returns, intraday returns, and firm-specific investor sentiment," *North American Journal of Economics and Finance*, vol. 55, Jan. 2021, doi: 10.1016/j.najef.2020.101287.

[21] RMukherjee,S Sadhu and AKundu, "Heart Disease DetectionUsing Feature Selection based KNN Classifier" Proceedings of Data Analytics and Management(ICDAM 2021). Lecture Notes on Data Engineering and Communications Technologies, pp. 577-585 vol. 90. Springer, Singapore.

[22] R Mukherjee et al., "Face Mask Detector Using Convolutional Neural Networks", 5th International Conference on Innovative Computing and Communications,ICICC, New Delhi, Feb 2022.

[23] D. P. Gandhmal and K. Kumar, "Systematic analysis and review of stock market prediction techniques," *Computer Science Review*, vol. 34, p. 100190, 2019, doi: 10.1016/j.cosrev.2019.08.001.

[24] Z. Hu, Y. Zhao, and M. Khushi, "A survey of forex and stock price prediction using deep learning," *Applied System Innovation*, vol. 4, no. 1, pp. 1–30, 2021, doi: 10.3390/ASI4010009.

[25] Rajendrani Mukherjee, K Sridhar Patnaik, "Introducing a Fuzzy Model for Cost CognizantSoftware Test Case Prioritization", IEEE TENCON 2019: Recent Advances in Program Analysis and Software Testing (RAPAST), Page 502-507, 17-20th October, 2019, Kerala, India.

[26] Kumar, G., Jain, S. & Singh, U.P. Stock Market Forecasting Using Computational Intelligence: A Survey. *Arch Computational Methods in Engineering* 28**,** 1069–1101 (2021). https://doi.org/10.1007/s11831-020-09413-5

[27] A. Sharma, D. Bhuriya and U. Singh, "Survey of stock market prediction using machine learning approach," 2017 International conference of Electronics, Communication and Aerospace Technology (ICECA), 2017,pp. 506-509, doi: 10.1109/ICECA.2017.8212715

## Biographies

**Partha Sarathi Paul** received the bachelor's degree in Electronics and Communication Engineering from Indian Institute of Technology, Kharagpur and the master's degree in Telecommunications from University of Maryland, College Park, MD, USA. He has more than thirty years experience in Automation in Industry, working with ABB and Siemens. He is currently working as an Assistant Professor at the Information Technology Department in Institute of Engineering, Kolkata. His research areas include Artificial Intelligence and Machine Learning.

**Dr. Rajendrani Mukherjee** is an Associate Professor in the Department of CSE, University of Engineering and Management, Kolkata. Prior to that, she has worked as Assistant Professor in Department of Information Technology at Calcutta Institute of Engineering and Management from 2012 to 2019. She has also worked in the software industry for 5 years with prominent MNCs like IBM and Fuzzy Logix. Her research interest mainly lies in machine learning, data analytics, process modelling and automation, software engineering domain. She has served as session chair (CIPR 2021) and reviewer (IEEE INDICON 2021) of many conferences. She is also reviewer of several SCI Indexed journals (Springer Multimedia Tools and Applications, SN Computer Science etc.). She has served as Mentor in Smart India Hackathon 2019. In 2021, she became AICTE certified Mentor from NITTTR Chennai. She has completed her PhD from BIT, Mesra. She has done her MS from University of North Carolina, Charlotte in 2009. She was a member of phi kappa phi honor society (2009) for achievement in graduating class. During her Masters she received Teaching Assistantship from UNCC. She completed her B. Tech from St Thomas College of Engineering & Technology, India in 2005. Prior to that, she received a national merit scholarship in 2001. She is an active member of IEEE.

# Codebook optimization using Jaya Algorithm for image compression

**Suvojit Acharjee, Prof. Sheli Sinha Chaudhuri**

*Department of ETCE, Jadavpur University*

acharjeesuvo@gmail.com, shelism@rediffmail.com

## Abstract.

Image compression is required to effectively manage today's communication infrastructure. The Linde–Buzo–Gray (LBG) algorithm is a powerful and reliable lossy image compression technique. Iterative refining is used by LBG to construct a local codebook. Various evolutionary algorithms were used to create a global codebook. However, the performance of various evolutionary algorithms is not consistent. Furthermore, these algorithms include algorithm specific parameters such as acceleration rate in particle swarm optimization (PSO), discovery probability in cuckoo search (CS), and so on. Improper value selection for these tuning parameters might lead to local minima. This article proposes utilizing the Jaya Algorithm (JA) to optimize the vector quantization codebook. JA has no algorithm specific tuning parameters, and its success is determined only by generic evolutionary algorithm parameters like maximum iteration and initial population numbers. The output from the proposed algorithm outperforms the CS, and PSO based vector quantization algorithms as well as the state-of-the-art pattern-based masking LBG algorithm.

**Keywords**. LBG, Jaya Algorithm, Image Compression, PSO, cuckoo search, Codebook.

## 1. INTRODUCTION

Compression can be classified into lossy and lossless categories. Lossless compression does not lose any information during compression. However, lossy compression allows the loss of information up to an extent. The removed information is often redundant in nature. The loss of this information has a negligible effect on the signal. The image compression techniques mainly employ the vector quantization algorithms (VQA) for lossy compression. The most popular VQA, Linde–Buzo–Gray (LBG) [1] algorithm works by minimizing the Euclidian distance between the codeword and the image vector. LBG successfully generates locally optimized codebook for image vectors. But it does not guarantee a global optimal code word. Also, the output of the LBG algorithm varies massively based on the initial condition of the algorithm. Therefore, researchers employ several evolutionary algorithms to find a global codebook for VQ.

The ant colony optimization-based (ACO) VQA [2] used wavelet coefficients and bidirectional graphs. Though the output of this process was better than the output of LBG, the speed of the algorithm was very slow. VQ was successfully accomplished using the Particle swarm optimization (PSO) algorithm [3]. The PSO based algorithm was faster than the ACO-based algorithm. However, the convergence of PSO becomes very unstable if any particle in the swarm has a high velocity. PSO was further modified in Quantum-behaved

Particle Swarm Optimization [4] (QPSO) which calculates the local particle using the particle's best fitness as well as the global best fitness. The Firefly Optimization Algorithm (FOA) [5] is based on the social characteristics of the firefly. Fireflies use their bioluminescence property for mating communication. The dark firefly moves toward the brighter firefly during mating. [6] But FOA face difficulty when brighter fireflies are absent from the search space. Chiranjeevi et al. [7] proposed a FOA-based VQA that solves this problem by allowing the firefly to fly at random in the absence of the bright firefly. The Bat Algorithm (BA)-based VQA (BALBG) [8] outperforms the FOA-based VQA (FOALBG) with proper tuning parameters such as frequency, pulse rate, and loudness. However, evolutionary algorithms such as PSO, BA, FOA, and others contain a number of algorithm-specific parameters. The algorithm's performance varies significantly when these operational parameters are not properly tuned. The discovery probability is the single algorithm-specific parameter in the cuckoo search (CS) algorithm [9]. As a result, it is far simpler than BA and FOA. VQ based on CS was simple to implement [10]. Despite the fact that CS reduced the number, the performance of these evolutionary algorithms is still heavily dependent on algorithmic-specific parameters. Incorrect tuning of these parameters can lead to local optima and delay convergence. The pattern-based masking LBG (PBMLBG) algorithm [11] used the local histogram peak to find the repetitive patterns inside the image vectors. These patterns are then used as the initial codebook of the LBG algorithm. But improper selection of the histogram peaks can lead to improper results [11]. Rao et al. [12] proposed the Jaya algorithm (JA), which depends only on general parameters of evolutionary algorithms. Previously, the JA successfully optimized a variety of engineering problems, including the block matching algorithm for motion estimation [13], fuzzy PIDF controller [14], and many others. The absence of algorithmic specific parameters helps the proposed algorithm to outperform the BALBG and PBMLBG.

The manuscript is structured as follows. Section two will introduce different VQ techniques based on evolutionary algorithm. Section 3 will outline the JA as well as the proposed JA based VQA. In section 4, the performance of the proposed algorithms is compared with the performance of state-of-the-art algorithms. Section 5 will bring the article to a conclusion.

## 2. OVERVIEW: VECTOR QUANTIZATION

The VQ is a lossy process that maps the image vectors into codewords. The image vectors are generated by subdividing an image into non-overlapping blocks. All codewords are stored and indexed inside the codebook. Every image vector will be assigned the index of its nearest codeword based on the Euclidian distance. The size of the codebook controls the quality of the output as well as the speed of the process. The decoder reconstructs the image based on the index and the codebook.

### *2.1. LBG Algorithm*

LBG algorithm [1] is the most popular algorithm to construct the codebook for an image vector. LBG reduce the distortion between the original and recovered image through repetitive iteration. The steps of the algorithm are following.

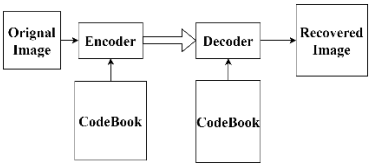


Figure 1. Encoding and Decoding process of vector quantization.

A) Generate initial codebook by randomly selecting $N_c$ number of codewords from the image vectors. Size of each image vector as well as the codewords are $N_b$.

B) Map the image vectors $\{I_1, I_2, \ldots, I_M\}$ to its nearest codewords $\{C_1, C_2, \ldots, C_{Nc}\}$.

$$flag_{mi} = \begin{matrix} true \\ false \end{matrix} \quad \begin{matrix} if\ |C_i - I_m| < |C_{j\in 1,..,N_c : j\neq i} - I_m| \\ otherwise \end{matrix} \qquad (1)$$

$flag_{mi}$ describes the position in the $\{M \times N_c\}$ Boolean flag matrix. This matrix is only true when $m^{th}$ image vector belongs to $i^{th}$ codeword.

C) Compute the centroid of the new clusters. These centroids are the new codewords $C'_i$.

$$C'_i = \frac{\sum_{m=1}^{M} I_m * flag_{mi}}{Number\ of\ vectors\ in\ the\ cluster} \qquad (2)$$

D) Compute the distortion ($d'$) with new codewords Algorithm terminates when present distortion is larger or equal to previous iteration (d). Else, the process repeats from step 2.

$$Algorithm\ continue\ when \quad (d - d') > 0 \qquad (3)$$

### *2.2. Evolutionary Algorithms based LBG Algorithm*

The codebook produced from LBG is localized one. Evolutionary algorithms were employed to find the globally optimized codebook. The steps of any evolutionary algorithm-based vector quantization algorithms are following.

A) Run the LBG algorithm and assign the output as one of the *n* number of solutions. Initialize rest of the *(n-1)* solutions randomly.

B) Calculate the fitness of every solution using equation 4.

$$F = \frac{N_b}{\sum_{i=1}^{N_c} \sum_{m=1}^{M} \sum_{j=1}^{N_b} ||I_{mj} - C_{ij}|| * flag_{mi}} \qquad (4)$$

C) Rank the solutions based on their fitness and generate new solutions for next iteration.

D) Until the termination requirements were met, repeat the process from step B.

## 3. JAYA ALGORITHM BASED VECTOR QUANTIZATION

JA is one of those evolutionary algorithms which does not contain any algorithm specific operational parameter. It only depends on the general evolutionary algorithm parameters i.e., maximum iteration and initial population size. Therefore, it is free from the possibility of premature convergence due to improper selection of tuning parameters. The steps of JA are described below.

A) Set the population size & maximum iteration. Also, randomly initialize the population.

B) Calculate the fitness of the solutions and identify best ($X_{best}$) and worst ($X_{worst}$) solution.

C) Generate new solutions using equation 5. $r_1$ and $r_2$ are random numbers between 0 & 1.

$$X_i' = X_i + r_1 * (|X_i - X_{best}|) - r_2 * (|X_i - X_{worst}|) \quad (5)$$

D) Accept the new solution if the fitness of new solution is better than the previous one.

E) Continue from step 3 until the termination requirements are met.

The new solution generation process in Jaya algorithm pushes the old solution closer towards the best solution. At the same time, old solution moves further away from the worst solution. The JA based VQA is referring the codebook as a solution. The fitness of the solutions or the codebooks are calculated based on equation 4. The aim of JA based VQA is to obtain an optimal codebook which will maximize the fitness. The details of JA based VQA algorithm are as follows.

A) Divide the whole image into image vectors $I = \{I_1, I_2, \dots, I_M\}$.

B) Merwe et al. [15] demonstrated that using a local codebook as the initial population of an evolutionary algorithm reduces the convergence time of evolutionary algorithms. Therefore, LBG algorithm was used to generate a codebook which was assigned as one of the initial populations in JA based VQA. Other populations are selected randomly from the image vectors. Initial population consist of *n* codebooks.

C) The algorithm uses Equation 4 to calculate the fitness of the population. The solutions are sorted based on their fitness. The codebook with the highest fitness will be at the top of the list, while the codebook with the lowest fitness will be at the bottom.

D) Equation 6 will generate the new solution for next iteration. This equation is a more specific version of equation 5 which was more elaborated for JA based VQA.

$$C'_{ijk} = C_{ijk} + r1 * (|C_{ij1} - C_{ijk}|) - r2 * (|C_{ijn} - C_{ijk}|) \quad (6)$$

E) The new codebook $C'_i$ will only replace $C_k$ when the fitness of new codebook $C'_k$ is better than the fitness of old codebook $C_i$.

F) The algorithm checks for the termination conditions. When the iteration is smaller than maximum iteration and error is not converged then repeat the process from step C.

## 4. RESULT AND DISCUSSION

### *4.1. Dataset, Initial Condition and Performance metrics*

In this experiment, the performance of the proposed algorithm's output is compared to the output of LBG, PSOLBG, QPSOLBG, FOALBG, BALBG, and PBMLBG utilizing bit rate per pixel (bpp), peak signal to noise ratio (PSNR), and calculation time. Four standard test images of 512×512 resolution ("Lenna.jpg", "baboon.png", "peppers.png", and "goldhill.png") are used to compare the performance of the proposed algorithm with the benchmark algorithms. The test images are divided into nonoverlapping 4×4 blocks to construct the image vectors. Therefore, each image creates 16384 image vectors. This experiment sets the initial population to 30 and the maximum iterations to 30.

$$bpp = \frac{\log_2 N_c}{N_b} \quad (7)$$

$$PSNR = 10 \log_{10} \left( \frac{255^2}{\text{mean square error between initial \& reconstructed image}} \right) dB \quad (8)$$

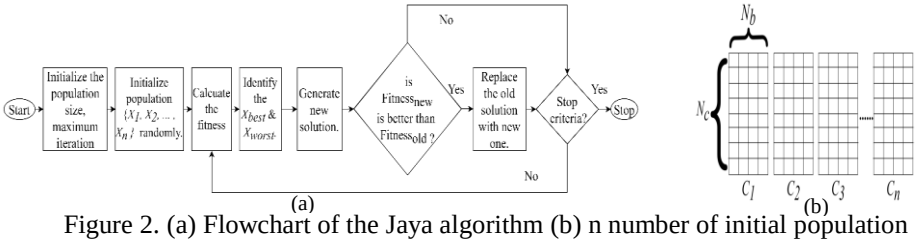


Figure 2. (a) Flowchart of the Jaya algorithm (b) n number of initial population

### *4.2. Discussion*

Proposed algorithm was compared with the benchmark algorithms utilizing the PSNR, bpp and computation time. The PSNR and the computation time presented in this manuscript are the average of the output from five separate execution of the algorithms. The codebook size is {8,16,32,64,128,256,512}. For "Lenna" image, the bpp vs PSNR performance in figure 3a clearly indicates that the proposed algorithm outperforms every other algorithm except PBMLBG. However, for every other test image, the bpp vs PSNR performance of the proposed algorithm outperforms all benchmark algorithms. This demonstrates that the suggested algorithm's reconstructed picture is superior than those produced by other techniques under consideration.

Tables one to four illustrate the execution time required by various algorithms with varying codebook sizes. Conclusions may be derived from this table that the proposed algorithm is quicker than the others for most of the scenario. However, the execution time of the proposed algorithm increases with the bpp. The speed of the proposed algorithm is lagging behind all benchmark algorithms when bpp is 0.5625. The proposed technique is always slower than the PBMLBG because the proposed algorithm requires more iterations to converge than the PBMLBG. When bpp is low, the proposed algorithm minimizes the calculation time of codebook optimization. However, it increases with bpp. Nevertheless, the proposed method consistently delivers the best reconstructed image.

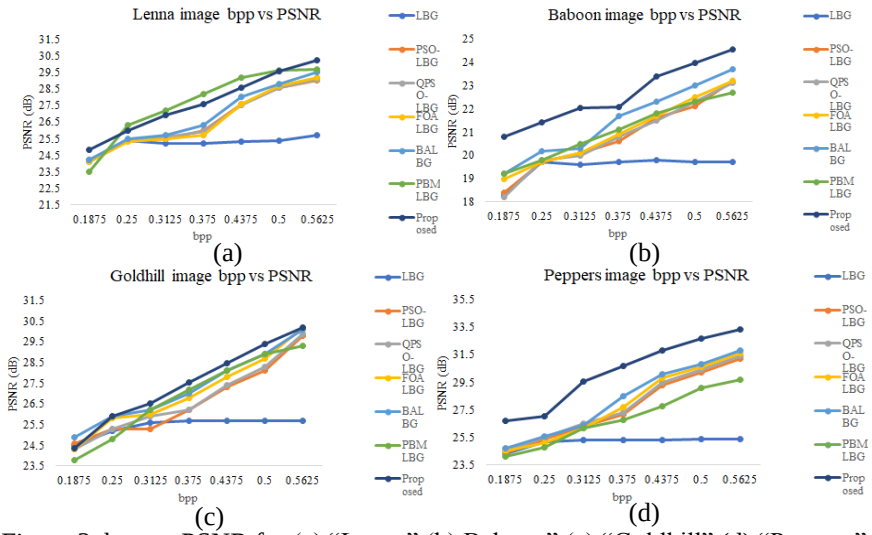


Figure 3. bpp vs PSNR for (a) "Lenna" (b) Baboon" (c) "Goldhill" (d) "Peppers"

**Table 1:** Average computation time (sec) at bpp =0.375 and block size=64

| Image | LBG | PSOLBG | QPSOLBG | FOALBG | BALBG | PBMLBG | Proposed |
|---|---|---|---|---|---|---|---|
| Lenna | 10.1 | 632.12 | 632.34 | 1453.21 | 678.12 | 11.2 | 254.11 |
| Peppers | 11.7 | 612.23 | 605.21 | 1301.21 | 612.23 | 11.63 | 147.68 |
| Baboon | 11.98 | 545.21 | 587.12 | 1450.21 | 743.12 | 10.77 | 138.82 |
| Goldhill | 14.71 | 598.32 | 645.32 | 1201.32 | 476.43 | 11.12 | 151.89 |

**Table 2:** Average computation time (sec) at bpp =0.4375 and block size=128

| Image | LBG | PSOLBG | QPSOLBG | FOALBG | BALBG | PBMLBG | Proposed |
|---|---|---|---|---|---|---|---|
| Lenna | 13.98 | 645.32 | 643.23 | 1012.21 | 598.21 | 11.89 | 511.63 |
| Peppers | 19.21 | 613.23 | 687.2 | 1102.2 | 643.23 | 11.71 | 375.32 |
| Baboon | 23.12 | 476.12 | 523.51 | 1051.97 | 976.21 | 12.12 | 303.59 |
| Goldhill | 17.98 | 845.12 | 876.12 | 1333.21 | 512.54 | 11.23 | 285.79 |

**Table 3:** Average computation time (sec) at bpp =0.5 and block size=256

| Image | LBG | PSOLBG | QPSOLBG | FOALBG | BALBG | PBMLBG | Proposed |
|---|---|---|---|---|---|---|---|
| Lenna | 20.84 | 902.92 | 887.71 | 786.77 | 662.13 | 12.11 | 802.15 |
| Peppers | 19.17 | 771.25 | 767.52 | 1001.32 | 587.21 | 12.12 | 663.96 |
| Baboon | 27.26 | 621.27 | 577.1 | 1021.92 | 578.21 | 12.13 | 620.47 |
| Goldhill | 30.72 | 925.34 | 554.32 | 843.21 | 987.34 | 12.33 | 610.04 |

**Table 4:** Average computation time (sec) at bpp =0.5625 and block size=512

| Image | LBG | PSOLBG | QPSOLBG | FOALBG | BALBG | PBMLBG | Proposed |
|---|---|---|---|---|---|---|---|
| Lenna | 34.21 | 701.23 | 723.18 | 962.38 | 787.24 | 12.22 | 1530.00 |
| Peppers | 37.32 | 962.21 | 901.27 | 667.25 | 512.23 | 12.12 | 1310.60 |
| Baboon | 21.32 | 643.23 | 698.47 | 751.26 | 843.12 | 12.33 | 1300.30 |
| Goldhill | 37.09 | 576.25 | 621.12 | 972.77 | 934.12 | 11.33 | 1240.30 |

## 5. CONCLUSION

Proposed algorithm in this article optimizes the codebook of VQ using JA. The proposed algorithm outperforms all benchmark algorithms in terms of PSNR. In this way, proposed algorithm increases the quality of reconstructed image with respect to all benchmark algorithm. Also, JA converges quicker than PSOLBG, QPSOLBG, BALBG, and FOALBG when bpp is low. Future versions of the proposed method may include the PBMLBG outputs as an additional initial solution to further speed up convergence.

## 6. REFERENCES

[1] Y. Linde, A. Buzo, and R. Gray, “An Algorithm for Vector Quantizer Design,” IEEE trans. commun., vol. 28, no. 1, pp. 84–95, 1980

[2] Rajpoot, N., Hussain, A., Ali, U., Saleem, K., & Qureshi, M., “A novel image coding algorithm using ant colony system vector quantization,” in International workshop on systems, signals and image processing Poznan, Poland, 2004, pp. 13–15.

[3] H.-M. Feng, C.-Y. Chen, and F. Ye, "Evolutionary fuzzy particle swarm optimization vector quantization learning scheme in image compression," Expert Syst. Appl., vol. 32, no. 1, pp. 213–222, 2007.
[4] Y. Wang et al., "A novel quantum swarm evolutionary algorithm and its applications," Neurocomputing, vol. 70, no. 4–6, pp. 633–640, 2007.
[5] Yang, X. S., & He, X. (2013). Firefly algorithm: recent advances and applications. arXiv preprint arXiv:1308.3898.
[6] Horng, M. H. (2012). Vector quantization using the firefly algorithm for image compression. Expert Systems with Applications, 39(1), 1078-1091.
[7] Chiranjeevi, K., Jena, U. R., Murali Krishna, B., & Kumar, J. (2016). Modified firefly algorithm (MFA) based vector quantization for image compression. In Computational Intelligence in Data Mining—Volume 2 (pp. 373-382). Springer, New Delhi.
[8] Karri, C., & Jena, U. (2016). Fast vector quantization using a Bat algorithm for image compression. Engineering Science and Technology, an International Journal, 19(2), 769-781.
[9] Yang, X. S., & Deb, S. (2014). Cuckoo search: recent advances and applications. Neural Computing and applications, 24(1), 169-174.
[10] Chiranjeevi, K., & Jena, U. R. (2018). Image compression based on vector quantization using cuckoo search optimization technique. Ain Shams Engineering Journal, 9(4), 1417-1431.
[11] Bilal, M., Ullah, Z., & Islam, I. U. (2021). Fast codebook generation using pattern-based masking algorithm for image compression. IEEE Access, 9, 98904-98915.
[12] Zitar, R. A., Al-Betar, M. A., Awadallah, M. A., Doush, I. A., & Assaleh, K. (2021). An intensive and comprehensive overview of JAYA algorithm, its versions and applications. Archives of Computational Methods in Engineering, 1-30.
[13] Dash, B., Rup, S., Mohanty, F., & Swamy, M. N. S. (2019). A hybrid block-based motion estimation algorithm using JAYA for video coding techniques. Digital Signal Processing, 88, 160-171.
[14] Debnath, M. K., Sinha, S., & Mallick, R. K. (2017). Application of fuzzy-pidf controller for automatic generation control using jaya algorithm. Int J Pure Appl Math, 114(9), 51-61.
[15] Van der Merwe, D. W., & Engelbrecht, A. P. (2003, December). Data clustering using particle swarm optimization. In The 2003 Congress on Evolutionary Computation, 2003. CEC'03. (Vol. 1, pp. 215-220). IEEE.

## Biographies

**Suvojit Acharjee** is a Ph.D. scholar at Jadavpur University. He has a research interest on soft computing, video coding and signal compression.

**Prof. Sheli Sinha Chaudhuri** has been serving the ETCE Department of Jadavpur University for the last 23 years. She has a research interest on the field of Machine Learning and Computer Vision.

# Haze Wireless Sensor System Development and Measurement

**Kama Azura Othman, Mohammad Aizat Farhan B. Ali, Shahrani Shahbudin**

*School of Electrical, College of Engineering, Universiti Teknologi MARA, 40450 Shah Alam, Selangor, Malaysia*

*azzuerra@gmail.com*

## Abstract.

Haze phenomenon often occurs in Malaysia. Haze arisen when the particles in the air such as dust, smoke, and other dry particles vague the clarity of the sky. When the dispersal of those combinations of dry particles concentrate, low hanging shroud will form that will spoil the visibility of the sky and may result with respiratory threat to human health. And thus, this work is aimed on developing a haze measurement system for detecting and evaluating the Air Pollutant Index (API). The developed wireless sensory system consists among others a microcontroller and a gas sensor module to read and evaluate the API reading. Alert message with content notification of the API readings is broadcasted to user via Short Message Services (SMS) through SIM900 GSM Module of the system. Outdoor measurement was conducted in industrial and residential area in Shah Alam, Selangor for system reliability and testing. The Outdoor testing showed the system successfully measured the API reading and sent alert message to a mobile device as expected.

**Keywords**. Global System for Mobile (GSM), Short Message Service (SMS), Air Pollutant Index (API), microcontroller

## 1. INTRODUCTION

Air pollution is worldwide phenomenon and required significant attention and need to be addressed. The haze phenomenon in South East Asia motivates the importance of providing API reading and alert system for citizen about the haze phenomenon threats. This phenomenon is sometimes caused by forest fires resulting from illegal slash-and-burn practices which then spread quickly to the neighbouring countries with the aid of a dry season. Haze phenomenon occurred when the dust, smoke and other dry particles obscure the clarity of the sky. Haze can be divided into 2 types, dry haze that consist of giant particles in the air such as smoke, dust, etc. and wet haze due to H20 condenses onto hydroscopic [1].

Haze can cause major health threat to the people. Haze can easily threat human health in short-terms and long- term affect. Examples of short-term effects are irritation of the eyes,

nose, and throat in healthy individuals. Besides that, it can also affect human lungs and heart especially those people that already have chronic heart or lung diseases such as asthma and heart failure. On the other hand, the long-term effects can cause cardiovascular effects such as heart attack and reduced lung development [2].

Malaysia is one of Southeast Asia countries that regularly affected by the haze phenomenon. Haze phenomenon leads to several problems such as increasing road accidents due to poor visibility, disturbing school progress and also create hazardous effects on human health. In September 2019, half a million of face mask was sent to state of Sarawak and 409 school were closed as the air pollution index reached unhealthy level due to haze [7]. In January 2022, ASMC based in Singapore alerted for haze condition to hit the northern part of Malaysia caused by hotspots burning in Cambodia and this put Malaysia to be in standby should the haze become worst [8]. Then in August 2022, Sri Aman in state of Sarawak showed hazy condition and reported with API index value of more than 100 [9].

This paper discusses the framework of developing low-cost wireless sensor system for API measurement. A gas sensor module is used to detect and measure gas particles for the developed system after which a microcontroller will process and interpret the API readings and sent SMS alert through GSM Module. TABLE I tabulates the API index consideration values applied in this work. The following section discussed methodology involved in this work and also sample of results with discussion presented in section that follows.

TABLE I. API AND CONDITION

| **Air Pollutant Index (API)** | **Condition** |
|---|---|
| Below 50 | Very Good |
| 51 – 100 | Good |
| 101 – 150 | Moderate |
| 151 – 200 | Unhealthy |
| Above 200 | Hazardous |

## 2. METHODOLOGY

This system is comprised of hardware and software development. This section describes the methodology employed in this work.

### *2.1. System Flowchart*

Figure 2.1, shows the system flowchart for this work which illustrates the process flow from the beginning to the end of the system. At initial state, the wireless sensor system is in standby mode in which the microcontroller waited for a request to activate gas sensor module for measurement. Upon receiving request through SMS containing letter 'R', microcontroller responded with the confirmation request and activate gas sensor module to begin the measurement. Once the reading is processed and recorded by the system, the API

value is sent back to user by means of GSM module. SMS notification was then received by user containing the current.

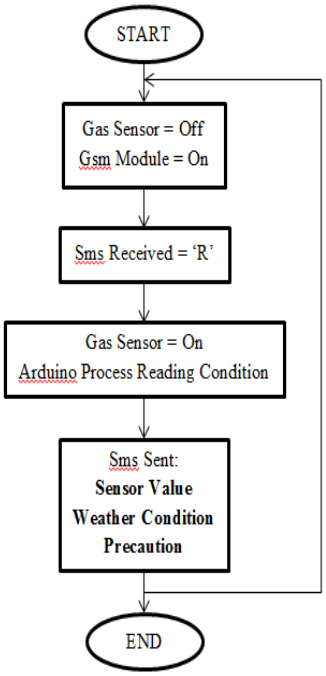


Figure 2.1. System flowchart.

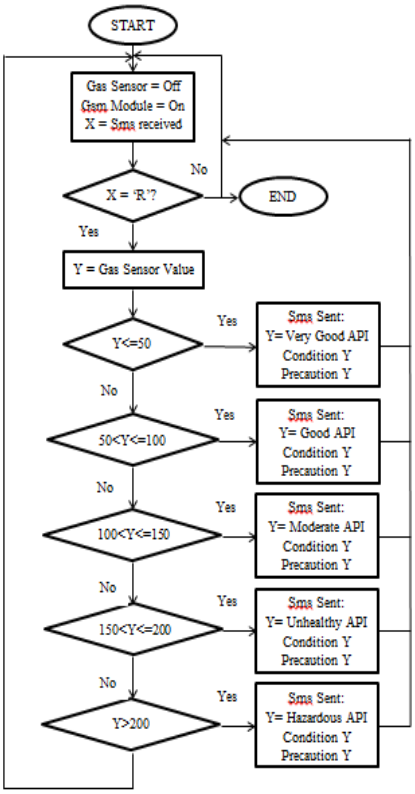


Figure 2.2. Software flowcharts.

Figure 2.2, illustrates the software flowchart developed for this project. A sketch or Arduino programming language is written following steps illustrated in the flowchart. The flowchart describes in more detail the evaluation process involved perform by the microcontroller once activation SMS received from user.

## 2.2. *Hardware Design*

Figure 2.3, illustrates the connections of gas sensor module and SIM900 GSM Module to Arduino UNO microcontroller board. And Figure 2.4, shows the hardware connection of this wireless sensor after assembly. The Vcc for gas sensor and GSM module (Red) is connected to the 5V pin of Arduino. Both ground (Black) pin of gas sensor and GSM module is connected to the ground pin of the Arduino board. The analog output of gas sensor (Blue) is connected to the A1 pin of Arduino board. The receiver pin (Green) of the GSM module

is connected to the transmitter pin 8 of Arduino board while the transmitter pin (Brown) of GSM module is connected to the receiver pin 7 of Arduino board.

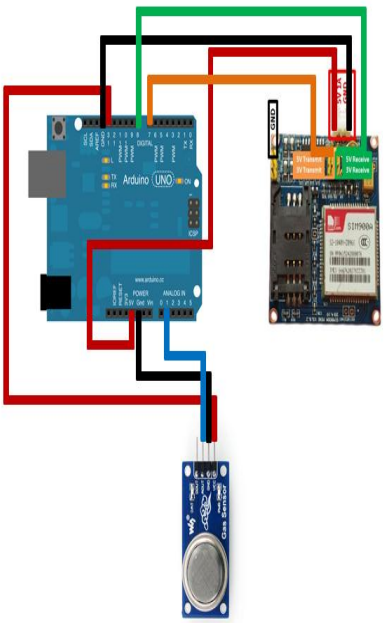

Figure 2.3. Wireless sensor circuit diagram.

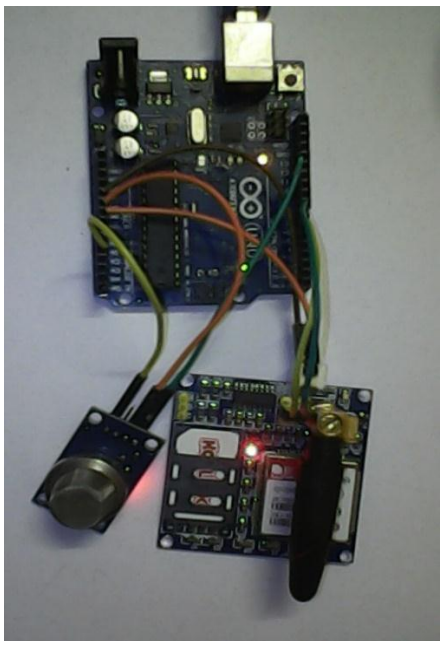

Figure 2.4. Hardware assembly for wireless sensor

## 3. RESULTS AND DISCUSSIONS

To evaluate the wireless sensor reliability, outdoor testing has been conducted in Shah Alam, Selangor. The location chosen for testing were at a residential area Seksyen 7 Shah Alam and industrial area Seksyen 16 Shah Alam, Selangor. System testing was performed starting from 10:00 A.M until 05:00 P.M for both selected areas. The outcomes are shown in TABLE II for residential and industrial area.

Figure 2.6, illustrates comparison of API readings between the residential area and industrial area. From the collected readings, the air quality in residential area was in good and healthy condition throughout the day. However, the air quality in industrial area gave unhealthy readings starting at 2.00 PM and lasted for two hours until 4.00 PM. This may be due to industrial activities happened in the area. For instance, factory releases smoke to the open air and after certain time that particles accumulated in the air became dense and cause the reading of API to be unhealthy.

TABLE II. API READINGS FOR RESINDETIAL AND IINDUSTRIAL AREAS

| Time (hour) | API Reading | |
|---|---|---|
| | Residential Area | Industrial Area |
| 10:00 A.M | 47 | 53 |
| 11:00 A.M | 49 | 77 |
| 12:00 P.M | 57 | 107 |
| 01:00 P.M | 65 | 146 |
| 02:00 P.M | 63 | 165 |
| 03:00 P.M | 59 | 151 |
| 04:00 P.M | 52 | 138 |
| 05:00 P.M | 46 | 103 |

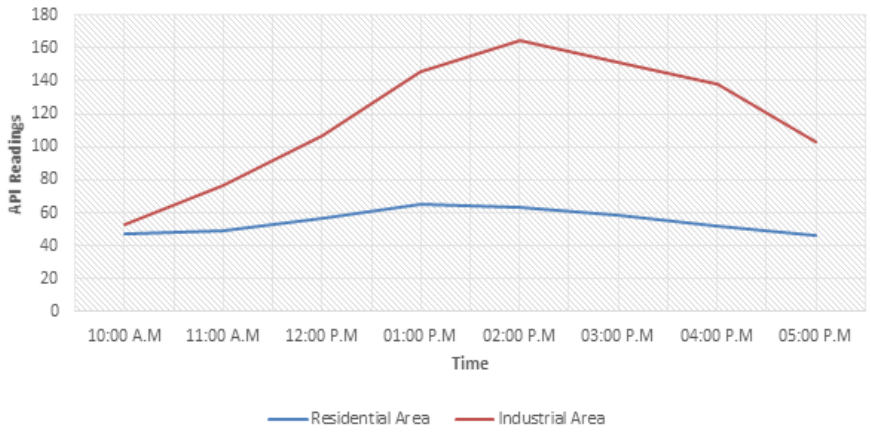


Figure 2.6. Comparison of API reading between residential and industrial area.

## 4. CONCLUSION

Low cost and low power Haze Wireless Sensor System is successfully implemented and tested consisting of a microcontroller, gas sensor module and GSM module. The developed system shows promising outcomes in sending out alert message related to API condition and air quality for area that regularly exposed to hazy conditions. Likewise, the systems offered ease of use monitoring of air quality and provide information and assistance in decision for outdoor activity. In all, it also promotes public safety towards harmful effect of unhealthy particles content in the air using Air Pollution Index (API) value.

## 5. ACKNOWLEDGEMENTS

Authors would like to express deepest gratitude to RMC UiTM Grant number: **600-RMC 5/3/GPM (052/2022)** and School of Electrical, College of Engineering, Universiti Teknologi MARA, Shah Alam, Selangor, Malaysia for supporting this work.

## 6. REFERENCES

[1] Kama Azura Othman, Norfazilah Li, Eda Hilyati Abdullah, Norhayati Hamzah, “Haze Monitoring System in city of Kuala Lumpur Using Zigbee Wireless Tehnology, WCE, 2013

[2] Hanna, Teoh, "Haze in Malaysia: Unhealthy air quality in Malacca, Selangor, Kuala Lumpur, Sarawak". The Straits Times. 14 September 2015.

[3] Eve Sonary Heng (22 October 2015). "Haze forces 4,778 schools to close today; 2,696,110 students affected". The Borneo Post. Retrieved 22 October 2015.

[4] Beawiharta / Reuters, "Indonesia declares emergency as brush-fire smoke chokes region". Al Jazeera America. 14 September 2015. Retrieved 15 September 2015.

[5] Wahyudi Soeriaatmadja (15 September 2015). "Thousands flee Pekanbaru as haze hits record high". The Straits Times. Retrieved 15 September 2015.

[6] "Brunei haze may last for a week". The Brunei Times. Thai PBS. 26 August 2015. Retrieved 14 September 2015.

[7] “Malaysia Sends Half a Million Face Mmasks to Haze-hit State, Shuts Schools”, Reuters online, 14 September 2019.

[8] “Smog from Cambodia brings haze to parts of Malaysia”, The Star Online, 22 January 2022

[9] “Slight haze causes unhealthy air quality at Sri Aman”, FMT Reporter, 12 August 2022.

## Biographies

**Kama Azura Othman** received the bachelor's degree in computer and information engineering from International Islamic University Malaysia in 1998, and the master's degree in telecommunication and information engineering from Universiti Teknologi MARA in 2007, respectively. She is currently working as a Senior Lecturer at the School of Electrical, College of Engineering Universiti Teknologi MARA Shah Alam, Selangor, Malaysia. Her research areas include Signal and Image Processing, wireless sensor system and IOT.

# EFFECT OF MODULATION INDEX ON TOTAL HARMONIC DISTORTION AND INDIVIDUAL HARMONICS IN A SINGLE-PHASE FIVE LEVEL SPWM BASED CHML INVERTER-A REVIEW

Gautam Ghosh

Department of Electronics & Communication Engineering,

Institute of Engineering & Management

Kolkata, India

gautam.ghosh@iemcal.com

Rajiv Ganguly

Department of Basic Science & Humanities,

University of Engineering & Management,

Kolkata, India

rajiv.ganguly@uem.edu.in

## Abstract.

An effort has been made to design a sinusoidal pulse width modulation based five-level inverter produced almost sinusoidal output waveform and to investigate how this inverter's other harmonics and overall harmonic distortion are affected by changes in the modulation index.

It is well known that commercial inverters, whether single-phase or three-phase, produce output voltage waveforms that are square waves or modified square waves, and as a result, contain harmonics of lower and higher orders. The effect of lower order harmonics in a commercial inverter may be eliminated or reduced by using suitable low-pass filter but, as the frequency is on the lower side of frequency spectrum, some portion of the fundamental also get filtered affecting the efficiency of the inverter. Besides, the use of low pass filter also increases the size of inverter as well as the cost.

**Keywords**. Cascaded H-bridge Multilevel Inverter; SPWM; Power Semiconductor Devices; Harmonic Factor (HF); Total Harmonic Distortion (THD); (CHMLI).

## 1. INTRODUCTION

A primary function of an inverter is to transform a DC input voltage into an AC output voltage with a sinusoidal waveform of the desired amplitude.

Commercial inverters, on the other hand, typically have waveforms that are square wave or quasi-square wave and contain lower and higher order harmonics. Inverter performance and lifespan are eventually impacted by this non-sinusoidal waveform. These inverters can be employed for low and medium power applications, while sinusoidal waveforms with less harmonics are needed for high power applications. Multilevel inverters (MLIs) are gradually replacing the old two level inverters. As staircase type voltage level (which looks like almost sine wave) can be synthesized with proper switching of the devices contained in numbers of H-bridges. More is the number of H-bridges, step level will be more and the waveform will look like sinusoidal. The introduction of high speed power semiconductor devices and the application of appropriate switching techniques allow for the elimination of lower and some higher order harmonics, improving fundamental component voltage and bringing total harmonic distortion (THD) of MLI inverters to an allowable level.

Amongst the different methods for systematically switching the power devices, space vector PWM and sinusoidal pulse width modulation (SPWM) techniques are frequently employed to regulate the output voltage waveform's amplitude and frequency.

This work uses simulation software matlab-simulink [18] with a unipolar switching scheme to examine the performance of a single-phase multicarrier based five level H-Bridge inverter employing SPWM (level shifting) approach with varied modulation indices. As mentioned, a multilayer inverter's voltage waveform is made up of numerous voltage steps that can be created by connecting various H-bridges in various ways, with each H-bridge having its own independent dc voltage source.

In general, multilayer inverters are helpful for high-power applications, and they are more efficient than traditional two-level inverters.

## 2. THEORETICAL BACKGROUND

### *2.1. Different PWM Techniques*

Power electronics and drive systems have seen a rise in the use of switching utilising PWM approaches.

No single PWM technique can be used for all applications. Several pulse-width modulation (PWM) approaches have been created for diverse industrial applications in accordance with the advanced technology in solid state power electronic devices and microprocessors.

The PWM approaches have been the focus of extensive research since the 1970s for the aforementioned reasons.

PWM's primary goals are to lower the output voltage's harmonic content and adjust the inverter's frequency and its output voltage.

Phase displacement control, Sinusoidal pulse width modulation, Harmonic Injection modulation, Single pulse width modulation, Multiple pulse width modulation, and Space Vector are just a few of the numerous PWM techniques.

The presence of medium and higher order harmonics in inverters using other methods, such as SHEPWM, limits the improvement of THD. The two PWM schemes that are most commonly used for multi-level inverters are the carrier based PWM (Sinusoidal PWM or SPWM) techniques and the space vector based PWM techniques.

The SPWM systems require relatively tiny size filters and are more adaptable and straightforward to apply.

By comparing a sinusoidal waveform with the necessary frequency to a triangle wave (Carrier signal) with a relatively high frequency, many pulses per half cycle are produced using this technique. For example, for five-level inverter- 4 carrier signals are required which may be of same frequencies or with varying frequencies with level shifting or phase shifting of carriers. In our study, level shifting with fixed carrier frequency has been used for a five level inverter (Figure 1).

### *2.2. A Brief of Unipolar Switching*

In contrast to bipolar switching, which switches the output between high and low, unipolar switching switches the output either from high (positive level) to zero or from low (negative level) to zero.

One such unipolar switching method is depicted in Figure 1. It employs the following switch controllers [4]:

When $v_{sine} > v_{tri}$, S1 is on, followed by

S2 when $-v_{sine} < v_{tri}$,

S3 when $-v_{sine} > v_{tri}$, and

S4 when $v_{sine} < v_{tri}$.

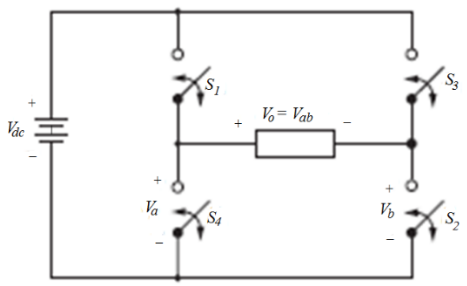


Figure 1 (a). H-bridge used for unipolar switching

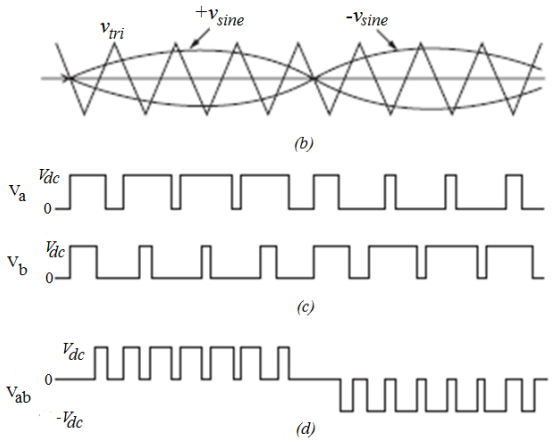


Figure 1. (b). PWM is created by comparing triangular carrier signals with a sinusoidal signal (the reference signal); (c) bridge voltages $V_a$ and $V_b$; and (d) output voltage $V_{ab}$.

When one switch in a pair is closed, the other is open, which is how complementary switching is done with switch pairs (S1, S4) and (S2, S3).

In Figure 1(a), voltages $V_a$ and $V_b$ alternate between $+V_{dc}$ and zero.

Figure 1(d) depicts the output voltage $V_o = V_{ab} = V_a - V_b$.

### *2.3. Traditional Single-Phase Half-Bridge Inverter*

Figure 2 (a) shows a traditional single phase half-bridge inverter with two levels that uses two MOSFETs and a single dc supply. Figure 2(b) displays the output voltage waveform for both resistive and inductive loads.

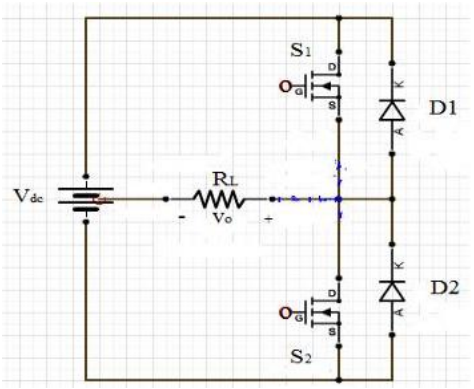


Figure 2(a). Traditional single phase half-bridge inverter with MOSFETs

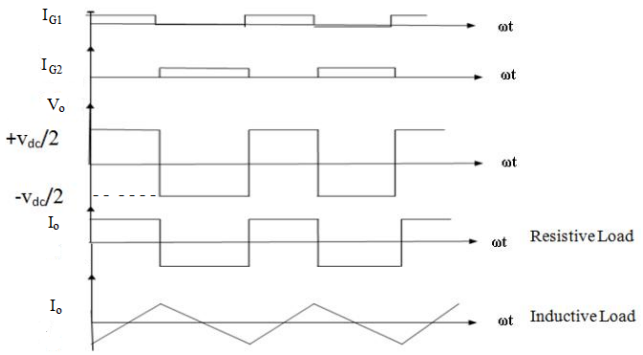


Figure 2 (b). Waveforms of voltage and current for resistive and inductive loads

In Figure 2(b), $I_o$ represents the current flowing through the load, and $I_{G1}$ and $I_{G2}$ are the gate currents of MOSFETs 1 and 2, respectively.
The switching time period of the devices can be altered to alter the frequency of the inverter output voltage. Each semiconductor device S1 and S2 is considered to conduct for the time that its gate pulse is present while under a resistive load and to commutate as soon as this gate pulse is removed, i.e., each switch conducts for a 180$^o$ conduction angle. The output wave patterns contain both lower order and higher order harmonics.
Even harmonic terms won't be present because of the waveform's quarter-wave symmetry; only odd harmonics will be present.
The following gives the formula for the instantaneous output voltage:

$$v_o(t) = \frac{2V_{dc}}{n\pi} \sin n\omega t, \quad \text{Where } n=1,3,5,\ldots \infty$$

The amplitude or peak of the nth component is,

$$V_n = \frac{2V_{dc}}{n\pi} = \frac{V_1}{n} \ldots\ldots\ldots\ldots\ldots\ldots (1)$$

The term $V_1 = \frac{2V_{dc}}{\pi}$ is the amplitude of fundamental component and common to all expressions for harmonic voltages. The harmonic factor $V_n/V_1$ is used to all formulas for harmonic voltages to obtain percentage of harmonics with respect to $V_1$.

According to Equation (1), the output voltage waveform contains harmonic frequencies that mostly affect the shape of the output voltage and are very challenging to filter out because they are close to the fundamental frequency. These frequencies include the third harmonic at 33.33%, the fifth harmonic at 20%, the seventh harmonic at 14.3%, and the ninth harmonic at 9.1%.

### *2.4. A Brief of Five-level Inverter and generation of PWM*

A five-level inverter is shown in Figure 3 [1, 5, 6, 7]. It uses two H-bridges connected in cascade. For generation of switching pulses using SPWM technique, a 50 Hz sinusoidal signal is compared with (m-1) i.e., four numbers triangular waves (Here m=5 for five level inverter) after level shifting of each carrier as shown in Figure 4. The switching pulses so generated are applied for switching on and switching off each power semiconductor devices (Here MOSFETs) in the H-bridges using unipolar switching scheme as mentioned above.

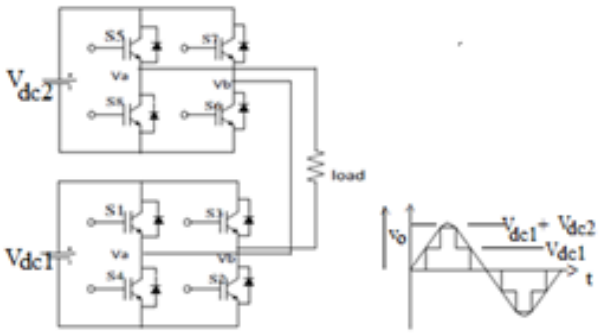


Figure 3. Cascaded five level H-bridge inverter

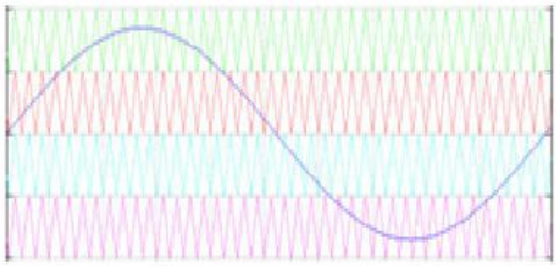

Figure 4. Level Shifted and In Phase Disposition (IPD) technique to generate switching pulses.

The output voltage's rms value is represented by

$$V_{rms} = V_{dc1}\left(\sum_{m=1}^{N_{p1}} \frac{P_{m1}}{\pi}\right)^{\frac{1}{2}} + V_{dc2}\left(\sum_{m=1}^{N_{p2}} \frac{P_{m2}}{\pi}\right)^{\frac{1}{2}},$$

Where,

$V_{dc1}$ and $V_{dc2}$ are respectively the dc source voltages of the two H-bridges,

$N_{p1}$ and $N_{p2}$ represent respectively the number of pulses per half cycle of the H-bridges, and

$P_{m1}$ and $P_{m2}$ represent respectively the width of the $m^{th}$ pulses of the H-bridges.

The output voltage of five level inverters employing the SPWM technique's harmonic analysis reveals that SPWM has the following significant characteristics.

1) The greatest harmonic amplitudes in the output voltage for modulation indices smaller than one are connected to harmonics of orders mf 1, where mf is the frequency modulation ratio.
   As a result, by increasing the number of pulses per half-cycle, it is possible to shift the main harmonic frequency's order to the higher side, where it may then be readily removed by a smaller filter.

   If mf is chosen even (unipolar switching), the other higher order harmonics with reduced amplitude associated with the output voltage waveform are mf $\pm$3…, 2mf $\pm$1, 2mf $\pm$3…, 3mf $\pm$ 3…, etc.; if mf is chosen odd (bipolar switching), the other higher order harmonics are mf $\pm$2, mf$\pm$ 4…, 2 mf $\pm$1, 2mf $\pm$3…, 3mf $\pm$2, etc.
2) Lower order harmonics become visible for modulation indices greater than 1, as the pulse width is no longer a sinusoidal function of the pulse's angular position.

Amplitude of fundamental is given by

V1 = mi. S.Vdc = 2mi.Vdc [S= no of H-bridges = 2 for five-level inverter and mi is the modulation index or amplitude modulation ratio]

Hence, mi controls the amplitude of the output voltage's fundamental frequency and is linearly proportional to mi as long as mi is less than 1.The amplitude of the fundamental increases with mi, but not linearly, if mi is bigger than 1.

## 3. SIMULATION RESULT

The MATLAB-SIMULINK simulation software [18] was used to simulate a single-phase five-level voltage source inverter circuit with two H-bridges similar to Figure 3. The carrier frequency was set to 1000 KHz, the modulating signal frequency to 50 Hz, and each voltage source was taken into consideration as being 100 V DC.

To determine the outcomes of the rms output voltage, fundamental voltage, harmonic voltages, and total harmonic distortion (THD), simulation has been done for various modulation indices. Figures 5, 6, and 7 display the MATLAB-SIMULINK simulation circuits. Figure 8 depicts the method for producing PWM pulses during simulation.

For various values of the modulation index mi, the values of the rms voltage, THD (In proportion with fundamental), fundamental, and other harmonic voltages are shown in Table I. Figures 9, 10, and 11 show visually how the rms voltage, fundamental voltage, THD, and other harmonic voltages vary for various values of the modulation index.

In Figures 12 and 13, the output voltage waveform for mi=0.8 is depicted without and with a filter, respectively.

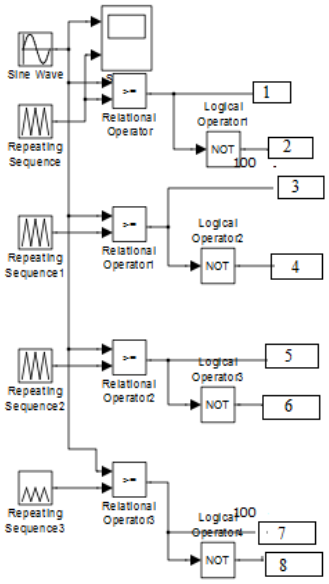


Figure 5. PWM Generation Circuit

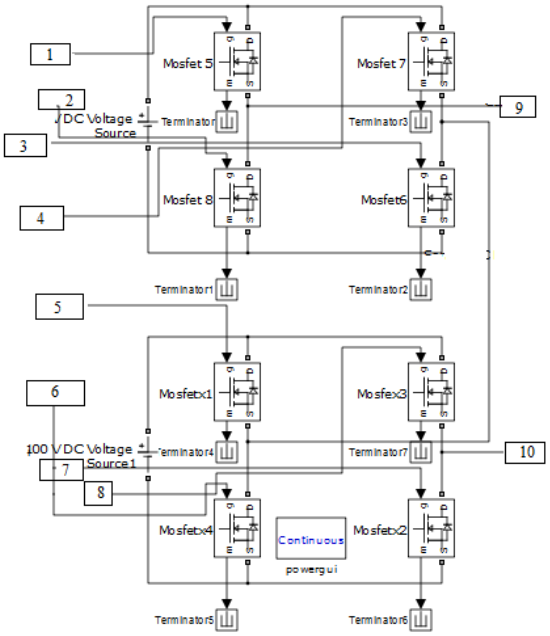


Figure 6. Main Inverter Circuit

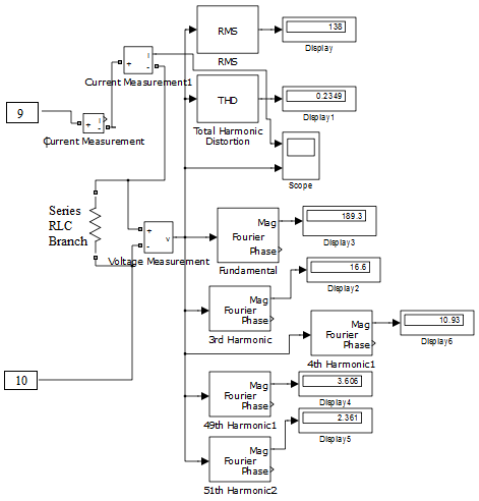


Figure 7. Different Parameter measurement Circuit

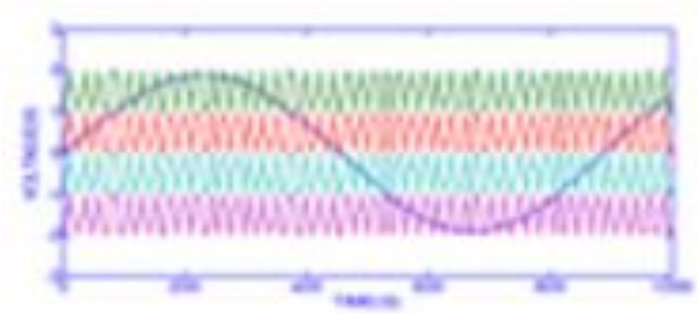

Figure 8. A Sinusoidal Signal is compared with different level shifted Carriers to generate PWM.

Table I. Showing effect of modulation index on THD and Harmonics.

| Mod Index | Value of different parameters | | | | | | | |
|---|---|---|---|---|---|---|---|---|
| | RMS Output Voltage (V) | Total Harmonic Distortion w.r.to Fundamental (%) | RMS Voltage of Fundamental (V) | RMS Voltage of 3rd harmonic (V) | RMS Voltage of 4th harmonic (V) | RMS Voltage of 49th harmonic (V) | RMS Voltage of 51st harmonic (V) | |
| 0.1 | 13.14 | 604.3 | 3.035 | 0.7884 | 0.1822 | 1.36 | 0.5179 | Without filter and only R load |
| 0.2 | 39.42 | 165.8 | 28.79 | 11.31 | 0.9083 | 9.645 | 7.071 | |
| 0.3 | 56.42 | 105.6 | 54.86 | 6.387 | 0.9706 | 5.853 | 5.269 | |
| 0.4 | 70.33 | 59.63 | 85.41 | 11.24 | 2.243 | 10.12 | 8.137 | |
| 0.5 | 78.13 | 40.89 | 102.3 | 2.059 | 0.9633 | 3.747 | 5.87 | |
| 0.6 | 82.79 | 35.31 | 110.4 | 7.926 | 0.4363 | 3.131 | 1.835 | |
| 0.7 | 99.12 | 37.27 | 131.3 | 5.203 | 0.9864 | 9.024 | 8.377 | |
| 0.8 | 114.4 | 33.73 | 153.3 | 1.91 | 1.525 | 5.675 | 10.5 | |
| 0.9 | 131.5 | 26.72 | 179.6 | 6.293 | 1.558 | 1.511 | 2.739 | |
| 1.0 | 141.3 | 21.72 | 195.2 | 3.34 | 1.837 | 2.457 | 3.597 | |
| 0.8 | 186.4 | 0.01 | 263.5 | 0.3583 | 0.228 | 0.103 | 0.1035 | With LC Filter and R load |
| 0.9 | 211.8 | 0.907 | 299.6 | 2.47 | 1.022 | 0.426 | 0.422 | |
| 1.0 | 232.7 | 0.8 | 329.1 | 2.247 | 0.4935 | 0.2816 | 0.284 | |

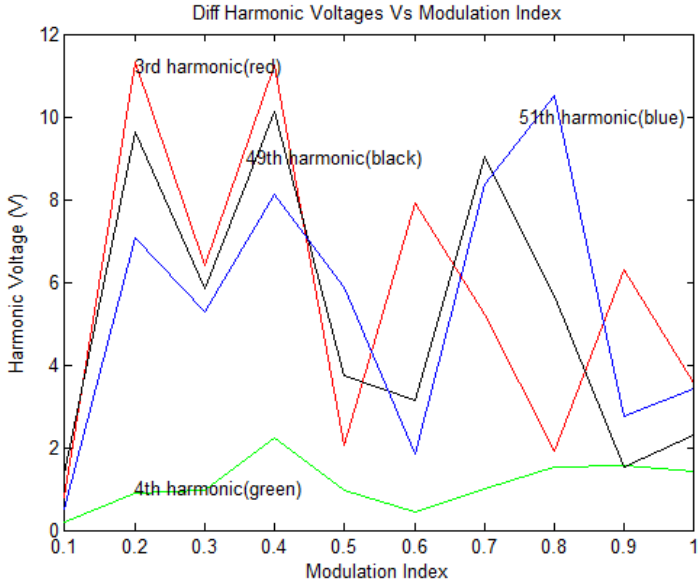


Figure 9. Different harmonic voltages with respect to different mi

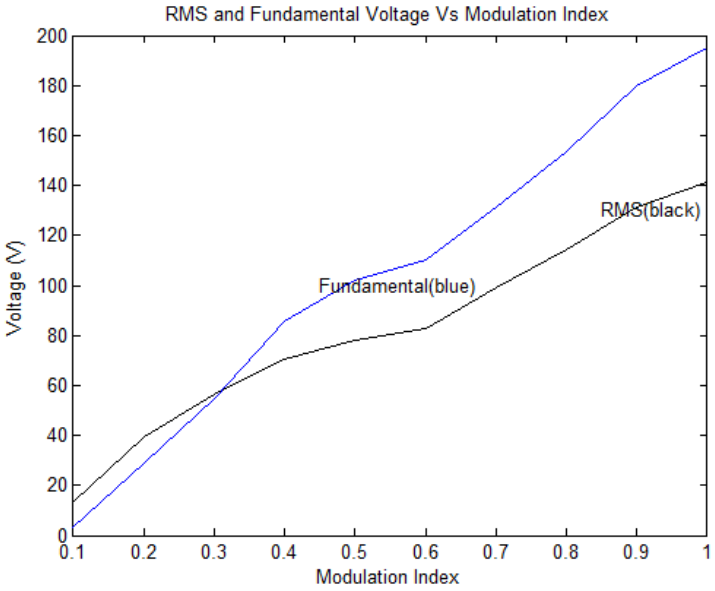


Figure 10. RMS and Fundamental Voltages.

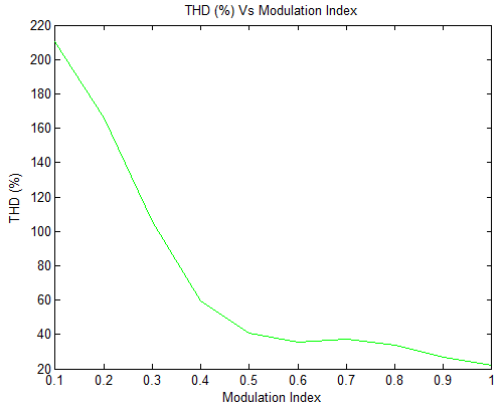


Figure 11. THD versus different modulation index

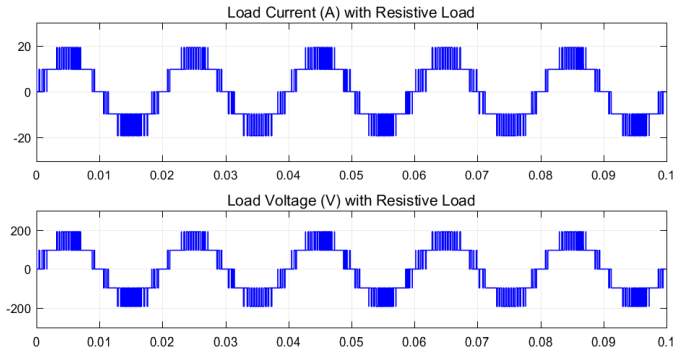


Figure 12. Load current and voltage waveform without filter

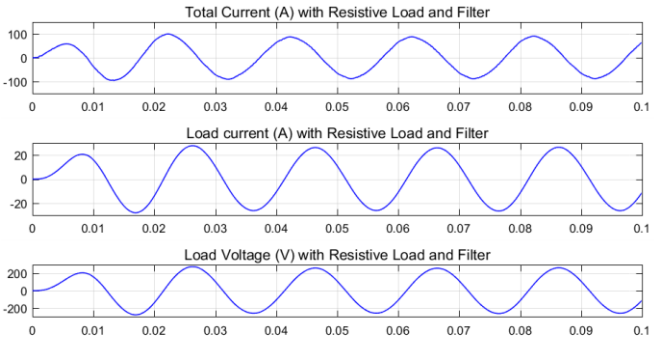


Figure.13. Load current and voltage waveform with filter

## 4. CONCLUSION

In order to reduce total harmonic distortion (THD), a single-phase, five-level cascaded H-Bridge inverter was designed. This research also examines the impact of modulation index on THD and the various harmonics present in the output voltage waveform.

According to the simulation results displayed in Figures 8, 9, and 10, the third harmonic has been dramatically reduced for mi=0.8, 0.9, and 1.0 from 33% (in the case of a typical two-level inverter) to 0.12%, 1.12%, and 0.8%, respectively. The THD decreased from 48.43% (in the case of a traditional two-level inverter) to 0.01%, 0.907%, and 0.8% for mi=0.8, 0.9, and 1.0, respectively. The current and voltage waveforms for resistive load and with low pass filter are almost sinusoidal. The fundamental voltage varies almost linearly as modulation index increases from 0.1 to 1.0.

## 5. ACKNOWLEDGMENT

The authors would like to express their gratitude to professors (Dr.) P.K. Sinha Roy and (Dr.) K. K. Ghosh of the Institute of Engineering and Management in Kolkata for their unfailing assistance and direction in advancing this research endeavor.

## 6. REFERENCES

[1] Gautam Ghosh, P K Sinha Roy, Rajiv Ganguly, " Performance of Cascaded H-Bridge multilevel Inverters of Different Levels and with different Modulation Index, IOSR Journal of Electrical and Electronics Engineering (IOSR-JEEE) e-ISSN: 2278-1676, p-ISSN: 2320-3331, Volume 14, Issue 2 Ser. I (Mar. – Apr. 2019), PP 08-15.

[2] Mohamed S. A. Dahidah, Georgios Konstantinou, Vassilios G. Agilities "A Review of Multilevel Selective Harmonic Elimination PWM: Formulations, Solving Algorithms, Implementation and Applications" IEEEE Transactions on Power Electronics, Vol. 99, Early Access, pp 1-16.

[3] Muhammad H. Rashid, "Power Electronics", and ISBN: 978-93-325-1844-5, Publisher: Pearson.

[4] Daniel W. Hart, "Power Electronics", ISBN-13: 978-0-07-132120, Publisher: McGraw Hill Education (India) Private Limited.

[5] Gautam Ghosh, P K Sinha Roy, Rajiv Ganguly. "Selective Harmonic Elimination in a Conventional Single Phase Full-Bridge Inverter with Adjustable Output", IOSR Journal of Electrical and Electronics Engineering (IOSR-JEEE) e-ISSN: 2278-1676, p-ISSN: 2320- 3331, Volume 13, Issue 4 Ver. II (Jul. – Aug. 2018), PP 51-57.

[6] Gautam Ghosh et. el., "*A* Comparative study of different multilevel inverters", 2017 1st International Conference on Electronics, Materials Engineering and Nano-Technology (IEMENTech), ISBN**:** 978-1-5386-1703-8

[7] Gautam Ghosh et. el., Selective harmonic elimination in a conventional inverter", 2017 8th Annual Industrial Automation and Electromechanical Engineering Conference (IEMECON), ISBN**:** 978-1-5386-3371-7

[8] Static Inverter with Neutralization of Harmonics, A. Kernick, J. L. Roof, T. M. Heinrich. AIEE Transactions, Pt. II (Applications and Industry), Vol. 81, May 1962. Pp. 59-68. Power Electronics. 12(6). pp. 971-982.

[9] J. N. Chiasson, L .M . Tolbert, K. J. McKenzie, and Z. Du (2004). A Complete Solution to the Harmonic Elimination Problem. IEEE Transaction on Power Electronics. 19. pp. 491-499.

[10] J.R. Wells, X. Geng, P.L. Chapman, P.T. Krein, and B.M. Nee (2007, Jan). Modulation-Based Harmonic Elimination. IEEE Transactions on Power Electronics. 22(1). pp. 336-340.

[11] Selective Harmonic Elimination of Single-Phase Voltage Source Inverter using Algebraic Harmonic Elimination Approach, https://www.researchgate.net.

[12] Gopesh Joshi; M. Bala Krishna. "Solving System of Non- Linear Equations using Genetic Algorithm", 2014 International Conference on Advances in Computing, Communications and Informatics (ICACCI), ISBN**:** 978-1-4799-3080-7.

[13] Gautam Ghosh et. el., "Six Lower Order Harmonics Elimination From Output Voltage Waveform Of Single Phase Full Bridge Conventional Inverter With Adjustable Output", 2019 IEEE 9th Annual Computing and Communication Workshop and Conference (CCWC), ISBN**:** 978-1-7281-0554-3.

[14] Kumara Sastry, David Goldberg, Graham Kendall, GENETIC ALGORITHMS.

[15] Gautam Ghosh et. el., " Finding Optimum Switching Angles Using Genetic Algorithm for SHE-PWM Two-Level Inverter", 2019 3rd International Conference on Electronics, Materials Engineering & Nano-Technology (IEMENTech), ISBN**:**978-1-7281-5543-2.

[16] Gautam Ghosh, Rajiv Ganguly, "Optimum Switching Angles For Multilevel SHE-PWM Inverter Using Genetic Algorithm", 2020 4th International Conference on Electronics, Materials Engineering & Nano-Technology (IEMENTech), ISBN:978-1-7281-9287-1.

[17] Gautam Ghosh, Rajiv Ganguly, " Control of Output Voltage with Elimination of Four Lower Order Harmonics in Single Phase Eleven-Level Cascaded H-Bridge Inverter", IOSR Journal of Electrical and Electronics Engineering (IOSR-JEEE) e-ISSN: 2278-1676, p-ISSN: 2320-3331, Volume 16, Issue 3 Ser. II (May – June 2021), PP 55-60.

[18] MATLAB R2017a and Optimization Toolbox, the Math Works, Inc., Natick, Massachusetts, United States.

## Biographies

**Gautam Ghosh** received the M. Tech degree from Indian Institute of Technology, Kharagpur/India and serviced in industry from 1978 to 2012 and 6then joined as assistant professor in Institute of Engineering and Management/Kolkata/India where he is still working as faculty in the Eletronics and Communication Engineering department. Presently he is pursuing Ph.D in University of Engineering and Management/Kolkata/India.He is a fellow member of Institution of Engineers (India). His current research area include power electronics, industrial automation, instrumentation, motor drives.

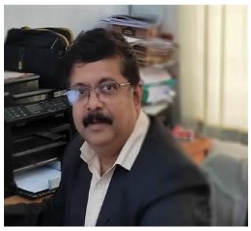

**Rajiv Ganguly** is currently a professor at the University of Engineering and Management, Kolkata. He obtained his Ph.D. in Engineering from the Jadavpur University – Kolkata, India. He has published a number of papers in Refereed Journals and chapters in books, and participated in a range of forums on solid state lighting, VLSI and IOT. His areas of interest include Solid State Lighting, VLSI and IOT.

# Null Placement in Uniform Linear Array by Phase Control of Edge Elements

**Sandipan Mitra**[1], **Soumyo Chatterjee**[2], **Sayan Chatterjee**[3]

[1]*Dept. of ECE, Institute of Engineering and Management, Kolkata-700091, India*
[2]*Dept. of ECE, Heritage Institute of Technology, Kolkata-700107, India*
[3]*Dept. of ETCE, Jadavpur University, Kolkata-700032, India*
*e-mail: (sandipanmitra97@gmail.com, soumyo.chatterjee@heritageit.edu and sayan1234@gmail.com)*

## Abstract.

This paper presents a novel method of null placement by controlling only the excitation phase of the edge elements of a uniformly excited linear antenna array. Antenna parameters such as directivity, First Null Beam Width (FNBW) and Half Power Beam Width (HPBW) are obtained analytically through array synthesis. Then the pattern gets degraded due to the required null placement. Subsequently to enhance the pattern, antenna parameters and to find out the optimum value of the excitation phase, suitable evolutionary algorithm has been employed. The whole simulation is carried out using a 10-element uniform, linear antenna array by two different approaches to comparatively study the effects.

**Keywords**. Null placement, Phase control, Edge element, Array symmetric method, Classical DE algorithm

## INTRODUCTION

In the modern era of communication system, a major role is played by antenna. Starting from Wi-Fi, Bluetooth, GPS, etc. to RADAR, SONAR, UAVs to Satellite Communications, every single wireless gadget requires an antenna and more specifically an antenna array [1]. But the objective of an antenna is not restricted to just transmitting and receiving signals, it should also be able to optimize radiated energy in some particular required direction and should be able to suppress it in other directions. Although the antenna directivity can be increased by increasing the number of array elements or by reducing the inter element spacing [2] but still suppression of unwanted signals is very essential for further increase in directivity. Generally, this suppression of unwanted signals is done by masking the interference signal from a particular direction. This method of masking is known as null placement and in earlier times researchers used to place nulls analytically [3-6], but later researchers found out that due to this analytical placement of null, various antenna parameters are deteriorating and moreover multiple null and wide null cannot be placed analytically. This gave rise to the use of evolutionary algorithms to overcome the limitations.

Researchers started applying evolutionary algorithms to overcome limitation in the form of pattern degradation of antenna array with null placements. Accordingly, Goudos et.al. [7] in his research work has compared different evolutionary algorithms by applying them to antenna design related problems. Then he concluded from the results that he found out, that Genetic Algorithms (GA), Particle Swarm Optimization (PSO) and Differential Evolution (DE) algorithms are some of the most popularly used algorithms in antenna design. His results also suggest that classical DE is one of the simplest and efficient among the three. Using this result, later Mathur et.al. [8] proposed a null placing method using PSO algorithm in uniform linear array and they obtained desirable results. This supports the results obtained by Goudos et.al. Another method of null placement has been discussed by researchers Hamza et.al. [9] in their work. It uses Genetic Algorithm along with the method suggested by Schelkunoff in order to increase the speed of beam steering and they also observed an improvement in the radiation pattern of the array and an increased accuracy in null placement. But they had done it for circular array. In the recent years' researchers Jamunaa et.al. [10] had worked on this null placement method with uniform linear array. They had approached with phase only control method where they had kept the amplitude of all the elements uniform and used evolutionary algorithm to optimize the phase of all the elements in order to place accurate null. From the results it was concluded that they could successfully place nulls. But they had done this method only for single null placement and they concluded that their work can be further studied and extended for multiple null. Chatterjee et.al. [11] in their work also, proposed a novel least perturbation based method of constrained null placement for a non-uniformly excited linear antenna array. They have carried out their work by controlling the excitation amplitude and phase of the edge elements which makes the antenna design less complex. But antenna array synthesis can also be done only by controlling the phase and keeping amplitude constant which reduces the runtime as well as cost.

So, these research works lead to the motivation of our method of null placement which has been discussed in this paper. So in the proposed method, only the phase of the edge elements is controlled. This has two advantages. Firstly, there is no requirement of attenuator which makes the appliance using the antenna array lighter and cheaper. And secondly, the design becomes simpler. Moreover, a uniformly excited linear antenna is taken so that the design time and complexity also reduces. The design of this antenna array has been approached by two methods. At first, the conventional method which gave rise to some drawbacks which leads to the second method of array symmetry. The analytical results are then optimized using classical DE algorithm which in turn improves the value of radiation parameters and optimizes the value of phase.

## PROPOSED METHOD

### *First Approach: Conventional Method*

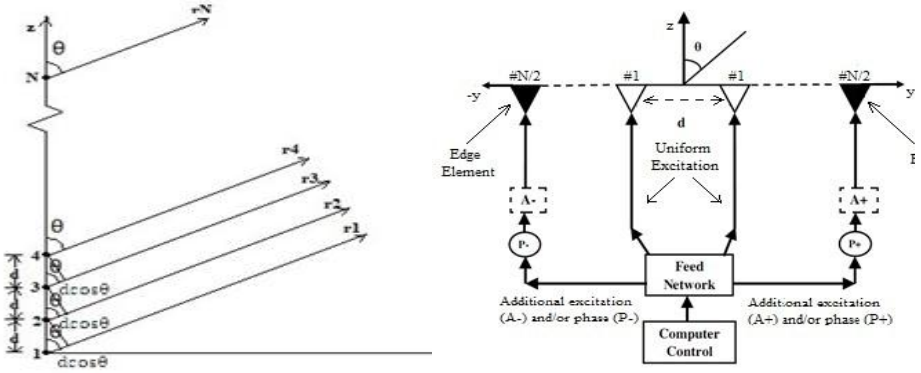


**(a)** **(b)**

Figure 2.1 Conventional Uniform Linear Array (a) Geometry, (b) Schematic diagram of edge element control

When a uniform linear array of N number of isotropic elements placed along the z-axis then the far field observation obtained is shown in Figure 2.1(a). So, the array factor of uniform linear array is given by equation (2.1),

$$\mathrm{AF}(\theta) = \left[e^{+j0(kd\cos\theta+\beta)} + e^{+j1(kd\cos\theta+\beta)} + e^{+j2(kd\cos\theta+\beta)} + \cdots + e^{+j(N-1)(kd\cos\theta+\beta)}\right] \tag{2.1}$$

$$\mathrm{AF}(\theta) = \left[\sum_{n=1}^{N} e^{j(n-1)(kd\cos\theta+\beta)}\right] \tag{2.2}$$

Now, let us assume $\psi = kd\cos\theta + \beta$, then the equation (2.2) will become,

$$\mathrm{AF}(\theta) = \left[\sum_{n=1}^{N} e^{j(n-1)\psi}\right] \tag{2.3}$$

In order to make the array factor more compact, both sides of the equation (2.3) is multiplied by $e^{j\psi}$, and the modified array factor is given by equation (2.4).

$$\mathrm{AF}(\theta)e^{j\psi} = \left[e^{j\psi} + e^{j2\psi} + \cdots + e^{j(N-1)\psi} + e^{jN\psi}\right] \tag{2.4}$$

Equation (2.3) is then subtracted from equation (2.4), and the expression becomes,

$$\mathrm{AF}(\theta)\left(e^{j\psi} - 1\right) = \left(-1 + e^{jN\psi}\right) \tag{2.5}$$

$$\mathrm{AF}(\theta) = e^{j\left[\frac{(N-1)}{2}\right]\psi}\left[\frac{\sin\left(\frac{N}{2}\psi\right)}{\sin\left(\frac{\psi}{2}\right)}\right] \tag{2.6}$$

Now, by taking the physical center of the array as the reference point, then the array factor in equation (2.6) will be reduced to,

$$\mathrm{AF}(\theta) = \left[\frac{\sin\left(\frac{N}{2}\psi\right)}{\sin\left(\frac{\psi}{2}\right)}\right] \tag{2.7}$$

The schematic diagram of edge element control in uniform linear array is shown in Figure 2.1(b). Array factor of N numbered linear array with uniform excitation is given by the equation (2.7) in which wave number $k = \frac{2\pi}{\lambda}$, where $\lambda$ is incident wave length, inter element spacing $d = \frac{\lambda}{2}$, and $\theta$ is the elevation angle. Array factor can be considered as the summation of array factor due to rest of the elements $AF_R(\theta)$ as represented by equation (2.9) and array factor due to edge elements $AF_E(\theta)$ which is represented by equation (2.10), and here $\psi = kd(\sin\theta - \sin\theta s)$.

$$AF(\theta) = AF_R(\theta) + AF_E(\theta) \tag{2.8}$$

$$AF_R(\theta) = \left[\frac{\sin\left(\frac{(N-2)}{2}\psi\right)}{\sin\left(\frac{\psi}{2}\right)}\right] \tag{2.9}$$

$$AF_E(\theta) = e^{j\left(\frac{N-1}{2}\right)\psi} + e^{-j\left(\frac{N-1}{2}\right)\psi} = 2\cos\left[\left(\frac{N-1}{2}\right)\psi\right] \tag{2.10}$$

Additional control for null placement are only the phases -P and +P that are being fed directly to the edge elements because amplitude is constant, so, A=1. So, the modified array factor contribution due to edge elements ($AF_E(\theta)|_m$) is given by equation (2.11).

$$AF_E(\theta)|_m = e^{-j(-P)}e^{-j\left(\frac{N-1}{2}\right)\psi} + e^{-jP}e^{j\left(\frac{N-1}{2}\right)\psi} \tag{2.11}$$

As the array is assumed to be symmetric, so –P = +P = P. So on adding the terms the equation (2.11) becomes equation (2.12).

$$AF_E(\theta)|_m = 2\cos\left[\left(\frac{N-1}{2}\right)\psi - P\right] \tag{2.12}$$

Consequently, modified array factor along is given by equation (2.13).

$$AF(\theta)|_m = AF_R(\theta) + AF_E(\theta)|_m \tag{2.13}$$

Now $\theta_n$ be the desired single null position in which total array factor $AF(\theta)|_m$ is considered as zero to achieve the desired result, which provides the final expression for array factor in equation (2.14). Then by substituting $\theta = \theta_n$ in equation (2.14) and solving, the required value of P is obtained in equation (2.15) where $\psi_n = kd(\sin\theta_n - \sin\theta_s)$.

$$AF(\theta)|_m = \left[\frac{\sin\left(\frac{(N-2)}{2}\psi\right)}{\sin\left(\frac{\psi}{2}\right)}\right] + 2\cos\left[\left(\frac{N-1}{2}\right)\psi - P\right] \tag{2.14}$$

$$P = -\frac{\pi}{2} + \frac{(N-1)\psi_n}{2} + \sin^{-1}\left(-\frac{\sin\left(\frac{(N-2)}{2}\psi_n\right)}{2\sin\left(\frac{\psi_n}{2}\right)}\right) \tag{2.15}$$

But this method has a drawback which is illustrated with an example in Figure 2.2 (a), (b). All the array factor plots have been simulated for 10 elements array, with 0.5λ inter element spacing beam steered at 20° and the null has to be placed at -34°. It must be noted that as isotropic elements are considered in the present investigation, the array factor plot itself represents the radiation pattern of the array.

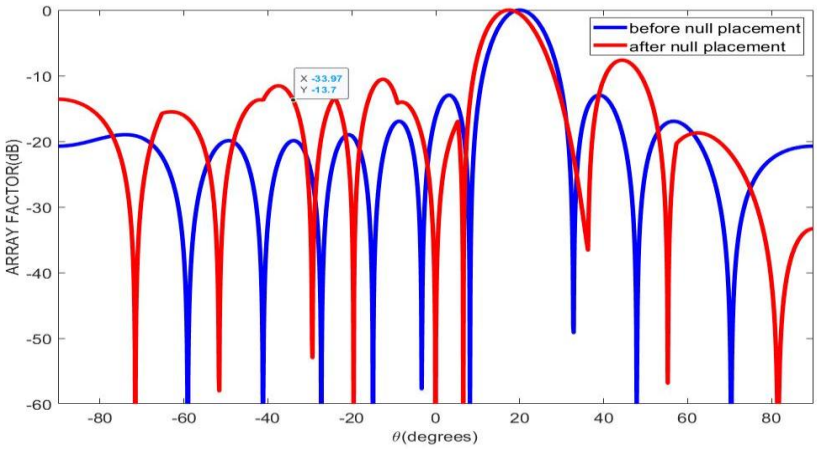


**(a)**

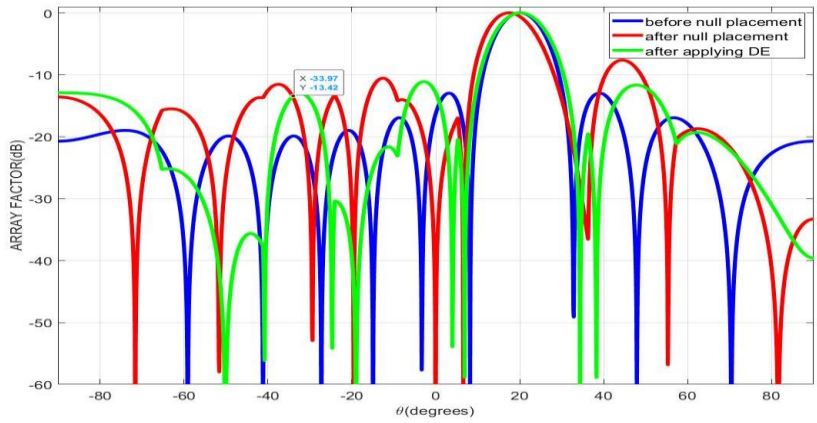


**(b)**

Figure 2.2 Conventional Uniform Linear Array Factor Null Placement at -34° (a) Analytical, (b) Using DE

It is observed from Figure 2.2 that no null is placed exactly at -34° and it has shifted towards -30°. Neither it could be placed analytically nor it could be rectified by applying DE. The reason behind this observation is that there are too many assumptions taken in this method such as the actual antenna array center is not at the origin, but during the mathematical calculations the physical center of the array is taken as the reference point for which the phasor part of the equation gets cancelled. So the algorithm cannot find the value of phase at certain points and hence it could not place the null properly resulting in the shift. This led the proposed method towards the second approach.

***Second Approach: Array Symmetric Method***

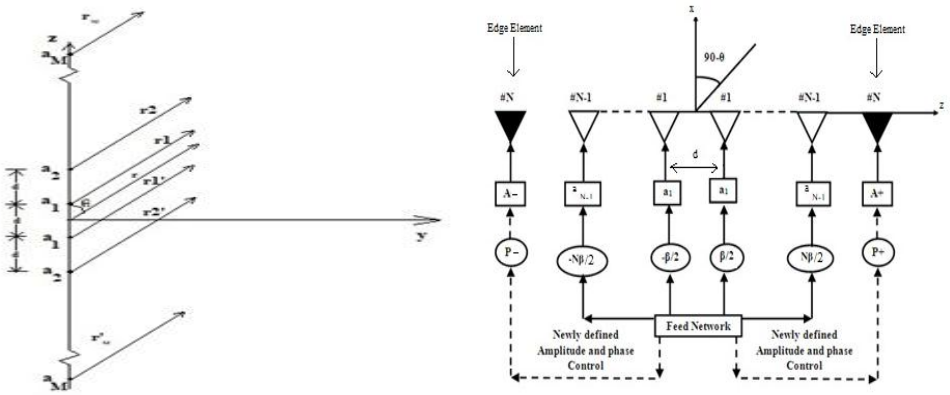


**(a)** **(b)**

Figure 2.3 Non-Uniform Symmetric Linear Array (a) Geometry, (b) Schematic diagram of edge element control

Generally, all the array elements in a non-uniform linear array have different excitation amplitudes. But in this proposed approach, all the excitation amplitude ($a_n$) values are set as 1, which makes the non-uniform linear array work as a uniform linear array. Since in this method already the antenna array is placed symmetrically along the z-axis so the actual center of the array already lies at the origin. So no assumption is required in this approach. Figure 2.3(a) shows the geometry of linear symmetric array. The array factor of linear array of 2N isotropic element is given by equation (2.16), where $k = 2\pi/\lambda$ is the wave number, $a_n$ is the excitation amplitude of nth element, d is the inter-element spacing.

$$AF(\theta) = 2\sum_{n=1}^{N} \cos\left[\left(\frac{2n-1}{2}\right) kd(\cos\theta)\right] \tag{2.16}$$

Figure 2.3(b) shows the schematic diagram of edge element control in non-uniform linear array. So, the array factor expression for 2N numbered beam steered uniformly excited linear array is given by equation (2.17).

$$AF(\theta) = 2\sum_{n=1}^{N} \cos\left[\left(\frac{2n-1}{2}\right) \psi\right] \tag{2.17}$$

Here, $\psi = kd(\sin\theta - \sin\theta_s)$, where $\theta_s$ represents the steered main beam position. Further, d is the uniform inter element spacing, $k=2\pi/\lambda$ is the wave number and θ is the elevation angle whose value lies within $-\pi/2$ to $+\pi/2$. Moreover, edge element contribution can be generalized as given in equation (2.18).

$$AF(\theta) = AF(\theta)|_{Rest} + AF(\theta)|_{Edge} \tag{2.18}$$

In equation (2.18), $AF(\theta)|_{Rest}$ and $AF(\theta)|_{Edge}$ has been given in equation (2.19) and (2.20) respectively.

$$AF(\theta)|_{Rest} = 2\sum_{n=1}^{N-1} \cos\left[\left(\frac{2n-1}{2}\right) \psi\right] \tag{2.19}$$

$$AF(\theta)|_{Edge} = 2\cos\left[\left(\frac{2N-1}{2}\right)\psi\right] \quad (2.20)$$

So, the edge elements for the linear array are directly fed with additional excitation phase -P and +P to the left and right edge element respectively. Consequently, modified array factor ($AF(\theta)|_{Edge\_m}$) for 2N numbered linear array is given by equation (2.21).

$$AF(\theta)|_{Edge\_m} = e^{-j(-P)}e^{-j\left(\frac{2N-1}{2}\right)\psi} + e^{-jP}e^{j\left(\frac{2N-1}{2}\right)\psi} \quad (2.21)$$

As the array is symmetric so by substituting P+ = P- = P in equation (2.21) the modified array factor is given by equation (2.22).

$$AF(\theta)|_{Edge\_m} = 2\cos\left[\left(\frac{2N-1}{2}\right)\psi - P\right] \quad (2.22)$$

Accordingly, the modified array factor of the complete array is given by equation (2.23).

$$AF(\theta)|_{modified} = 2\sum_{n=1}^{N-1}\cos\left[\left(\frac{2n-1}{2}\right)\psi\right] + 2\cos\left[\left(\frac{2N-1}{2}\right)\psi - P\right] \quad (2.23)$$

Now $\theta_n$ be the desired single null position in which total array factor $AF(\theta)|_{modified}$ is considered as zero to achieve the desired result. So, by substituting $\theta = \theta_n$ in equation (2.23) and solving, the required value of P is obtained in equation (2.24) where $\psi_n = kd(\sin\theta_n - \sin\theta_s)$.

$$P = -\frac{\pi}{2} + \frac{(2N-1)\psi_n}{2} - \sin^{-1}\left(\sum_{n=1}^{N-1}\cos\left[\left(\frac{2n-1}{2}\right)\psi_n\right]\right) \quad (2.24)$$

Hence, the effectiveness of the proposed method has been illustrated in Figure 2.4 (a), (b) through design instances of a 10 elements linear array with main beam position at 20°. Single null placement at -34° has been considered. The inter element spacing has been kept at 0.5λ.

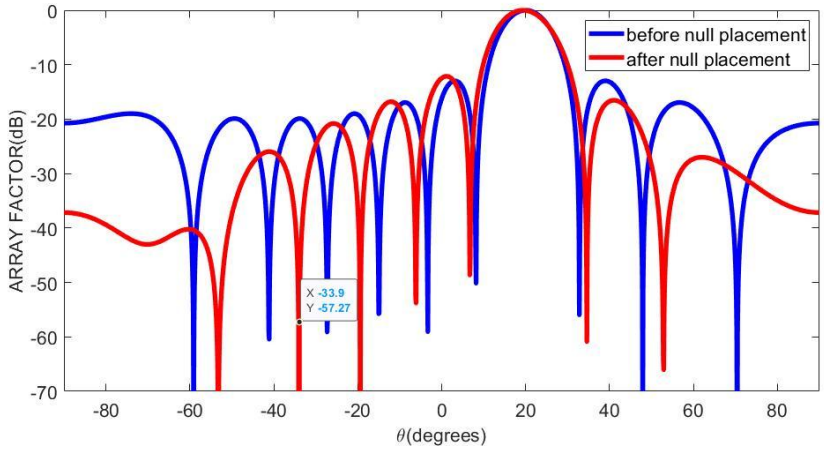


**(a)**

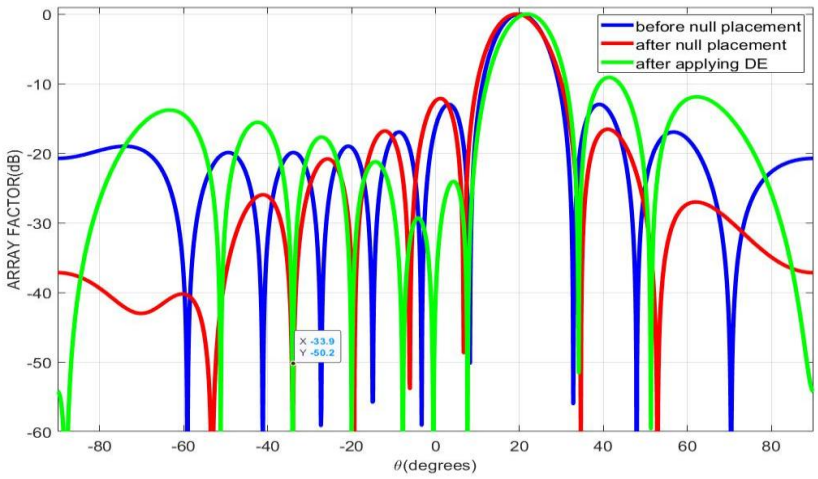


**(b)**

Figure 2.4 Uniform Symmetric Linear Array Factor Null Placement at -34° (a) Analytical, (b) Using DE

From Figure 2.4 it is observed that null can be exactly placed where it is required which in this case is -34°, both analytically and by applying DE. The convergence curve in Figure 2.5 also shows that this is the best fit value.

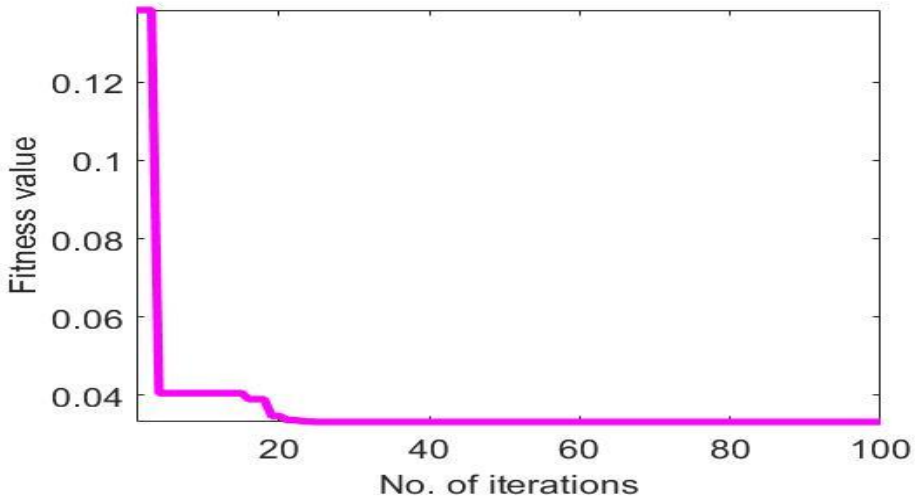


Figure 2.5 Convergence curve of Uniform Symmetric Linear Array Factor with Null at -34°

Multiple null placement can also be achieved by this proposed method of symmetric array. Such an example has been illustrated in Figure 2.6 through design instances of a 10 elements

linear array with main beam position at 20°. One null placed at -34° while the other at -9°. The inter element spacing has been kept at 0.5λ.

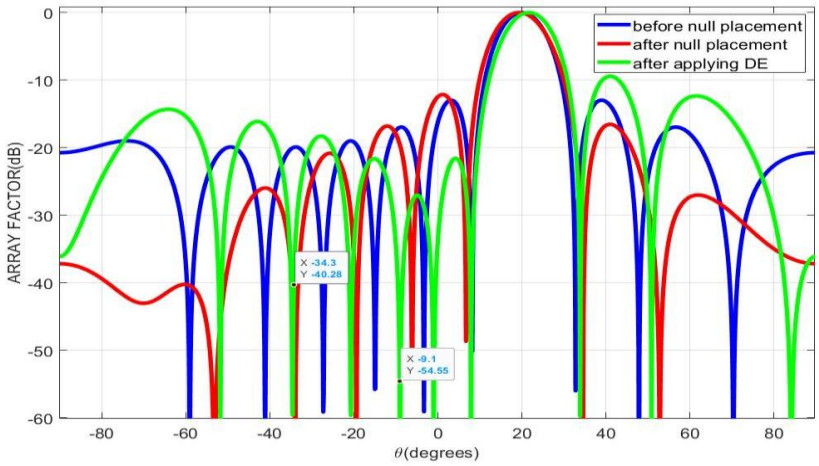


Figure 2.6 Uniform Symmetric Linear Array Factor with Null placed at -34° and -9°

The convergence curve in Figure 2.7 also shows that this is the best fit value. While Table 2.1 shows the comparative study of parametric effect, before and after the application of DE and for both single as well as multiple null.

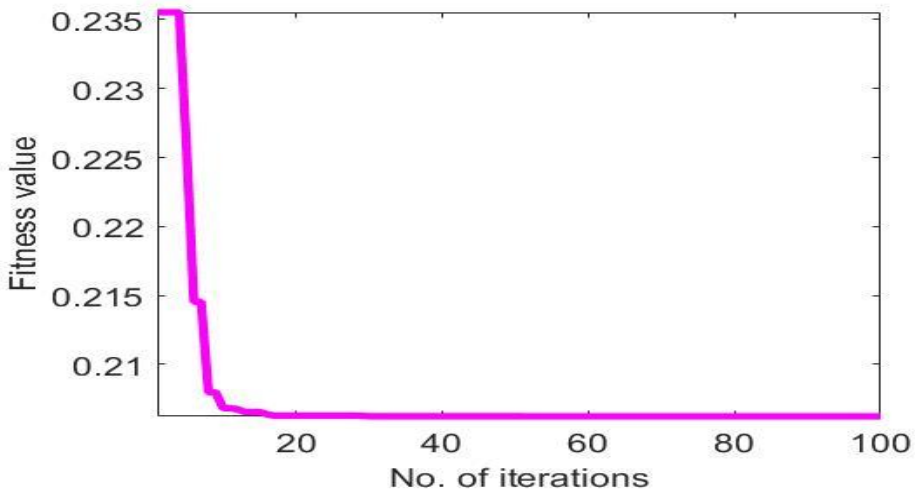


Figure 2.7 Convergence curve of Uniform Symmetric Linear Array Factor with Null at -34° and -9°

Table 2.1 Parametric effect on radiation characteristics before and after applying DE

| | **HPBW (in degrees)** | **FNBW (in degrees)** | **Directivity (in dB)** | **Optimized phase (in terms of wavelength)** |
|---|---|---|---|---|
| **Before Null Placement** | **10.8** | **24.5** | **10** | **-** |
| **After Analytical Null Placement** | **11.9** | **27.6** | **9.7199** | **13.0323** |
| **After applying DE for Single Null** | **11.1** | **26.2** | **9.7212** | **0.8971** |
| **After applying DE for Multiple Null** | **11.1** | **25.7** | **9.7198** | **0.7935** |

## CONCLUSION

This article demonstrates the method of phase control of edge elements through array symmetric approach for null placement analytically. The effectiveness of the design has been illustrated using an example of 10 elements array. Further performance improvement of the method has been carried out using classical DE algorithm. Thus from the results obtained it can be observed that the proposed method can perfectly place null, both single as well as multiple as well as it can improve the radiation parameters values which deteriorated due to analytical null placement. And last but not the least, this proposed method can perfectly optimize the value of excitation phase. Hence, it can be concluded that the proposed method is fit for single and multiple null placement and has the ability to handle multiple objectives. So, it can be used to design linear antenna arrays for any number of array elements.

**Acknowledgement** This work is supported by Scientific Education Research Board; Government of India vide sanction letter number: CRG/2020/000917.

## REFERENCES

[1] C.A. Balanis, 'Antenna theory: analysis and design', John wiley & sons; 2015 Dec 28.

[2] K.P. Dutta, 'Study of Broadside Linear Array Antenna with Different Spacing and Number of Elements', International Journal of Advanced Engineering Research and Science. 2017;4(5), p. 237181.

[3] S.A. Schelkunoff, 'A mathematical theory of linear arrays', The Bell System Technical Journal. 1943 Jan;22(1), pp. 80-107.

[4] S. Applebaum, 'Adaptive arrays', IEEE Transactions on Antennas and Propagation. 1976 Sep;24(5), pp. 585-98.

[5] I.S. El-Azhary, M.S. Afifi, P.S. Excell, 'A simple algorithm for sidelobe cancellation in a partially adaptive linear array', IEEE transactions on antennas and propagation. 1988 Oct;36(10), pp. 1482-6.

[6] T.H. Ismail, M.M. Dawoud, 'Null steering in phased arrays by controlling the element positions', IEEE Transactions on Antennas and Propagation. 1991 Nov;39(11), pp. 1561-6.

[7] S.K. Goudos, C. Kalialakis, R. Mittra, 'Evolutionary algorithms applied to antennas and propagation: A review of state of the art', International Journal of Antennas and Propagation. 2016 Aug 25;2016.

[8] A. Mathur, T.A. Ajith, S. Saxena, 'Antenna Design Optimization with Desired Null Placement Using Particle Swarm Optimization Algorithm', 2018 International Conference on Advances in Computing, Communication Control and Networking (ICACCCN) 2018 Oct 12 (pp. 768-773). IEEE.

[9] A. Hamza, H. Attia, 'Fast beam steering and null placement in an adaptive circular antenna array', IEEE Antennas and Wireless Propagation Letters. 2020 Jul 17;19(9), pp. 1561-5.

[10] D. Jamunaa, G.K. Mahanti, F.N. Hasoon, 'Synthesis of phase-only position optimized reconfigurable uniformly excited linear antenna arrays with a single null placement', Journal of King Saud University-Engineering Sciences. 2020 Sep 1;32(6), pp. 360-7.

[11] S. Chatterjee, B. Bandyopadhyay, S. Chatterjee, A. Majumdar, 'Least Perturbation Based Method of Multi-Objective Null Placement in Linear Antenna Array using Evolutionary Algorithms', Radioengineering. 2022 Sep 1;31(3), p. 431.

## Biographies

**Sandipan Mitra** was born in Kolkata in 1997. He received the bachelor's degree in electronics and communication engineering from University of Engineering and Management, Kolkata in 2020, the master's degree in electronics and communication

engineering from Institute of Engineering and Management, Kolkata in 2022, respectively. His research areas include patch antennas, antenna arrays, and body mounted antennas.

**Soumyo Chatterjee** was born in Bolpur, West Bengal, India, in 1981. He received his B. Tech in Electronics and Communication Engineering from BIET, Suri, India in 2005. He completed his master's degree from ETCE Department of Jadavpur University, India in 2009. He has completed his Ph.D. degree from Jadavpur University on the topic of pattern synthesis of antenna array using evolutionary algorithms in January 2020. He is presently working as an Assistant Professor in the Department of ECE Heritage Institute of Technology, India. His research interests are antenna array, RF device modelling, evolutionary algorithms.

**Sayan Chatterjee** was born in Kolkata, India, in 1980. He received BE degree (gold medal) in 2003 and received ME degree in 2005. He has completed his Ph.D. degree in 2015 from Jadavpur University. He has worked in SAMEER, India, as a Scientist and was involved in the design of various strategic microwave subsystem and systems from 2005 to 2009. He was deputed to California Institute of Technology, Northridge in 2007 as visiting scholar. Presently he is an Associate Professor in the Department of ETCE at Jadavpur University, Kolkata. He has received AICTE Carrier award for young teacher in 2015. He is a senior member of IEEE since 2008 and was served as treasurer and secretary of the IEEE Kolkata section from 2014 to 2017. His research interest includes microwave and millimeter wave antennas, passive devices, SIW based subsystem and the design of wide band slotted array antennas, device modeling.

# Comparative study of GaN HEMT on recent trends and future scope along with its applications

**Avishek Saha[1], Arindam Chakraborty[1], Hindol Bhattacharjee[2], Rajiv Ganguly[1], Monojit Mitra[3].**

Department of Electronics and Communications Engineering.

*[1] Institute of Engineering and Management Kolkata 700091, India.*

*[2] Malla Reddy College of Engineering and Technology Hyderabad, India.*

*[3] IIEST Shibpur, India.*

*avisheks426@gmail.com, arindam.chakraborty@iemcal.com, hindolkuttu@gmail.com, rajiv.ganguly@iemcal.com, monojit_m1@yahoo.co.in.*

## Abstract.

Gallium nitride has already finds a large scale implementation in the field of optoelectronics and is greatly used in LED lights and it is also well-known material in power applications. Its low operating resistance and high breakdown voltage makes it a great choice to rely on for future implementations of power semiconductors with higher throughput. GaN HEMT (High Electron Mobility Transistor) also finds a large scale implementation in radiofrequency and high power solicitations. It pivots in the field of guided missiles, wireless communication. GaN HEMT are proved to provide higher drain current, cut-off frequency while preserving breakdown Voltages. All of this is possible due to the fact that GaN has higher naturalistic polarization effect and larger band gap energy. Essentially, this study covered a comprehensive review of GaN HEMT as well as its applications in many fields.

**Keywords**. LED, optoelectronics, RF electronics, EV, HEMT, GaN HEMT.

## 1. INTRODUCTION

Nowadays GaN is being widely used in various applications, as a basic semiconductor material of devises. The major applications of GaN semiconductor are light-emitting diode (LEDs) and high electron mobility (HEMTs). Due to unique properties like wide-band-gap, high electron mobility, high frequency response, better thermal stability, high switching frequency, GaN is getting a lot of attraction in many sectors like optoelectronics, power electronics, and RF applications. Monolithically manufactured HEMTs have a number of advantages, such as reduced parasitic resistance and capacitance, which increases the power efficiency of the circuit [1], [2]. HEMTs are frequently used in radar, broadcast receivers, and cellular telephones, among other applications. E. J. Lum et.al have pointed out the features of HEMT as well as HBTs. According to his paper it is shown that HEMT performs three times better that MESFET in terms of power efficiency [3]. In LED applications depletion type HEMT is used, but in switching applications and power electronics, normally-off HEMT is needed with high threshold voltage.

This review paper is written following these foot-steps- first we have discussed the background and the structures of depletion type and enhancement type HEMTs. After that various applications of GaN-HEMTs are discussed thoroughly followed by upcoming proposals in different fields. At last future scopes are discussed.

# 2. BACKGROUND AND STRUCTURE

## *2.1. Structure of HEMT*

The unique property of HEMTs is in producing high carrier mobility 2-D electron gas at equilibrium [4], [5]. A buffer layer is used to overcome the problem of lattice mismatch among two crystals [6], [7]. Throughout the last decade various structural modifications are incorporated to decrease the gate leakage issue and enhance the drain current. Field plates are also used to reduce short-channel-effects (SCEs) for short-gate-length HEMT. In recent times, Air Bridge field plates have also been employed to increase the breakdown voltage of the High electron mobility transistor [3]. The material characteristics of wide band-gap Group III-V materials, especially nitride group semiconductors like GaN, AlN along with SiC, GaAs, are compared with conventional Silicon semiconductor in Table-1.

| | Si | GaN | AlN | InN | GaAs | Sic |
|---|---|---|---|---|---|---|
| Band gap | 1.12 | 3.4 | 6.2 | 0.9 | 1.42 | 3.26 |
| Dielectric Constant | 11.8 | 8.9 | 8.5 | 15.3 | 13.1 | NA |
| Thermal Conductivity | 1.5 | 1.3 | NA | NA | 0.5 | 4.9 |
| Break Down Field | 0.3 | 3 | 11 | Low | 0.4 | 3 |
| Electron Mobility | 1350 | 440 | 300 | 70-250 | 8500 | 720 |
| Lattice Constant | 5.43 | 3.19 | 3.11 | 3.53 | 5.65 | 3.08 |

Table 1: HEMT's Material Characteristics [3]

## *2.2. Structure of GaN HEMT*

The two primary forms of GaN HEMT are enhancement type and depletion type. In the case of enhancement type AlGaN/GaN HEMT, we will get the current only if when we give the positive gate voltage. In the case of depletion type AlGaN/GaN HEMT, we will get the current in the channel, even if we do not give the gate voltage.

### *2.2.1. Structure for Normally-On GaN HEMT and review*

Fig-1 depicts a D-mode or depletion mode structure of AlGaN/GaN HEMT. From bottom to top, 1–5 um buffer layer is placed on the top of the silicon substrates followed by unintentionally doped GaN, a AlN spacer layer of 0.7–1.2 nm, and an $Al_xGa_{1-x}N$ barrier layer. $Al_xGa_{1-x}N$ thickness and Al molar fraction (x) are varied between 15 to 30nm and 0.15 to 0.4 respectively. The energy bands of hetero junctions generate a sharp quantum well that is bent downward at which high-intensity electrons are confined at the AlGaN/GaN interface because of the polarization effect with band gap mismatch of AlGaN/GaN [8].

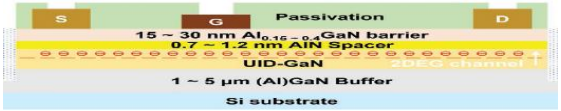


Fig-1: Schematic device structure of normally-on GaN HEMT structure [9].

### *2.2.2. Structure for Normally-Off GaN HEMT and review*

In switching applications and power electronics high positive threshold voltage and normally-off operation is preferred for obvious reason. To achieve normally off operation several structural modifications have been incorporated. Fig-2 shows that under the gate region, an Mg-doped P-type AlGaN is grown. The 2DEG under the Schottky gate is depleted as a result of the increased Fermi level by P-AlGaN, and the conduction band is raised. With a positive gate voltage (Vg > Vth > 0), the device turns on and normally-off operation achieved [10],[11].


Fig-2: p-AlGaN gate enhancement-type HEMT [9].

Two schematics for recessed-gate normally-off HEMTs are shown in Fig-3 and Fig-4. MIS-HEMT construction with a slightly recessed gate and a slender Aluminium Gallium Nitride barrier underneath the gate dielectric [12], [13]. The recessed gate is moved into the AlGaN barrier layer. The threshold voltage rises as the gate electrode gets closer to AlGaN/GaN interface. Normally-off functioning is attained when the depletion zone is created at the AlGaN/GaN interface.

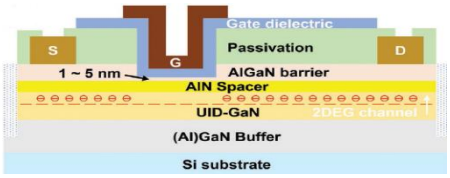


Fig-3: Recessed-gate MIS-HEMT [9].

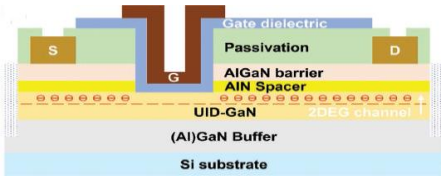


Fig-4: Recessed-gate MIS-FET [9].

In Fig-5, a limited quantity of fluorine ions enter the channel during implantation and appear as impurities that could cause mobility-impairment. Normally-off operation can be achieved by using ultra-thin AlGaN barrier [14], [15], [9].

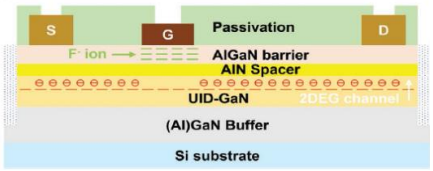


Fig-5: Fluorine gate HEMT [9].


Fig-6: Ultra-thin HEMT [9].

## 3. GAN HEMT IN OPTOELECTRONICS

The metal organic CVD through selective growth method has already been used to build monolithically integrated AlGaN/GaN to create HEMT and blue LED on sapphire substrates. Few recent literatures are published on GaN HEMT based white LED, where GaN HEMT and LED chip is fabricated in one single chip to light with a wave length of 470

nm N-GaN electrode of current controlled LED and channel region of voltage controlled transistor (HEMT) is connected directly in Fig-7. This is an integrated structure of HEMT-LED [1], [2].

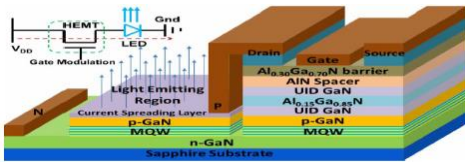


Fig-7: Cross-sectional schematic of HEMT-LED on sapphire substrate [1], [2].

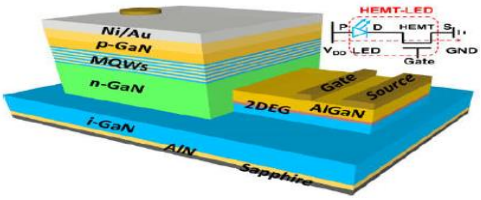


Fig-8: Schematic of the metal-interconnect-free HEMT-LED device using the GaN/AlN buffer [1], [2].

To fully capitalize on the long lifespan of GaN LED chips, the LED system must be enhanced using an on-chip GaN HEMT driver. GaN HEMTs can deliver output current exceeding 1A with great power efficiency. For HEMT-LED monolithic integration technology to be successful, two key elements must be taken into account I) selective epitaxial growth using metal-organic chemical vapour deposition or II) selective epitaxial removal [16], [17].

## 4. GAN HEMT IN RF AND POWER ELECTRONICS

Applications of power equipment with a rated voltage of 1700 V is often divided into three categories: lower-voltage, mid-voltage, and high-voltage equipment. Applications for mid voltage operate between 10 and 35 kV Fig-9.

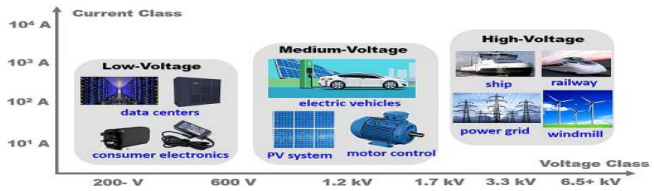


Fig-9: Representative implementation of power electronics applications [18].

The common power device is realized on the basis of lowest on-resistance, high breakdown voltage, as well as modest turn-on or turn-off power losses regardless of voltage or current classes (i.e., switching diminution). SiC is well known material and widely used as substrate materials in HEMT, for high temperature tolerance.

GaN HEMTs are recently used in power electronics applications with a voltage range of 15V to 650V GaN has become great choice of interest compared to silicon and SiC. High power applications need fast switching frequencies, hence GaN HEMTs are being used in wireless charging and rapid adapters. Shrinking of parasitic elements makes it possible to generate high power with high frequency [18].

In Radio-frequency applications AlGaN/GaN or AlGaAs/GaAs HEMTs shows better frequency response compared to conventional semiconductors.

## 5. GAN HEMT IN VEHICULAR TRANSPORT

Transition to electric vehicles is confronting a number of new obstacles, including the limited number of charging stations and the density of the batteries. For charging up the batteries electric vehicles use several power electronics converters. High cost of these devices, constrained voltage rating, sophisticated gate driver design, and control of thermal resistance become biggest challenges [6], [19], [20].

In the aircraft sector, reliability is more important than price. GaN HEMTs allow for the creation of more compact and lightweight cooling systems by reducing the amount of heat generated by the power electronics. GaN greatly enhances the power density of shipboard converters as well as the ability of switches to function in high temperature [6].

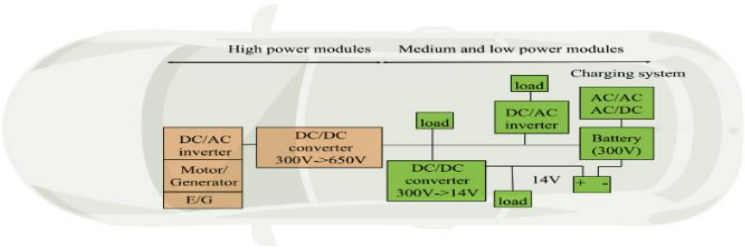


Fig-10: Electric vehicle power electronic components [6].

GaN based devices is anticipated to lower costs and increasing the acceptance of GaN technology and encouraging the creation of more efficient electric vehicles for transport. More electric ships, heavy-duty vehicles, off-road vehicles, and aircraft are just a few examples of what could be in the near future [6].

## 6. PROPOSAL FOR DEVICE IN DIFFERENT FIELD

In high power applications and millimetre wave applications, GaN HEMTs are a renowned area for research due to its higher breakdown voltage (3.3MV/cm) and high velocity electron ($2.51x10^7$). Better frequency response is achieved by reducing the device gate size as shown in Fig-12. However, much more gate length reduction results in a small channel effect [3].

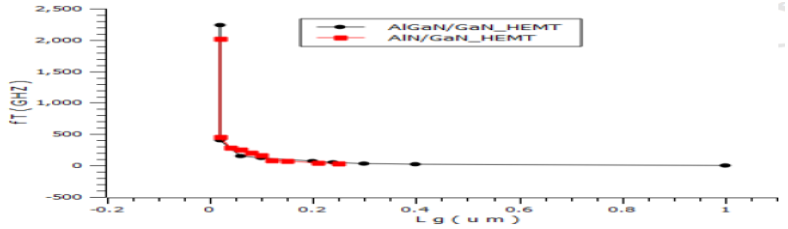


Fig-11: Gate Length V/s Cut-off frequency characteristics of a GaN HEMTs.[3], [20].

The modern wireless power systems uses advanced coil technology and high power amplifiers incorporating GaN HEMTs rather than Si transistors [6].

Gallium Nitride HEMT are particularly applicable for radiofrequency and high power intensive activities because to their wide band gap properties. GaN HEMTs also have significantly greater switching frequency compared to Si-based devices. Therefore, they are suitable for high-speed or wireless charging as well as electrified transportation [18]. Several

modifications have done on HEMT structures to enhance the drain current. GaN materials have gained a lot of popularity recently and are useful for improving HEMTs' DC characteristics. GaN is a special kind of material with a 3.4 eV energy gap and a high breakdown voltage of 3MV/cm [3].

## 7. CONCLUSION

A general review of GaN HEMT along with its applications on different fields is discussed in this paper. Along with that it has also been discussed that GaN based HEMT device are an excellent choice for optoelectronics, radio frequency applications or high power applications, and vehicular transport. But the biggest challenges for GaN HEMT devices is high cost. GaN HEMT devices has limited voltage rating which is another biggest challenge. The complex gate driver design in the production of ICs using GaN are the areas that needs to be improve.

## 8. FUTURE SCOPE

GaN HEMT has great prospects of further exploration in the near future because of its unique characteristics. GaN HEMT has wide band gap due to high breakdown voltage with high cutoff frequency and has much more wide application in higher frequency domain. Due to high mobility and high carrier concentration, it is much more suitable for switching applications. While we incorporating any other composite materials like InGaN, then it can be also used as a driver circuit for the LED.

## 9. ACKNOWLEDGMENT

I would like to acknowledge the support shown by Dr. Gourango Sundar Taki and Dr. Satyaranjan Bhattacharyya who guided us during preparation for the manuscript.

## 10. REFERENCES

[1] Zhao Jun Liu, Member, IEEE, Tongde Huang, Student Member, IEEE, Jun Ma, Chao Liu, and Kei May Lau, Fellow, IEEE, “Monolithic Integration of AlGaN/GaN HEMT on LED by MOCVD”.

[2] Chao Liu, Yuefei Cai, Xinbo Zou, Member, IEEE, and Kei May Lau, Fellow, IEEE “Low-leakage High-breakdown Laterally Integrated HEMT-LED via n-GaN Electrode”.

[3] A.S. Augustine Fletcher, D. Nirmal. "A survey of Gallium Nitride HEMT for RF and high power applications", Superlattices and Microstructures, 2017.

[4] Z. Li, J. Waldron, T. Detchprohm, et al., “Monolithic integration of light- emitting diodes and power metal-oxide-semiconductor channel high- electron-mobility transistors for light-emitting power integrated circuits in GaN on sapphire substrate,” Appl. Phys. Lett., vol. 102, no. 19, p. 192107, 2013.

[5] J. Ajayan and D. Nirmal, “20-nm T-gate composite channel enhancement-mode metamorphic HEMT on GaAs substrates for future THz applications" J Comput Electron Vol 16(2016), pp 1291–1296.

[6] Keshmiri, N., Wang, D., Agrawal, B., Hou, R., & Emadi, A. (2020). Current Status and Future Trends of GaN HEMTs in Electrified Transportation. In IEEE Access (Vol. 8, pp. 70553–70571). Institute of Electrical and Electronics Engineers (IEEE).

[7] A. T. Schremer, J. A. Smart, Y. Wang, O. Ambacher,N. C. Macdonald, J. R. Shealy, Appl. Phys. Lett. 2000, 76, 736C.
[8] J. Zhang, Y. Hao, J. Zhang, J. Ni, Sci. China Ser. F: Inf. Sci. 2008, 51, 780.
[9] J., Cheng, W., Wang, Q., Cheng, K., Yu, H., & Chai, Y. (2021). Recent Advances in GaN-Based Power HEMT Devices. In Advanced Electronic Materials (Vol. 7, Issue 4, p. 2001045). Wiley.
[10] X. Tang, B. Li, H. A. Moghadam, P. Tanner, J. Han, S. Dimitrijev, IEEE Electron Device Lett. 2018, 39, 1145.
[11] X. Li, M. Van Hove, M. Zhao, K. Geens, W. Guo, S. You, S. Stoffels, V.-P. Lempinen, J. Sormunen, G. Groeseneken, IEEE Electron Device Lett. 2018, 39, 999.
[12] G.Guodong,"90-nm-gated AlGaN/GaN HEMT with fT & fmax of 132 GHz & 205 GHz", IEEE International Conference on Electron Devices and Solid-State Circuits (EDSSC), 2014.
[13] Jiangfeng Du, " Design optimisation of AlGaN/GaN metal insulator semiconductor high electron mobility transistor with high-K/low-K compound gate dielectric layer for millimeter-wave application", Micro & Nano Letters, Vol. 11, Iss. 9, pp. 503-507, 2016.
[14] Shih-han yi,"High Performance Metal-Gate/High-κ GaN MOSFET With Good Reliability for Both Logic and Power Applications", Journal of the electron device society, volume 4, no. 5,2016.
[15] F. Medjdoub,"High-Performance Low-Leakage-Current AlN/GaN HEMTs Grown on Silicon Substrate", IEEE electron device letters, vol. 32,no. 7,2011.
[16] F. G. Kalaitzakis, E. Iliopoulos, G. Konstantinidis, et al., "Monolithic integration of nitride-based transistor with light emitting diode for sens- ing applications," Microelectron. Eng., vol. 90, pp. 33–36, Feb. 2012.
[17] J. Ajayan and D.Nirmal, "22 nm In0:75Ga0:25As channel-based HEMTs on InP/GaAs substrates for future THz applications", Journal of Semiconductors, vol. 38, no. 4, 2017.
[18] Koon Hoo Teo, Yuhao Zhang, Nadim Chowdhury, Shaloo Rakheja et al. "Emerging GaN technologies for power, RF, digital, and quantum computing applications: Recent advances and prospects", Journal of Applied Physics, 2021.
[19] M. Kanechika, T. Uesugi, and T. Kachi, ''Advanced SiC and GaN power electronics for automotive systems,'' in IEDM Tech. Dig., Dec. 2010, pp. 324–327.
[20] G.Guodong, "Low ohmic contact AlN/GaN HEMTs grown by MOCVD", Journal of semiconductor, Volume 34, Number 11 , 2013.

## Biographies

**Avishek saha** received the bachelor's degree in Electronics & communication engineering from Narula Institute of Technology, Agarpara, Kolkata, West Bengal 700109, in 2021 and is pursuing master's degree in Microelectronics & VLSI Technology from Institute of Engineering and Management, Kolkata, West Bengal 700091.

**Mr. Arindam Chakraborty** is currently an assistant professor at the Institute of Engineering and Management, Kolkata. He obtained his M. Tech. in Microelectronics and VLSI Design from the Jadavpur University – Kolkata, India. Mr. Chakraborty has published a number of papers in research Journals and chapters in books, and participated in different reputed conferences on solid state lighting, VLSI and IOT. His areas of interest include Solid State Lighting, Image Processing, Embedded System Design and IOT.

**Mr Hindol Bhattacharjee** is working as an assistant professor at **Malla Reddy College of Engineering and Technology (**Autonomous Institution - UGC, Govt. of India)**, Hyderabad, India**. He is pursuing his Ph.D. from NIT-Arunachal Pradesh. His research interest is device physics, modelling and simulation. He completed bachelor's degree in ECE domain from CEMK, Kolaghat. He pursued his master's degree from IEM, Kolkata in VLSI design and Microelectronics.

**Dr. Rajiv Ganguly** is currently a professor at the Institute of Engineering and Management, Kolkata. He obtained his Ph.D. in Engineering from the Jadavpur University – Kolkata, India. Dr. Ganguly has published a number of papers in Refereed Journals and chapters in books, and participated in a range of forums on solid state lighting, VLSI and IOT. His areas of interest include Solid State Lighting, VLSI and IOT.

**Dr. Monojit Mitra** is a Professor & former Head, Department of Electronics and Telecommunication Engineering at Indian Institute of Engineering Science & Technology (IIEST), Shibpur. At present he is the Head of Purabi Das School of Information Technology. He was also a visiting professor at the University of Jadavpur and the University of Kolkata. He has over 30 years of experience in the field of research, especially in the field of fabrication of IMPATT diode and developed microwave source using the indigenous diode for the development of solid state radar system.

# Optical Property Study of Electrodeposited Tin Oxide Thin Film

[1]Uddipan Agasti, uddi345@gmail.com , Institute of Engineering and Management, Kolkata, India
[2]Soumik Kumar Kundu, soumik.kundu@iemcal.com , Institute of Engineering and Management, Kolkata, India
[3]Samit Karmakar, iem.samit@gmail.com, Institute of Engineering and Management, Kolkata, India
[4]Bibhuti Bhushan Show, bibhutishow1978@gmail.com , Jadavpur University, Kolkata, India
[5]Sayan Chatterjee, sayan.chatterjee@jadavpuruniversity.in , Jadavpur University, Kolkata, India

## Abstract.

Tin oxide ($SnO_2$), a common n-type semiconductor is extensively used in the detection of various gases due to its stable bandgap and excellent physical-chemical properties. In this paper, the $SnO_2$ is made by the electro-deposition method using a Zinc electrode on FTO glass. This reaction is done at room temperature with an acidic aqueous solution containing primary salt as $SnSO_4$.The optical properties of $SnO_2$ were investigated by utilising UV-VIS spectrophotometry.

**keyword:** Tin oxide, *thin film, UV-Vis Spectrophotometry*

## 1. INTRODUCTION

$SnO_2$, the first semiconductor material used commercially for methane detection [1] is a typical n-type metal oxide semiconductor with a broad and stable bandgap of 3.6eV [2]. Features like high transparency, high conductivity, and large mobility make SnO2 a widely accepted and appreciable gas-sensing material [3,4]. This rutile-type crystalline structure at room temperature [5] is not only used for gas sensing [6,7] but also as electrocatalytic anodes [8], solar cells [9] and catalysts [10,11]. Electrical conductivity can be enhanced by increasing the number of charged particles by doping [1]. Over the years researchers have used a number of techniques such as Chemical Bath Deposition (CBD) [12], Controlled Precipitation Method [13], Nitric Acid Leaching [14], Electrodeposition [15], Thermal Evaporation Technique [16], Sol–Gel [17] and Hydrothermal [1].

Chang et al 2002[18] successfully electrochemically deposited nanostructured $SnO_2$ on copper substrate and chose $SnCl_2$ as the tin-based salt at a temperature of 85° C followed by a heat treatment in a vacuum at 400°C for prominent crystallinity. Aditia et al 2011[12] deposited $SnO_2$ thin film by Chemical Bath Deposition on a glass substrate. Choosing the precursor as $SnCl_2.2H_2O$ and the catalyst as urea, varied the calcination temperature of the substrate and thereby proving that a higher calcination temperature would have been better for crystallinity. Kyoungkeun et al [14] leached Pb-free solder in nitric acid in a Pyrex glass reactor equipped with a heat sink to maintain the thermal equilibrium. The leaching efficiencies were directly proportional to temperature and HNO3 concentration thereby achieving 99.986% pure $SnO_2$. Junie Jhon M. Vequizo et al 2010[4] fabricated Sno2 thin film by electrodepositing SnSo4 and Nitric Acid on indium-tin-oxide (ITO) at room temperature with an acidic pH. The working solution was oxygen-bubbled which was used as an oxygen precursor for the better deposition of the substrate. Zheng et al 2021[1] doped graphene on Sno2 and obtained a 96.112 sensing response to methane at 243°C.$SnO_2$-NP was prepared hydrothermally using SnCl4.5H20 for 8 Hrs. Quaranta et al 1999[17] had a sol-gel setup for fabricating $SnO_2$/Os gas sensitive thin film. Os doping improved the sensitivity of tin oxide and made promising progress in order to make low-cost methane sensors. Ibarguen et al 2006[13] synthesized tin oxide nanoparticles by controlled precipitation. An optimal pH yielded the desired product with major phase 6.25 with potentiometric and conductimetric titrations at 350°C. Even at 600°C, it showed high reactivity. Naz et al 2020[19] conducted the experiment successfully using the chemical co-precipitation method on hydrated stannous salt followed by annealing them at 400°C,500°C, and 600°C.Elango et al 2015[20] green synthesized $SnO_2$ nanoparticles from Persia Americana seed extracts of size in the range of 4nm at low cost without doing any harm to the environment.

In this paper, we have synthesized tin oxide thin films by means of the electrodeposition method and optical characteristics have been investigated. We have chosen Electrodeposition because of its effectiveness, rapid synthesis time and low cost. The process was conducted at room temperature with optimal pH for better deposition. Further analytical study (UV-VIS) was done to verify the purity and other aspects of the thin films.

## 2. EXPERIMENTAL

### 2.1 Materials

In this experimental procedure, the materials utilized were stannous sulfate ($SnSO_4$), analytical reagent, tartaric acid($C_4H_6O_6$), analytical reagent, potassium nitrate ($KNO_3$), analytical reagent, nitric acid ($HNO_3$), distilled water ($H_2O$).

### 2.2 Synthesis of $SnO_2$ Thin Film

The tin oxide thin films were synthesized using the electrodeposition method. 0.1 M stannous sulfate was dissolved in 5ml distilled water and magnetic stirring was applied till a fine solution was obtained. 0.85 gm tartaric acid was added to the solution and a magnetic stir was applied for as long as a homogeneous solution was formed with fine white particles floating in it. 0.1 potassium nitrate was first dissolved in 5ml water and added dropwise to the above solution until the solution becomes just clear that is the solution at that very instant becomes transparent and no more drops were added. The pH of the solution was maintained at 2.2 using nitric acid (1:10 V/V). The solution was left for a few minutes to make sure that everything dissolves uniformly. Clean FTO glass and extremely clean, polished zinc rod were submerged and connected with wires. Figure 2.1 shows the experimental setup. The entire setup was kept undisturbed till a white crystalline layer is obtained on the FTO. The FTO was dried up and heat treated at 600°C for 2 hrs in order to oxidize the free tin ions that may be present in the thin film and to have a strong deposition of tin oxide over the FTO. In Figure 2.12 some of the thin films synthesized have been shown.

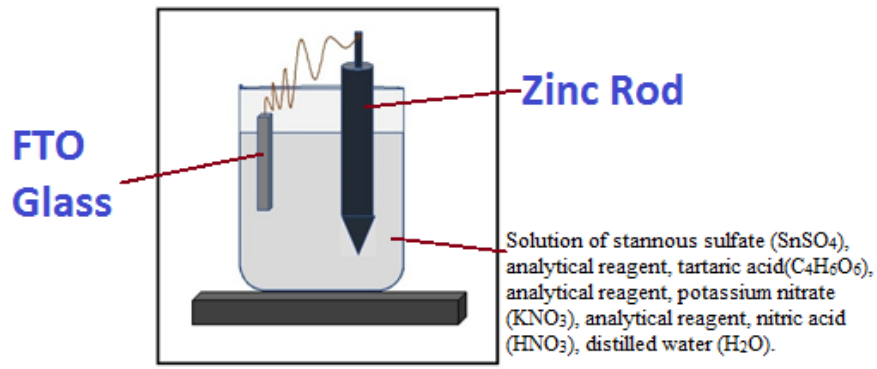


Figure 2.1. Schematic Representation of the Setup


Figure 2.12. Tin Oxide Thin Film

### 2.3 Characterization

The optical characterization of the thin film was performed with UV-Vis Spectrophotometry in the instrument JASCO UV, present in Jadavpur University under the model V-730. The measuring range was set at 800nm-200nm with a data interval of 0.2nm, bandwidth -1.0nm, and response time of 0.06s. So reasonable and accurate results could be made from this.

# 3. RESULTS AND DISCISSION

## 3.1 Optical Characterisation of $SnO_2$ Thin Film

### 3.11 UV-Vis absorbance

The optical properties were measured with JASCO UV by plotting a graphical relationship between absorbance wave spectra of tin oxide thin film and wavelength of UV. In figure 3.11, the graph can be divided into prominent two regions, one the region between the range of 200 nm-525nm where the absorbance was compatible to an extant and peak absorbance at 407.9 nm was observed which indicates a red shift or bathochromic shift with that respect to that of 312 nm found by Bhagwat et al 2015[21]. The other is between 525nm-800nm, in which there is a decrease in absorbance with an increase in wavelength, and a steady curve decrease is observed.

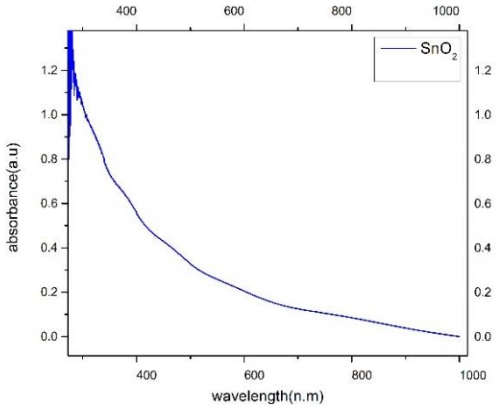


Figure 3.11. Absorbance Vs Wavelength

### 3.12 Band Width

The optical analysis of absorbance spectra is done by tauc plot, which gives the relationship between absorption coefficient(α) and photon energy(hv) by the equation 3.12 [21]

$$(\alpha h\nu)^n = K(h\nu - E_g) \qquad \textbf{(3.12) [21]}$$

Where α denotes the absorption coefficient, h is plank's constant ($6.62\times10^{-34}$ $m^2kg/s$),$\nu$ is the frequency, Eg is the estimated optical bandwidth of the thin film and n is the nature of transmission which in this case is taken as 2 due to the direct bandgap nature of tin oxide.[21] As we can see in Figure 3.12, the graph has x coordinates as $h\nu$ and y coordinates as $(\alpha h\nu)^2$ ,and a straight line is extrapolated which meets the energy axis at 3.04 eV. Thus, estimating the optical bandwidth of the synthesized material to be 3.04 eV which is within the range of (2.5– 3.4 eV) as stated by Elango et al 2015[20].

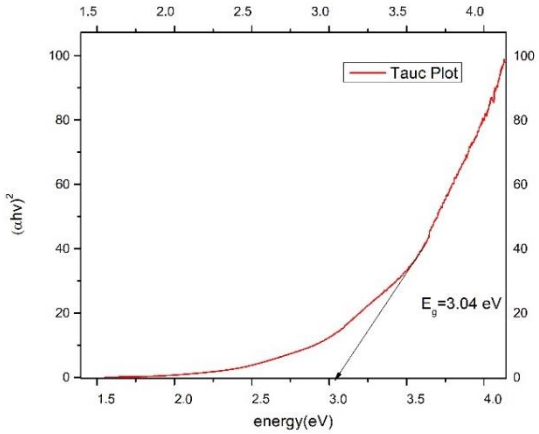


Figure 3.12. Tauc Plot of the Thin Film

## 4. CONCLUSION

A cost-effective and replicable procedure for synthesizing tin oxide has been demonstrated in this paper. Since the process is in an early phase, it needs to be optimized. A distinct redshift is seen in the bandgap of the substrate which could be reduced by controlling the amount of chelating agent (in this case tartaric acid) dissolved in the solution so that the speed of tin oxide deposition can be regulated. Or by heat treatment of the thin films for better oxidation. Nevertheless, the rough estimates indicated that the process is an advantageous one and can be further optimized.

## 5. FUTURE WORK

In the future, for better characterization XRD (X-ray Powder Diffraction), SEM (Scanning electron microscope), and other analysis techniques should be conducted to have a clearer idea about the morphological, elemental, etc characterization of the material. Tin oxide is used for a variety of applications especially gas sensors, which could be fabricated after the initial stages.

## 6. ACKNOWLEDGEMENT

All the authors would like to that both Institute of Engineering and Management, Kolkata, India and Jadavpur University, Kolkata, India for extending their cooperation in every way possible. And last but not the few words of appreciation for my friends and colleagues namely Ms. Pratisruti Chatterji, Suswan Biswas and Avik Pathak.

## 7. REFERANCE

[1] H. Zheng, Y. Zhou, B. Xu, Y. He, T. Jiang and X. Guo, "Sensing Properties of SnO2/Pd/Graphene Composites," 2021 Photonics & Electromagnetics Research Symposium (PIERS), 2021, pp. 900-905, doi: 10.1109/PIERS53385.2021.9694926.

[2] C.Y. Kuo, K.H. Huang, S.Y. Lu, Electrochem. Commun. 9 (2007) 2867.

[3] Martinez-Gazoni, R. & Allen, Martin & Reeves, R.. (2018). Conductivity and transparency limits of Sb-doped Sn O 2 grown by molecular beam epitaxy. Physical Review B. 98. 10.1103/PhysRevB.98.155308.

[4] Junie Jhon M. Vequizo *et al* 2010 *Jpn. J. Appl. Phys.* 49 125502

[5] L.A. Errico, Ab initio FP-LAPW study of the semiconductors SnO and SnO2, Physica B Physics of Condensed Matter 389 (2007) 140–144

[6] I. Aruna, F. E. Kruis, S. Kundu, M. Muhler, R. Theissman, and M. Spasova: J. Appl. Phys. 105 (2009) 064312.

[7] H. Keskinen, A. Tricoli, M. Marjaki, J. M. Makela, and S. E. Pratsinis: J. Appl. Phys. 106 (2009) 084316

[8] P. Duverneuil, F. Maury, N. Pebere, F. Senocq, and H. Vergnes, Surf. Coat. Technol. 151–152, 9 (2002).

[9] M. A. El Khakani, R. Dolbec, A. M. Serbenti, M. C. Horrillo, M. Trudeau, R. G. Saint-Jacques, D. G. Rickerby, and I. Sayago, Sens. Actuators B Chem. 87, 321 (2002).

[10] T. Tagawa, S. Kataoka, T. Hattori, and Y. Murakami, Appl. Catal. 4, 1 (1994).

[11] P. W. Park, H. H. Kung, D. W. Kim, and M. C. Kung, J. Catal. 184, 440 (1999).

[12] Rifai, Aditia & Iqbal, Muhammad & Tapran, Nugraha & Nuruddin, Ahmad & Suyatman, Suyatman & Yuliarto, Brian. (2011). Synthesis and Characterization of SnO2 Thin Films by Chemical Bath Deposition. AIP Conference Proceedings. 1415. 231-233. 10.1063/1.3667263.

[13] Ibarguen, C. & Mosquera, Adolfo & Parra, Rodrigo & Castro, Miriam M. & Paez, Jorge. (2007). Synthesis of SnO2 Nanoparticles Through the Controlled Precipitation Route. Materials Chemistry and Physics. 101. 433-440. 10.1016/j.matchemphys.2006.08.003.

[14] Yoo, Kyoungkeun & Kwangseok, Lee & Jha, Manis & Lee, Jae-chun & Cho, Kuk. (2016). Preparation of Nano-Sized Tin Oxide Powder from Waste Pb-Free Solder by Direct Nitric Acid Leaching. Journal of Nanoscience and Nanotechnology. 16. 11238-11241. 10.1166/jnn.2016.13485.

[15] Chen, Xiangping & Liang, Jianyu & Zhou, Zhentao & Duan, Huanan & Li, Boquan & Yang, Qiming. (2010). The preparation of SnO 2 film by electrodeposition. Materials Research Bulletin - MATER RES BULL. 45. 2006-2011. 10.1016/j.materresbull.2010.07.029.

[16] Chowdhury, Fatema & Choudhury, Shamima & Hasan, Firoz & Begum, Tahmina. (2011). Optical Properties of Undoped and Indium-doped Tin Oxide Thin Films. Journal of Bangladesh Academy of Sciences. 35. 10.3329/jbas.v35i1.7975.
[17] F Quaranta, R Rella, P Siciliano, S Capone, M Epifani, L Vasanelli, A Licciulli, A Zocco,
A novel gas sensor based on SnO2/Os thin film for the detection of methane at low temperature,Sensors and Actuators B: Chemical,Volume 58, Issues 1–3,1999,Pages 350-355,
ISSN 0925-4005.
[18] S. T. Chang *et al* 2002 *Electrochem. Solid-State Lett.* 5 C71
[19] Naz, Shaheen & Javid, Iqra & Konwar, Subhrajit & Surana, Karan & Singh, Pramod & Sahni, Mohit & Bhattacharya, Bhaskar. (2020). A simple low cost method for synthesis of SnO2 nanoparticles and its characterization. SN Applied Sciences. 2. 10.1007/s42452-020-2812-2.
[20] Ganesh Elango, Subramanian Manoj Kumaran, Sekar Santhosh Kumar, Soundrapandian Muthuraja, Selvaraj Mohana Roopan,Green synthesis of SnO2 nanoparticles and its photocatalytic activity of phenolsulfonphthalein dye,Spectrochimica Acta Part A: Molecular and Biomolecular Spectroscopy,Volume 145,2015,Pages 176-180,ISSN 1386-1425
[21] Bhagwat, A.D., Sawant, S.S., Ankamwar, B.G. and Mahajan, C.M., 2015. Synthesis of nanostructured tin oxide (SnO2) powders and thin films prepared by sol-gel method.

## 8. Biographies

**Uddipan Agasti** received the Indian School Certification (ISC) from National Gemes Higher Secondary School, Kolkata, India in 2019. He is currently studying bachelor's degree from Institute of Engineering and Management, Kolkata, India. His research areas include basic electronics, nanoelectronics, gas sensors, microelectronics, nanoparticles.

**Prof. Soumik Kr. Kundu** is currently working as an Assistant Professor at Institute of Engineering and Management, Kolkata, India in the department of Electronics and Communication. His area of interest includes Magnetron Sputtering, Nano Material Synthesis, Photocatalytic water splitting, ECR-PE CVD.

**Prof. Samit Karmakar** is currently working as an Assistant Professor at the Department of Electronics & Communication Engineering, Institute of Engineering and Management, Kolkata. His research areas include Materials Sc. & Nano-Technology, Graphene, Quadrupole Residual Gas Analysis. He has been serving as a reviewer for many highly-respected journals.

**Dr. Bibhuti Bhushan Show** is currently working as an Assistant Professor, Inorganic Chemistry, at Jadavpur University, Kolkata, India. His area of research includes material science, Thin Films Semiconductors, Thin Film Deposition, Thin Films and Nanotechnology, Oxides, Nanoparticles.

**Dr. Sayan Chatterjee** is currently working as Professor at Jadavpur University, Kolkata, India in the Department of Electronics & Telecommunication Engineering. His research area includes Antennas (waveguide base structure), RF circuits, slotted array antenna, fractal antenna, waveguide passive structure, harmonic suppression in filter, PSO based evolutionary computing for antenna array synthesis.

# To Generate High resolution Deep Space Images using Real-ESRGAN

Varad Joshi
*dept. of computer engineering*
*VESIT*
Mumbai, India
2019varad.joshi@ves.ac.in

Rushabh Rijhwani
*dept. of computer engineering*
*VESIT*
Mumbai, India
2019rushabh.rijhwani@ves.ac.in

Mr. Richard Joseph
*dept. of computer engineering*
*VESIT*
Mumbai, India
richard.joseph@ves.ac.in

## Abstract.

As the space technology industry is burgeoning in the field of deep space exploration, researchers are compelled to test their psyche in analysis of the celestial bodies wrapping our universe. Eventually giving rise to machinations of new and sophisticated algorithms and systems that help to distil and reveal more about deep space that is yet abstruse to many of us. The current devices in this industry include some of high tech telescope and observatories are capable of taking incredible pictures of the deep space, which although are fortuitous in helping the space scientists to study the deep space entities, but the obscurity of those images impede the elucidation of the outer bound space entities;rendering the scientists unable to summarise much from the input. Thus, to overcome this cumbersome task of scratching the heads to get information from already low resolution image, we are aiming to build a model that enhances the low resolution of such space objects to high resolution data that will ease the task of space scientists in scrutinising the deep space bodies, eventually expediting the research process. The model we will be using to aid our problem is, Super Resolution General Adversarial Network(SRGAN)

**Index Terms—High Resolution, Low Resolution, Deep Space data, Super Resolution General Adversarial Network, GAN.**

## I. INTRODUCTION

General Adversarial Networks or GAN in short: are becoming more cohesive which in turn has flourished its popularity in the research sphere as compared to the obsolete Convolutional Neural Networks. These GAN models provide more accurate results and also their cost function is near peripheral after being trained for sufficient epochs. The prodigious GAN architectures can help in upscaling of the low-resolution images and video content into the high-resolution entities.SRGAN is able to Upsample a muffled input image to recover a high resolution output of the same image.The SRGAN has glossified that extensive mean-opinion-score (MOS) test has had huge remarkable gains in regards to perceptual quality. SRGAN's MOS scores are more comparable to the primordial high-resolution pictures' scores than any other cutting-edge approach. Traditional super resolution networks and existing algorithms even though were less byzantine, they were not able to display pellucid images that would have helped significantly in deep space research if they were cogent enough. Hence, to decode these barriers, we decided to go with SRGAN model, that would eventually augment the image quality and obviate the possibility of studying the low resolution, downsampled images.

## .II. OVERVIEW

### A. Problem Statement

The practice of boosting an image's resolution from low-resolution (LR) to high-resolution is known as "image super resolution" (HR).It mostly alludes to using various methods to convert downsampled photos into upsampled, high definition images. With the aid of its generative adversarial nature, SRGAN exploits perceptual function loss to synthesize high resolution images from low resolution photos.The primary objective of the paper is focused on those far away, millions of light years distant inter galactic bodies, whose data isn't readily accessible in image format.Although some high-end telescope maybe able to capture these bodies aesthetically but are somewhat obtainable only in scant proportion and have distorted images.Thus, to speed up the task of research and bolstering the analysis phase in department of space science, Our team is driven to create a cutting-edge model that makes use of sophisticated real-time algorithms to provide us with the best results possible.Eventually decreasing the peril in the approach and giving results simultaneously.

### B. Our Inspiration

The images procured from the below mentioned space devices are contorted.The scientific importance of super resolution is that it is used to enhance the warped images that are obtained from deep space observatories devices.The traditional algorithms and deep learning models are able to restore the enhanced version of distorted images to a certain extent,but the results are not persuasive enough. Hence, it becomes very perplexing to process the images for scientific purposes. Our model thus helps in overcoming these travails in the path of novelty and exploration.

### C. Objective

1. To simplify the indigation procedure in the field of space science.

2. To popularise the use of more advanced and complex models in order to get results with high precision.

3. Recovery of enhanced images from convoluted input space images.

4. System that is affordable, convenient, and easy to use.

5. To galvanize and lionize the neophytes in the field of astronomy to come up with such fastidious and lucrative solutions.

## III. THEORY

Super Resolution General Adversarial Network or also known as SR-GAN; is a deep learning model proposed by researchers at twitter.SR-GAN is generally used for SISR(single image super resolution). The primary objective of this model is to reclaim the quality textures of the ground truth data of the image that had been distorted due to upsampling of the input image or noise or any other factor. SR-GAN uses a deep network with an adversary network in order to give HR(high resolution) images as the output. SR-GAN uses a perpetual loss function which is made up of adversarial loss and content loss. The solution to the natural image is propelled by the adversarial loss function, multitudinous where a discriminator is used to differentiate between the original input image i.e. the ground truth data and the generated super resolution image from the generator.

### A. Survey of the Existing systems

To augment the resolution of the deep space photos, we used a Super Resolution General Adversarial Network model. This model belongs to the GAN family and is one of the most well- known and popular ones.According to our research, SinGAN, SR-CNN, ESRGAN, deeply recursive convolutional network (DRCN), and efficient subpixel convolutional neural network were the most widely utilised models for this application (ESPCN). For the purpose of reconstructing the Compressed Sensing Magnetic Resonance Imaging, a new model based on conditional generative adversarial network (DAGAN) (CS-MRI) was presented. According to the literature survey, our new model provides better accuracy and efficiency than other convolutional neural networks like ESRGAN and few architectures like Enhanced Deep Super-Resolution network(EDSR) which supervises specific super-resolution scale and Multi-scale Deep Super-Resolution system(MDSR)that creates a single model from multiple scales of high-resolution images. SinGAN model as well as conditional GAN models showed accuracy less than 75 percent which is less as compared to our ”Real ESRGAN” model. Some of the Convolutional neural networks that use single image dehazing process had higher perceptual loss function and take more processing as well training time than SRGAN model used in this system. While studying the other models, we found out their experimental results in usage and then compared it with SRGAN model. For reference purposes,we are providing picturesque results for better visualisation.


Fig.1.Result comparison between different image resolution models

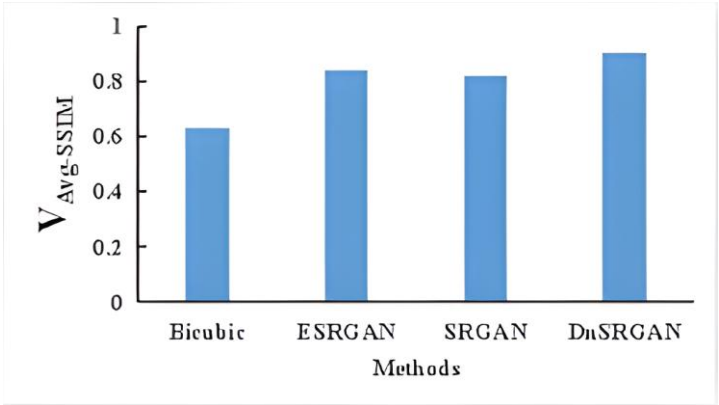


Fig. 2. Graphical comparison of different image resolution models.

### B. Limitations and Research Gap

Some of the models like SRCNN, ESPCN, DRCN incorporate higher loss functions that can increase the complexity of the training phase. Additionally, it has been discovered that newer works use GAN or reinforcement learning before vision restoration. Blind SR can be categorised into two different groups, the first of which uses explicit degradation representations and typically has two parts: degradation prediction and conditional restoration. On the other hand, inaccurate degradation assessments will inevitably produce artefacts. Before training a unified network to overcome blind SR, another strategy is to collect/precipitate training pairs that are as near to real-world data as possible.

## .IV. SR-GAN FOR SUPER RESOLUTION OF DEEP SPACE IMAGES

### A. Architecture

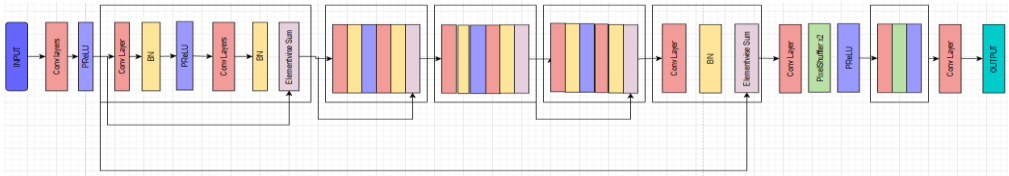


Fig. 3. SRGAN generator

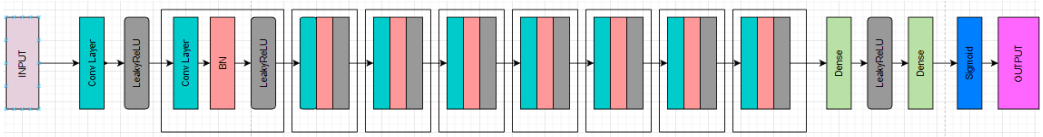


Fig. 4. SRGAN discriminator

The above figure represents the architecture of SR-GAN(super resolution general adversarial network).The model consists of two main blocks.

#### 1. Generator.

The SR-GAN architecture is based on the ResNet architecture and consists of a generator, Batch Normalisation and Parametric ReLU. The main task of the discriminator is to check both the generated image of the generator and then try to distinguish between them. While training, a gaussian filter is applied to the high resolution image(IHR) which then gives us a low resolution image (DHR) of the same high resolution by applying a downsampling operation.

#### 2. Discriminator.

The SR-GAN is based on the architecture of DC-GAN which is known as deep convolutional general adversarial networks. The primary task of the discriminator is to discriminate between the input images and those produced by the generator. After the 512 feature maps, two dense layers follow them along with a layer of activation function i.e. LeakyReLU.

•Input low resolution is interpreted as C x H x W

•Input high resolution image and input super resolution image is interpreted as C x rW x rH

1. The Generator function gives the HR(high resolution) image which is actually classified as a super resolved image of the corresponding low resolution image.

2.Discriminator D is trained to discern between genuine images and super resolved images

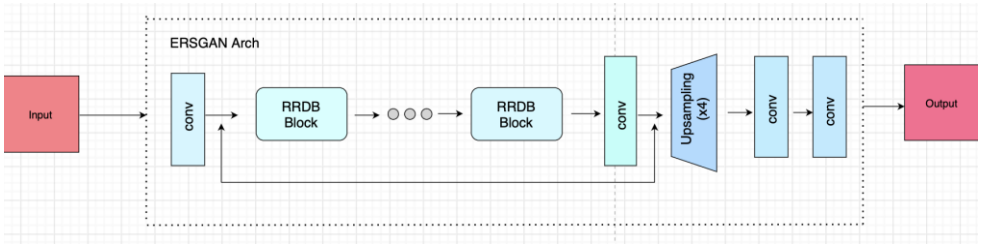


Fig. 5 Real-ESRGAN Architecture

The Real ESRGAN can do high computation on a mini batch of input images and of high degradation space than its predecessor. In order to solve this, we have used a u-net architecture for our discriminator. The U-Net may give the generator detailed per-pixel feedback and produce realness values for each pixel.

**B. Loss Function of SR-GAN**

The total loss i.e. the perpetual loss of SRGAN is the sum of content loss and the adversarial loss. Content Loss: Two types of losses are used in the SRGAN architecture. Image super resolution models commonly use pixel wise MSE loss of the SRResnet architecture. This loss alone is not able to deal with the high frequency content and hence, loss function of different VGG layers are used which are based on the ReLU activation function layer of VGG-19 model. The loss is hence defined as:

$$l_{MSE}^{SR} = \frac{1}{r^2WH}\sum_{x=1}^{rW}\sum_{y=1}^{rH}(I_{x,y}^{HR} - G_{\theta_G}(I^{LR})_{x,y})^2$$

Fig. 6. Content Loss

$$l_{VGG/i.j}^{SR} = \frac{1}{W_{i,j}H_{i,j}}\sum_{x=1}^{W_{i,j}}\sum_{y=1}^{H_{i,j}}(\phi_{i,j}(I^{HR})_{x,y} - \phi_{i,j}(G_{\theta_G}(I^{LR}))_{x,y})^2$$

Fig. 7. VGG content loss in SR-GAN

Adversarial Loss: The Adversarial loss is given as output from the discriminator and input into the generator for the generator to learn to generate pragmatic high resolution images which are more similar to the ground truth data. It is a loss function that lets the generator

win the war by helping it to generate a high resolution image making it difficult for the discriminator to distinguish between the original image and the generated image.

$$l_{Gen}^{SR} = \sum_{n=1}^{N} -\log D_{\theta_D}(G_{\theta_G}(I^{LR}))$$

Fig. 8. Adversarial loss of SRGAN

The sum of adversarial loss of the generator and the content loss is equivalent to the perpetual loss

$$l^{SR} = \underbrace{l_{\mathrm{X}}^{SR}}_{\text{content loss}} + \underbrace{10^{-3} l_{Gen}^{SR}}_{\text{adversarial loss}}$$

Fig.9 Perpetual Loss

**C. Loss Function of Real-ESRGAN**

A more effective perpetual loss has been used in Real ESRGAN which is different than that used in SRGAN, where the features are constrained before the activation takes place unlike after which we can see is the case in SRGAN. In the previous model i.e. the SRGAN model the perpetual loss was defined at the activation layer in order to minimise the distance between two features. But in this model, the features are used before the activation function which will be able to overcome the following drawbacks. The first drawback that this model addresses is that the activated features are very sparse even after a deep neural network and the Second drawback it addresses is that use of features after activation has resulted into incompatible brightness in the output or the super resolved image when it is compared to the ground truth images.The perpetual loss or the total loss of Real ESRGAN is given in the figure.10.:

$$L_G = L_{\text{percep}} + \lambda L_G^{Ra} + \eta L_1,$$

Fig. 10 Perpetual Loss in Real-ESRGAN where,

$$L_1 = \mathbb{E}_{x_i} ||G(x_i) - y||_1$$

Fig.11. represents the content loss of the Real ESRGAN.

**D. Algorithm and Process Design.**

In figure 12, the first order layer represents the classical image degradation model to synthesize various input images. The first layer consists of blur (model blur is used as a convolution with linear blur filters), Resize (downsampling) and Noise (we usually consider gaussian noise and poisson noise).

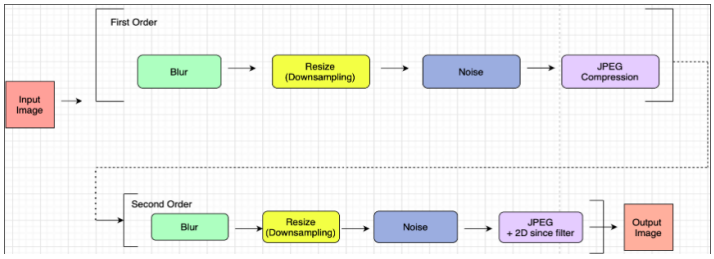


Fig. 12 Input Image Processing in Real-ESRGAN

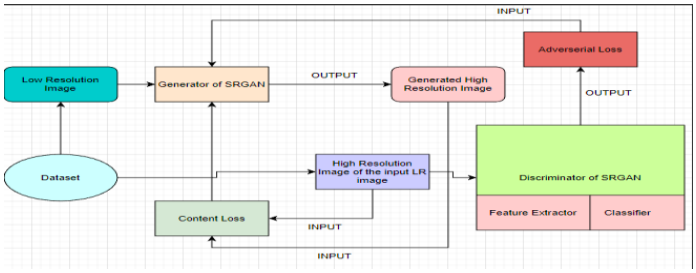


Fig. 13 Algorithm and Process Design

## V. EXPERIMENTAL RESULTS

### .A. Analysis

Fig .15. First image represents the low resolution image and the second image is the super resolved image i.e. the output image of the Real ESRGAN

Our final model exhaustively includes sampling of the distorted images and produces highly elucidated space body images using proper resolution techniques. The suggested methodology saves significant time and is practical and close to certain. After testing the model on several images of deep space, the output images have sharper and richer texture

when compared to the lower resolution images and the peak signal-to-noise ratio has improved..In the formula given below, MAXi is basically the maximum possible value of the pixel of the image.The average PSNR or the peak signal-to-noise ratio is 29.791 and structural similarity index turn out to equal to 0.8215 Where PSNR and SSIM are given by the formula which is explained in the figure .22

$$PSNR = 10 \cdot \log_{10}\left(\frac{MAX_I^2}{MSE}\right)$$
$$= 20 \cdot \log_{10}\left(\frac{MAX_I}{\sqrt{MSE}}\right)$$
$$= 20 \cdot \log_{10}(MAX_I) - 10 \cdot \log_{10}(MSE).$$

$$\mathrm{SSIM}(x,y) = \frac{(2\mu_x\mu_y + c_1)(2\sigma_{xy} + c_2)}{(\mu_x^2 + \mu_y^2 + c_1)(\sigma_x^2 + \sigma_y^2 + c_2)}$$

Fig. 22 PSNR and SSIM Formula

## VI. CONCLUSION

We Successfully implemented the model for generating high resolution deep space images captured by the telescope and with the help of this ”Super Resolution General Adversarial Network” model, we can easily enhance the resolution of any images of deep space objects up-to 1024X1024. Since the model in use is a bit convoluted, it requires high-end machines to run it.Also it requires enormous computation power and takes more time to train and show expected results as compared to other models in question. With the enhancement in the structure of hidden layers of Real ESRGAN we can expect to get more quality assured results in case of real world problems. In comparison to the classical degradation detection process for images and models Real ESRGAN has improved a lot but changes like adding an optimizer, more compatible activation.

## 1. REFERENCES

[1] Daniel Glasner, Shai Bagon, and Michal Irani. Super-resolution from a single image. IICCV, 2009.

[2] Demiray, B.Z., Sit, M. Demir, I. D-SRGAN: DEM Super-Resolution with Generative Adversarial Networks. SN COMPUT. SCI. 2, 48 (2021).

[3] Lian, S., Zhou, H., Sun, Y. (2019). FG-SRGAN: A Feature-Guided Super-Resolution Generative Adversarial Network for Unpaired Image Super-Resolution. In: Lu, H., Tang, H., Wang, Z. (eds) Advances in Neural Networks – ISNN 2019. ISNN 2019. Lecture Notes in Computer Science(), vol 11554. Springer, Cham.

[4] Liu, J., Chen, F., Wang, X., Liao, H. (2019). An Edge Enhanced SRGAN for MRI Super Resolution in Slice-Selection Direction. In: , et al. Multimodal Brain Image Analysis and Mathematical Foundations of Computational Anatomy. MBIA MFCA 2019 2019. Lecture Notes in Computer Science(), vol 11846. Springer, Cham.

[5] J. Li, L. Wu, S. Wang, W. Wu, F. Song and G. Zheng, ”Super Resolution Image Reconstruction of Textile Based on SRGAN,” 2019 IEEE International Conference on Smart Internet of Things (SmartIoT),2019, pp. 436-439, doi: 10.1109/SmartIoT.2019.00078.

[6] B. Liu and J. Chen, ”A Super Resolution Algorithm Based on AttentionMechanism and SRGAN Network,” in IEEE Access, vol. 9, pp. 139138-139145, 2021,

[7] Zhong, Z., Chen, Y., Hou, S., Wang, B., Liu, Y., Geng, J., Fan,S., Wang, D., Zhang, X.: Super-resolution reconstruction method of infrared images of composite insulators with abnormal heating based on
improved SRGAN. IET Gener. Transm. Distrib. 16, 2063– 2073 (2022).
[8] Eirikur Agustsson and Radu Timofte. Ntire 2017 challenge on single
image super-resolution: Dataset and study. In CVPRW, 2017.
[9] Google drive link:Google drive link

## Biographies

**Varad Joshi** is currently pursuing a bachelor's degree in computer engineering from Vivekanand Education Society's Institute of Technology,Chembur-Mumbai, Affiliated to University of Mumbai. He is in Final Year of Engineering and has worked in the field of Machine Learning, AI and Software Development. He's intended to graduate in the year 2023.

**Rushabh Rijhwani** is currently pursuing a bachelor's degree in computer engineering from Vivekanand Education Society's Institute of Technology,Chembur-Mumbai, Affiliated to University of Mumbai. .

# Optimizing Deep Learning Neural Networks: Brain to Computer Interface EEG-Based Imagined Word Prediction for Speech Disability

**Babu Chinta[1,*] , Dr. Moorthi M.[2]**

[1]*Reseaarch Scholar, Anna University, Chennai, India- 600025.*
[2]*Professor, Department of Biomedical/Medical Electronics, Saveetha Engineering College, Chennai, India-602117.*
[*]*Author email: babuchinta2019@gmail.com*

## Abstract.

This idea starts with vowel recognition and then designs a vowel GUI. Five One Versus Rest (OVR) classifiers are created in the next step. QSVM had 91.1% accuracy over 10 trials and 10 patients. Five classifiers (FDT, LDA, QSVM, WkNN, and Subspace Discriminant Classifier) are created using the One Versus Rest (OVR) technique and tested (SDC). Classifiers must identify "A, E, I, O, and U," fake vowels. PCA can improve classifier quality. This upgrade boosts performance by 20%, which is significant. And other side the deep learning CNN model is used. Alexie and training a BCI with EEG-based imagined word prediction, since they can distinguish up, down, right, left, and up to ten words from visual inputs. Alex Net outperformed Google Net in transfer learning. It had a higher accuracy (91.3%), recall (92.4%), precision (91.0%), and F1 score (91.7%) for the seven features. Reducing the number of recoverable attributes from seven to four decreased performance ratings from 85.4% to 84.8%, then 84.9% to 83.6%.

**Keywords**. Brain Computer Interface, Convolutional Neural Network, Principal Component Analysis, Quadratic Support Vector Machine.

## 1. INTRODUCTION

When a person uses a BCI to send out messages or orders, those signals bypass the normal output channels of the brain, which consist of the brain's nerves and muscles (Wolpaw et al., 2002). Patterns of electrical brain activity are recorded and stored in an EEG-based BCI, for example. The use of a BCI provides its user with a new means of communicating with the outside world, it can be used to help restore a wide range of senses and abilities, including sight, hearing, movement, speech, and thought. Since the advent of biomedical signal processing techniques, electroencephalography (EEG) data has been widely implemented in the areas of Brain Computer Interface and the detection of neurological diseases. Researchers working in the field of brain-computer interfaces (also known as BCIs) have recently moved their focus to the development of innovative Humans have developed augmentative communication and control technologies for people with severe neuromuscular disorders. Our increased understanding of how the brain works, the widespread availability of powerful, low-cost computer equipment, and the recognition of the needs and potentials of people (Wolpaw et al., 2002).

A wide variety of classification methods are now being used in BCI research and development. Current categorization techniques for EEG data were examined by researchers [5]. Algorithms are broken down into four distinct categories: Matrix/tensor, adaptive learning, and deep learning classifiers. In this study, we explore some of the key challenges associated with correctly categorizing EEG data. Each classifier's design philosophy, plus its pluses and minuses, are laid forth in detail. Also, the study examines the stability, dynamicity, and normalization of each classifier. Consistent with what the researcher has done before [6]. The topic of the classifier's applicability is also explored in this study. Future prospects for the classifiers are examined to wrap up the study. Improved accuracy in EEG feature classifiers is an area where further work is needed. [7].

## 2. LITERATURE REVIEW

For emotion recognition, a Deep Learning Network (DLN) with Principal Component Based Covariate Shift Adaptation was developed. based on EEG data [1]. (PCBCSA). In this study, employed DLN to investigate the unknown feature correlation between the input signals, which contributed significantly in the learning process. Hierarchical feature-based DLN implementation uses Stacked Auto Encoder (SAE). So, used a three-layer stack of autoencoders with two soft-max layers, one for valence and one for arousal, to estimate the emotion classification.

X. Zhang, L. et al [2] encountered difficulties in correctly identifying the subject's or person's mind from the raw brain signals analyzed due to the low quality and noise inherent in these signals. Pre-processing, which is typically the initial stage, is also a time-consuming process. Therefore, they proposed Unified Deep Learning [UDL] to aid human-machine cognition. The suggested framework initially considered employing electroencephalography (EEG), but has now expanded to include fMRI stands for functional magnetic resonance imaging, while magnetoencephalography measures brain activity (MEG). The raw brain impulses were uploaded to a cloud server, where they were analyzed using a convolutional deep learning model that varies from person to person.

N. Kumar, K. et.al [3] utilized bi-spectral analysis, with phase information obtained via phase signal detection, to define the non-Gaussian components of the EEG signals and reveal the link between the frequency components. The bi spectrum quantitative emotional features were derived using a Valence-Arousal model. The EEG signals were collected using a two-channel EEG signal machine, then preprocessed to reduce artefacts caused by EOG, and then filtered using a Butterworth algorithm.

J. Atkinsona and D. Campos et al [4] recognized the difficulties in EEG signal categorization and recognition, specifically that automatic recognition is typically limited to a small number of emotion classifications. Scientists have proposed a new method of emotion identification combining brain-computer interfaces and electroencephalograms in an effort to solve these problems.

## 3. PROPOSED METHOD

### *Implementation loops*

#### *a. EEG signal properties*

The EEG machine serves as the foundation of the entire setup. The EEG gadget has 16 sensors, and their positions are predetermined according to the 10-20 system. Out of the total of sixteen sensors, two are set as benchmarks. These two sensors will rest on the mastoid bones, which are located behind the ears. Fp1, Fp2, F3, F4, F7, F8, C3, C4, T3, T4, P3, P4, T5, T6, O1, O2 are the locations of the sixteen sensors. Each of these sensors provides a unique "channel" of information. The sensors' readings will be based on the brain's electrical impulses, generated by neurons.

The data from the EEG gadget is transferred to the computer through Bluetooth. There are a total of 25 channels in the incoming data, an increase of 9 channels from before. These nine channels carry timestamps, counters, marker signals, synchronization signals, gyro measurements, and more. Assuming a sample rate of 128Hz, the EEG equipment collects data once every 0.0078125 seconds. A total of 256 samples are taken over the course of the two-second recording and then analyzed using a matrix. In this case, the matrix would have 256 columns and 25 rows. The signal is then passed through a high pass filter, which attenuates the DC offset and eliminates any low-frequency disturbances. There is a cutoff frequency of 5 Hz in the high pass filter. In order to use MATLAB for classifier training, data is typically stored in a computer in a matrix format.

#### *b. Combined PCA/Quadratic SVM for vowel recognition*

Figure 3.1 shows the enhanced EEG-based vowel detection system block architecture using PCA and quadratic SVM. Data is sampled at 128 hertz using the EEG machine. Reduced sample sizes per recording as a result of the improved sampling rate will drastically cut down on the time and energy required to train and test classifiers. Each activity recording will have 256 sets of data. Because Principal Component Analysis (PCA) will rotate data and identify the direction with the highest degree of variation, it is used by the system instead of Common Spatial Features (CSP). This technique works well with information that does not cover every available experiment.

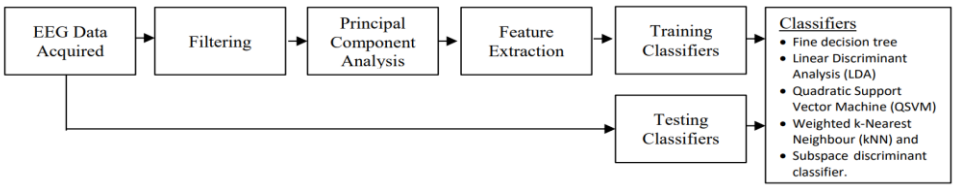


Figure 3.1. The improved EEG vowel identification system showing the PCA and quadratic SVM integrating

To train classifiers, PCA is used. The data in the predictor columns are transformed into the answer field. FDT, LDA, SVM, WkNN, and SD classifiers are the first five classifiers trained. In order to aid these classifiers in their classification efforts, principal component analysis can be used to determine which direction has the most data variance. Five-fold cross-validation is used to train the classifiers' data. As a result, the initial dataset was split into five parts, two of which would be used for training and the other two for validation. A new batch of data is then used to train the classifier and validate it. The training process will continue to repeat as long as the classifiers validate with each successive set and acquire new values for their weights. One classifier model is retained from the data and utilized for prediction. Resulting from repeated recording and classifier-training sessions, a final recording is made to test the classifiers. The data is scrubbed and then stored. Afterward, the saved classifier model is applied to the archived data for predicting purposes. The classifier model will provide a number between one and five to indicate its recommended course of action.

### *c. Word Prediction Using CNN*

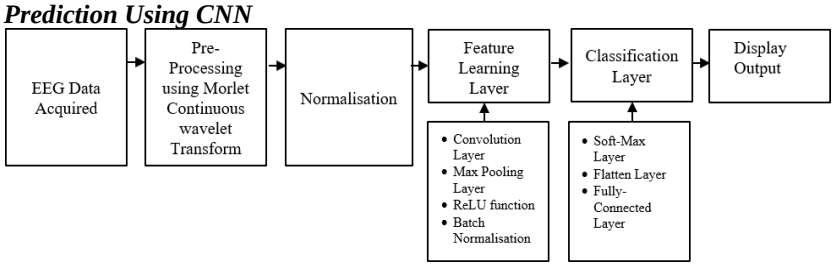


Figure 3.2. Block diagram for word recognition

Figure 3.2 shows the block diagram for word recognition. The EEG signals are converted into a 3D scalogram image using the Continuous Wavelet Transform (CWT), and the word imagined is predicted using a convolutional neural network (CNN), that can capture image time- and spatial-dependencies with the right filter.

#### *i. Pre-processing using Morlet Continuous Wavelet Transform*

The size and structure of the dataset were verified by loading before any preprocessing or normalization of label value could be carried out. The window function in CWT controls the primary wavelet function and can be resized and moved to suit the features of the desired wavelet. Thus, windowing can be performed over a longer time for low frequency and a shorter period for high frequency. Additionally, the variance analysis window can be split in two, simultaneously allowing for a detailed investigation of low- and high-frequency information in a non-stationary EEG signal. Because Morlet wavelet CWT is better suited for non-stationary EEG signals, it was used for the spectral analysis.

#### *ii. Alex net*

Alex net is an 8-layer deep convolutional neural network that has been trained on more than a million signals, making it capable of signal prediction across 1000 object categories. Both the fully linked layer and the output layer have 1000 classification outputs, and this number is utilized to categories the signals. However, this task requires the production of 10 distinct classifications. In order to get to an epoch where the fully connected layer can do the classification, weights and biases were fine-tuned at each iteration using backpropagation. Finally, the trained CNN model will be tested by feeding its output from the fully connected layer into a soft-max classification layer for labelled final classification. The SoftMax layer produces 10 outputs, which is the desired number of outputs (left, right, up, down, front, back, stop, pick, red, blue).

#### *iii. Training Model Setup*

In this part, we compare two trained models and pick the one that performs best in terms of accuracy and training time. The Alex net and the Googlenet are two trained models that are compared in this experiment. Googlenet is trained with an epoch of 165 because it needs more time to learn, while Alex net is educated with an epoch of 85. The Alex net is more accurate than the Googlenet despite increased epoch and training time. Performance & result analysis.

#### *iv. PCA and Quadratic SVM & 9-trail classifier accuracy*

This test an appearance at the accuracy of classifiers trained with only one trial the classifiers' efficiency when only one trial, or recording session, is used during training. This presents a problem for the concept of developing a reliable and precise classifier with a minimum of training time. The classifier must be flexible

enough to accommodate subtle shifts in the data. First session of Subject 1's recordings is used to train all five classifiers, as indicated in Table 3.1. The purpose of this experiment is to see how much of an effect principal component analysis (PCA) has on classifier performance, as well as how much of an effect more data has on classifier performance. As demonstrated in Table 3.2, this test will also reveal whether or not direct correlations between training data availability and classifier performance are statistically significant. To replicate Subject 1's result from the preceding experiment.

Table 3.1. Accuracy of one-trial classifier performance

| Classifier | Accuracy (%) |
|---|---|
| Fine Decision Tree (FDT) | 81.06 |
| Linear Discriminant Analysis (LDA) | 82.03 |
| Quadratic (SVM) | 89.01 |
| Weighted (WkNN) | 80.06 |
| Subspace Discriminant (SD) | 87.08 |

Table 3.2. Accuracy of 9-trials classifier performance

| Classifier | Accuracy (Without PCA %) | Accuracy (With PCA %) |
|---|---|---|
| Fine Decision Tree (FDT) | 68.02 | 87.06 |
| Linear Discriminant Analysis (LDA) | 72.02 | 89.07 |
| Quadratic (SVM) | 68.05 | 91.01 |
| Weighted (WkNN) | 73.08 | 88.00 |
| Subspace Discriminant (SD) | 60.08 | 89.08 |

***v. Vowel classifier accuracy***

The assumption is that different classifiers have different capabilities when it comes to identifying vowels. To describe the vowels "a," "e," and I for instance, a quadratic support vector machine (SVM) may be preferable, while a linear discriminant analysis (LDA) may be preferable, as indicated in Table 3.3. In order to identify the most appropriate class of responses, classifiers are trained utilizing the OVR principle.

Table 3.3. Accuracy of classifiers in classifying each task.

| Vowels | Fine Decision Tree (FDT) (%) | Linear Discriminant (LDA)(%) | Quadratic SVM (%) | WeightedKNN (%) | Subspace Discriminant (%) |
|---|---|---|---|---|---|
| A | 82.02 | 89.02 | 96.00 | 86.03 | 89.02 |
| E | 86.03 | 89.07 | 91.00 | 89.06 | 88.01 |
| I | 87.09 | 86.09 | 92.00 | 89.03 | 89.02 |
| O | 88.00 | 91.00 | 88.05 | 85.09 | 90.03 |
| U | 87.04 | 90.02 | 88.03 | 88.01 | 89.02 |

Among these five classifiers, quadratic SVM performs the best. As a result, PCA has been demonstrated to enhance classifier quality. This enhancement boosts performance by around 20% in accuracy, which is a notable amount. The test outcomes in section four detail the overall performance of each classifier. A quadratic support vector machine (SVM) classifier is the most often used algorithm for classification.

***vi. Word Prediction using CNN***

A majority of the data (80%) was used for training the model, with the remaining (20%) used for testing and validation. According to Model 1, the results of the 10 tests given to each participant are presented in Table 4.4, whereas those according to Model 2 are presented in same Table 3.4. These tables show the generated and recorded results for each trained model used in the learning of EEG signal classification using 4 features extracted, including the Recall, Precision, Accuracy, and F1 scores for each trained model.

Table 3.4. Model-1 and Model-2 performance in tests using 4-feature data

| Participants | Recall (%) | | Precision (%) | | Accuracy | | F1 score | |
|---|---|---|---|---|---|---|---|---|
| | Model1 | Model 2 | Model 1 | Model 2 | Model 1 | Model 2 | Model 1 | Model 2 |
| 1 | 91.01 | 81.08 | 89.06 | 89.08 | 90.04 | 89.08 | 90.03 | 85.06 |
| 2 | 86.04 | 77.08 | 83.02 | 76.01 | 85.04 | 77.05 | 84.08 | 76.09 |
| 3 | 87.07 | 79.01 | 85.03 | 79.04 | 86.03 | 79.03 | 86.05 | 79.02 |

| | | | | | | | | |
|---|---|---|---|---|---|---|---|---|
| 4 | 86.02 | 77.05 | 84.07 | 75.05 | 85.07 | 75.05 | 85.04 | 76.05 |
| 5 | 85.08 | 75.04 | 83.02 | 74.07 | 83.02 | 74.02 | 84.05 | 75.00 |
| 6 | 86.06 | 87.02 | 84.01 | 86.05 | 85.05 | 86.01 | 84.08 | 86.03 |
| 7 | 90.08 | 88.09 | 88.05 | 89.01 | 89.08 | 88.01 | 89.06 | 88.05 |
| 8 | 91.02 | 93.03 | 93.02 | 92.05 | 94.05 | 92.02 | 92.02 | 93.09 |
| 9 | 87.06 | 86.01 | 86.01 | 85.08 | 86.01 | 85.01 | 86.08 | 87.04 |
| 10 | 93.07 | 90.06 | 91.04 | 88.07 | 92.08 | 88.07 | 92.05 | 89.06 |
| Average | 88.07 | 83.07 | 86.08 | 83.06 | 88.00 | 84.06 | 88.08 | 83.06 |

## 4. DISCUSSION & PERFORMANCE ANALYSIS

This study shows how to use a brain-computer interface (BCI) and electroencephalogram (EEG) to anticipate words. In this experiment, we first compared three distinct ILR values (0.0001, 0.0003, and 0.0005). We used an ILR of 0.0001 because it permits a room to attain an accuracy of over 70.68%, taking into account both the maximum feasible accuracy and the largest difference in validation and training loss. The proceeding two models are performance in tests using four-feature data. In terms of training time, Alexnet's 85 epochs were chosen since they required less time in the lab yet produced better results. Furthermore, Table 8 describes the results of a comparison of the two CNN models' performance when tested on data containing either 7 or 4 extracted features.

Table 4.1. Two model performance comparison

| **Used several features extracted** | **Performance of Models** | **Recall (%)** | **Precision (%)** | **Accuracy** | **F1-score** |
|---|---|---|---|---|---|
| 7 | Model -1 | 92.04 | 91.00 | 91.03 | 90.07 |
| | Model- 2 | 87.07 | 85.08 | 87.00 | 79.03 |
| 4 | Model- 1 | 84.04 | 82.09 | 83.08 | 83.06 |
| | Model- 2 | 82.07 | 82.06 | 82.06 | 82.06 |

Table 4.1 shows that when using all of the performance evaluation criteria for 7 and 4 extracted features, model 1 (Alex net) performs better than the rest. When 7 extracted features were applied, Alexnet's accuracy increased to 91.3%. In addition, When the number of extracted features was lowered from 7 to 4, all performance measures in both trained models decreased, though only by an average of 3.3%.

Table 4.2. Comparing developed models to literature

| **Performance of parameters analysis** | **Model -1 Outperforms** | | **Model -2 Outperforms** | | **Kocturova& Juhar, 2021 [31]** | **Netzer, Frid & Feldman, 2020 [32]** |
|---|---|---|---|---|---|---|
| Used several features extracted | 4 | 7 | 4 | 7 | 9 | - |
| Recall (%) | 85.04 | 92.04 | 83.07 | 88.07 | 89.085 | - |
| Precision (%) | 83.09 | 91.00 | 83.06 | 86.08 | 85.096 | - |
| Accuracy | 84.08 | 91.03 | 83.06 | 88.00 | 85.062 | 71.06 |
| F1- score Measure | 84.06 | 91.07 | 83.06 | 80.03 | 87.080 | - |

Table 4.2 contrasts the new models with those already in the literature [31, 32]. In comparison to model 2 (Googlenet), [31], and [32], it is clear that the accuracy of the generated model 1 has been enhanced by a significant margin (3.79%, 6.71%, and 27.90%). They have extracted a more manageable subset of features and evaluated the performance of the systems and models we have developed. Alexie was the better model than Googlenet due to its 91.3% accuracy after being trained with 80 epochs, 64 batches, the scalogram pre-processing strategy, an 80:20 split between the training and validation sets, and an initial learning rate of 0.0001. With this level of accuracy, researchers can expand their efforts to cross-participant analysis to gather a larger sample size for testing and refining the system's deep-learning neural-network foundations to make them appropriate for use in mobile apps based on EEG.

## 5. CONCLUSION

This concept begins with vowel recognition and subsequently develops a vowel user interface. Using the One Versus Rest (OVR) method, five classifiers (FDT, LDA, QSVM, WkNN, and Subspace Discriminant Classifier) are developed and evaluated (SDC). Classifiers must identify the fictitious vowels "a, e, I, o, and u." With an accuracy of 90.1% across 10 trials and 10 individuals, QSVM is the most precise classifier of the

five. PCA helps increase classifier quality. This improvement increases performance by 20%. And the CNN model with deep learning is utilised. The Alex net transfer learning model was deemed to be superior to Googlenet because it achieved an accuracy of 91.3% whereas Googlenet had only 89.7% accuracy. Cross-participant analysis, which will expand participant numbers, will benefit from this high accuracy.

## 6. REFERENCES


[1] S. Jirayucharoensak, S. Pan-Ngum and P. Israsena, "EEG-Based Emotion Recognition Using Deep Learning Network with Principal Component Based Covariate Shift Adaption", The Scientific World Journal, Vol. 1, pp. 1-10, 2014.

[2] X. Zhang, L. Yao, S. Zhang, S. Kanhere, Salil, Sheng, Michael and Y. Liu, "Internet of Things Meets Brain-Computer Interface: A Unified Deep Learning Framework for Enabling Human-Thing Cognitive Interactivity", Journal of Latex Class Files, Vol. 14, No. 8, pp. 1-8, 2015.

[3] N. Kumar, K. Khaund and M. S. Hazarika, "Bi-spectral Analysis of EEG for Emotion Recognition", Procedia Computer Science, Vol. 84, No. 1, pp. 31-35, 2016.

[4] J. Atkinsona and D. Campos, "Improving BCI-based emotion recognition by combining EEG feature selection and kernel classifiers", Expert Systems with applications, Vol. 47, No. 3, pp. 35-41, 2016.

[5] F. Lotte, L. Bougrain, A. Cichocki, M. Clerc, M. Congedo, A. Rakotomamonjy, F. Yger, "A review of classification algorithms for EEG-based brain-computer interfaces: a 10-year update", Journal of Neural Engineering, Vol. 15, Vol. 3, 2018, pp.1-29.

[6] L. Ravi, S. Sathish Kumar, Chow Him Mun, "Improved Speech Recognition using Neural Network", The International Journal of Applied Engineering Research, Vol.9, No. 18, 2014, pp. 4297-4325.

[7] L. Wookey, J. S. Jessica, O. Busra, S. S. Bong, M. Azizbek, L. Suan, "Bio signal Sensors and Deep Learning-based speech recognition: A Review", Sensors, 2021, pp. 1-22.

[8] K. Gautam, T, Co, C. Mason, H. Yan, T. H. Ahmed, "Improving EEG based Continuous Speech Recognition", 2019, arXiv:1911.11610.

[9] M. Beomjun, K. Jongin, P. Hyeong-Jun, L. Boreom, "Vowel Imagery Decoding toward Silent Speech BCI using Extreme Learning Machin with Electroencephalogram", BioMed Research International, 2016, p. 1-11.

[10] A. D. Khalid, H. Laila, Z. S. Saadeh, H. Mohammed, S. Ramzi, H. A. Sharhabeel, "An efficient speech recognition system for arm-disabled students based on isolated words" Computer Applications in Engineering Education, Vol. 26, No. 2, 2018, pp. 285-301.

[11] J. T. Panachakel, A. G. Ramakrishnan, "Decoding Covert Speech from EEG - A Comprehensive Review", Neuro Science, 2021

[12] C. Sandhya, S. R. Anandha, A. Kavitha, "Identification of vowels in consonant-vowel-consonant words from speech imagery-based EEG signals", Cognitive Neurodynamic, Vol. 14, 2020, pp. 1- 19.


## Biographies

BabuChinta Completed his B.Tech in Electronics and Communication Engineering from Jawaharlal Nehru Technological University Kakinada, Andhra Pradesh, India. Post-Graduation (M.Tech) in Communication Systems obtained from Andhra University, Vishakapatnam, Andhra Pradesh, India. Present he pursuing Ph.D. at Anna University, Chennai. He had 5 years of teaching experience and he published papers on reputed journals. His research interests on Signal & Image processing, Artificial Intelligence, Brain to Computer Interface, and Speech signal Processing.

**Dr.M.Moorthi** is a Professor & Head of the Department in the Biomedical Engineering at Saveetha Engineering College, Chennai. He has professional teaching experience of over 20 years. His areas of research interest are Digital image processing and Multimedia Compression, Microprocessor and Microcontroller. He is Anna University Recognized Supervisor for Ph.D/M.S Scholars. He has obtained several funding from AICTE,CSIR,BRNS, IEEECurrently, he is the IEEE Student branch and Society advisor at Saveetha Engineering College. He is currently acting as an Executive member in IEEE Photonics Society, Madras section.Duzce University. His research areas include mobile security, deep learning, and social network analysis.

# 9's Complement Encoder using QCA Schematics

**[1]Sristi Chakraborty, [2]Koustav Chaki, [3]Ratna Chakrabarty**

*[1] Techno Main Salt Lake, Kolkata, West Bengal, under Maulana Abul Kalam Azad University of Technology.*

*[2, 3] Institute of Engineering and Management, Kolkata, West Bengal.*

## Abstract.

Quantum Dot Cellular Automata (QCA) is an emerging technique that utililizes confiment and tunnelling of electrons and nano-scale particles to execute logical computational functions. The foundation of QCA is electron confinement in cells consisting of quantum mechanical interactions between the AlGaAs substrate within which quantum wells are formed, where the probability of an electron occurrence can be adjusted by shifting the transverse polarization applied to the cell. Digital Logic Combinational or Sequential Topologies can be realised utilising nanoscale QCA cells, this paper will demonstrate a novel method to implement a 4 bit counting operation using a Fixed Polarized Input, using 18x18 nm2 cells with 4-Quantum Confinement Wells visualised as dots or holes in the software QCADesginer(2.0.3), by Walus K., which allowed us to model most Logical CMOS circuitry at ease.

**Keywords**. Coulombic Blockade, Electron Confinement, Tunnelling, Cellular Automata

## 1. INTRODUCTION

QCA cells, proposed in 1993, Lent et al.[1, 2] can be represented as a square planar structure of 18x18 nm2 which has 4 quantum wells that are capable of electron confinement, and are generally doped with 2 extra electrons. Upon polarization, it is possible for the electrons to tunnel between the adjacent vertical well. This is provided via underlying clocking wires each shifted by a phase of 90º, namely Clock 0 to 3. These clocking signals essentially govern the cell configuration. The state of the cells can be classified into SHIFT, HOLD, RELEASE and RELAX, which will determine the cells mode of operation.

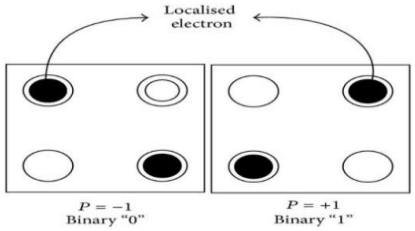


Figure 1. Two Possible polarization states which can be inferred as binary logic [1, 0]

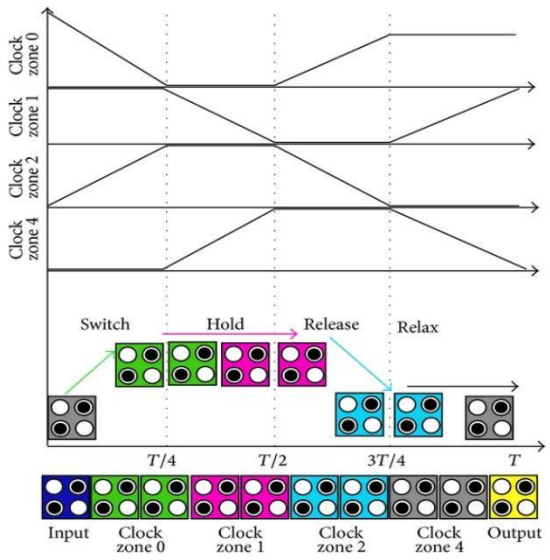


Figure 2. Clocking for Data Transmission across zones [3]

However, the ideal operating conditions of QCA based implementations is to isolate the system from any external energy by keeping the temperatures as low as 4-10 K to keep the Kink Energy[4] between the cells minimal for an ideal adiabatic switching of QCA cells which is essential for their intended applications and advantages over any other computing systems, as it enables data transmission without any actual flow of current [5] making it extremely efficient when working at clocking speeds in the range of Tara-Hertz switching speeds, with nearly negligible energy dissipation.[6], [7] .

## 2. LOGICAL DESIGN AND QCA IMPLEMENTATION

Following the general design of a 9's complement converter, with 4 input and output cells designated in the schematic. A basic logic circuit would include a 4-bit BCD [8]–[10] input labelled accordingly as $A_0$, $A_1$, $A_2$ and $A_3$. Similarly, the output cells were indexed with Y from 0-3. A simple logic circuit is presented in Fig 3, upon which the final QCA schematic is based upon.

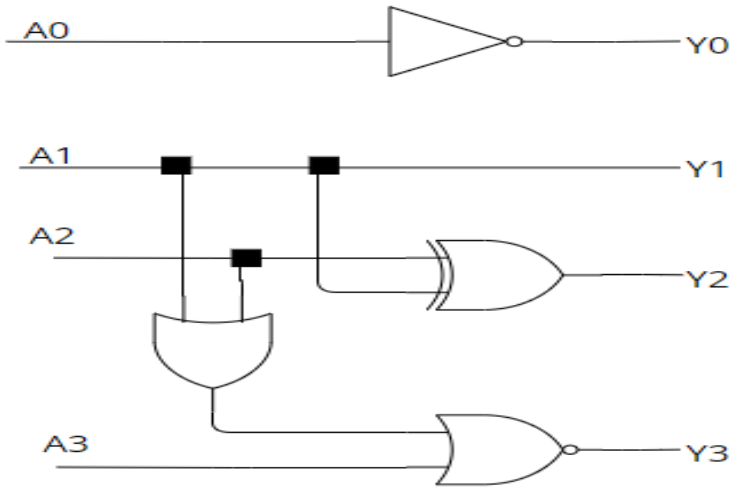


Figure 3. The Generic Logic Structure of a 9s Complement Converter

A Binary Coded Decimal Digit's 9's Complement would classify as the BCD that would result in a decimal value of 9 when added. This principle of conversion yields positive results for the BCD < 9, else would result in a negative signed number.

TABLE 1. TRUTH TABLE FOR INPUT AND ITS 9'S COMPLEMENT VALUES

| BCD | 4-bit Binary Equivalent | | | | 9's Comp | 4-bit Binary Equivalent | | | |
|---|---|---|---|---|---|---|---|---|---|
| 0 | 0 | 0 | 0 | 0 | 9 | 1 | 0 | 0 | 1 |
| 1 | 0 | 0 | 0 | 1 | 8 | 1 | 0 | 0 | 0 |
| 2 | 0 | 0 | 1 | 0 | 7 | 0 | 1 | 1 | 1 |
| 3 | 0 | 0 | 1 | 1 | 6 | 0 | 1 | 1 | 0 |
| 4 | 0 | 1 | 0 | 0 | 5 | 0 | 1 | 0 | 1 |
| 5 | 0 | 1 | 0 | 1 | 4 | 0 | 1 | 0 | 0 |
| 6 | 0 | 1 | 1 | 0 | 3 | 0 | 0 | 1 | 1 |
| 7 | 0 | 1 | 1 | 1 | 2 | 0 | 0 | 1 | 0 |
| 8 | 1 | 0 | 0 | 0 | 1 | 0 | 0 | 0 | 1 |
| 9 | 1 | 0 | 0 | 1 | 0 | 0 | 0 | 0 | 0 |

In order to establish the relation between the Inputs and the Outputs in a QCA structure, the logic gates were established using majority gates [11] and inverter gates. Redundant cells were removed and Clocking zones were optimised for an ideal performance of the Converter.

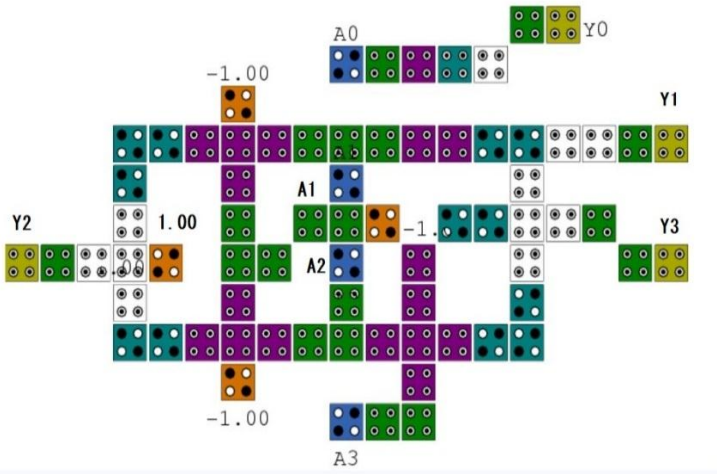


Figure 4. Proposed Schematic of a 9's complement BCD encoder

The depicted circuit shows an equivalent logic circuit in a QCA domain where the input BCD in its binary representation is converted to its 9's complement, which is useful in subtraction/addition of higher bit numbers with ease. Especially in the case of Signed Subtraction Methods. This circuit adds to the plethora of designs that are available as design analogies for CMOS to QCA migration. However, fabrication challenges are still well beyond our present limits for an idealised operation.

### *2.1. Simulation Results*

The outputs are obtained via the bistable approximation engine, with the QCA Designer allows changing the number of recorded samples by increasing the number of iterations. Same can be done for the Clock Zone frequency by using various arrangements of the clocking wires underneath the main cell, however, there will be a proposed maximum limit of switching frequency due to presence of Quantum Coherence between the cells, the exact value of the limit is dependent on the area of the design and the number of cells used.

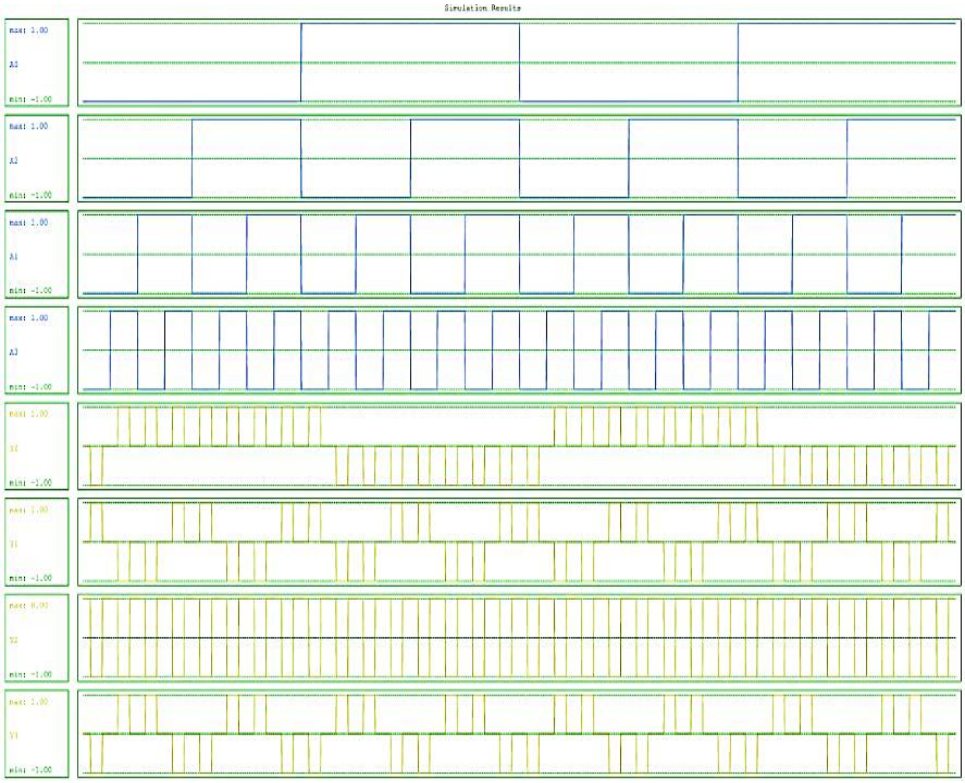

Figure 6. Converted Outputs as Simulation Results

The resultant output clearly demonstrates that the conversion of BCD encoding can be further realized for the creation of a robust ALU block made of purely QCA cells, capable of handling much higher bit operations at a scale of almost Terahertz speeds of processing.

## 3. REFERENCES


[1] C. S. Lent, P. D. Tougaw, W. Porod, and G. H. Bernstein, "Quantum cellular automata," Nanotechnology, vol. 4, no. 1, pp. 49–57, 1993.

[2] P. D. Tougaw, "A device architecture for computing with quantum dots," Proceedings of the IEEE, vol. 85, no. 4, pp. 541–557, 1997.

[3] L. Bonci, M. Gattobigio, G. Iannaccone, and M. MacUcci, "Simulation of time evolution of clocked and nonclocked quantum cellular automaton circuits," J Appl Phys, vol. 92, no. 6, p. 3169, Aug. 2002.

[4] L. R. C. Fonseca, A. N. Korotkov, K. K. Likharev, and A. A. Odintsov, "A numerical study of the dynamics and statistics of single electron systems," J Appl Phys, vol. 78, no. 5, pp. 3238–3251, 1995.

[5] M. MacUcci, M. Gattobigio, and G. Iannaccone, "Proposed experiment to assess operation of quantum cellular automaton cells," J Appl Phys, vol. 90, no. 12, pp. 6428–6433, Dec. 2001.

[6] L. Bonci, G. Iannaccone, and M. Macucci, "Performance assessment of adiabatic quantum cellular automata," J Appl Phys, vol. 89, no. 11 I, pp. 6435–6443, Jun. 2001.

[7] C. Ungarelli, S. Francaviglia, M. Macucci, and G. Iannaccone, "Thermal behavior of quantum cellular automaton wires," J Appl Phys, vol. 87, no. 10, pp. 7320–7325, May 2000.

[8] A. O. Orlov, I. Amlani, G. Toth, C. S. Lent, G. H. Bernstein, and G. L. Snider, "Experimental demonstration of a binary wire for quantum-dot cellular automata," Appl Phys Lett, vol. 74, no. 19, pp. 2875–2877, May 1999.
[9] A. O. Orlov et al., "Experimental demonstration of clocked single-electron switching in quantum-dot cellular automata," Appl Phys Lett, vol. 77, no. 2, pp. 295–297, Jul. 2000, doi: 10.1063/1.126955
[10] C. S. Lent and P. D. Tougaw, "Lines of interacting quantum-dot cells: A binary wire," J Appl Phys, vol. 74, no. 10, pp. 6227–6233, 1993.
[11] R. Laajimi, A. Ajimi, L. Touil, and A. Newaz, "A Novel Design for XOR Gate used for Quantum-Dot Cellular Automata (QCA) to Create a Revolution in Nanotechnology Structure," International Journal of Advanced Computer Science and Applications, vol. 8, no. 10, 2017

## Biographies

Sristi Chakraborty is currently the BTech student of Computer Science and Engineering (Data Science) at Techno Main Salt Lake under Maulana Abul Kalam Azad University of Technology, West Bengal, India.

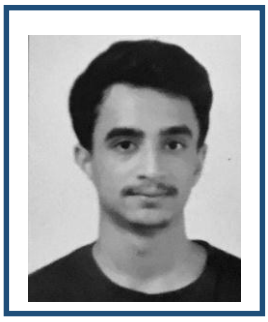

Koustav Chaki received his Postgraduate Degree from the Institute of Engineering and Management, West Bengal, India. He is currently working as a Research Scholar at the Department of Electronics and Communication Engineering at Institute of Engineering and Management, Kolkata. His research areas include VLSI Design Fabrication and Micro-Electronics.

Ratna Chakrabarty is the Professor of the Department of Electronics and Communication Engineering at Institute of Engineering and Management, West Bengal, India. Her research areas includes Quantum dot Cellular Automata and communication engineering.

# Development & Property study of Partially Depleted Silicon-On-Insulator MOSFET

**Bidyendu Ghoshal, Samit Karmakar*, Soumik Kr. Kundu, Mili Sarkar, G. S. Taki**

*Institute of Engineering and Management, Kolkata 700091, India*

*bidyendughoshal@gmail.com; *samit.karmakar@iem.edu.in; mili.sarkar@iem.edu.in; gstaki@iem.edu.in, soumik.kundu@iem.edu.in (*https://orcid.org/0000-0002-0858-5168)*

## Abstract

The results of process and device simulation using Silvaco TCAD tools to develop a Partially Depleted Silicon-On-Insulator Metal Oxide Semiconductor Field Effect Transistor (PD SOI MOSFET) are presented in this paper. The purpose of this simulation work is to investigate the drain current and global device temperature variation of the device as the oxide material consisting of the buried oxide layer changes from Silicon dioxide ($SiO_2$) to Hafnium dioxide ($HfO_2$) and Zirconium dioxide ($ZrO_2$). The results also show the energy band diagrams for all three oxide materials. The device is virtually fabricated with ATHENA software, simulated with ATLAS software in the DeckBuild environment, and all graphs are plotted in Silvaco with TonyPlot.

**Keywords**. Silicon-On-Insulator, MOSFET, Silvaco, ATHENA, ATLAS.

## 1. INTRODUCTION

The Silicon on Insulator Metal Oxide Semiconductor Field Effect Transistor (SOI-MOSFET) has several distinct properties, including lower parasitic capacitance, protection from electrostatic discharge, minimal short channel effects (SCEs), lower noise, and improved sub-threshold slope, excellent adaptability, improved radiation hardness, minor fringing capacitance, appealing isolation, latch-up security, high velocity, high temperature, and high-recurrence execution. Most of the research works in developing SOI-based integrated circuits benefit from these characteristics (ICs) [1].

Long back ago, J.E Lilienfield patented the first field effect transistor concept, titled "Method and Apparatus for Controlling Electric Currents," which evolved into the modern metal oxide semiconductor field effect transistor, MOSFET. He proposed a three-terminal device in which the source-to-drain current is controlled by a gate field effect and is dielectrically isolated from the rest of the device. The device's active component is made of a thin semiconductor film deposited on an insulator. Coincidentally, the first proposed FET was an SOI device [2]. Partially Depleted SOI device design is easier to manufacture but it requires more sophisticated device and circuit design to mitigate the effects of the floating-body.

Technology Computer-Aided Design (TCAD) is a design and simulation software which acts as a virtual platform for designing, fabricating, and then operating semiconductor devices such as Bipolar Junction Transistor (BJT), Metal Oxide Semiconductor Field Effect Transistor (MOSFET), and so on. This is critical for

understanding and testing the functionality of the designed device structure before proceeding with the real-time fabrication process and aids in the extraction of device parameters by studying the device's simulated characteristics.

DeckBuild is SILVACO's virtual platform-based wafer fabrication program's front-end Graphical User Interface (GUI). The framework of this program connects a wide range of process and device simulation tools available through SILVACO and allows them to work in an organized, glitch-free, and efficient manner. DeckBuild's pull-down menus aid in syntax creation and provide basic simulation controls. ATLAS and ATHENA are frameworks for multidimensional device simulation. As a result, the SOI MOSFETs can be generated in the ATHENA simulation environment using its layout-based simulation syntax, and ATLAS is used to solve the device's outputs [3].

ATHENA can simulate physical etching, shallow implant, RTA diffusion process stages, and local oxidation to create silicon islands. Among standard models for BULK and SOI technologies, ATLAS offers the following features for SOI-specific device simulation: Self-heating model for modelling of negative differential resistance, impact ionisation model for breakdown and kink effect [4].

The version of Silvaco DeckBuild used to write the code is 5.2.14.R. Version 5.2.3.R Silvaco TonyPlot is used to show the resulting device and graphs.

## 2. MATERIALS

In this paper, the main focus are three materials: $SiO_2$, $HfO_2$ and $ZrO_2$.

Silicon dioxide ($SiO_2$) films on silicon serve as the foundation for metal-oxide semiconductor (MOS) field-effect transistors (FET), which are at the heart of the majority of today's very-large-scale integrated (VLSI) circuits. The study and understanding of the properties of these films, as well as the physics of $SiO_2$, are thus critical to the semiconductor industry [5].

The main reasons for using $SiO_2$ are its excellent insulating properties of at low and medium electric fields, as well as the development of $SiO_2$ is relatively simple and via inexpensive growth techniques.

Oxygen-ion ($^{16}O^+$) implantation into silicon produced buried $SiO_2$ layers. Watanabe and Tooi [6] were the first to report the formation of $SiO_2$ layers in silicon via oxygen-ion implantation.

$HfO_2$ has a high melting temperature, low thermal conductivity, and a high dielectric constant (relative to $SiO_2$ and other gate dielectrics). $HfO_2$ was investigated as a high-k gate dielectric due to its higher dielectric permittivity than that of $SiO_2$. Because of its high melting temperature and low thermal conductivity, hafnium dioxide ($HfO_2$) has long been used as a refractory material [7].

With its excellent chemical and physical properties, zirconium oxide ($ZrO_2$), also known as zirconia, has applications such as fuel cells, gas sensors, optoelectronics, catalysts, and corrosion resistant materials. $ZrO_2$ is an important luminescent material with good optical transparency and a potential candidate for photocatalytic applications

due to its high surface area and presence of a large number of oxygen vacancies, with a band gap of >5 eV [8].

The material properties for $HfO_2$ and $ZrO_2$ considered for this paper is shown in Table: I.

TABLE: I TABLE OF MATERIAL PROPERTIES [9][10][11]

| **Material** | **Material Properties** | | | | | |
|---|---|---|---|---|---|---|
| | ***Permittivity*** | ***Thermal Conductivity (W/mK)*** | ***Affinity*** | ***Band Gap (eV)*** | ***Conduction Band Density*** | ***Valence Band Density*** |
| $HfO_2$ | 25 | 1 | 2 | 5.9 | 75 | 150 |
| $ZrO_2$ | 29 | 2 | 1.64 | 5.8 | 11 | 15 |

TABLE: II TABLE OF IMPLANT MOMENTS [13]

| **Material** | **Impurity** | **Impurity Concentration** (ions/ $cm^2$) | **Energy (keV)** | **Implant Moment Data** | | | |
|---|---|---|---|---|---|---|---|
| | | | | ***Range (Micron)*** | ***Std. Dev (Micron)*** | ***Gamma*** | ***Kurtosis*** |
| $HfO_2$ | Boron | 8.0e12 | 100 | 0.2171 | 0.075 | -0.0154 | 2.3748 |
| | | 9.5e11 | 10 | 0.0252 | 0.075 | 0.5152 | 2.8775 |
| | Phosphor | 3.0e13 | 20 | 0.0198 | 0.075 | 0.6216 | 3.1655 |
| | Arsenic | 5.0e15 | 50 | 0.0243 | 0.075 | 0.5738 | 3.1171 |
| $ZrO_2$ | Boron | 8.0e12 | 100 | 0.3081 | 0.075 | -0.3166 | 2.6510 |
| | | 9.5e11 | 10 | 0.0416 | 0.075 | 0.3669 | 2.6613 |
| | Phosphor | 3.0e13 | 20 | 0.0294 | 0.075 | 0.4814 | 2.9370 |
| | Arsenic | 5.0e15 | 50 | 0.0344 | 0.075 | 0.4193 | 2.9775 |

The data of table: II is found from the software SRIM version SRIM-2008.04. Moments define the tables and spatial moments that are employed within the analytical implant models.

The predicted range is specified by RANGE (RP); the units are in microns. The standard deviation is specified by STD.DEV, and the units are in microns. The third and fourth moments are specified by Gamma (skewness) and Kurtosis respectively [12].

## 3. VIRTUAL FABRICATION PROCESS OF SOI MOSFET USING ATHENA SIMULATOR

For the base model, The SOI MOSFETs used in this study were made on p-type (100) UNIBOND SOI wafers with a buried oxide of 1 micron. ATHENA (Silvaco) and ATLAS (Silvaco) were used to simulate the process conditions and two-dimensional (2-D) device characteristics, respectively. Boron-ion implantation was performed on 100 pears to introduce an impurity into the channel region. The top silicon layer was then thermally oxidised to a thickness of 0.03 micron. The gate oxide layer is formed through diffusion with dry oxygen. A 0.2 micron thick layer of polysilicon layer is deposited. Now, a photolithography step followed by vertical etching, defines the length of the transistor gate contact. Following the formation of the gate oxide layer, the gate is formed. The polysilicon layer is deposited using conformal deposition and etched until it is half the length of the desired gate. Prior to performing polysilicon doping, oxidation will be performed using Fermi method. Due to non-planar 2-D polysilicon structure, the compress method is used. Following polysilicon oxidation, the polysilicon is doped with phosphorus to form an n+ polysilicon gate. The source/drain junction formed by doping arsenic. The arsenic dose staying constant, but the doping energy varies with the thickness of the SOI layer to achieve the same doping concentration for all structures. Before depositing the metal layer, a high dose (5e15 ions/cm2) of arsenic is implanted with 50 pears to build the low resistance of the source and drain regions. A portion of the gate oxide layer is etched to open a contact window for the metal. The metal-S/D contact will then be deposited and etched, leaving only the metal-S/D contact. [14].

Finally, the SOI MOSFET is contacted (from left to right: source, gate, drain) and the electrical behavior of the device is examined. The half structure is then mirrored to produce the full structure. The gate, source, and drain terminals are all defined. There will also be a command to define a flat electrode on the simulation structure's bottom that will serve as the body terminal.

For other test models in the buried oxide layer, $HfO_2$ and $ZrO_2$ are used instead of $SiO_2$. Implant moment data given in Table: I for both $HfO_2$ and $ZrO_2$ are used for the implantation of previously mentioned boron, arsenic, and phosphorus dosage.

## 4. RESULTS & DISCUSSION

The figure 1 shows the SOI MOSFET devices fabricated using Athena. The main difference as this paper focuses on is the buried oxide layer. First device in Figure 1 has $SiO_2$ (blue

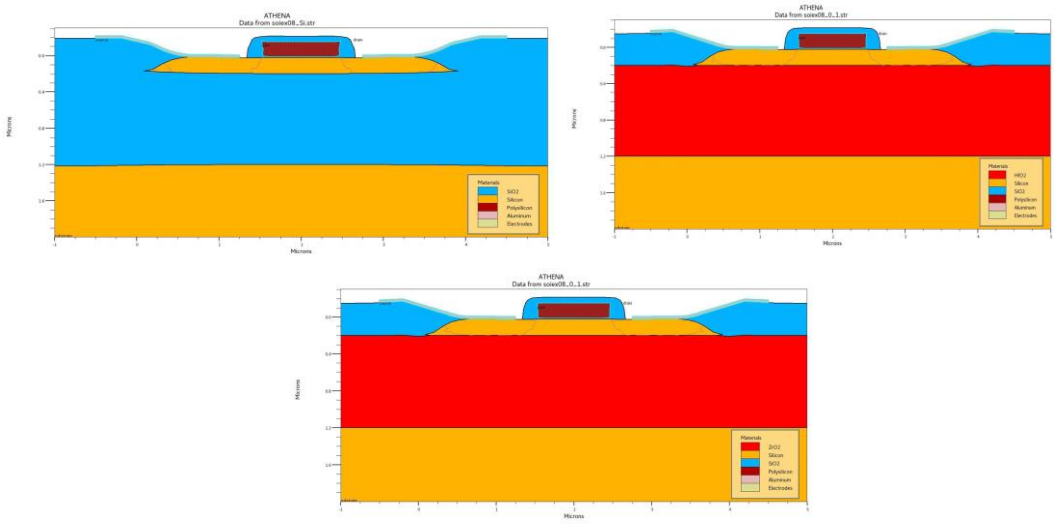

Figure 1: PD-SOI MOSFETs Using $SiO_2$, $HfO_2$ and $ZrO_2$ as buried oxide material

region) as the buried oxide. Second device contains $HfO_2$ and the last device contains $ZrO_2$ (red region).

Figure 2 displays all three devices with their net doping concentration. Net doping concentration $p0=(N_A-N_D)$, where $N_D$ represents the net n-type dopant concentration on the n-side and $N_A$ represents the net p-type dopant concentration on the p-side.

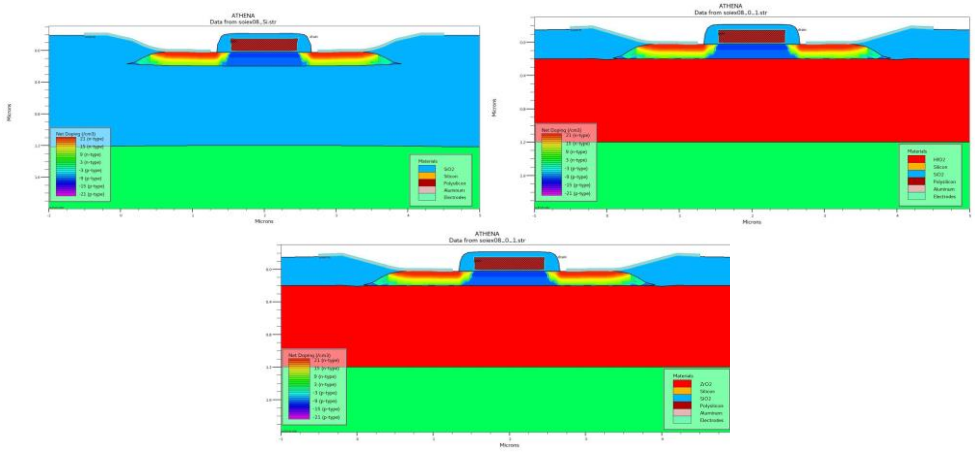

Figure 2: Net Doping Concentration of PD-SOI MOSFETs Using $SiO_2$, $HfO_2$ and $ZrO_2$ as buried oxide material

The newton approach defined in the method statement was chosen as the numerical algorithm for this system of equations. The semiconductor equations are also defined using this statement. carr=2 will solve the potential equation as well as the hole and electron continuity equations.

At each of these bias conditions, the gate voltage is ramped to 0.5, 1, 3, and 5 V and a solution is saved. Using the load command, each solution is then used as the initial starting point for simulating the Ids/Vds characteristics. The terminal characteristics are

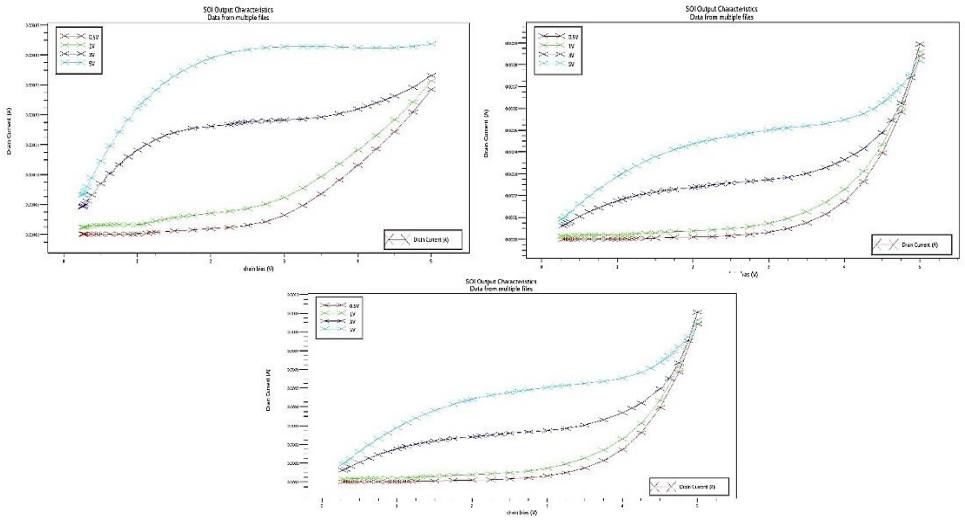

Figure 3: Drain Bias VS Drain Current Graph of PD-SOI MOSFETs Using $SiO_2$, HfO and ZrO as buried oxide material

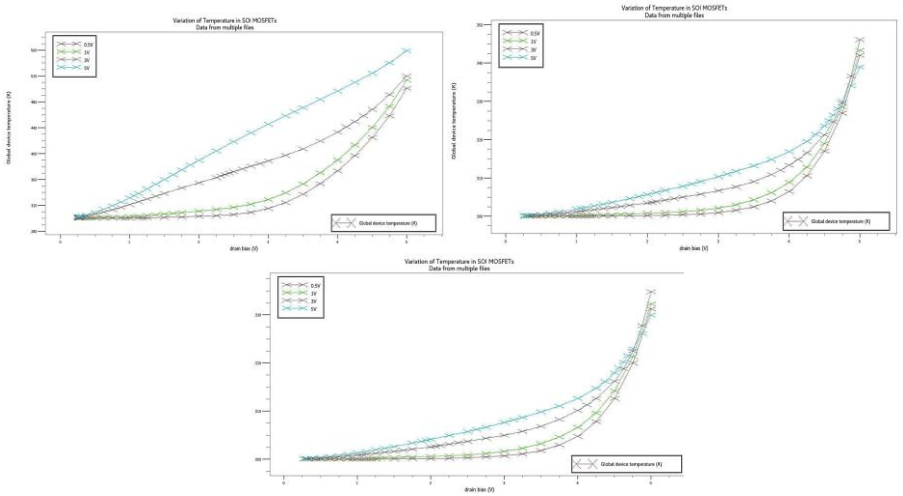

Figure 4: Drain Bias VS Global Temperature Graph of PD-SOI MOSFETs Using $SiO_2$, $HfO_2$ and $ZrO_2$ as buried oxide material

then saved in a logfile, and the drain bias sweep is applied using a solve statement. After that, the procedure is repeated for each gate voltage.

Figure 3 shows the variation in drain current for the same drain bias given for all three devices. Vg (gate voltage) is taken as 0.5V, 1V, 3V and 5V.

Figure 4 is the output of plotting global temperature variation for the same drain bias profile which was taken for Figure 3 which shows less temperature to be generated for the High-K Dielectric materials compared to $SiO_2$ for the same drain bias.

Figure 5 shows the lattice temperature of the 3 devices. The hcte.el parameter in the DeckBuild code specifies the electron energy balance equation, as well as the lattice heat flow formula is solved with Giga framework by establishing the parameter

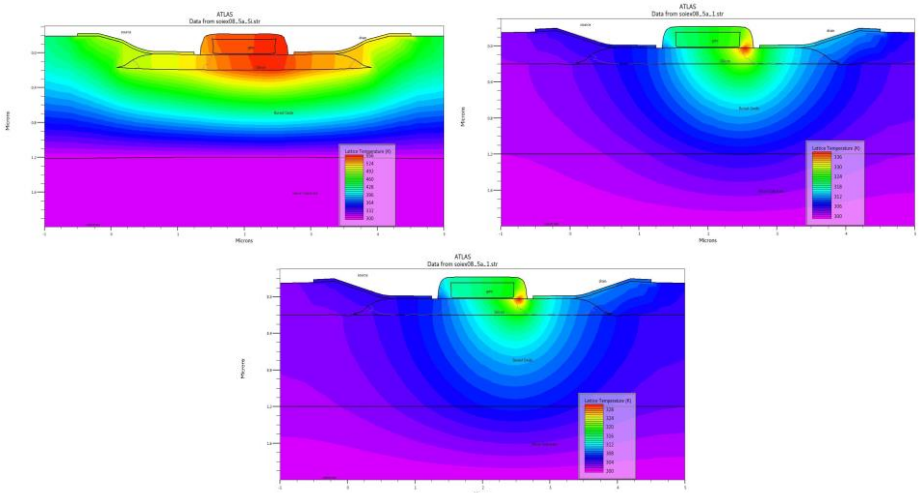

Figure 5: Lattice Temperature of PD-SOI MOSFETs Using $SiO_2$, $HfO_2$ and $ZrO_2$ as buried oxide material

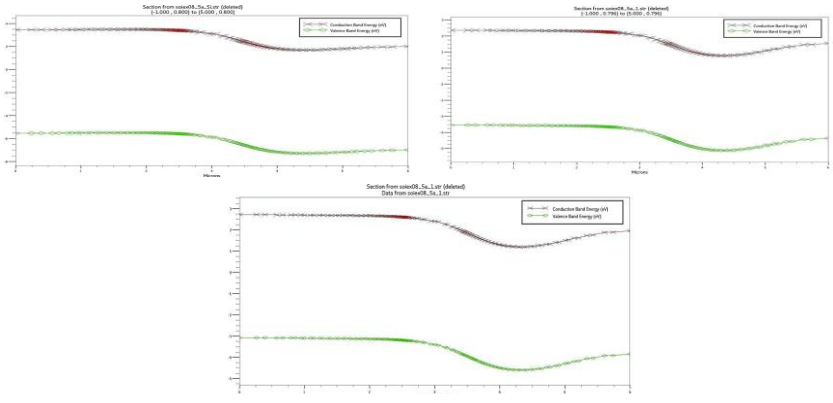

Figure 6: Energy band diagram of PD-SOI MOSFETs Using $SiO_2$, $HfO_2$ and $ZrO_2$ as buried oxide material

lat.temp. Improvement can be seen in terms of lessening the area affected by high lattice temperature in the devices where $HfO_2$ and $ZrO_2$ are used instead of $SiO_2$.

Figure 6 displays band bending of conduction band and valence band for all three devices. The parameters val.band, con.band and band.param are used to get the energy band diagram.

## 5. CONCLUSION

This paper observes how a PD-SOI MOSFET is fabricated using SILVACO TCAD. It also observes the device structure, net doping concentration and lattice temperature due to changing the buried oxide layer from $SiO_2$ to high-k dielectric materials such as $HfO_2$ and $ZrO_2$ can bring changes to the device. Device characteristics such as the variation in drain current and global temperature with drain bias and band diagram is shown here. The observations show how high-k dielectric materials can improve semiconductor device characteristics and give better results compared to materials such as $SiO_2$.

## 6. ACKNOWLEDGMENT

I deeply acknowledge Prof. Satyaranjan Bhattacharyya for providing guidance during preparation of the manuscript.

## 7. REFERENCES

[1] Verma, J.P.N., Mani, P. Surface Potential Modeling and Performance Investigation of Delta Doped DMG SOI MOSFET for Improved AF Parameters. Silicon 14, 8845–8854 (2022). https://doi.org/10.1007/s12633-021-01593-4.

[2] Kumawat. Jyoti and M. Yadav. Synthesis of Effect of Self Heating Effect on Electrical Characteristics in SOI MOSFET. International Journal of Soft Computing and Engineering (IJSCE) ISSN: 2231-2307, Volume-7 Issue-4, September 2017.

[3] Bhuyan, M.H., Islam, M.T. Study of an n-MOSFET by designing at 100 nm and simulating using SILVACO ATLAS simulator. IOSR Journal of VLSI and Signal processing 12(1):7-15 (2022). DOI:10.9790/4200-12010715.

[4] Silvaco Simulation Standard "The Industry Standard of SOI Technology From Process To Circuit Simulation" (1999). https://www.silvaco.com/simulation-standard/the-industry-standard-of-soi-technology-from-process-to-circuit-simulation/

[5] Verwey, J. F., Amerasekera, E. A., & Bisschop, J. (1990). The physics of SiO2layers. Reports on Progress in Physics, 53(10), 1297–1331. doi:10.1088/0034-4885/53/10/002.

[6] Izumi, K., Doken, M., and Ariyoshi, H., "C.M.O.S. devices fabricated on buried SiO2 layers formed by oxygen implantation into silicon", Electronics Letters, vol. 14, p. 593, 1978. doi:10.1049/el:19780397.

[7] Johnson, B., & Jones, J. L. (2019). Structures, Phase Equilibria, and Properties of HfO2. Ferroelectricity in Doped Hafnium Oxide: Materials, Properties and Devices, 25–45. doi:10.1016/b978-0-08-102430-0.00002-4.

[8] Horti, N. C., Kamatagi, M. D., Nataraj, S. K., Wari, M. N., & Inamdar, S. R. (2020). Structural and optical properties of zirconium oxide (ZrO2) nanoparticles: effect of

calcination temperature. Nano Express, 1(1), 010022. doi:10.1088/2632-959x/ab8684.
[9] McPherson, J., Kim, J.-Y., Shanware, A., & Mogul, H. (2003). Thermochemical description of dielectric breakdown in high dielectric constant materials. Applied Physics Letters, 82(13), 2121–2123. doi:10.1063/1.1565180
[10] Silvaco Athena User Manual August 13, 2015 Page 364
[11] https://www.azom.com/properties.aspx?ArticleID=133
[12] Li, Jinping, Meng, Songhe, Niu, Jiahong, Lu, Hantao. (2017). Electronic structures and optical properties of monoclinic ZrO2 studied by first-principles local density approximation + U approach. Journal of Advanced Ceramics, 2017, 6(1): 43-49. doi:10.1007/s40145-016-0216-y.
[13] Silvaco Atlas User Manual December 15, 2020 Page 1374, 1693
[14] Bustam, M. S. A., Sauki, N. S. M., Ismail, L. N., Sihab, N., Razak, F. A., & Muhamad, N. A. (2020). Study the effect of channel doping concentration on electrical properties of SOI MOSFET using Silvaco TCAD simulator. Proceedings of The 7th International Conference on Electronic Devices, Systems and Applications (ICEDSA2020). doi:10.1063/5.0033565.

## Biographies

**Bidyendu Ghoshal** received the bachelor's degree in Electronics & Communication engineering from Techno Main, Saltlake, India in 2021 and is pursuing master's degree in Microelectronics & VLSI Technology from Institute of Engineering and Management Kolkata, India.

**Prof. Samit Karmakar** is currently working as an Assistant Professor at the Department of Electronics & Communication Engineering, Institute of Engineering and Management, Kolkata. His research areas include Materials Sc. & Nano-Technology, Graphene, Quadrupole Residual Gas Analysis. He has been serving as a reviewer for many highly-respected journals.

**Prof. Soumik Kumar Kundu** is currently working as an Assistant Professor at the Department of Electronics & Communication Engineering, Institute of Engineering and Management, Kolkata. His research areas include Materials Sc. & Nano-Technology, Graphitic Carbon Nitride.

**Prof. Mili Sarkar** is currently working as an Assistant Professor at the Department of Electronics & Communication Engineering, Institute of Engineering and Management, Kolkata. His research areas include Digital and Analog VLSI circuits. She has been serving as a reviewer for many highly-respected journals.

**Dr. G. S. Taki** is currently working as a Professor at the Department of Electronics & Communication Engineering, Institute of Engineering and Management, Kolkata. His research areas include Materials Sc. & Nano-Technology and he specializes in RF & Microwave Engineering, Ion source, Accelerator physics & Engineering. He has been serving as a reviewer for many highly-respected journals.